Investigating the Impact of Single Molecule Fluorescence Dynamics on Photo Activated Localization Microscopy Experiments

THÈSE N^{O} 5517 (2012)

PRÉSENTÉE LE 8 OCTOBRE 2012
À LA FACULTÉ DES SCIENCES DE LA VIE
LABORATOIRE DE BIOLOGIE À L'ÉCHELLE NANOMÉTRIQUE (SV/STI)
PROGRAMME DOCTORAL EN PHYSIQUE

ÉCOLE POLYTECHNIQUE FÉDÉRALE DE LAUSANNE

POUR L'OBTENTION DU GRADE DE DOCTEUR ÈS SCIENCES

PAR

Paolo ANNIBALE

acceptée sur proposition du jury:

Prof. H. Rønnow, président du jury
Prof. A. Radenovic, directrice de thèse
Prof. A. Diaspro, rapporteur
Prof. R. Maggio, rapporteur
Dr A. Verkhovski, rapporteur

ÉCOLE POLYTECHNIQUE
FÉDÉRALE DE LAUSANNE

Suisse
2012

Abstract

When fluorophores are densely packed in a biological sample, localizing them one at a time is one of the paths to optical super-resolution. Photo Activated Localization Microscopy (PALM) is one of the methods of this burgeoning field that presents a large promise for addressing physical and biological questions requiring non-invasive, high-resolution optical imaging at the nanoscale. Since this work began when PALM was only two years old, the thesis contains a significant portion of research on the technique itself, and has therefore a marked methodological cut.

The principal, and recurring, theme is the investigation of the single molecule fluorescence dynamics of the fluorophores used, that in the end determine to a large extent the ensemble imaging performance as well as the interpretation of the data. A few assumptions reported in the literature are questioned, and, beginning with a discussion of the properties of a bright fluorescent protein, mEos2, we propose an original approach based on the use of the temporal information besides the spatial one when treating PALM data. This allows both a more accurate quantification of the number of fluorophores activated in the sample as well as the correct identification of relevant biological structures, such as clusters, on the plasma membrane of cells.

The second theme is the application of PALM to probe the functional arrangement of an important class of cell membrane proteins, through the study of the prototypical G protein-coupled receptor $\beta 2$-Adrenergic Receptor. First, the well studied biological properties of this family of signaling proteins are used to validate the potential of this approach. Then, PALM is used to gain new insight on the basal arrangement of $\beta 2$-AR in a relevant biological context using tools from spatial point pattern analysis. Provided that appropriate control experiments are performed, PALM is shown to have the potential to be included in the palette of the available techniques to study membrane protein organization. An important finding is the quantification of a cell-type specific clustering of this receptor in cardiomyocite-like cells.

Finally, some technical issues relevant to dual color imaging, in particular concerning the axial stability of the microscope, are addressed as a third, perspective theme, together with a detailed first-time characterization of three representative fluorescent protein pairs currently available for dual color PALM imaging.

Keywords: fluorescence microscopy; single molecule detection; optical super-resolution; total internal reflection; fluorescent proteins; adrenergic receptor.

Résumé

Lorsque des fluorophores sont concentrés dans un échantillon biologique, les localiser un à un est un des chemins d'accès á la super-résolution optique. La Microscopie Photo Activated Localization Microscopy (PALM) est l'une des méthodes de ce domaine en plein essor qui est très promettant pour faire face à des questions physiques et biologiques qui nécessitent une imagerie optique à haute résolution et non-invasive à l'échelle nanométrique.
Lorsque ce travail a commencé le PALM n'existait que depuis deux ans, donc la thèse contient une partie importante de recherche sur la technique elle-même, et a un caractère méthodologique.

Le thème principal et récurrent de ce travail est l'enquête sur les propriétés moléculaires des fluorophores utilisés, qui jouent un rôle important en déterminant l'interprétation des données. Nous avons remises en question des hypothèses présentes dans la littérature, et, á partir des propriétés d'une protéine fluorescente très lumineuse, mEos2, nous proposons une approche originale basée sur l'utilisation de l'information temporelle ainsi que spatiale lors du traitement des données PALM. Cela permet une quantification plus précise du nombre de fluorophores activés dans l'échantillon ainsi que l'identification correcte des structures biologiques pertinents sur la membrane plasmique des cellules.

Le deuxième thème de ce travail de thèse est l'application du PALM pour sonder l'organisation fonctionnelle d'une classe importante de protéines membranaires, à travers l'étude du récepteur prototypique couplé aux protéines G, le récepteur $\beta 2$-adrénergique. Premièrement, les propriétés biologiques bien étudiées de cette famille de protéines de signalisation sont utilisés pour valider le potentiel de cette approche. Ensuite, le PALM est utilisé pour acquérir de nouvelles connaissances sur l'arrangement de base de la $\beta 2$-AR dans un contexte biologique pertinent à l'aide des outils de l'analyse de la distribution spatiale des points. Si des expériences de contrôle appropriées sont toujours effectuées, la thèse démontre que le PALM a le potentiel d'être inclus dans la palette des techniques disponibles pour étudier l'organisation des protéines membranaires. Une constatation importante est la quantification d'un regroupement de ce récepteur dans les cellules de type cardiomyocytes.

Enfin, certains aspects techniques liés à l'imagerie bicolore, en particulier concernant la stabilité axiale du microscope, sont abordées comme le troisième thème de la thèse, avec une caractérisation détaillée pour la première fois de trois paires de protéines fluorescentes prototypiques pour l'imagerie bicolore en PALM.

Mots-clés : microscopie à fluorescence ; détection de la molécule isolée ; optique super-résolution ; réflexion totale ; protéines fluorescentes ; récepteur adrénergique.

Reading guide

Chapter one motivates the title, discussing the main ideas behind PALM and single molecule spectroscopy. A compact literature review is followed by a discussion of the requirements for single molecule imaging, and an explanation of how the information from individual fluorescent molecules is distilled into a super-resolution image.

The experimental setup and the software developed to control the instruments are discussed in chapter two. Since an important ingredient of single molecule imaging is the improvement of signal to noise ratio, a section of the chapter is a somewhat detailed diversion discussing the experimental realization of Total Internal Reflection microscopy.

The main results of the research work are introduced in chapter three. The common photochromic properties of photoactivatable fluorescent proteins are reviewed in the first part of the chapter. Our findings on the intermittent blinking and switching behaviour of mEos2, one of the newest and most promising PALM fluorophores are discussed, and the case is made about the need to establish an unambiguous correspondence between fluorescent emission and individual molecules. The rest of the chapter is devoted to discuss a method to take into account molecular blinking by comparing in-vitro experiments and computer simulations.

The extension of these ideas to a biological context is introduced in chapter four by comparing two opposite cases in the arrangement of a plasma membrane protein: a negative and a positive control for clustering. The arrangement of a fluorophore fused to a plasma membrane targeting sequence is used as a negative control for functional interaction, and it is compared to the arrangement of the β2-AR undergoing endocytosis. In this case the receptor is known to form aggregates at or near the plasma membrane. This crucial experiment allows to develop a method to reliably identify clustering in a PALM measurement using the temporal domain information contained in the data.

Using the tools developed in the previous two chapters, chapter five presents images of the plasma membrane arrangement of β2-AR in the cardyomyocite-like cell line H9C2. PALM is used to calculate the fraction of receptor assembled into clusters, and how this value changes across different cell types, and under different biochemical treatments.

Chapter six explores the potential of multi-color PALM imaging to probe sub-diffraction limit interactions between proteins with different labels. Using a setup axially stabilized to better than 5 nm we compare the performance of three different pairs of fluorescent proteins that can be used in dual color PALM. Fusion constructs are imaged either in vitro or at the cell plasma membrane. The better performing pair is identified, and a concluding perspective application to a co-clustering study at the plasma membrane is presented.

The concluding remarks go through the three main themes discussed in this thesis: PALM and the implications of single molecule photophysics in protein counting, PALM and membrane receptors and finally PALM used to study the interaction of two different species. For each of these themes perspective developments are discussed.

During my thesis, I wrote the following publications on PALM. The first and third papers are the basis for chapter 3. The Nature Methods work corresponds to chapter 4. The results of the Journal of Biological Chemistry paper are presented in chapter 5. Chapter 6 is the basis for a manuscript in preparation. A full list of publications can be found in the CV at the end of the thesis.

- P. Annibale, M. Scarselli, A. Kodyan, A. Radenovic, Photoactivatable Fluorescent Protein mEos2 Displays Repeated Photoactivation after a long-lived dark state in the red photoconverted form, *The Journal of Physical Chemistry Letters*, 1, 1506-1510 (2010)
- P. Annibale, S. Vanni, M. Scarselli, U. Roetlisberger and A. Radenovic, Identification of clustering artifacts in Photo Activated Localization Microscopy, *Nature Methods*, 8, 527-528 (2011)
- P. Annibale, S. Vanni, M. Scarselli, A. Radenovic, Quantitative PhotoActivated Localization Microscopy, unraveling the effects of photoblinking, *PloS One*, 6, 1-8 (2011)
- M. Scarselli, P. Annibale, A. Radenovic, Cell-type-specific $\beta 2$ adrenergic receptor clusters identified using photo-activated localization microscopy are not lipid raft related, but depend on actin cytoskeleton integrity, *The Journal of Biological Chemistry*, 287, 16768-16780 (2012).
- P. Annibale, M. Scarselli, M. Greco, A. Radenovic, Axial stabilization of a commercial setup enables 15 nm registration accuracy and 35 nm colocalization precision in dual color super-resolution experiments using photoactivatable fluorescent proteins *in preparation*

Contents

Abstract (English/Français) iii

Reading guide vii

List of figures x

List of tables xiii

1 Single molecules and Photo Activated Localization Microscopy 1

1.1 Photo Activated Localization Microscopy 1
1.2 Single molecule imaging 2
1.3 Single molecule localization 4
1.4 Data Analysis 6

2 Development of the super-resolution microscope 11

2.1 Introduction 11
2.2 Excitation setup 11
  2.2.1 Photo-activation beam 13
  2.2.2 Acousto Optic Tunable Filter 13
  2.2.3 Total Internal Reflection 14
2.3 Axial Stabilization by TIR 19
2.4 Detection 21
  2.4.1 EM-CCD camera 21
  2.4.2 Detection Beamsplitter 27
2.5 Overall synchronization of the setup 28

3 Investigating the effects of photoblinking in a prototypical photoconvertible fluorescent protein 31

3.1 Photoactivatable fluorescent proteins and reversible fluorescence switching 31
3.2 mEos2: unexpected switching behavior 35
  3.2.1 PolyVinyl Alchool measurements 35
  3.2.2 Computer simulations of experimental results 42
3.3 Discussion 53

4 Identification of clustering artifacts in Photo Activated Localization Microscopy 55

4.1 Introduction 55
4.2 Analysis of clustering artifacts in Photo Activated Localization Microscopy 58
4.3 Discussion 63

5 The membrane distribution of β2-Adrenergic Receptor **65**
5.1 Introduction 65
5.2 Treating membrane heterogeneities using the point pattern picture 69
5.2.1 The clustered fraction method 70
5.2.2 Ripley's K function analysis 70
5.3 Measurement of the clustered fraction and $L(r) - r$ function of cell membrane receptors 72
5.4 Cell-type specific and cytoskeletal dependence of β2-AR clusters in H9C2 cell line 76
5.5 Discussion 85

6 Development of accurate dual-color PALM imaging **87**
6.1 Introduction 87
6.2 Strategies in dual-color super-resolution microscopy 88
6.3 Aligning the two-color imaging channels 90
6.4 nm-range stabilization of the imaging plane 95
6.4.1 Experimental determination of the registration accuracy 97
6.5 Choosing the fluorophore pair for dual-color PALM 100
6.5.1 mEos2-Dronpa 101
6.5.2 PSCFP2-mEos2 103
6.5.3 PSCFP2-pamCherry1 109
6.6 Dual-color imaging using PSCFP2-pamCherry1 114
6.6.1 Protein fixation 118
6.7 Discussion 120

7 Conclusions and Perspectives **121**
7.1 Conclusions 121
7.2 Future directions 123

A Choice of clustering parameters **127**

B Photophysical model for mEos2 **133**

C Materials and Methods **137**
C.1 Molecular Biology 137
C.2 Functional assay 138
C.3 Cell culture 139
C.4 Sample fixation 140
C.5 Protein purification and in-vitro sample preparation 140
C.6 Spectra 141

D β2-AR in CHO cells and M3 muscarinic receptor in HeLa and H9C2 cell lines. **143**

Bibliography **157**

Acknowledgements **159**

Curriculum Vitae **161**

List of Figures

1.1 Concept of PALM imaging . . . 3
1.2 Single molecule frame . . . 5
1.3 Diagram of how the PALM data are analyzed. . . . 7
1.4 Diagram of how the PALM data are analyzed (continued). . . . 8
1.5 Distributions of single molecule properties . . . 9
1.6 From the diffraction limit to PALM depending on SNR . . . 10

2.1 Excitation platform top . . . 12
2.2 Excitation platform side . . . 12
2.3 Side view of the scope . . . 14
2.4 TIR configurations . . . 16
2.5 Ray tracing TIR configuration b . . . 17
2.6 Epifluorescence to TIRF 1 . . . 18
2.7 Epifluorescence to TIRF 2 . . . 19
2.8 Polarizations in TIRF . . . 20
2.9 Axial stabilization optics . . . 20
2.10 PID panel . . . 21
2.11 Andor iXon DU-897 EM-CCD camera . . . 22
2.12 Schematics of the frame transfer mechanism . . . 23
2.13 Schematics of the readout modes and of the timings of the different regions of the CCD camera chip during a typical acquisition . . . 24
2.14 Snapshot of the block diagram of the initialization step of the camera in the LabView code controlling the PALM setup . . . 25
2.15 Snapshot of the configuration step of the camera. . . . 26
2.16 Experimental Photon Transfer Curve of the Andor iXon DU-897 obtained using the conventional output amplifier (green markers) or the EM amplifier with a gain of 100 (red markers). . . . 27
2.17 Front Panel of the Virtual Instrument controllingl the PALM setup. . . . 29

3.1 Absorbance and emission spectra of the wtGFP chromophore. . . . 32
3.2 Proposed model for the switching and blinking behavior of the T203F and T203Y GFP mutants . . . 32
3.3 Evolution of the absorption spectrum of Dronpa . . . 33
3.4 On-Off swtiching behavior of Dronpa in ensemble fluorescence measurements . . . 34
3.5 Scheme for the reversible switching observed in E222Q mutants . . . 35
3.6 Absorbance, excitation and emission spectra of Eos . . . 36
3.7 Single molecule kymograph for an individual mEos2 molecule . . . 38

3.8 Histograms of the measured *on*-times for single molecular frames together with simple exponential fits . . . 39
3.9 Amount of localized molecules in a diluted PVA sample as a function of the time interval t_d. (reprinted from Annibale *et al.* [40]) . . . 40
3.10 Representation of molecular localizations using a Gaussian Probability Distribution Function. . . . 41
3.11 Measured Empirical Cumulative Distribution Function . . . 43
3.12 Photophysical parameters of mEos2 in PAGE . . . 45
3.13 Simulated PALM localization density curves as a function of t_d . . . 47
3.14 Experimental (markers) and simulated (blue line) total numbers of mEos2 molecules . . 48
3.15 Single molecule kymographs of 6 blinking/reactivating molecules. . . . 49
3.16 Semi-empirical fit to simulated data. . . . 51
3.17 Fitting to simulated missed counts curves under different conditions. . . . 52
3.18 Calibration curve for the concentrations extracted by fitting eq. 3.5 to PALM data. . . . 52

4.1 Signal transduction in G protein-coupled receptors . . . 56
4.2 Confocal images of cells expressing β2-AR . . . 58
4.3 TIRF-PALM image of a region of the cell expressing β2-mEos2 . . . 59
4.4 Protein clustering on plasma membrane . . . 61
4.5 Snapshots of molecular clusters on the plasma membrane of fixed HeLa cells. . . . 62

5.1 TIRF images of H9C2 cells . . . 66
5.2 Estimation of the transfection levels in H9C2 cells . . . 66
5.3 From TIRF to PALM . . . 67
5.4 Colocalization of β2 and actin in an H9C2 cell. . . . 68
5.5 Clustering on the plasma membrane . . . 71
5.6 Ripley's analysis of redwood forest . . . 72
5.7 Spatial point pattern analysis of SrcN15-mEos2 on the plasma membrane of HeLa cells. . 73
5.8 Point pattern of β2-mEos2 on the plasma membrane of an H9C2 . . . 74
5.9 Map of the localized centers for mEos2 (red) and Dronpa (green) molecules activated in PAGE at low concentration . . . 75
5.10 PALM images and cluster analysis of β2-AR labeled with mEos2 (β2-mEos2) on the plasma membrane of HeLa cells before and after agonist addition. . . . 77
5.11 Histogram of the measured clustered fraction in HeLa under different stimulation conditions . . . 78
5.12 PALM images and cluster analysis of β2-mEos2 on the plasma membrane of H9C2 cell line 79
5.13 Histogram displaying the distribution of the number of molecules belonging to each clusters . . . 80
5.14 Comparison of Ripley's $L(r) - r$ function calculated for β2 in basal conditions . . . 81
5.15 PALM images and cluster analysis of β2-mEos2 on the plasma membrane of H9C2 . . . 81
5.16 a) Histogram of the measured clustered fraction in H9C2 under different stimulation conditions: SrcN15 as a control, β2-AR in basal conditions . . . 82
5.17 PALM images and cluster analysis of β2-mEos2 and of the non-clustering peptide SrcN15-mEos2 on supported cell-membrane sheets of H9C2 cells. . . . 83
5.18 H9C2 cells were transfected with GFP-actin, fixed and then imaged in TIRF geometry. . . 84
5.19 Comparison of the measured clustered fraction across different experimental subgroups. 85

6.1 Localization precision in dual-color PALM. . . . 89

6.2 Registration protocol 90
6.3 Registration grid 92
6.4 Chromatic offset 93
6.5 Registration protocol 96
6.6 Validation of registration protocol 97
6.7 Lateral drift 98
6.8 Protocol for dual-color PALM imaging 99
6.9 Modes of dual-color imaging 101
6.10 mEos2 photoconversion 102
6.11 Dronpa 103
6.12 mEos2-Dronpa single molecule 104
6.13 Evolution of the fluorescence of mEos2(R) and PSCFP2(G) 106
6.14 Absorption spectrum of PSCFP2-mEos2 fusion 107
6.15 mEos2-PSCFP2 single molecules 108
6.16 Ensemble spectroscopic characterization of PSCFP2-pamCherry fusion protein 110
6.17 pamCherry1-PSCFP2 single molecules 111
6.18 Contour plot of the localization precision of pamCherry1 PSCFP2 112
6.19 Evolution of the number of PSCFP2 fluorophores in a sequential dual-color experiment . 113
6.20 Dual-color artifact free imaging of a pair of membrane proteins 115
6.21 PALM image of the β2-AR undergoing constitutive intrnalization 116
6.22 DIC image of HeLa cell and overlay of red channel PALM image showing clathrin coated pits on the plasma membrane 117
6.23 β2-mEos2 diffusion upon fixation 119

A.1 Comparison of the measured clustered fraction across different experimental subgroups. 127
A.2 Spatial point pattern of β2-mEos2 measured in an H9C2 cell 128
A.3 Simulated spatial point patterns displaying clustering 129
A.4 $(L(r)-r)_{max}$ vs experimental clustered fraction for β2 basal 130
A.5 Measured clustered fraction for β2 basal, SrcN15 and β2 -actin and β2 -cholesterol in H9C2 cells plotted vs sample density. 131

B.1 Graphical comparison between a one and a two dark states models. 133
B.2 Comparison between one and a two dark states models. 135

C.1 Functional characterization and cell expression of the constructs β2-mEos2 139
C.2 Spectral signatures of the pairs of Photo-Activatable fluorescent proteins discussed in this chapter, as well as a combination of the optical filters used in the emission path. a) mEos2 and Dronpa. b) PSCFP2 and mEos2. c) and mEos2 prior to photoconversion. d) Set of dichroic mirrors and emission filters used in the dual color setup 141

D.1 PALM image of the M3 muscarinic receptor labeled with PSCFP2 144
D.2 PALM image of the β2-Adrenergic receptor labeled with mEos2 145

List of Tables

6.1 Test of three PALM PA-FPs fusion constructs in multiple environments 100
6.2 Photoconversion efficiencies for the three pairs of PA-FP investigated so far. 113

1 Single molecules and Photo Activated Localization Microscopy

1.1 Photo Activated Localization Microscopy

The best resolution that can be achieved by diffraction limited optical techniques is two orders of magnitude coarser than the molecular level. Photo Activated Localization Microscopy (PALM) is a fluorescence microscopy technique that allows to obtain optical super-resolution (images with discernible features below the diffraction limit, as defined by Abbe's criterion $d = \frac{\lambda}{2NA}$, where λ is the wavelength of light and NA is the numerical aperture of the optical system) by means of the sequential localization of individual fluorescent emitters. This approach to achieve optical resolution at the molecular level requires two steps: first the identification of each molecule through some distinguishing optical property, and second its precise localization [1]. If the emission from two neighboring molecules is made distinguishable, and the photons coming from each of the two can be identified, then it is possible to overcome the diffraction limit. Once a set of photons from a specific molecule is collected, its image in the light microscope corresponds to a diffraction limited spot, known as the Point Spread Function (PSF) of the microscope. However it is possible to localize the molecule as the center of this spot with an accuracy that depends on the Signal to Noise Ratio (SNR) rather than on the size of the PSF.

It is insightful to review two attempts to identify single molecules below the diffraction limit, prior to the widespread application of optical super-resolution methods since 2006. In 1999 van Oijen *et al.* [2] exploited the fact that at low temperature each molecule has a precise optical transition, and depending on the local environment, it may slightly differ from the one of a neighboring molecule. Therefore, by carefully tuning the energy of the excitation light it is possible to selectively excite two molecules in the same diffraction limited volume. In another instance, Qu *et al.* [3] reported on the observation of the fluorescence time trace of a nanoscopic molecular aggregate. Photobleaching events (i.e. irreversible destruction of the chromophore) were used to identify the photons coming from each individual molecule, despite belonging to the same diffraction limited volume.

The development of photoactivatable fluorescent proteins, or the use of pairs of organic dyes to obtain reversible switching between active and inactive states, opened the way to the use of temporal multiplexing when imaging individual fluorophores. In other words, it allowed to distinguish the emission from many fluorophores within the same diffraction limited region by turning them on one at a time. The concept was developed in a somehow parallel way by three independent groups, giving rise to three similar techniques that are known as PALM, fPALM and STORM [4], [5], [6].

Historically other concepts to achieve optical resolution below the diffraction limit were developed in a parallel way. Among them, the idea of exploiting stimulated-emission-depletion to reduce the size of the excitation PSF in a laser scanning microscope developed into STED microscopy, the other important member of the family of optical super-resolution methods [7]. The following discussion will be confined to PALM, as originally proposed by Betzig *et al.* [4]. The method relies on the use of fluorophores that can be simplistically modeled as two-states systems and are able to switch from a dark *off* to a bright *on* state. We will discuss in more detail in chapter 3 the mechanisms that give rise to this interesting property in fluorescent proteins. The cornerstone of the method is represented by the possibility of measuring a sample where all the fluorophores are *off*, and then to obtain very precise localization information by turning them *on* one at a time using violet light.

Under appropriate conditions individual fluorophores can be seen even by the naked eye, and the localization precision of an individual emitting source can be significantly smaller than the full width half maximum of the PSF of the microscope. Once a fluorophore has emitted a certain amount of photons, the chromophore is destroyed, in a process commonly known as photobleaching. By imaging in cycles those frames containing a sparse population of *on* fluorophores, replacing those that bleach with new ones activated from the *off* state, PALM is capable of sequentially localizing a large number of molecules within a relatively small region of space, as illustrated in figure 1.1 a. The position of the centers of each localized molecule represent the super-resolution image, containing spatial information that would be lost if all the molecules had been activated at once, as shown in figure 1.1 b, c and d.

The first PALM work [4] addressed both intracellular and plasma membrane structures, including the mitochondrial matrix, the lysosomal membrane, focal adhesion complexes and the retroviral protein Gag budding at the cell plasma membrane. This seminal work was soon followed by reports on dual-color PALM imaging [8], live fPALM of membrane clusters [9] (this and related works will be discussed in more detail in chapter 5) and focal adhesion complexes [10]. Extension to three dimensional imaging was developed observing focal adhesions with a stunning axial resolution below 20 nm by Shtengel *et al.* [11], using an interferometric approach named iPALM.

Greenfield *et al.* [12] were the first to propose explicitly the use of PALM as a way to actually count individual proteins, in their effort to understand the E-Coli chemotaxis network. A large part of this thesis work is devoted to the understanding of the conditions that support this assumption, with a particular attention to the fluorescence dynamics of the individual fluorescent proteins used in PALM experiments. Besides being a powerful imaging tool, PALM is ultimately a single molecule spectroscopy method, and as such is extremely sensitive to the photophysical properties of the fluorophores that are employed.

1.2 Single molecule imaging

As previously mentioned, the human eye can see the light from a single molecule in the eyepiece of a microscope that efficiently collects the emitted photons. The optical detection of single molecules requires that a particle emits light, that the detection system is sensitive enough and the imaging system has enough spatial resolution. Finally, and most importantly, it is necessary that there is a sufficient Signal to Noise Ratio (SNR) (for an exhaustive review on single molecule imaging, see [13] and references therein). A fluorescent single molecule can be interpreted as a geometrical absorber having a typical cross section to visible light $\sigma \sim 10^{-15}\ cm^2$, corresponding to $\sim 0.1\ nm^2$.

Ideally any fluorophore can be represented as a two state system, driven from the ground to the

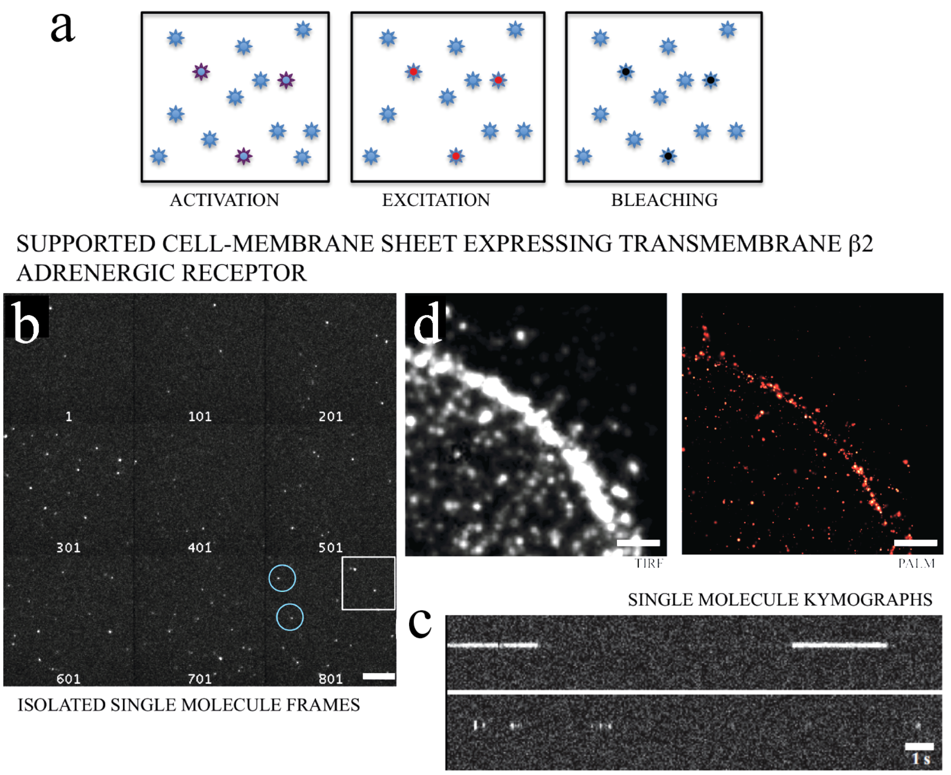

Figure 1.1: Concept of PALM imaging. a) a few molecules are activated to the *on* state out of a large pool of inactive (*off*) molecules. Active molecules are imaged until bleached, and their position and localization uncertainty stored after they have bleached. The sequence is repeated until no more molecule are present in the sample. b) The experimental data is therefore represented by a large sequence of images each containing a few fluorescent bursts from single molecules. c) The fluorescent traces are then regrouped and single molecule images are fit to find the molecular coordinates. d) The image resulting from the ensemble of these super-resolution coordinates (right) compares favorably to the diffraction limited case (left).

excited state by the absorption of a single photon. Depending on the structure of the molecule, the temperature and the host matrix, not all of the photons absorbed will be emitted, since non-radiative decay pathways coexist together with radiative decay. The ratio between the emitted and absorbed photons determines the Quantum Yield (Q.Y.) of the fluorophore, ideally one, most typically a fraction of this value. For example, EGFP, a bright fluorescent protein derived from wtGFP [14], has a $Q.Y. \sim 0.6$. The lifetime of the excited state τ determines the maximum number of photons that can be absorbed per unit time by the fluorophore, determining the saturation intensity I_s. Lifetimes for the excited state are typically comprised between one and ten ns, placing the maximum emission of a fluorophore, in the ideal case, to 10^9 photons per s, corresponding to 1 nW of emitted power. Typical excitation powers in the Total Internal Reflection Fluorescence (TIRF) configuration that will be described in the following chapter span the range between one $\frac{W}{cm^2}$ and one $\frac{kW}{cm^2}$. [1]

Typical absorption cross sections for GFP-like fluorescent proteins are in the range of $\sigma_{GFP} \sim 10^{-16} cm^2$ and when exciting at one $\frac{kW}{cm^2}$ the resulting absorbed power is in the range of 0.1 pW, resulting in $\sim 3 \cdot 10^5$ photons per second at 550 nm. Using the $Q.Y._{EGFP} = 0.6$, then $1.8 \cdot 10^5$ photons are emitted. Only a fraction of these photons will be collected by the objective, given the finite Numerical Aperture (N.A.) of the system. Using a typical $NA \sim 1.4$ results in a collection angle of $\theta \sim 70^o$ and a collection efficiency of 0.2, resulting in 36000 collected photons if the molecule emits continuously for 1 s. Typical detector efficiencies range from 0.1 to 0.9, depending on the type of detector and the spectral range. In the case of an average 0.5 detection efficiency, the number of photons detected will be ~ 20000.

This number shall be larger that the sum of the detector noise and the fluorescence background. As we will see in the following chapter in relation to TIRF, the reduction of the excitation volume is an effective way to improve the SNR in single molecule experiments, since effects such as residual fluorescence and Raman scattering of the host matrix scale as the illuminated volume [15]. Background sources such as reflections of the excitation light can be minimized using good quality optical filters and dichroic mirrors to separate excitation from fluorescence signal (typical emission filters reduce the signal from wavelengths outside the emission window of about six orders of magnitude). If the environment hosting the single molecule is very clean, background fluorescence can be greatly reduced . We will see in more detail that Electron Multiplying Charge Coupled Devices cameras (EM-CCD) such as the one used in this thesis, provide a readout noise as low as 5 counts/exposure, one order of magnitude below the minimum signal that can be expected even using the lowest excitation value of one $\frac{W}{cm^2}$.

1.3 Single molecule localization

An important concept is that, although the image of a point-like object such as a single molecule is a diffraction-limited large spot on the detector, as shown in figure 1.2 b, it is possible to find the center of this spot with sub-wavelength accuracy if the SNR is high enough. This concept was discussed in the framework of fluorescence microscopy by Thompson *et al.* [16] in 2002, who demonstrated that calculating the centroid of individual fluorescent particles enables localization and tracking to a precision of one order of magnitude greater than the microscope resolution, i.e. the diffraction limit. The localization precision ultimately depends on the SNR, and scales as $\frac{1}{\sqrt{N}}$ in the shot noise limited case (high signal) and as $\frac{1}{N}$ in the background limited case (low signal). The complete formula for the localization accuracy in two dimensions (assuming the isotropy of the single molecule emission) is

---

[1] The relation between molar extinction coefficient ϵ, that will be used in the following, and the cross section σ is given by $\sigma = 3.82 \cdot 10^{-21} \epsilon$

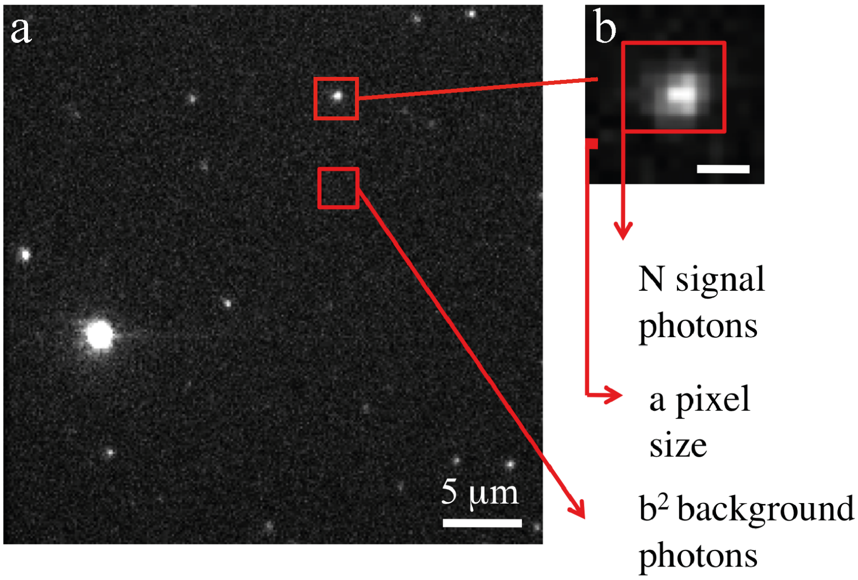

Figure 1.2: Single molecule frame. a) EM-CCD camera frame (50 ms exposure) displaying single molecules embedded in a Poly Acrylamide matrix together with a bright fiducial bead (Tetraspek, Invitrogen). From a single molecule N signal photons are calculated by integrating over a molecular window. b^2 background photons/pixel are calculated where the molecule is absent. The EM-CCD pixel size 1a is defined by the ratio of the physical camera pixel and the system magnification (133.33 nm in this case). b) single molecule image. The number of signal photons $N \sim 1500$. The number of background photons per pixel $b^2 = 20$. Scale bar is 500 nm.

given by:

$$\sigma^2 = \frac{s^2 + \frac{a^2}{12}}{N} + \frac{8\pi s^4 b^2}{N^2 \cdot a^2} \tag{1.1}$$

where s is the standard deviation of the microscope point spread function (approximated to a Gaussian), a is the pixel size and b^2 the number of background photons per pixel in the image. The first term, $\frac{s^2}{N}$ corresponding to the shot noise limited term, is easy to understand as the standard error of the mean of a distribution of photon locations scattering according to the microscope PSF. $\frac{a^2}{12}$ is an additive term due to the finite pixel size. $\frac{8\pi s^4 b^2}{N^2 \cdot a^2}$ is due to the background contribution, and its derivation can be found in [16]. Mortensen *et al.* [17] demonstrated that equation 1.1 underestimated the uncertainty of approximately 30%, and corrected it proposing the formula:

$$\sigma^2 = \frac{s_a^2}{N}\left(\frac{16}{9} + \frac{8\pi s_a^4 b^2}{N \cdot a^2}\right) \tag{1.2}$$

where $s_a^2 = s^2 + \frac{a^2}{12}$. This corrected expression for the localization precision will be used throughout this thesis.

1.4 Data Analysis

Each PALM experiment is therefore composed of a large stack of frames (such as the one displayed in figure 1.2), each containing a few single molecules in the active state. Each fluorescent emitter is associated to a bright peak over a dark background. Depending on the exposure time, the photophysics of the fluorophore and the excitation power, a single molecule may be *on* across multiple frames, including dark frames where the fluorescence has temporarily disappeared. The localization described in the previous section can be performed meaningfully only after that the molecule has permanently photobleached after exhausting its photon budget. Therefore all the frames where an individual molecule appeared should be integrated together to yield a molecular image containing the full signal arising from that molecule. For this reason the algorithm that analyzes the data and fits the molecular peaks needs to keep track of the history of each fluorescent spot.

This process is illustrated in figure 1.3 and figure 1.4. Starting from the first, the frames of the PALM stack are analyzed one by one (figure 1.3, b). The i^{th} frame is filtered using a combination of a Laplace (sharpening) and Gaussian (smoothing) filters that enhance the bright molecular peaks and reject both weak background and hot pixels. The position of those molecular peaks whose maximal intensity is larger than m times the standard deviation of the image is calculated and each localized peak is compared to the peaks localized in the $i^{th}-1$ frame to determine whether it is a new peak, a prosecution of a previous peak or a fiducial marker peak (figure 1.3, b). If in a given position a peak is not observed anymore for at least t_d frames, it is deemed permanently bleached. Around each peak a Region of Interest (ROI) of a few pixels in size is calculated (figure 1.3, c).

Once a peak is bleached, all the molecular frames associated to it are integrated and the resulting pixel values converted to photons via the photon conversion factor calculated for the camera at the selected

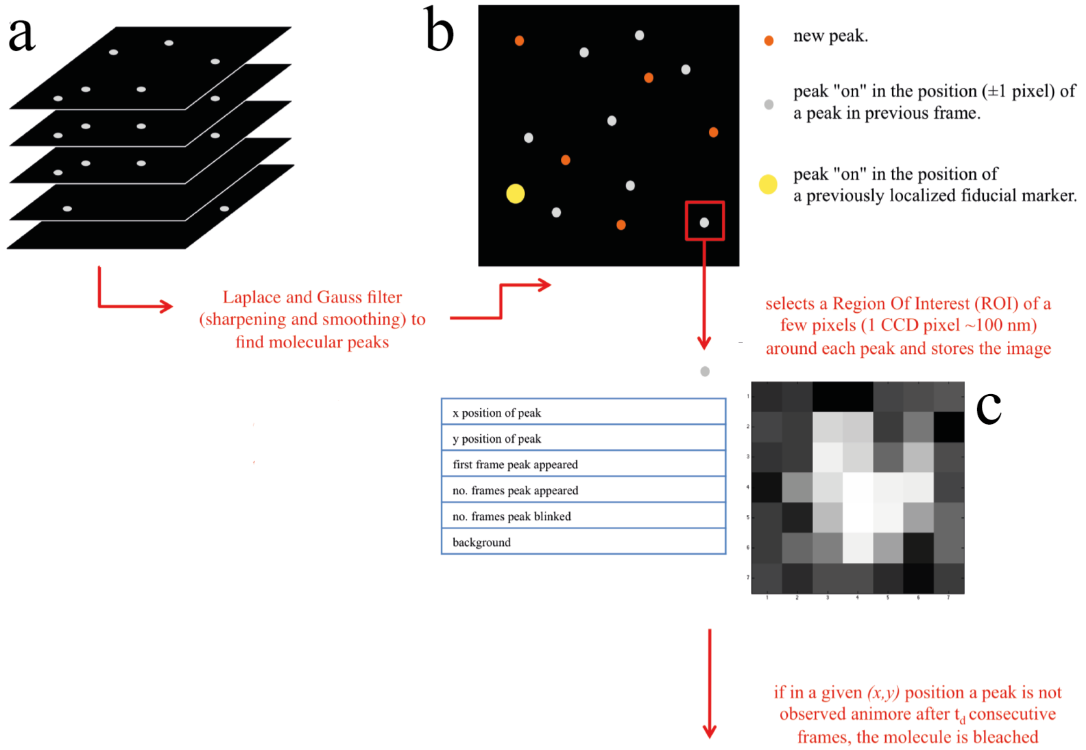

Laplace and Gauss filter (sharpening and smoothing) to find molecular peaks

selects a Region Of Interest (ROI) of a few pixels (1 CCD pixel ~100 nm) around each peak and stores the image

if in a given *(x,y)* position a peak is not observed animore after t_d consecutive frames, the molecule is bleached

Figure 1.3: Diagram of how the PALM data are analyzed. a) The stack of single molecule frames is cycled, and each frame is processed (Laplace and Gauss filter) to identify molecular peaks. Molecular peaks can belong to either fiducials, single molecules appearing in a given position at a given time or single molecules appearing in a given position for the first time. The local image of each peak is stored in a buffer together with informations about the position, the number of frames the peak has been on, and how many frames it was off.

gain level (more details in chapter 2). A circular binary mask with a radius equal to the PSF of the microscope is applied to the image (figure 1.4, b) and a background (figure 1.4, a) image based on the first frame prior to the appearance of the molecule is subtracted from the signal. The total number of photons from the resulting image is calculated, and if below a threshold (e.g. 100 photons) it is discarded. If the molecule is deemed bright enough, the molecular image is compared to a $x-y$ matrix of closely spaced gaussian functions representing the microscope PSF, and for each position a χ^2 value is calculated. The position of the gaussian mask minimizing the χ^2 determines the $x-y$ position of the molecule, as illustrated in figure 1.4 c, for four arbitrary selected positions of the gaussian mask. The localization precision for each molecular peak is then calculated according to equation 1.2.

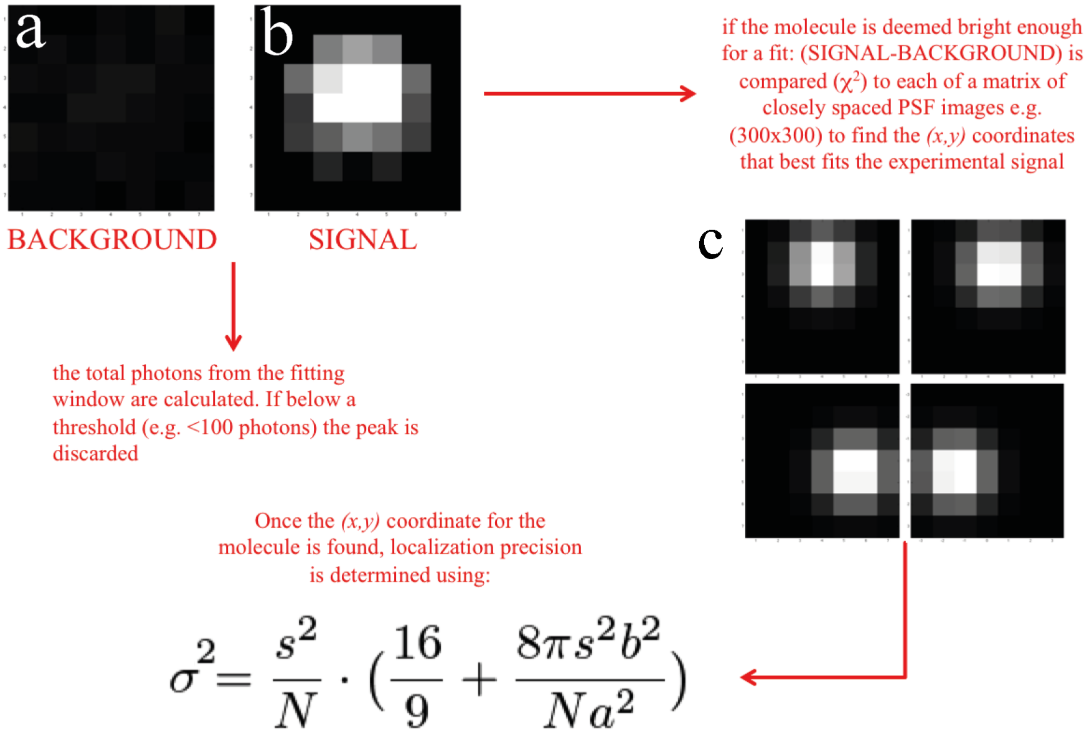

if the molecule is deemed bright enough for a fit: (SIGNAL-BACKGROUND) is compared (χ^2) to each of a matrix of closely spaced PSF images e.g. (300x300) to find the *(x,y)* coordinates that best fits the experimental signal

the total photons from the fitting window are calculated. If below a threshold (e.g. <100 photons) the peak is discarded

Once the *(x,y)* coordinate for the molecule is found, localization precision is determined using:

$$\sigma^2 = \frac{s^2}{N} \cdot \left(\frac{16}{9} + \frac{8\pi s^2 b^2}{N a^2}\right)$$

Figure 1.4: Diagram of how the PALM data are analyzed (continued). If a peak is not observed anymore at a given place for a certain amount of frames above a threshold t_d, then it can be fit. Once a peak is bleached the integrated frames associated to it are converted to photons via the photon conversion factor of the camera. A circular mask is applied around the brightest pixels. A background picture is calculated from the frame previous to the first peak appearence and multiplied for the number of frames that the peak was on.

Figure 1.5 displays the distributions for four important parameters measured for each single molecule in a representative PALM experiment performed by photoactivating in vitro ~ 2600 molecules. It is possible to determine, for instance, the number of molecules localized over time, a value depending on the photoactivation rate and that typically displays a saturating behavior of the form $1-e^{-t}$ since the molecular pool is slowly depleted by photobleaching. Histograms for the localization precision, lifetime of the single molecule and total signal photons collected can be easily calculated. In this case the time allowed for a molecule to go dark without bleaching, i.e. t_d, is set to just a few frames. We will see in the next chapters the importance of tuning this value accurately. Most of the molecules localize to better than 40 nm, and the mean localization precision achieved by using the bright photoactivatable fluorescent protein (PAFP) mEos2 is 18 nm. A single molecule is observed to emit fluorescence on average 250 ms, though the temporal distance between first photoactivation and bleaching is 0.5 s, indicating that the molecule spends approximately half of its time in a nonfluorescent dark state. On average, 2500 signal photons are collected from each molecule prior to bleaching. This wealth of information can be used to select subsets of molecules, e.g. focusing only on the molecules displaying a better localization precision.

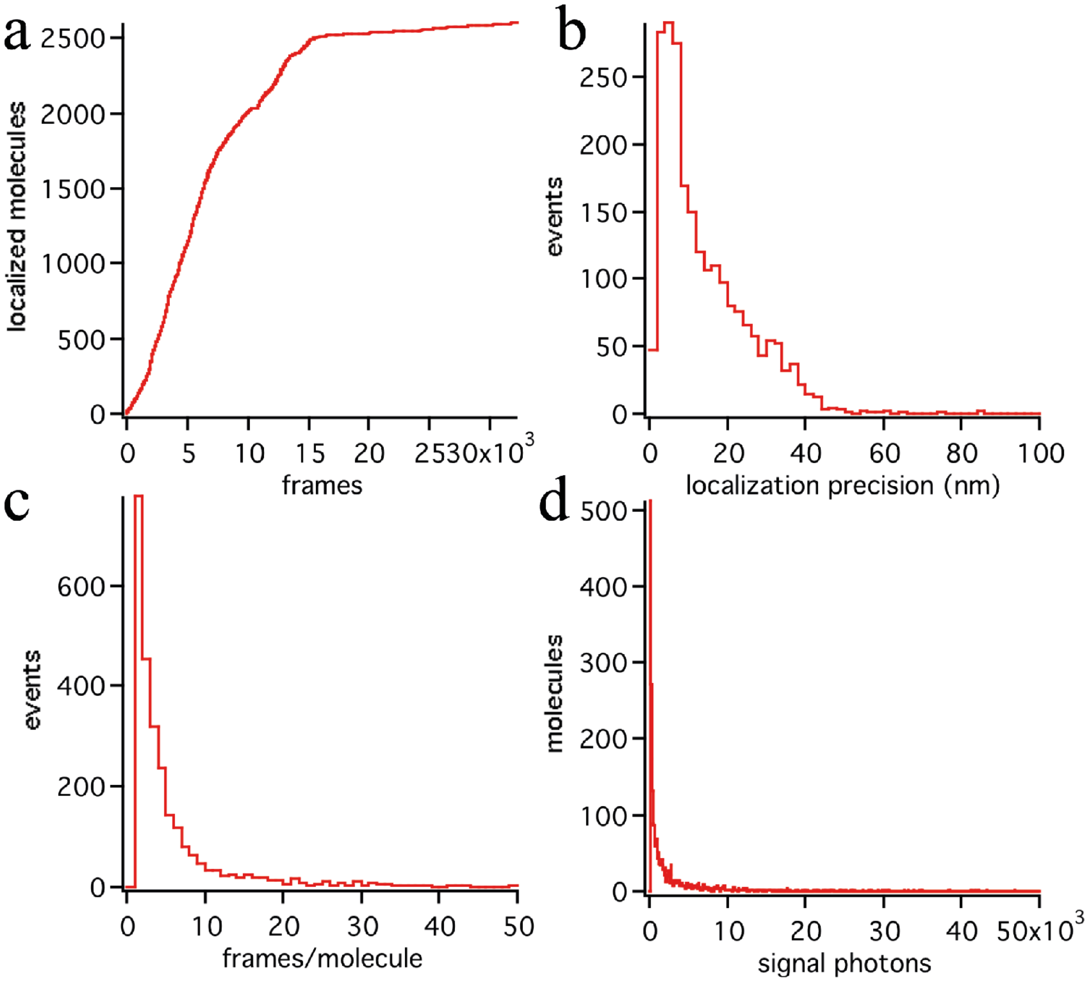

Figure 1.5: Distribution of molecular properties in a typical in-vitro experiment using the photoconvertible fluorescent protein mEos2. one frame= 50 ms. a) Number of molecule localized over time in a PALM experiment. b) Histogram of the localization precision. c) Histogram of the molecular lifetime. d) Histogram of the collected signal photons/molecule.

Once the coordinates of each molecule are known, and the localization error is calculated according to equation 1.2, it is possible to render a super-resolution PALM image. A new image with a pixel size generally below 10 nm, and often below 5 nm, is generated. Each molecule is represented by a 2D Gaussian function, with a standard deviation σ_{xy} determined by the localization precision and centered on the coordinates determined by the Gaussian mask fit illustrated in figure 1.4 c. In our work the emission from the molecules is treated as isotropic, and a unique σ is used for both axes. Figure 1.6 illustrates the concept of gain in resolution in moving from a diffraction limited PSF with a varying SNR to a 2D Gaussian function, normalized to unity, centered around the centroid of fluorescence emission and having a standard deviation depending only on SNR. When extended to many molecules, localized one at a time, this results in the striking difference that is displayed between the two panels in figure 1.1, d.

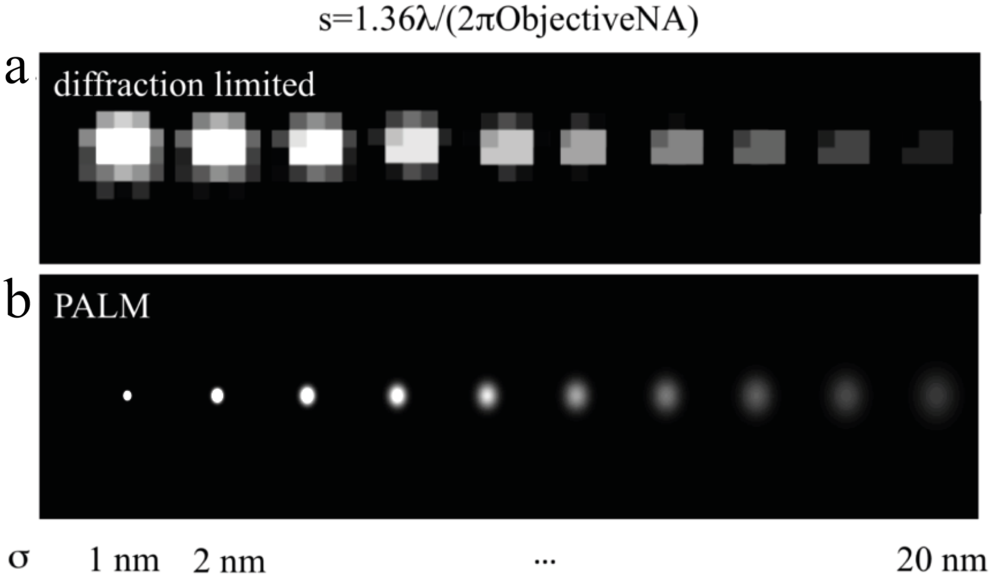

Figure 1.6: Transition from diffraction limited PSF to 2D rendering Gaussians as a function of the single molecule SNR. a) Molecular PSFs with decreasing SNR. b) A Super Resolution Image is generated with a pixel size 1/10 of the original one. Each localized molecule in *a* is rendered as a 2D Gaussian distribution that has a standard deviation given by the localization precision.

2 Development of the super-resolution microscope

2.1 Introduction

The experimental apparatus required to perform PALM is a fluorescence microscopy setup, capable of Total Internal Reflection (TIR) of the excitation light at the sample and provided of a detector (typically an EM-CCD) sensitive enough to measure the signal arising from individual fluorophores. The setup used in this work was built *ex novo* around the frame of a commercially available inverted microscope (Olympus IX81 and IX71). The excitation part of the setup (light sources, shuttering, steering and beam-shaping optics) was customized on an independent optical platform and coupled via free-space to the microscope. The current chapter will describe the key components of the setup, addressing in detail the arrangement of the excitation platform, the optical assembly to drive the system into TIR and finally the detection side, including a discussion of the triggering mechanism involving the EM-CCD camera and the control software.

2.2 Excitation setup

Figure 2.1 and 2.2 display a top and side view respectively of the excitation platform of the experimental setup. As figure 2.2 displays, the entire excitation optics is arranged on an independent platform sitting on the main optical table, following at large the layout proposed by [18]. This layout guarantees the stability of the excitation optics, and at the same time reduces the need for beam adjustment components by placing the height of the excitation beams at the same level of the microscope entry port by means of adjustable legs. The microscope sits next to the excitation platform on the main optical table, and in between the rear port of the microscope and the excitation platform there is a $x-y-z$ translation stage holding the relay lens to steer the beam into TIR. The setup has three lasers, two for excitation (a 561 nm diode laser and a 488 nm diode laser, respectively indicated as no. 1 and no. 4 in figure 2.1) and one for photoactivation (a 405 nm diode laser, not shown in figure 2.1). The beams from the two excitation lasers are combined by the dichroic mirror no. 5, and enter the front window of an Acousto Optic Tunable Filter (AOTF) (no. 6). The first order of the beam deflected by the Bragg grating within the AOTF exits with an angle of $\sim 2.4^o$ with respect to the incident beam, and the intensity of this beam can be modulated via an analog input. After being reflected by mirror no. 7, the beam goes through a $\lambda/4$ wave-plate (no. 8) that induces circular polarization, and is expanded by ten times through the beam expander no. 9. The diameter of the expanded beam is reduced to approximately 10 mm by an aperture and is again reflected by two mirrors (no. 11 and no. 12). The

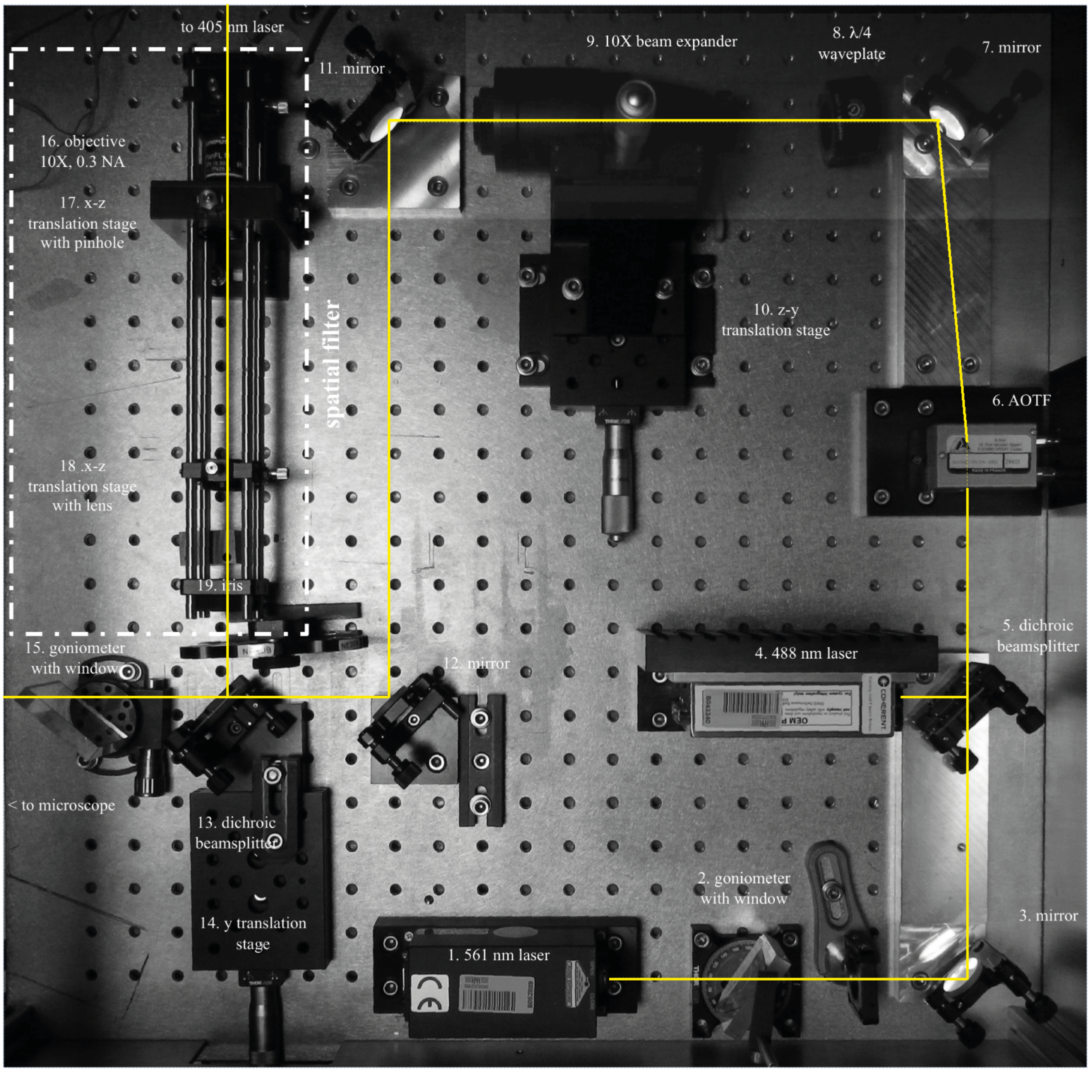

Figure 2.1: Picture showing a top-view of the ecitation setup. 1. Spectra Physics 561 nm, 100 mW excitation laser, 2. Melles Griot 9.5 mm fused silica window (SQW-2037-UV) on rotating goniometer, 3. Semrock 25.4 mm MaxMirror, 4. Coherent Sapphire 488 nm, 25 mW excitation laser, 5. Chroma T495lpxr dichroic mirror, 6. Acousto Optic Tunable Filter, A.A. OptoElectronics, Orsay, France 7. (as 3.), 8. Melles Griot $\lambda/4$ waveplate, (ACWP 400-700-06-4 CVI Melles Griot, Albuquerque, NM, USA) 9. Thorlabs BE10M-A 10X beam expander, 10. y-z pair of micrometric translation stages 11. (as 3.), 12. (as 3.), 13. Semrock Di01-R405 dichroic mirror, 14. y micrometric translation stage, 15. Melles Griot 9.5 mm fused silica window (SQW-2037-UV) on rotating goniometer, 16. Olympus 10X objective, 0.33 N. A., 17. 10 μm pinhole mounted on x-z micrometer translation stage, 18. f=150 mm plano-convex collimation lens. The optical path lies ~ 4 cm above the optical table surface.

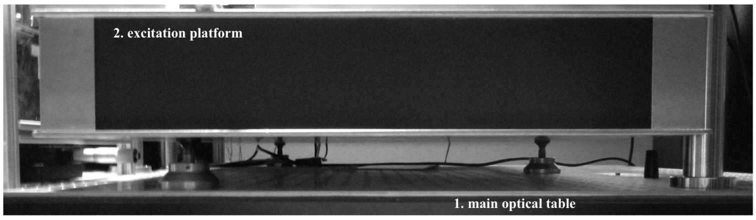

Figure 2.2: Picture showing a side view of the excitation platform standing on top of the main optical table.

action on the kinematic mounts holding these mirrors allows to precisely align the beam to the optical axis of the microscope. The collimated excitation beams are combined with the activation beam by the dichroic beamsplitter no. 13, and a fine co-axial alignment of the two can be achieved by movement of the translation stage no. 14 as well as of the kinematic mount holding no. 13.

Due to the observed profile of poor quality, the photoactivation beam, goes through a spatial filter, made of a low Numerical Aperture focusing objective (no. 16), a 10 μm pinhole, (no. 17) and a collimating lens (no. 18). The aligned and collimated excitation and activation beams go through the rotating window no. 15 before being focused on the back focal plane of the objective by the lens shown in figure 2.3 b. Figure 2.3, a display a side view of the microscope frame, showing the position of the TIR steering optics along the beam path in between the microscope and the excitation platform. Figure 2.3 b, shows a picture of the rear port of the microscope through the TIR relay lens. The role of the half mirror (no. 3) will be discussed in relation to the axial stabilization setup included in the system.

2.2.1 Photo-activation beam

Guided by the principle of minimizing the number of optical components in the light path, neither of the excitation lasers beams was treated or spatially filtered, aside for the aperture at the exit of the beam expander no. 9. However, the output of the 405 nm laser (Coherent, Cube, 50 mW) presented such a poor appearance that it was necessary to manipulate the beam profile to achieve a roughly gaussian beam and a homogeneous illumination profile in the sample plane. We therefore installed a spatial filter, as indicated in the dashed region of figure 2.1. A spatial filter is an opto-mechanical component targeted at the removal of the higher frequency components of the beam. Practically the collimated beam exiting from the laser is focused by a 10X 0.33 N.A. Objective (no. 16) into a plane where a small pinhole (10 μm diameter) can be adjusted by means of fine micrometer screws. The pinhole selectively allows only certain frequencies to propagate, removing most of the components altering the original beam. The propagating light is then collimated again by the no. 18 lens (the telescope formed by the 10X objective and the lens acts effectively also as a beam expander). The 405 nm laser is provided of a TTL input as well as of an analog power control, and it can be shuttered independently up to an 150 Mhz rate.

2.2.2 Acousto Optic Tunable Filter

Both excitation beams pass through an AOTF (no. 6 in figure 2.1). The main purpose of this element in the setup is to allow the fast shuttering needed to synchronize the detection and excitation. An incident linearly polarized laser beam gives rise to two principal outgoing laser beams, namely an 0^{th} and a $\pm 1^{st}$ order, deflected by 2.4^{o} with respect to the incident beam. The AOTF regulates the amount of power being deflected in the 1^{st} order that is also the one steered towards the microscope. The AOTF allows to modulate the intensity of the 1^{st} order, achieving a modulation efficiency (ratio between the 1^{st} and 0^{th} order) up to 90%. The deflection can be interpreted as arising from the conservation of energy and momentum in the collision between an incoming photon and a phonon in the crystal with a high piezo-optic coefficient generated by piezoelectric element subjected to a controllable radio frequency. Frequencies of 130.5 Mhz and 108.2 Mhz were used to modulate 488 nm and 561 nm laser beams respectively. The rise time of the 1^{st} order when a line is activated is in the μs range. The AOTF employed in our setup has 8 independent channels able to modulate 8 independent wavelengths simultaneously using an analog input between 1 and 10 V. The output power of a laser line passing the AOTF grows monotonically as a function of the analog modulation voltage up to a maximum power value P_{max}. Above the corresponding V_{max} value the power output decreases. Furthermore, the polarization output (required to be linear before entering the AOTF) is flipped by 90^o. A common analog blanking input (1-10 V) allows to shutter simultaneously all the lines.

2.2.3 Total Internal Reflection

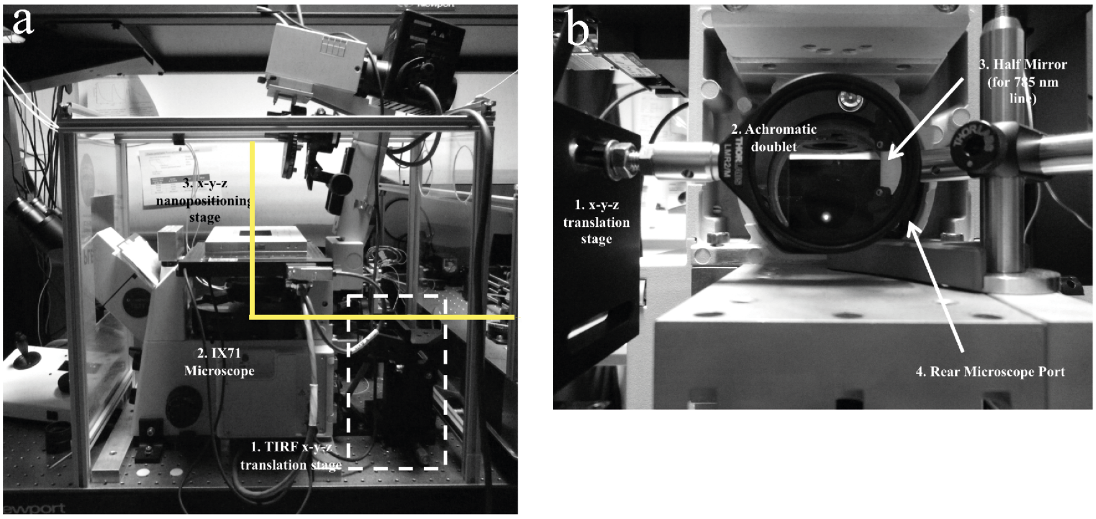

Figure 2.3: a) Side view of the IX71 microscope frame, showing the position of the TIRF steering optics along the beam path in between the microscope and the excitation platform. 1. TIRF module, 2. microscope body, 3.$x-y-z$ nano-positioning stage (LPS100 series, MadCity Labs, Madison, USA) b) rear port of the microscope through the TIRF relay lens. 1. $x-y-z$ micrometric translation stage, 2. achromatic doublet 250 mm, 3. Half mirror mounted on cantilever platform 4. rear port of the IX71 microscope

Before addressing in detail the role of the relay lens in the current configuration, we will review the concept of TIR Fluorescence (TIRF) and the possible strategies to achieve it in the current setup. The concept of total internal reflection of a plane wave propagating in a medium 1 through an interface with a medium 2 of a lower index of refraction $n_2 < n_1$ can be easily understood in the light of Snell's law of refraction:

$$n_1 sin(\theta_1) = n_2 sin(\theta_2) \tag{2.1}$$

The angle of incidence of the propagating beam $\theta_1 = \theta_c$ is called critical angle, since it results in $\theta_2 = 90^o$, and in this condition the refracted beam will not propagate through the medium 2, but rather run along the interface. For values of $\theta_1 > \theta_c$ the incoming beam will be reflected. The fact that complete (or total) reflection does not occur was hinted already by Newton, and the first quantitative work in the field was provided by Quincke in the second half of the 19th century, to the conclusion that so-called evanescent waves appear in the second medium (n_2) close to the interface (see [19] and references therein). Since these initial reports, it has long been known that the intensity of the evanescent field decays exponentially from the interface $I(z) = I_0 \cdot e^{-\frac{z}{d}}$, where z is the propagation direction orthogonal to the interface between the two dielectrics and d, the decay length, is given by:

$$d = \frac{\lambda}{4\pi} \cdot \left(n_1^2 \sin^2(\theta_1) - n_2^2\right)^{-0.5} \tag{2.2}$$

for $\theta_1 > \theta_c$.

It should be noted, and the reader can address the discussion in [20], that I_0, the intensity at $z = 0$, can be several times larger than the incident intensity for angles close to the critical angle, and that in the visible range the intensity decays $\frac{1}{e}$ within a wavelength of the interface. This property of evanescent light was quickly seized in the seventies as an efficient way for selective illumination of the portion of a sample closest to a support glass surface in fluorescence microscopy. TIRF became popular as a truly selective illumination method, as compared to confocal microscopy, where the selective imaging of a plane within the sample is achieved by confocal detection (and therefore loss of signal), rather than by the selective illumination of the plane in the sample. In recent years new techniques such as 2-photon microscopy [21] and selective plane illumination microscopy [22] (with interesting developments in the super-resolution field, such as the recent work by Cella-Zanacchi *et al.* [23]) have extended the concept of selective excitation to planes well within the specimen, but it should be remarked that TIRF was a pioneering method in this regard. In cell biology studies [24] TIRF allows to selectively observe the regions of contact between fluorescently labeled cells and a glass support, including anchors for cell motility or convergence points for cytoskeletal filaments. The obvious advantages of TIRF imaging are the suppression of most of the background arising from fluorophores beyond the decay length of the TIR field and the possibility of tuning the decay length d, by carefully increasing the incidence angle beyond θ_c.

Originally conceived using a prism-based design, e.g. using a thick glass element such as a dovetail prism to couple the light into the coverslip at the critical angle, later on TIRF became popular also in *through-the-objective* configuration [25]. If the N.A. is greater of 1.4 then it is possible to couple into the rear of the objective lens rays at an angle such that the outgoing beam will have an exit angle greater than the critical-one for the glass-air interface. In the original attempt an opaque circular mask was used to block the central part of a beam focused on the back focal plane of the objective, thus allowing to pass only those rays crossing the back focal plane (BFP) far from the optical axis. Later on, direct focusing of a beam in a spot lying a sufficient radial distance away from the optical axis, was found to be the most practical solution: it yields a collimated beam output from the front lens of the objective, and its exit angle can be adjusted by translating the focal spot radially in the BFP.

Historically we explored three configurations to achieve TIRF, all three achieved using either a 60X or a 100X 1.45 N.A. Olympus Objectives. All three approaches are through-the-objective, and what changes is the way the beam is brought in focus in the BFP. The first configuration, adapted from the layout proposed by Shroff *et al.* [18], is shown in figure 2.4 a. It is based on the telescope L_1-L_2 to generate an image of the beam focused by the lens L_3 on the surface of the mirror M in the BFP of the objective. If $f_{L1} = f_{L2}$ then L_1 and L_2 form a $4f$ system and a translation of x mm of M will result in corresponding and equal translation of the focused spot in the BFP. For any choice of the lenses L_1 and L_2, as far as the distance between the BFP and L_1 is equal to f_{L1}, the distance between L_2 and and M is equal to f_{L2} and the separation of L_1 and L_2 is equal to $f_{L1} + f_{L2}$ then the surface of the mirror M and the BFP are conjugated planes. If on the one hand this configuration has the advantage of minimizing the moving mechanical parts (only the translation stage supporting M), on the other hand it requires a significant effort for the proper alignment of the three lenses L_1, L_2 and L_3, the exact parallelism between L_1 and

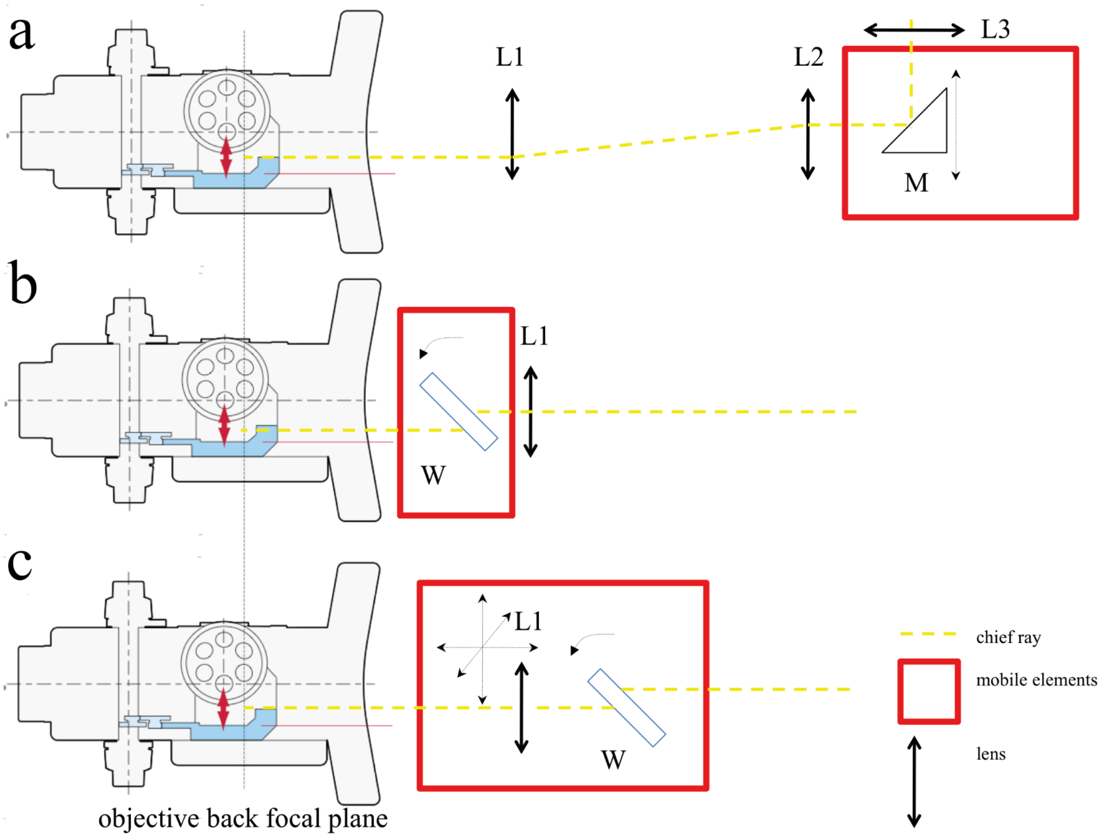

Figure 2.4: a) TIR configuration based on a movable mirror (M) and a 4f relay system to generate an image of the focused beam in M in the back focal plane of the objective. b) The collimated beam impinges on L_1, that focuses it in the back focal plane, on axis. The position of the focused spot is translated by means of a rotating window (9.5 mm, fused silica, Melles Griot) sitting in between L_1 and the BFP. c) The collimated beam impinges on the rotating window W, to align it to the optical axis of L_1. L_1 sits on an $x - y - z$ stage in order to translate the focused spot in the BFP.

L_2, sitting respectively on the microscope and on the excitation platform, being the most difficult to achieve and maintain over time.

Following the arrangement proposed by Hassler in his dissertation [26], the configuration was simplified, reducing the assembly to a collimation lens L_1 and a thick window W on a rotating goniometer. This is shown in figure 2.4 b. The effect of the parallel air-glass-air interface is to achieve a lateral offset of the chief ray of the converging beam, maintaining its direction unaltered. According to geometrical optics considerations this configuration appears quite effective, requiring only the use of a longer focal distance achromatic doublet as L_1, in our case $f = 300$ mm. Furthermore, both the window W and the lens L_1 can be solidly bound to the microscope frame, requiring only a collimated beam to impinge on L_1. A closer look at this approach, e.g. by the ray tracing simulation displayed in figure 2.5 a, shows that the focal spot undergoes a significant axial shift upon tilting the window (b), becoming asymmetric and falling beyond the diffraction limit represented by the circle in figure 2.5 b. The resulting final offset between epifluorescence and TIRF is approximately 3.7 mm (d). This approach therefore requires a frequent re-adjustment of the lens L_1, requiring the introduction of another mechanical degree of freedom in the setup.

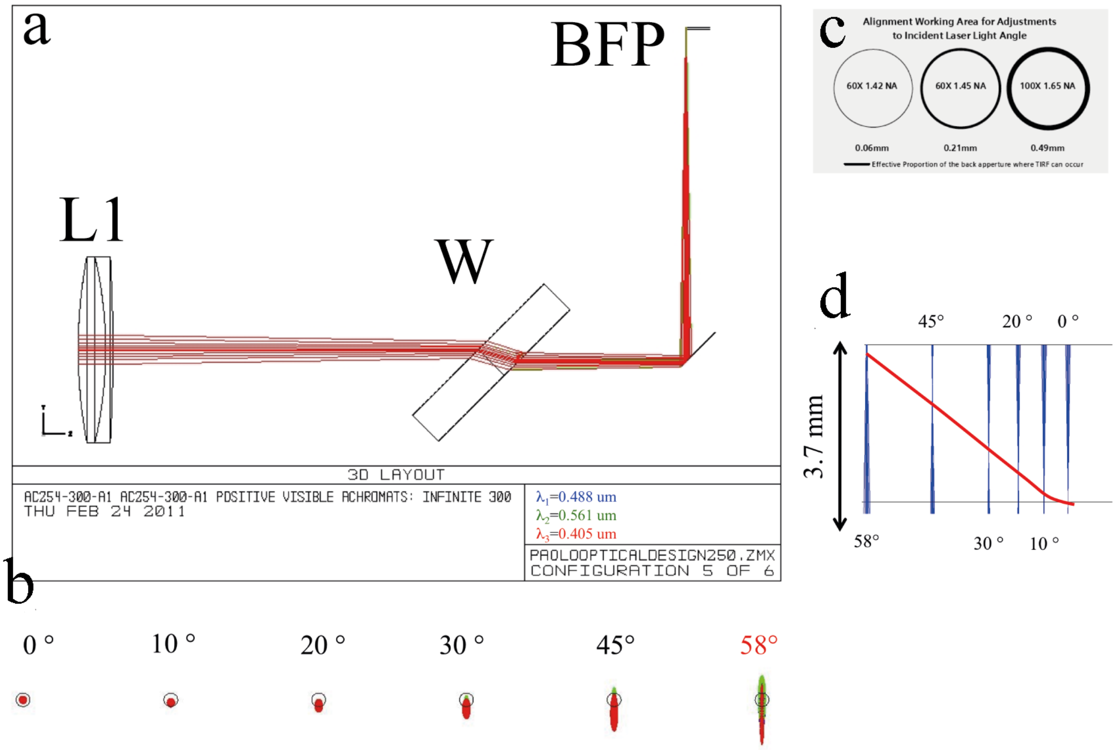

Figure 2.5: a) Ray tracing simulation (using Zemax, Radiant Zemax, LLC, Washington, USA) of the three wavelelengths used in a PALM experiments using the configuration described in figure 2.4 b. b) changes of the focal spot in the BFP upon tilts in the window angle required to achieve the critical angle. c) Annular region in the BFP where TIRF is allowed. d) Offset of the focal spot along z as a function of the beam angle.

The third and final configuration employed, depicted in figures 2.1 and 2.3, uses L_1 on an $x-y-z$ translation stage. Translation of L_1 perpendicular to the optical axis determines an offset of the focal spot in the BFP. However, since the collimated beam impinges off-axis on L_1, a translation of the illumination spot at the sample is also observed. This effect can be corrected by translating the collimated beam again on the optical axis of L_1 by means of a rotating window W (no. 15 in figure 2.1). In this configuration, once TIRF is achieved, the totally internally reflected beam can be seen exiting the rear port of the microscope, and travelling back through L_1. A 1.45 N.A. objective can achieve a maximum ray exit angle of $asin(\frac{N.A.}{n}) = asin(\frac{1.45}{1.518}) = 73^o$. Conditions for TIR in air and in aqueous media are respectively $\theta_c = 58.9^o$ and $\theta_c = 41.2^o$. Using the current configuration c, and placing a glass element on top of the coverslip to thwart TIR, a clean beam profile was observed for angles up to 72^o using the 60X objective and up to 68^o using the 100X objective, in both cases well beyond θ_c. This optical configuration has also the advantage of a good stability and ease of alignment.

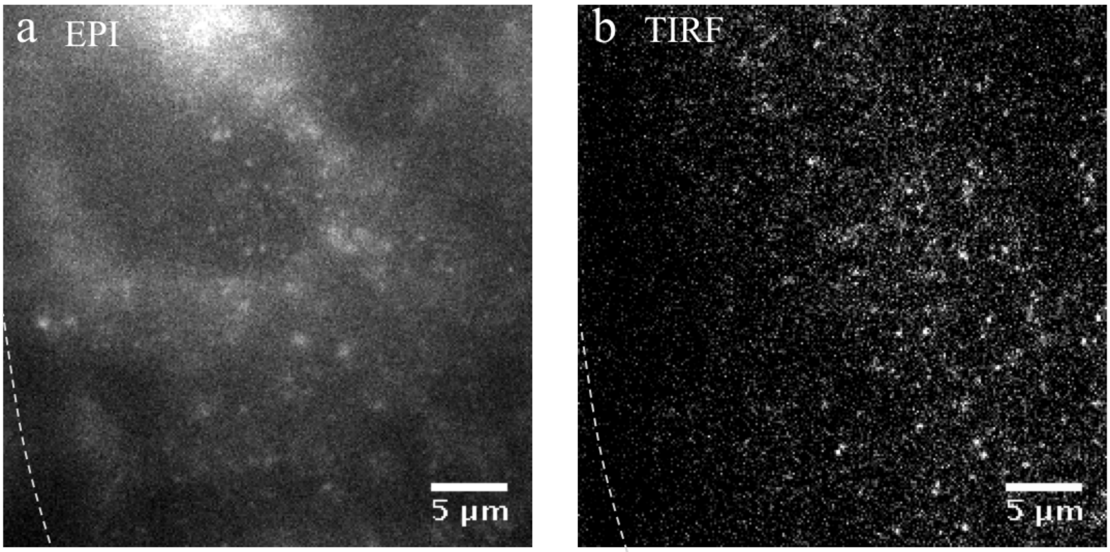

Figure 2.6: a) Epifluorescence image of a living HeLa cell expressing the construct β2-mEos2 on the plasma membrane. b) TIRF image of the same sample, allowing the identification of single mEos2 fluorescent molecules.

As expected, when moving from epifluorescence illumination to TIRF, the measured fluorescence coming from a thick sample, i.e. a plasma membrane labeled cell, dramatically decreases, allowing the identification of single fluorescent molecules at the coverslip/sample interface. Figure 2.6 illustrates the dramatic rejection of labeled components and autofluorescence background when moving to TIR illumination of living HeLa cells transiently expressing the membrane label β2-mEos2, excited at 488 nm and observed in the so-called GFP channel between 500 nm and 545 nm. Even in a 50 ms snapshot of the plasma membrane of a living cell, spots arising from single mEos2 molecules are clearly identified. Another example of the background rejection capabilities of TIR is shown in figure 2.7, where the epifluorescence and TIRF image of a live HeLa cell expressing the protein clathrin marked with Red Fluorescent Protein (RFP), are compared. The large clathrin clusters are clearly visible at the plasma membrane even in epifluorescence, but their contrast increases and more of them appear once the background fluorescence from the body of the cell is rejected.

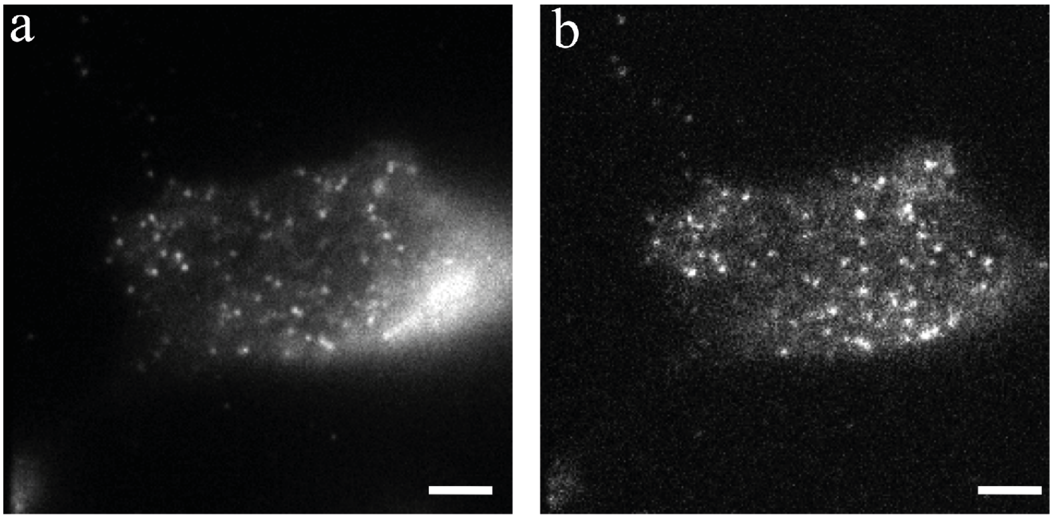

Figure 2.7: a) Epifluorescence image of a living HeLa cell expressing the construct clathrin light chain -RFP on the plasma membrane. b) TIRF image of the same sample illustrating the rejection from out of focus background fluorescence. Scale bar is 5 μm.

TIR polarization

As reported by Axelrod *et al.* [20], the beam steered into TIR may have either a linear or an elliptical (circular in the limiting case) polarization. The electric field vector $\vec{E}$ can be decomposed in two components, parallel ($E_{\parallel}$) and perpendicular ($E_{\perp}$) to the incidence plane. Once in the lower refraction index region, i.e. the sample, $E_{\parallel}$ cartwheels in the incidence plane with a phase delay with respect to the incident vector. On the other hand $E_{\perp}$ oscillates in the sample plane parallel to the coverslip. The linearly polarized laser output is rotated by 90^o by the AOTF. If no further polarization altering elements were introduced in the light path, the sample would be irradiated only by $E_{\perp}$. We introduced a $\frac{\lambda}{4}$ waveplate, indicated by no. 8 in figure 2.1, to determine circular polarization. A schematic of the evolution of the polarization in the beam path of our TIRF setup is shown in figure 2.8.

2.3 Axial Stabilization by TIR

The reflected beam of a totally internally reflected laser line can also be exploited as a sensor of the relative objective to sample distance. Figure 2.9 a displays schematic of the optical setup devised to drive a feedback loop in order to keep the relative sample to objective distance constant. The laser line from a 785 nm pigtailed diode laser (Thorlabs, LPS-785-FC) is collimated by a 12.5 mm lens and focused on the back focal plane of the objective after reflection on the half mirror pictured in figure 2.3 b. The diode is placed in a heat sink (Thorlabs LM9LP) and is driven by a power supply (Thorlabs, EK2000). The collimated beam is then focused on the BFP far enough from the optical axis to undergo total internal reflection at the sample-coverslip interface. The reflected laser line is steered back by two half mirrors (Figure 2.9 b) on a quadrant photo diode (QPD, Pacific Silicon QP50-6SD2), where the reflected spot moves along one direction proportionally to the separation between the objective lens and the coverslip. The difference signal from the two halves of the photodiode is then supplied to the NI USB 6229 acquisition card, and provides the input for the software PID controlling the nano-positioning

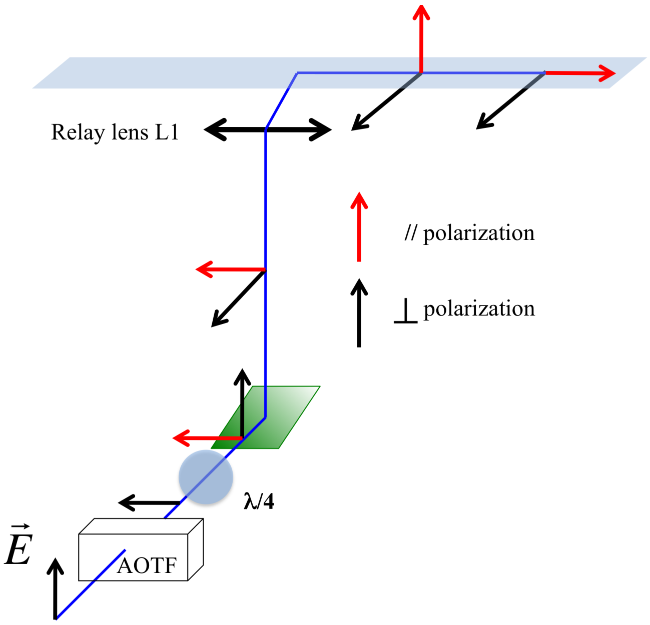

Figure 2.8: Polarization effects when a linearly propagating beam passes through the AOTF, a $\lambda/4$ waveplate and the objective lens entering the sample at the critical angle. Adapted from [20].

stage z-axis by serial communication.

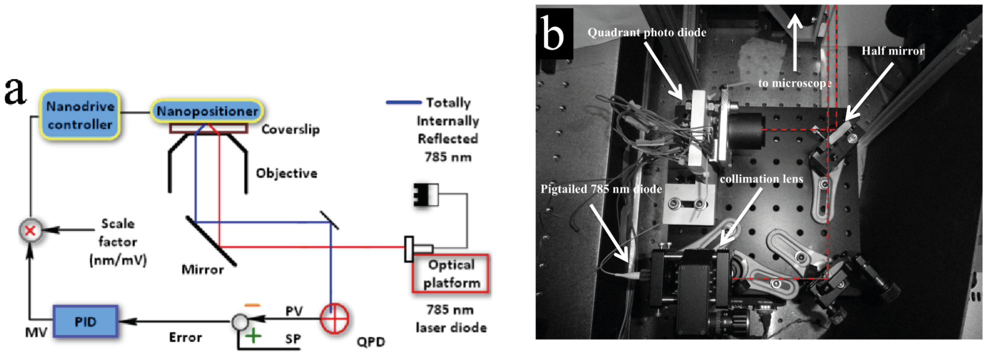

Figure 2.9: a) Schematics of the axial stabilization setup. b) Top view of the optical assembly for axial stabilization.

The PID controller, a part of the PALM control software that we developed, (LabView, National Instruments, Austin, Texas, USA), receives as an input the voltage value from the Top-Bottom output of the QPD (process variable in no. 3 and time trace displayed in no. 4 in figure 2.10). The PID controller compares this value to the set-point, corresponding to the signal measured when the sample is in focus, and acts on the z-axis of the nano-positioning stage to maintain their difference (error) minimal (no. 6 in figure 2.10). Before each measurement it is necessary to calibrate the $\frac{nm}{V}$ ratio by moving up and down in steps the nano positioning stage. The Proportional, Integral and Derivative gains are adjusted in order to make the response of the PID as stable as possible. As a result we are able to maintain the objective-coverslip distance stable for the entire duration of a typical PALM experiment of ~ 1h within a few nanometers. As displayed in figure 2.10 b, during an acquisition of more than 40 minutes the piezo displaces of approximately 500 nm (blue trace) along the z-axis to keep the objective-coverslip

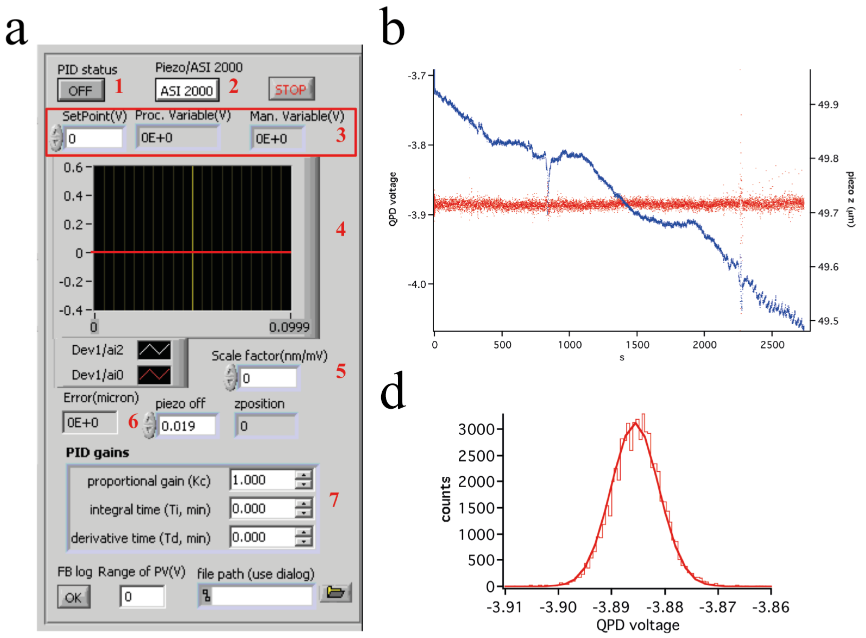

PID status: OFF

Piezo/ASI 2000: ASI 2000

SetPoint(V): 0

Proc. Variable(V): 0E+0

Man. Variable(V): 0E+0

Scale factor(nm/mV): 0

Error(micron): 0E+0

piezo off: 0.019

zposition: 0

PID gains

proportional gain (Kc): 1.000

integral time (Ti, min): 0.000

derivative time (Td, min): 0.000

Range of PV(V): 0

Figure 2.10: a) PID panel. 1. Feedback enable toggle 2. toggle to switch between coarse axial control (Z axis resolution= 50 nm) and NanoPositioning control (Z axis resolution=0.2 nm) 3. Set-point, PID input and output variables 4. TOP-BOTTOM signal from QPD 5. scale factor converting from V to nm 6. error in μm between current position and set-point 7. Proportional, Integral and Derivative gains. b) red trace: the voltage read from the QPD, blue trace: z-displacement of the piezo. c) Histogram of the QPD voltage trace. The calibration scale factor is $1 \sim \frac{nm}{mV}$.

distance constant (red trace). As the histogram in figure 2.10 illustrates, the standard deviation of the points of the trace is 4.46 mV, corresponding to approximately 5 nm. The use of this component of the setup will be extensively discussed in chapter 6.

2.4 Detection

2.4.1 EM-CCD camera

The timings of the AOTF and of the photo-activation laser are tightly connected to the operation of the EM-CCD camera. Our PALM setup runs an Andor iXon DU-897 Electron Multiplying camera, mounting a 512x512 active area chip capable of frame transfer operation. As in all CCD cameras, the detector is made of a 2D array of pixels, in this specific case of 16 μm side; each pixel is a semiconducting device generating a charge (electron-hole pairs) proportional to the number of incident photons, up to a maximum saturation value known as full-well. The charge of each column of pixels is shifted by the application of a gated voltage (vertical clocking) into a shift register, that is then read-out by an amplification and analog to digital (A/D) conversion step. The camera is operated in the common *image* mode, where the Digital Units generated at each pixel by the incident photons can be recovered. The camera can acquire individual snapshots, with a certain exposure time during which the entire active area will be collecting photons. After this, a vertical shift will move all the charges generated in each pixel of a row into a cell of the shift register. The vertical shift speed is in the range of a few μs per

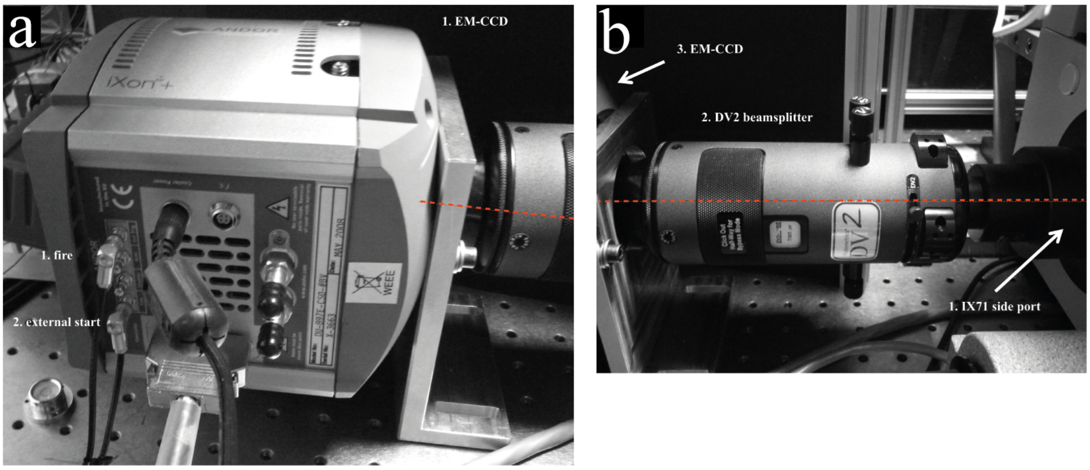

Figure 2.11: Andor iXon DU-897 EM-CCD camera on its support *L* bracket showing the input-output connections. The front female C-mount is connected to the male thread of the DV2 beamsplitter element.

pixel, therefore to transfer the entire active area to the shift register the camera it takes no more than 1.5 ms (number of rows times vertical shift speed). The readout speed of the A/D stage of the shift register ranges from 1 to 10 Mhz for this specific camera. The readout time for the entire chip is therefore 26 ms. In addition, the iXon possesses an extended readout register (i.e. more than double than the 512 pixels strictly required for collecting the charge of each column). The second part of the register is used for the Electron Multiplication stage: the charges in the shift register are accelerated by a high voltage, and generate additional charges by impact ionization. A gain factor, the EM Gain, can be changed in order to change this voltage, thus determining a linear increase of the average number of secondary charges generated during the amplification. The amplification process enables to detect even very low signals that would normally be obscured by the readout noise, e.g. the intrinsic electronic noise of the A/D conversion stage. The multiplication generates an additional noise, resulting in a multiplicative factor of $\sqrt{2}$ for the original shot-noise of the measurement. The camera has two independent amplifiers, one for conventional operation and one for operation with the EM register.

An important feature of this camera is the possibility of operating in frame transfer mode. The chip has an effective area that is twice the one of the active region that is normally exposed to light. The other half is covered by an opaque mask, and is used as a storage region of the image enabling to free within 1.5 ms (vertical shift time) the active area for another exposure while the storage region is read out (see figure 2.12). The advantage of frame transfer is that it enables a much higher frame rate as compared to a traditional acquisition since the time interval between two frames in FT mode is 1.5 ms, whereas in conventional readout it is equal to the readout time, namely 27.5 ms. While for conventional acquisition mode the exposure time can be arbitrarily set, in frame transfer it finds a lower bound in the readout time, since a vertical shift of the active area can not commence until the storage area has been fully read out. It shall be noted here that, although the camera is provided of a mechanical shutter, the timescales normally employed in low light imaging with an EM-CCD tend to be comparable to the rise time of any mechanical device, making a control of the effective exposure time by means of mechanical shuttering unfeasible and inaccurate. When operating in frame transfer mode the very short interval between an exposure and the following one makes shuttering of the excitation light

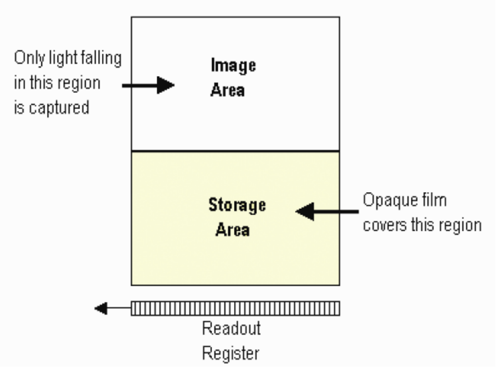

Figure 2.12: Schematics of the frame transfer mechanism, showing the division of the camera chip into image and storage area, and the readout register. (adapted from Andor SDK User's guide, v. 2.8 2008)

almost not necessary (though recommended). When operating in conventional mode, instead, the role of the AOTF in shuttering the excitation beam is important.

An acquisition cycle of multiple frames, i.e. a kinetic cycle, can be either externally triggered (TTL input) or its start can be controlled by software. In most PALM experiments maximizing the frame rate is of paramount importance, given the large number of frames required to obtain a super-resolution image. Therefore we operate the camera in FT mode, with exposure times ranging from 10 to 100 ms depending on the illumination conditions and the fluorophores used. A scheme of the timings used in the setup is reported in figure 2.13, where the exact interplay between the translation of charges in the image area, storage area and shift register of the chip is illustrated.

Each exposure is internally triggered after a software start signal controlled by a custom software developed in LabView. Informations such as the region of the imaging area to be readout, the horizontal (shift register) and vertical (image area) shift speeds and the bit depth of the A/D conversion can be all customized (see figure 2.14).

The way photons are converted into digital counts is of great importance, since all the PALM analysis is conducted using actual photon values to determine thresholds and calculate the localization precision. More obvious parameters such as the exposure time or the level of the Electron Multiplication Gain can be adjusted online (see figure 2.15). Typical values used in our experiments were 10 Mhz readout speed using the EM register A/D converter, resulting in a 14 bit data depth ($2^{14} = 16384$ digital units (d.u.)). The typical electron multiplication gains employed are in the range of 25-200. Using the electron multiplication register at 10 Mhz the conversion between d. u. and charges generated in the CCD pixels is given by the nominal photon conversion factor (according to the manufacturer's data sheet):

$$\phi = \frac{11.3}{EM_{gain}} \frac{e^-}{digitalunits}$$

The photon conversion factor can be also obtained by direct inspection, together with the effective dynamic range of the camera for the chosen readout channel. Figure 2.16 displays the photon transfer curve [27] of our camera using the conventional register and using the EM register with a gain of 100. The photon transfer curve is obtained by plotting in a log-log plot the variance of the measured CCD signal vs the intensity. Varying (but homogeneous) intensity signal on the chip can be obtained by changing the power of a stable light source or by modifying the exposure time of the camera upon constant illumination. The curve would normally display three regions: one of constant variance at

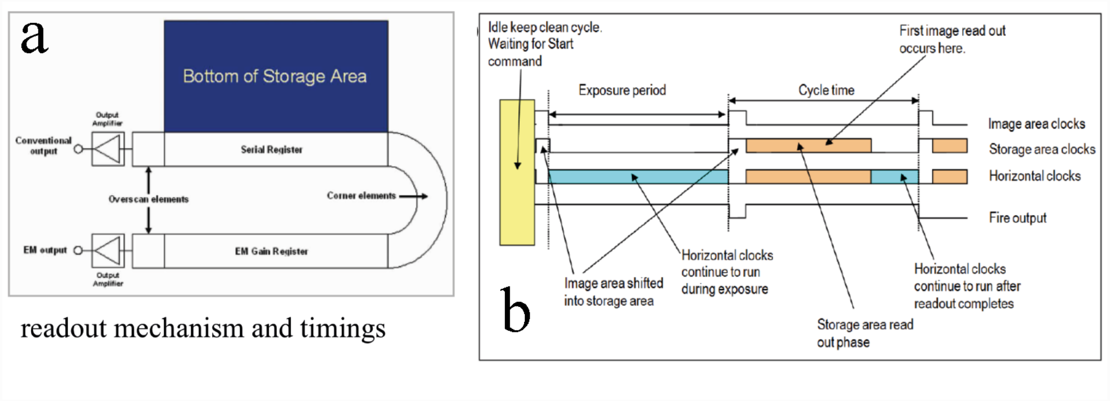

Figure 2.13: Schematics of the readout modes and of the timings of the different regions of the CCD camera chip during a typical acquisition. a) Schematics depicting how the storage area is readout in the shift register. The shift register can either be readout directly by a conventional A/D converter and amplifier or be shifted into the electron multiplying register and go through the EM A/D converter and amplifier. b) Timing of the different regions of the chip: prior to a software command commencing the acquisition the image area is constantly shifted in the storage region, during the so-called keep-clean mode. Upon a start command the vertical image area clocks responsible for shifting the electrons into the storage area are idle, and the same applies to the storage area, that is empty. The shift register (empty) is continuously readout. The TTL fire output of the camera is high. After the exposure time has elapsed the vertical clocks of both the image and storage area are high, to shift quickly the charges from the image to the storage area. The horizontal shift register during this brief interval is idle. During readout the image area is idle, the vertical clocks of the storage area move the charges in the shift register one row at the time, and the horizontal clocks move them into the amplifier. (adapted from Andor SDK User's guide, v. 2.8 2008)

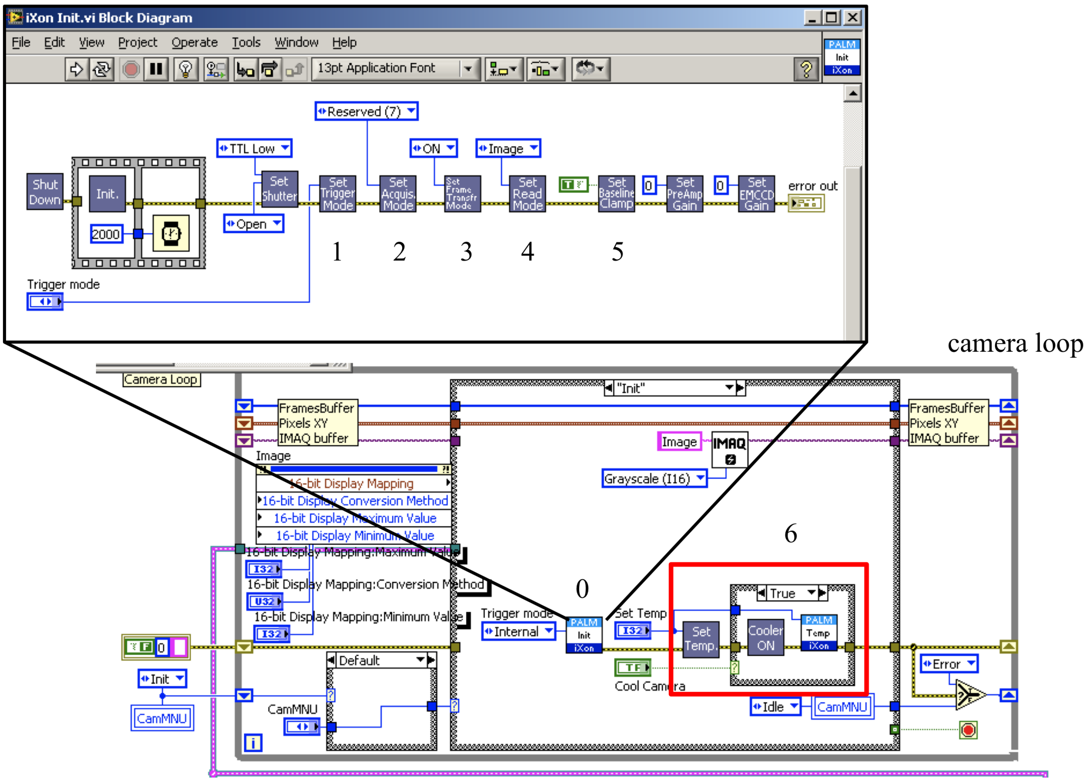

Figure 2.14: Snapshot of the block diagram of the initialization step of the camera in the LabView code controlling the PALM setup. 1. Determination of the triggering mode of the camera, set to internal mode for most of the experiments. 2. Determination of the acquisition mode, i.e. single image, kinetic series or continuous kinetic serie until abort signal is provided 3. activation of frame transfer mode 4. image mode of acquisition 5. Enabling of baseline clamp, to stabilize the baseline of the measurement based on the readout from the masked portion of the chip 6. Cooling cycle of the camera (minimum temperature by Peltier cooling is -75^o.

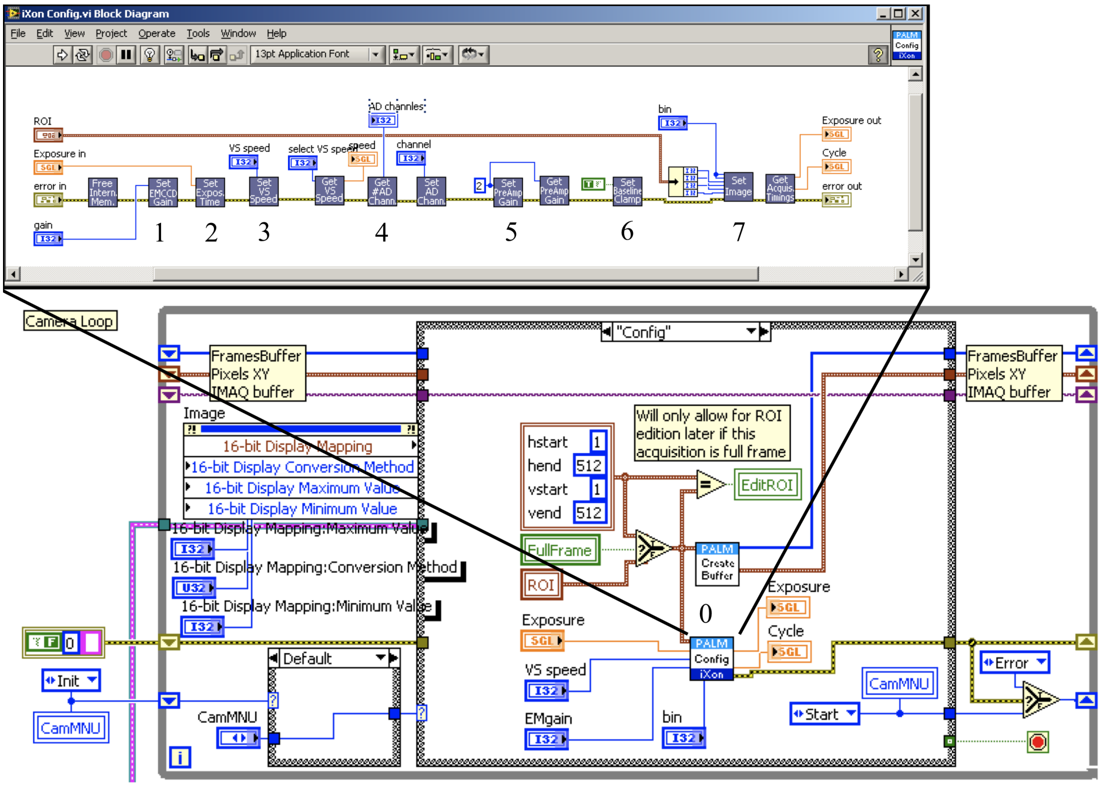

Figure 2.15: Snapshot of the configuration step of the camera. 1. Setup of the EMCCD gain 2. Setup of the exposure time 3. Setup of the vertical shift speed (typical 3.3 μs/pixel) 4. Choice of the A/D conversion stage, either conventional or EM register 5. Determination of the pre-amplification gain, typical 5.3X 6. Confirmation of baseline clamp mode 7. Definition of the region of the chip to be imaged and potential binning

low signal representing the constant readout noise, one of slope 0.5 dominated by shot noise (since $\sigma = \sqrt{N}$ and $\mu = N$) and finally a full-well region where the variance begins to decrease though the signal increases. The intensity where this deviation from the 0.5 slope occurs determines the effective dynamic range of the sensor. A power law fit in the EMgain=100 curve displays the region where the slope is 0.5 (0.46). From this region the photon conversion factor can be extracted by simply dividing the signal by the variance $\frac{S}{\sigma^2_{shot}}$, obtaining the value 0.08, that after four years of operation compares well to the nominal value of $\frac{11.6}{100} = 0.12$ provided by the manufacturer. Interestingly, the deviation from the 0.5 slope straight line begins to occur at signal values of approximately 10^4 digital units, i.e. 60% of the nominal value. Interestingly this results is in agreement with the measured dynamic range extracted from cameras of other manufacturers, e.g. as reported in reference [28].

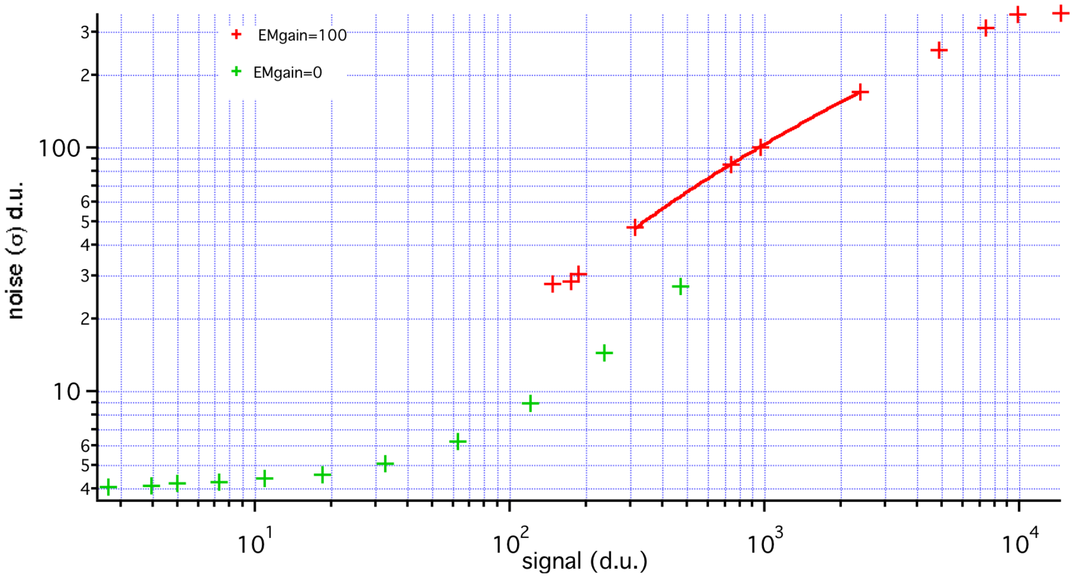

Figure 2.16: Experimental Photon Transfer Curve of the Andor iXon DU-897 obtained using the conventional output amplifier (green markers) or the EM amplifier with a gain of 100 (red markers).

The readout plateau is not clearly visible in the 100 EM gain curve due to our limitation in reducing the exposure time to a value smaller than 0.005 s for a 64 times 64 pixel region in frame transfer mode. However, using the conventional amplifier, the readout plateau can be clearly detected. Since in single molecule spectroscopy the probability that in a single frame the regime of full well is ever reached is fairly low, we are confident that our setup is well performing and we used the measured photon conversion value throughout our analysis, since all thresholds and fittings in the PALM code are performed on an image displaying the actual number of photons/pixel values.

2.4.2 Detection Beamsplitter

The imaging region of the detector can be used to simultaneously detect multiple emission bands. In our setup we used the commercial beamsplitter displayed in figure 2.11 (Photometrics DV2 system). The DV2 carries a dichroic mirror placed in a sliding cube, and fixed relay mirrors that allow to generate a reflected (lower wavelength, blue shifted) and transmitted (longer wavelength, red shifted) image on the the two halves of the CCD chip. By the movement of two razor-blade like shadow masks the DV2 selects a 256x512 central region of a full view image, and through the beamsplitter the red-shifted portion of the fluorescence is relayed onto one 256x512 half of the chip, whereas the blue-shifted portion of the emitted fluorescence occupies the other half. Translation and tilt mechanical axes allow to fine align the two images, so that within ±1 pixel the y-coordinate of each object is the same in each channel, whereas $x_{green} = x_{red} + 256$. The issue of the accurate sub-pixel registration of the two imaging channels will be discussed in detail in the last chapter of this work.

2.5 Overall synchronization of the setup

As previously mentioned, the overall excitation and detection arms of the setup are controlled and synchronized by a custom code that was developed in LabView as a part of this thesis work. With the objective of synchronizing the control of all the hardware under a unique program, LabView was chosen in order to exploit the available drivers that most instrument manufacturers develop for this programming language.The camera acquisition is triggered by the software, and the device operates in the internal triggering mode (Andor run till abort mode). During exposures, the camera fires a TTL high signal, that is fed to the AOTF. In fact, to exploit the full dynamic range of the AOTF modulation input (0-10 V) the fire TTL output of the camera enters the + input of an Operational Amplifier (OpAmp LM139W) acting as a comparator circuit. The − input of OpAmp is connected to a DC voltage acting as a reference, and set to 0.4 V, just above the TTL low voltage value. A $V_{cc} = 10$ V supply drives the circuit and is fed to the output when the + terminal is above the reference. Otherwise a TTL low is supplied. Two input channels of the AOTF are independently modulated via an analog input (0 to 10 V) controlled by the software. The 405 nm photo-activation laser is independently triggered by a software controlled TTL pulse (this digital output is left high when operating in CW photo-activation) and an analog input (0 to 5 V). All the analog input-output between the PC and the hardware is performed through a National Instrument NI-6229 USB card.

Figure 2.17 displays the user interface of the LabView Virtual Instrument programmed to control the PALM setup. The data acquired from the camera are both displayed (no. 1) and spooled to a high speed SAS hard drive (no. 4). Once the camera acquisition parameters have been set (no. 2), it is possible to begin an acquisition. Acquisition can run either in continuous activation, with a cycle time dictated by the readout time + exposure time and a constant high TTL signal to the 405 nm activation laser, in alternative it can run in pulsed mode, where sequences of a predefined number of frames are read, separated by an activation interval of arbitrary duration. During this activation interval the TTL output fed to the 405 nm laser is high, and during the readout interval it is low. The excitation and activation power values can be changed during the acquisition (no. 3), whereas once an exposure time and a EM gain value are set, it is not possible to modify them unless the acquisition is restarted. The controls highlighted in no. 5 allow to move either the nano-positioning stage or the MS-2000 motorized stage to a defined $x - y - z$ coordinate. The calibrate button allows to move either of the stages in a calibration grid of an arbitrary number of points and step-size, and is used during the registration of the imaging channels. The axial feedback controls (no. 6) were discussed in detail in section 2.3.

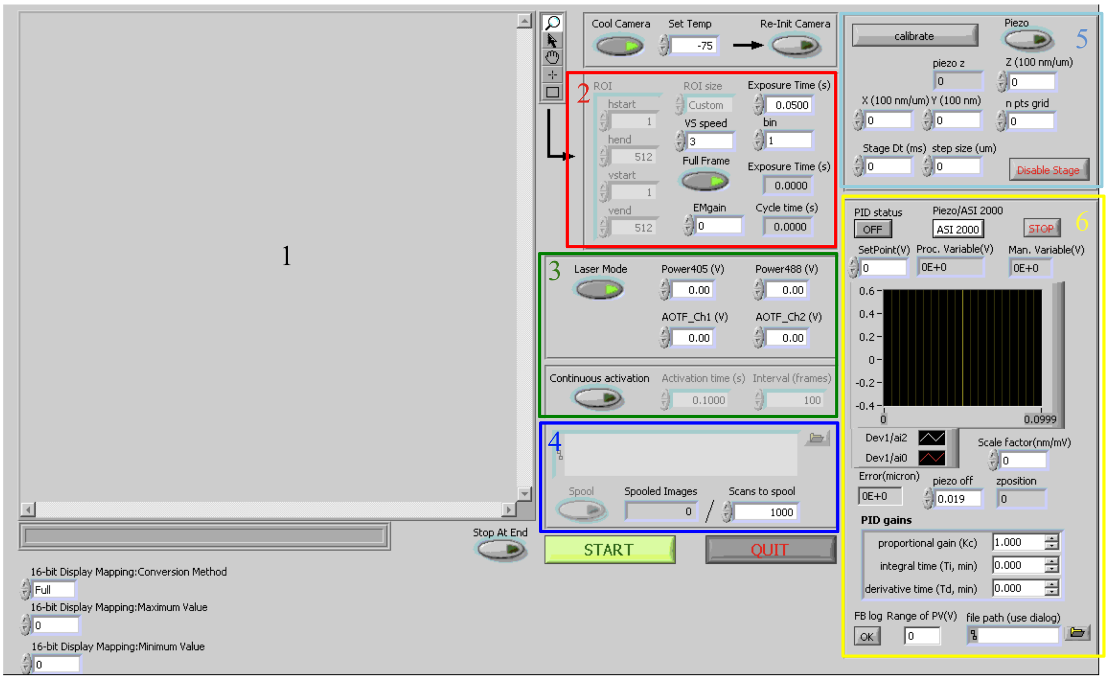

Set Temp -75

ROI size Custom

hstart 1

hend 512

vstart 1

vend 512

Exposure Time (s) 0.0500

VS speed 3

bin 1

Exposure Time (s) 0.0000

EMgain 0

Cycle time (s) 0.0000

Power405 (V) 0.00

Power488 (V) 0.00

AOTF_Ch1 (V) 0.00

AOTF_Ch2 (V) 0.00

Activation time (s) 0.1000

Interval (frames) 100

Spooled Images 0 / Scans to spool 1000

16-bit Display Mapping:Conversion Method Full

16-bit Display Mapping:Maximum Value 0

16-bit Display Mapping:Minimum Value 0

piezo z 0

Z (100 nm/um) 0

X (100 nm/um) 0

Y (100 nm) 0

n pts grid 0

Stage Dt (ms) 0

step size (um) 0

Piezo/ASI 2000 ASI 2000

SetPoint(V) 0

Proc. Variable(V) 0E+0

Man. Variable(V) 0E+0

Scale factor(nm/mV) 0

Error(micron) 0E+0

piezo off 0.019

zposition 0

proportional gain (Kc) 1.000

integral time (Ti, min) 0.000

derivative time (Td, min) 0.000

Range of PV(V) 0

Figure 2.17: Front Panel of the Virtual Instrument controllingl the PALM setup. 1. Image Window 2. EM-CCD configuration panel: definition of the region of interest in the image area, EM gain value, exposure time and binning 3. Laser control panel allowing to control the photo-activation power (0-5 V corresponding to 0 to 50 mW), and the two AOTF channels regulating respectively the transmitted 488 nm and 561 nm power. (0-10 V) 4. Data saving window 5. Nanopositioning stage window, to control the y-y movement of the piezo stage and perform a square-grid scan of the field of view for channel registration and 6. z-axis feedback loop, displaying the srt-point value to be held constant, and the output of the three channels (Right-Left, Top-Bottom and Summed Intensity) from the quadrant photodiode used in the feedback mechanism. Integral, proportional and differential parameters can be customized in the PID controller.

3 Investigating the effects of photoblinking in a prototypical photoconvertible fluorescent protein

3.1 Photoactivatable fluorescent proteins and reversible fluorescence switching

In 1997 Dickson *et al.* reported [29] on two GFP [14] mutants (T203F and T203Y) that displayed at the single molecule level an an on/off blinking and switching behavior: single fluorescent proteins went into an apparently long lived dark state, from which they could be recovered only by 400 nm light irradiation. This seminal paper outlined a very important feature of certain GFP mutants, namely the possibility of sizably shifting the equilibrium between the neutral form of the chromophore (corresponding to the 396 nm band of wtGFP chromophore, its absorption spectrum being displayed in figure 3.1 a) and its anionic (or deprotonated) form, the latter corresponding to the 490 nm absorption band, by using near ultraviolet light. It was previously shown that this equilibrium can be modified by changes of the solution pH [30]. This indicates, as reflected by the naming of the two bands, that their interconversion relies on the exchange of a proton at the chromophore site. In wtGFP the neutral state is lower in energy than the anionic one, and thermal relaxation from the anionic to the neutral state can therefore occur. In the case of the mutants proposed by Dickson and colleagues, it appears that the lower energy state of the chromophore is instead the anionic one (figure 3.1 b).

At the single molecule level this resulted in the observed reappearence of individual T203F molecules, seemingly bleached after prolonged dark time intervals, upon irradiation with ~ 400 nm light. By calculating the distribution of the intervals of time when the single molecules were not emitting, the authors measured a double exponential nature of the *off*-times histograms, leading them to propose the model shown in figure 3.2: the fluorophore can reversibly switch between a neutral *off*-state and a bright *on*-state simply by 405 nm or 488 nm irradiation. The presence of the intermediate state I accessible from the excited state of A is proposed to account for the shorter of the two *off*-times constants.

These findings offered for the first time the perspective of a controllable photochromism in GFP-like fluorescent proteins. A further remarkable development in this direction was reported in 2002, by the observation that the mutation of Threonine 203 into an Histidine leads to a mutant of wtGFP (T203H, commonly known as PAGFP) where the equilibrium between the two forms of the chromophore is radically altered in favor of the neutral state (absorbance shown in figure 3.1 c). Under normal conditions PAGFP is almost completely dark with respect to 488 nm excitation, while 405 nm illumination leads to a rearrangement of the chromophore structure determining a significant increase of the anionic

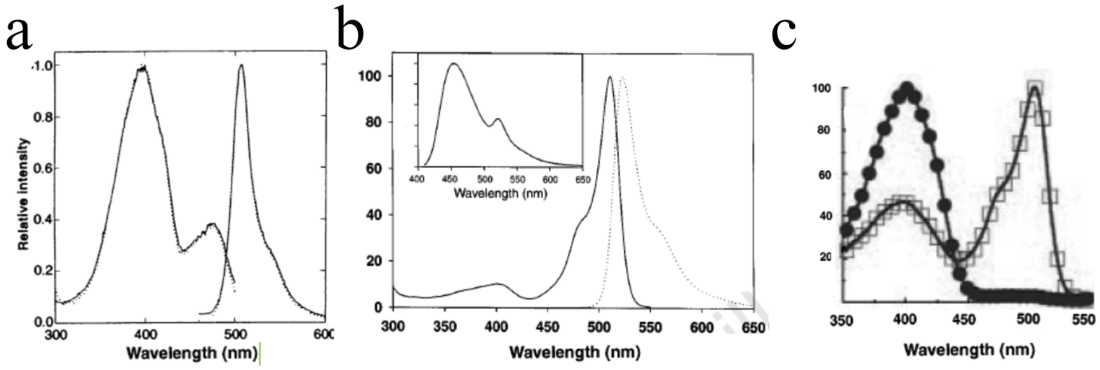

Figure 3.1: a) Absorbance and emission spectra of the wtGFP chromophore. The two bands of the chromophore correspond to the protonated state (396 nm) and to the deprotonated state (490 nm). b) Absorbance and emission (inset) of the T203F mutant. c) Absorbance of PAGFP prior (circles) and after photoconversion (squares) (adapted respectively from [14], [29] and [31]).

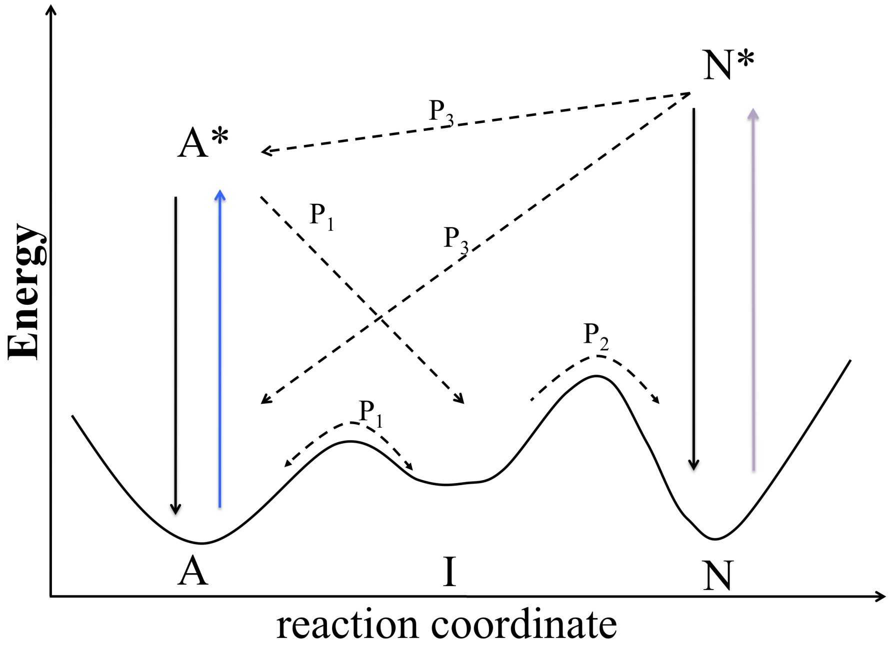

Figure 3.2: Proposed model for the switching and blinking behavior of the T203F and T203Y GFP mutants (adapted from [29]). 488 nm irradiation leads to excitation from $A \rightarrow A^*$. From A^* the system can fall into the intermediate I or the long lived neutral dark state N. Recovery from N can happen by 405 nm irradiation, and interconversion either to A or to A^*.

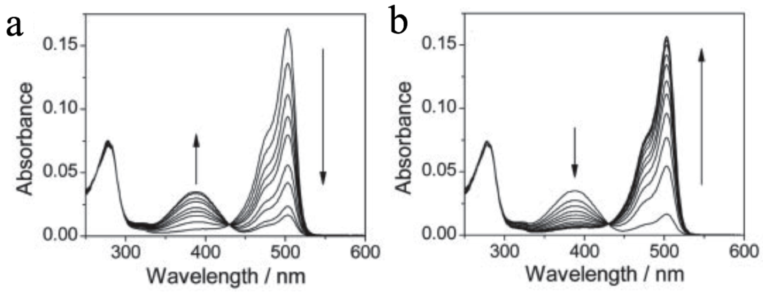

Figure 3.3: a) Evolution of the absorption spectrum of Dronpa upon 488 nm and b) 405 nm irradiation (bottom) (adapted from [33]).

population (the bright A state according to figure 3.2) [31]. The photoconversion leads to a 100-fold enhancement for the PAGFP anionic band and this property was first successfully employed to observe the diffusion of a pool of photoconverted PAGFP from the nucleus in the cytosol of COS cells. This work made it clear that the presence of neutral dark state can be exploited to obtain an efficient optical switcher.

In 2004, Ando *et al.* observed [32] that one mutant of a GFP-like protein obtained from the coral family *pectinidae* displayed a reversible photoswitching mechanism, i.e. the possibility to cycle multiple times (up to 100 in the original report) between a bright *on*-state and a dim *off*-state using two different illumination wavelengths. The mutant, baptized Dronpa, is a green fluorescent protein that has its absorption maximum at 503 nm. Upon 488 nm irradiation it can be efficiently converted into a dim *off*-state, having an absorption band peaking at 390 nm. The bright *on*-state can be efficiently recovered upon 405 nm irradiation, as shown in figure 3.3.

In analogy to the fluorophores discussed so far, the two major absorption peaks can be interconverted by means of a pH change, allowing to attribute the 390 nm band to the protonated neutral state, and the 503 nm band to the deprotonated state of the chrmophore. The observation of an isosbestic point at 430 nm and a monoexponential kinetic for each of the two bands, confirms this observation. Therefore optical switching connects reversibly the protonated and the deprotonated forms and Dronpa by all practical means can be regarded as a switching molecule, hopping between a deprotonated *on*-state and a protonated *off*-state, as shown in figure 3.4 a. The fluorophore deactivates very efficiently both in-vivo (figure 3.4 a and b) and in-vitro (figure 3.4 c). The reversible activation of a single Dronpa molecule is displayed in figure 3.4 c, and the number of photons collected for each burst is shown in figure 3.4 d. In a typical experiment each Dronpa molecules emits on average 100-150 photons, before switching back to the *off*-state. This value is close to the background signal, making this fluorophre difficult to localize with a good accuracy. The extremely efficient photoswitching is, therefore, a drawback for the efficient localization of Dronpa at the single molecule level: superresolution techniques such as PALM and STORM will benefit from efficient but not too rapid photoswitching rates since the localization precision is ultimately dependent on the number of detected photons per molecule per cycle.

The general photophysical properties of Dronpa, and of many GFP-like mutants, appear to be well explained by a mechanism [34] of photoconversion/photoswitching involving the photo-isomerization of the chromophore. A recent study [35] identified in the E222Q mutation the key to restore reversible photoswitching in GFP-like mutants. The optical switching determines a conformational change of the chromophore from a lower energy cis- state to a higher energy trans- state. Each of the two states has an independend protonation equilibrium, with different pK_a values. Both the neutral and anionic trans- forms can relax thermally to the ground cis- state. In the case of Dronpa, the high pK_a of the trans form ensures that at neutral pH (i.e. physiological conditions) the trans- chromophore resides in its neutral dark form. Irradiation with 405 nm reverts to the cis- form, where the lower pK_a brings

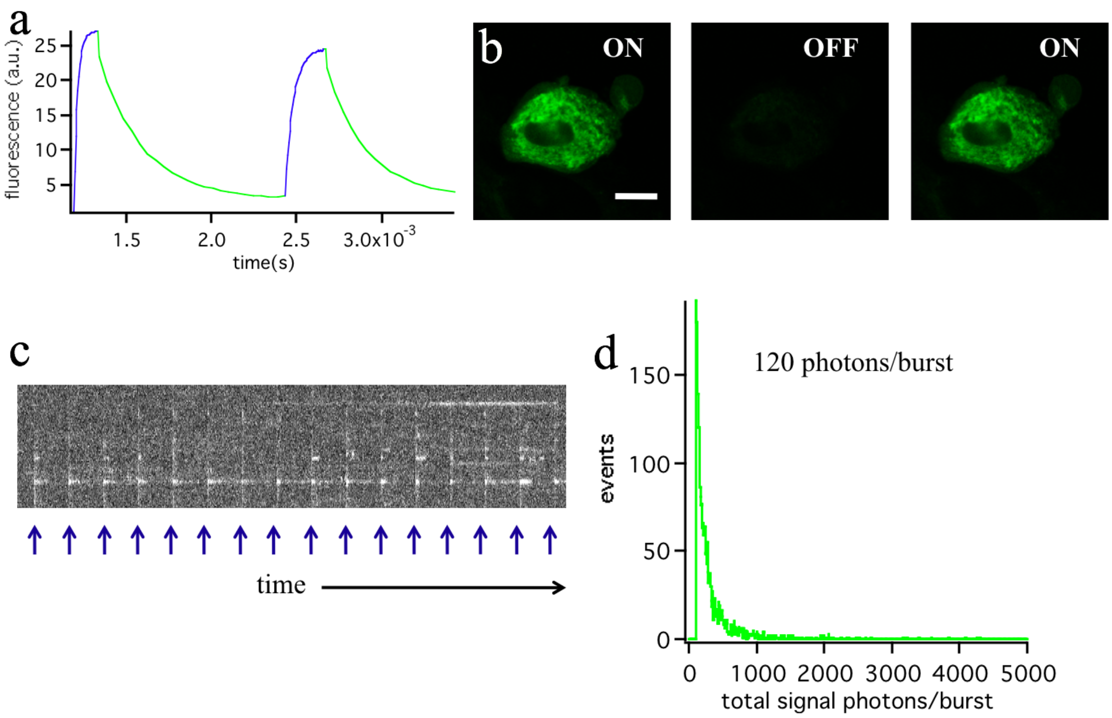

Figure 3.4: a) On-Off swtiching behavior of Dronpa in ensemble fluorescence measurements and b) expressed on the cell membrane (scale bar 10 μm) of HeLa cell bound to the receptor $\beta 2$. c) Kymographs of the single molecule traces subjected to pulsed 405 nm activation (arrows) in a 1%Poly Vinyl Alchool matrix (see Appendix C). d) Histogram of the number of photons/burst collected from the molecules displayed in c): an average of 120 photons per burst are collected, which compares to approximately 100 background photons.

the chromophore in the anionic (deprotonated) dark state. Depending on the spectral overlap of the neutral and anionic bands, an equilibrium between the two populations is always present and it is therefore not possible to completely push the reaction in one direction optically.

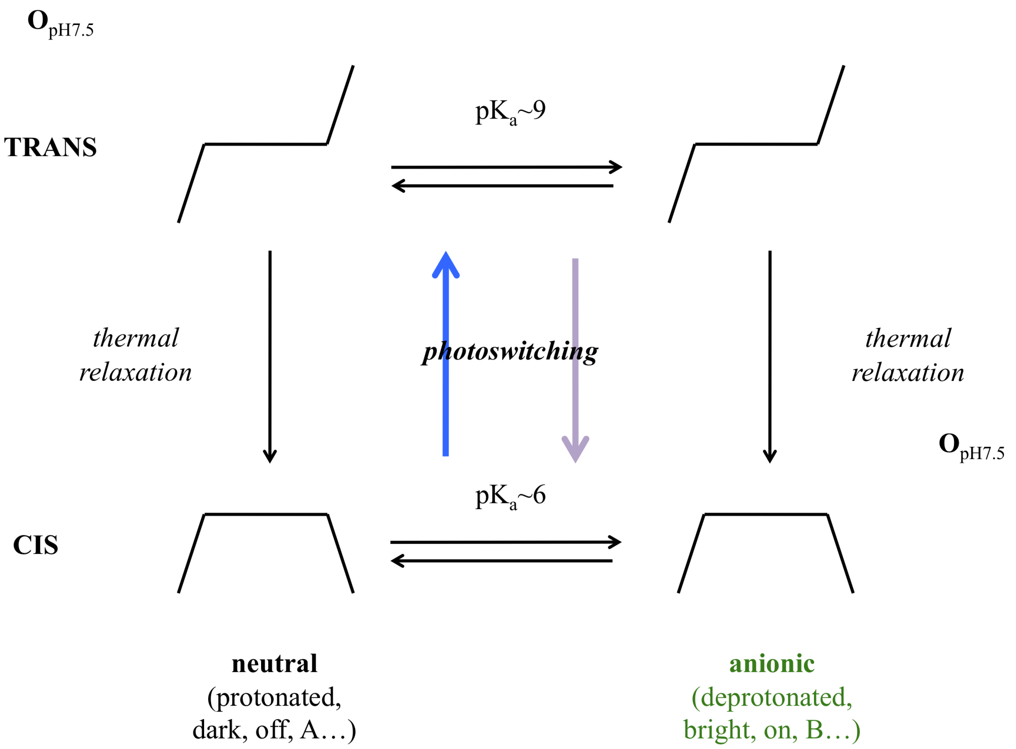

Figure 3.5: Scheme for the reversible switching observed in E222Q mutants (adapted from [35]). $O_{pH7.5}$ indicates the residence state of the fluorophore at neutral pH.

3.2 mEos2: unexpected switching behavior

3.2.1 PolyVinyl Alchool measurements

Another class of fluorescent proteins was discovered in 2002, when it was shown that a mutant of the fluorescent proteins from the coral *Trachyphylla Geoffroy* was able to photoconvert from the green to the red form upon prolonged irradiation with near UV light. This protein was named Kaede [36]. In 2004, a different coral, *Lobophylla Emprichii*, provided Eos, another green to red photoconvertible tetrameric fluorescent protein that could be engineered to obtain a dimeric and in particular a monomeric variant, named mEos [37]. Kaede, Eos and other proteins of this class share a similar structure (for an updated list and a recent review on photoactivatable fluorescent proteins see [38] and references therein) and we will focus on the second of these two proteins.

The green form of the Eos chromophore displays the pH dependent interconversion bewteen a 390 nm band and a 505 nm one that we have seen for wtGFP (Figure 3.6 A and C). Photoconversion from the

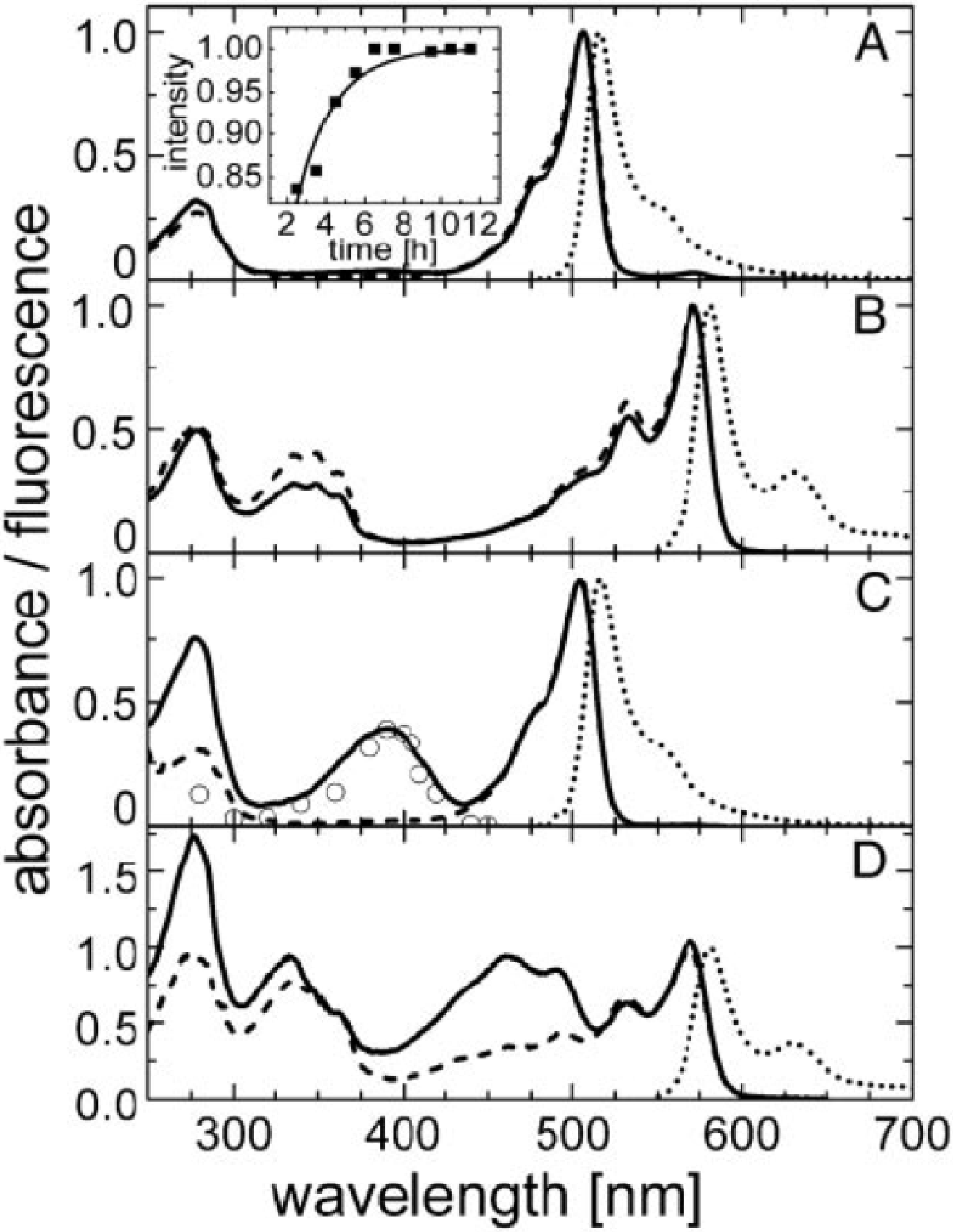

Figure 3.6: Absorbance, excitation and emission spectra of Eos (adapted from [37]) at pH 7 and pH 5.5. Solid line, absorbance; dashed line, excitation and dotted line, emission. (A and C) represent the green species at pH 7 and pH 5.5 respectively. Excitation (emission) spectra were measured with emission (excitation) set to 520 (490) nm. O, conversion yields scaled to absorbance. (Inset) Chromophore maturation at 27 ^{o}C B and D represent the red species at pH 7 and pH 5.5 respectively. Excitation (emission) spectra were measured with emission (excitation) set to 590 (560) nm.

green to the red form takes place as the result of the cleavage of the first 62 aminoacids of the protein, and the marked pH dependence (increased photoconversion efficiency at lower pH) strongly suggests that the photoconversion takes place through the neutral state of the chromophore. Upon cleavage the chromophore stays in the larger fragment, approximately 20 kDa, whereas the first eight kDa of the protein are cleaved. The red chromophore has an extinction coefficient of 67000 $\frac{1}{M \cdot cm}$ and a quantum yield of 0.62. It appears (Figure 3.6 B and D) that the red chromphore also possesses a protonated form, with a band at approximately 450 nm, that appears at acid pH. Most unfortunately, the monomeric variant of this protein matures only below 30^oC, making it unuseful for mammalian cell expression. However in 2009, an improved version of Eos, termed mEos2, was reported [39]. mEos2 is reportedly able to mature efficiently at 37 ^oC and to undergo the transition from the green to the red form upon 405 nm irradiation.

Just four mutations of the original wtEos were needed to obtain this new monomeric variant. We decided to use mEos2 as a PALM probe due to its high brightness and monomeric form. Our initial observations of mEos2 confirmed the expected photoconversion behavior. However, measurements at the single molecule level highlighted an interesting feature. We prepared solutions containing mEos2 molecules purified by nickel affinity chromatography after expression in bacterial competent cells (see Appendix C) in order to obtain samples containing immobilized mEos2 molecules at arbitrary concentrations. Moving in the opposite direction with respect to PALM measurements, we prepared samples at such a dilution level (< 1 nM) that the probability of finding two molecules in the same diffraction limited region is extremely low. We could therefore investigate the fluorescent dynamics of individual mEos2 molecules.

We observed multiple reactivations of photoconverted (red from) mEos2 molecules immobilized in a Poly Vinyl Alchool (PVA) matrix, on timescales ranging from a few to several tens of seconds. This is clearly illustrated in the single molecule kymograph of figure 3.7, a. To understand if this is a general property of mEos2, and to establish how many single molecules undergo the observed reversible dark-bright transition, we collected and inspected the fluorescent traces in PVA, determining that roughly half of the molecules undergo at least one reversible switching event [40]. The reactivation behavior observed at the single molecule level is consistent with the evolution of the absorbance spectrum of the partially photoconverted form of mEos2 shown in figure 3.7 b: upon irradiation at 561 nm an increase of the 450 nm band is observed, corresponding to a light induced population of the dark-state.

This observation, paired with the finding that most of the traces do not display any multi-step photobleaching, is quite a strong evidence of a reversible, Dronpa-like photoswitching mechanism in the red chromophore of mEos2. It is worthwhile to mention that, despite multiple attempts, it was not possible to obtain a complete photoconversion of mEos2 by 405 nm irradiation, independent of illumination power or duration. In all cases, above a certain irradiation threshold, the chromophore appears to get damaged, and the intensity of both the 505 nm and 575 nm bands appears to decrease. For this reason it was not possible to investigate by means of absorbance spectroscopy at the ensemble level the red photoconverted form of mEos2 alone, since irradiation with 405 nm light has the competing effects of re-activating the red form and eliciting photoconversion from the green to the red form.

In our single molecule experiments we alternated cycles of 20 s Continuous Wave (CW) activation to cycles where 405 nm irradiation was absent (upon continuous 561 nm excitation) in order to obtain *on-* and *off*-times histograms under both conditions for the red photoconverted form of mEos2 at the single molecule level (figure 3.8). *On*-times histograms in PVA displayed a mono-exponential shape, with an approximately ~ 20% longer lifetime in the absence of the activation light. *off*-times were better fit to bi-exponential curves and displayed a twofold increase of the longer *off*-time constant when 405

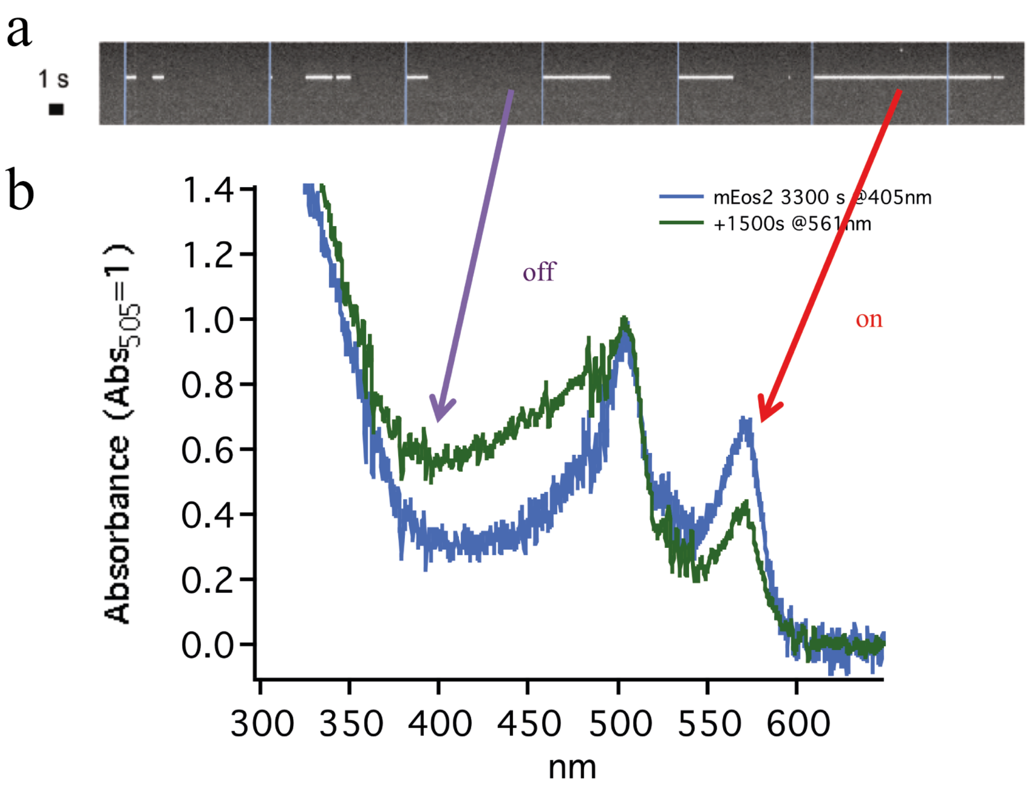

Figure 3.7: a) Single molecule kymograph for an individual mEos2 molecule in Poly Vinyl Alchool 1%, upon pulsed 405 nm irradiation. b) Spectral evolution of partially photoconverted mEos2 upon irradiation at 561 nm, displaying an increase of the 450 nm absorbance, corresponding to the protonated form of the red chromophore.

nm light is absent, from 4.1 ± 0.1 s to 8 ± 2 s. The bi-exponential nature of the *off*-times constants

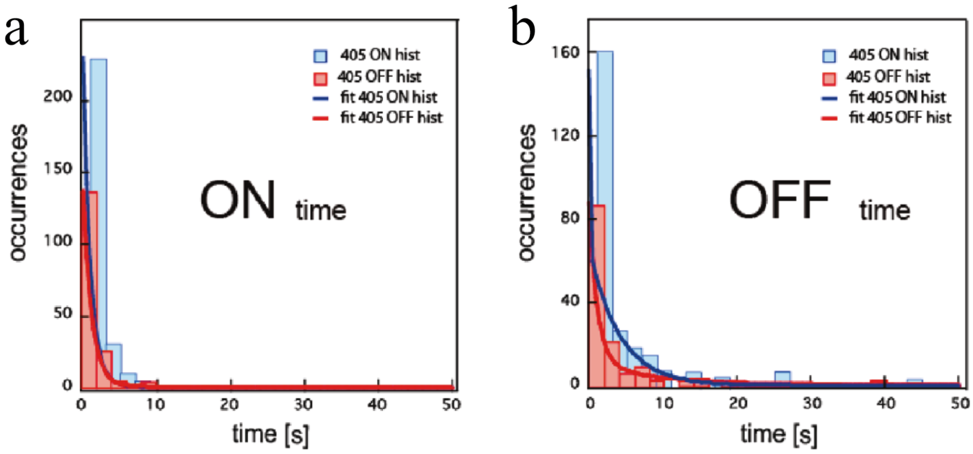

Figure 3.8: a) Histograms of the measured *on*-times for single molecular frames together with simple exponential fits. Red plot corresponds to traces measured when the activation light was absent, whereas blue traces correspond to measurement intervals when a weak 20 s CW pulsed 405 nm illumination was supplied. Time constants for the *on*-times, in the presence and absence of 405 illumination, are respectively 1.02±0.02 s and 1.21±0.02 s. b) Histograms of the measured *off*-times and superimposed double-exponential fits. Short time constants for the *off*-times, in the presence and absence of CW 405 illumination, are respectively 0.06± 0.01 s and 1.1± 0.01 s, whereas the long *off*-time constants are 4.1± 0.8 s and 8±2 s. (reprinted from Annibale *et al.* [40])

displayed in figure 3.8 is in agreement with the scheme proposed by Dickson *et al.* [29] and the model displayed in figure 3.2. The presence of two *off*-times constants, both affected by the photoactivation power, indicates that we can assume the existence of an intermediate state, which recovers to the bright form either spontaneously or by 405 nm activation, and a longer lived dark state in which the molecule can switch due to 561 nm irradiation and that can be recovered primarily by 405 nm irradiation. This is supported by the marked reduction of the long *off*-time constant upon 405 nm irradiation.

The dark state is therefore most likely the protonated form of the red chromophore. Although there is no structural evidence in this direction, the interconversion between the bright fluorescent state and the long lived dark state can be interpreted using as a working hypothesis the isomerization model proposed in figure 3.5. The hypothesis [40] that the red form of mEos2 displays a switching mechanism between the protonated form of the chromophore and a bright de-protonated state has been recently corroborated by the development of a non photoconverting mEos2 mutant, named mGeos. By replacing the His62 aminoacid where the cleavage and subsequent photoconversion take place in mEos2, Chang *et al.* [41] demonstrated that it is possible to obtain a fluorescent protein that does not photoconvert to the red form but displays a reversible switching mechanism between a dark and a green form. The dark state is associated to the 390 nm band also visible in the green form of mEos2, it is assumed by the authors to be the protonated form of the chromophore, and it is suggested that the chromophore isomerization is the reason for the observed switching.

From now on we will address the phenomenon of intermittent fluorescence emission from a single molecule under the general definition of *blinking*, without explicitly distinguishing between a blinking (fast) and a switching (slow) timescale. This choice is clearly understood in the framework of CW photoactivation, where separating the two timescales sharply is difficult, and, as we will see shortly, is the only possible choice when moving from PVA to another, more physiological matrix such as Poly Acrylamide.

If on the one hand the existence of a blinking behavior in an efficient switching molecule such as Dronpa, is characterized by an average *off*-time (under CW 405 nm irradiation in PVA) of the order of 60 ms [33], on the other hand a less efficient and bright switcher such as mEos2 can instead yield much longer *off*-times, as we have seen in figure 3.7, of the order of seconds and up to tens of seconds. This difference of one order of magnitude in the duration of the *off*-times is the reason why this blinking behavior is relevant to PALM imaging: given the stochastic nature of the photoactivation mechanism discussed in the previous chapter, the longer the molecule blinks *off*, the higher the probability of confusing it with another, new molecule, photoactivating for the first time in the same spatial location.

This is a key point, and we recall here a parameter that will be used throughout the course of this work, t_d. The parameter t_d is the maximum allowed *off*-time for a molecule that has blinked off; after this time, any fluorescence observed in the same location is attributed to a new molecule. Since the original PALM fitting algorithm [4] routinely integrates all the consecutive frames displaying fluorescence, including dark times in between them up to t_d before fitting a molecular peak, it is then clear how the choice of t_d will influence the number of localized molecules. The number of localized molecules and the appearance of the resulting super-resolution image itself can change quite dramatically upon the choice of t_d, making a rational choice of its value an important issue in analyzing the data coming from a PALM measurement.

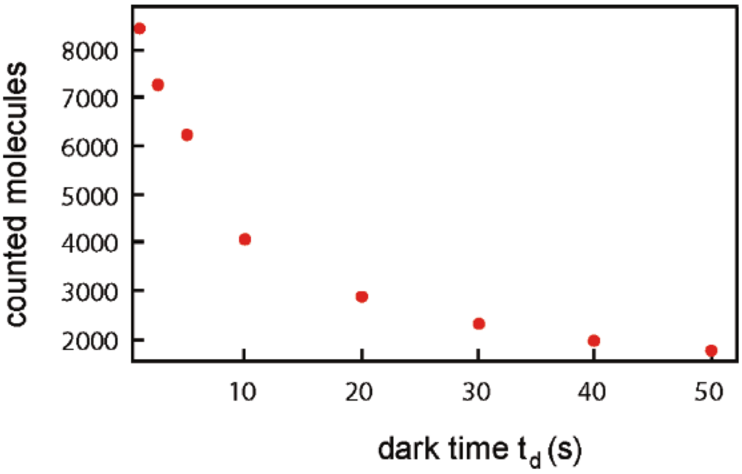

Figure 3.9: Amount of localized molecules in a diluted PVA sample as a function of the time interval t_d. (reprinted from Annibale *et al.* [40])

Our data in PVA, reported in figure 3.9, show an exponential decay of the number of localized molecules as a function of t_d, with a $\frac{1}{e}$ decay at ~ 20 s upon pulsed activation (0.1 Hz). We will discuss in the following the relation between the interpulse spacing and the *off*-times constant. For the moment it is important to notice that the number of counts changes dramatically upon modification of t_d. Furthermore, this implies that the information conveyed by the pointillistic reconstructed image is affected substantially. It should be emphasized that the original representation of PALM pictures by Betzig and coworkers [4] is based on the concept of probability distribution of finding the molecule in a given

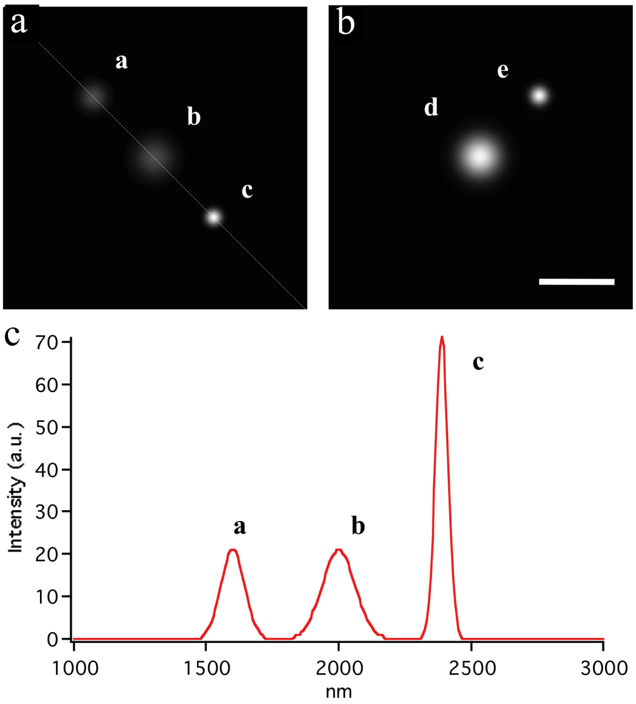

Figure 3.10: Representation of molecular localizations using a Gaussian Probability Distribution Function. a) *a* is the normalized Gaussian fit of a molecule that emitted $2 \cdot N_1$ photons; *b* it the superposition of the independent fits of two molecules having emitted each N_1 photons and *c* is the fit of a molecule having emitted $3 \cdot N_1$ photons. b) *d* is the superposition of the independent fit of $n = 5$ molecules having emitted each N_1 photons and *e* is the fit of an individual molecule that emitted $5 \cdot N_1$ photons. c) Line profile from panel a.

position, each molecule represented by a normalized 2D-Gaussian probability distribution function; in this representation the net effect of multiple localizations of the same molecule (overcounting) will be a decrease of the average localization precision and a loss of resolution. When displaying PALM pictures using the probability map representation, e.g. when molecules are displayed as 2D Gaussians, we recall that the standard deviation σ is given by the localization precision:

$$\sigma^2 = \frac{s_a^2}{N} \cdot \left(\frac{16}{9} + \frac{8\pi s_a^2 b^2}{N a^2}\right) \tag{3.1}$$

where b^2 represents the number of background photons per pixel of the fitting window, a the pixel size, $s_a = s^2 + \frac{a^2}{12}$ with s the microscope point spread function and N the total number of collected photons. Blinking results in multiple spots, each with a smaller intensity than the one originated from the ideal non-blinking molecule.

Notably, if a molecule blinks twice (or n times), then the summed intensity of the two (or n) Gaussians fitted to each of the two (or n) frames subsets will be the same as the one arising from the fit of the integrated frames. This can be seen easily since the peak of the fitting Gaussian curve scales as $max = \frac{N^2}{A \cdot N + B \cdot b^2}$, with A and B two arbitrary constants. The net effect of the blinking/reactivation will be, however, an increased apparent σ, and a consequent loss in resolution, since σ^2 scales as $\frac{1}{N} + \frac{1}{N^2}$. Therefore if $N_1 = 2N_2$ and $b_1 = 2b_2$ then $max_1 = 2max_2$ and $\sigma_1^2 = 0.5\sigma_2^2$. This observation is graphically summarized in figure 3.10.

What would be then the *right* value of the temporal threshold t_d in order to regroup the traces and obtain both an image and a spatial point pattern as representative as possible of the underlying biological structure? If the average *off*-time of the blinking fluorophore exceeds the frame rate of the acquisition, let us say 20 Hz, then a dark time $t_d = 0.05$ s will clearly result in significant overcounting. On the other hand, a longer t_d might avoid counting the same molecule twice, but in a densely labeled sample it might induce grouping of fluorescent traces belonging to neighboring but different molecules (i.e. activated within the same detector's pixel).

From figure 3.9 it is clear that the number of localized counts is dramatically influenced by the choice of a dark time t_d and that it is connected to the number of photoblinks a molecule can undergo. By mixing the fluorophores in a polymeric matrix, spin-coated (see Appendix C for details on sample preparation) on the coverslip, we experimentally generated a *random* pattern. We expect that the right t_d will provide us a completely spatially random pattern (CSR). The theoretical cumulative probability distribution function for the inter-particle distances is known, and in the unit circle it yields [42]:

$$TCDF(t) = 1 + \frac{1}{\pi} \cdot \left(2 \cdot (t^2 - 1) \cdot acos(\frac{t}{2}) - t \cdot (1 + \frac{t^2}{2}\sqrt{1 - \frac{t^2}{4}})\right) \tag{3.2}$$

where t is the inter-molecular distance. If we plot in a quantile-quantile [43] plot the theoretical cumulative distribution function of the inter-molecular distance vs the experimental one we would expect a linear relationship only if the experimental distances arise from CSR. Figure 3.11 shows that the curve is far from linear at small intermolecular distances for low t_d values, whereas CSR is achieved as t_d is progressively increased up to 50 s, corresponding to five switching cycles per fluorophore. In a diluted sample, the choice of a long t_d therefore addresses in the most straightforward way the issue of molecular blinking.

3.2.2 Computer simulations of experimental results

The measurements in PVA highlighted an interesting phenomenon, posing a relevant question about how to treat PALM data using a fluorophore such as mEos2 that displays, besides photoconversion, an inefficient reversible switching yielding long *off*-times. Though very popular for single molecule experiments with organic dyes, PVA immobilization was previously demonstrated (see supplementary information in [33]) to influence the photophysical properties of GFP-like fluorescent proteins, possibly altering the conformation of the chromophore. This results, for example, in the faster thermal recovery of the de-protonated state in single Dronpa molecules in PVA (hours) as compared to bulk measurements (several days).

For this reason all further in-vitro single molecule experiments discussed in this thesis will be performed in PolyAcrylamide Gels (PAGE) [44] (see Appendix C for sample preparation). PolyAcrylamide is a synthetic polymer that can be prepared to provide an immobilization matrix with an effective median pore radius between 0.5 nm and 3 nm by the simple device of adjusting the ratio between the total Acrylamide concentration and the concentration of a cross-linking agent, Methylenebisacrylamide. PAGE has ben used for more than forty years for protein electrophoresis and immobilization, and is a widespread immobilization matrix in single molecule experiments [45].

Our objective is now to find the condition that generates spatial point patterns as devoid as possible of photoblinking induced artifacts when imaging densely labeled samples where the probability that two

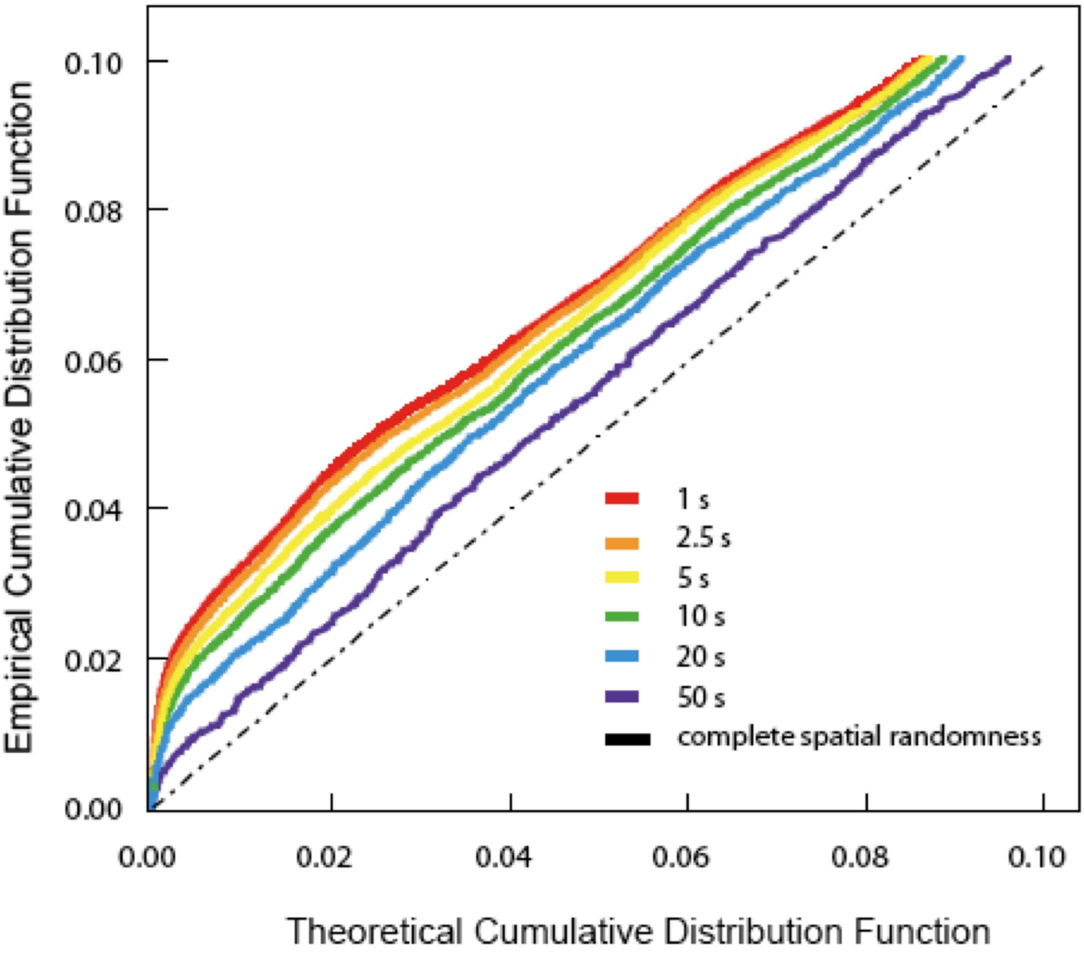

Figure 3.11: Measured Empirical Cumulative Distribution Function (EDF) plotted against the Theoretical Cumulative Distribution Function (TDF) for complete spatially random distributed points. Experimental data are calculated from samples of mEos2 molecules subjected to pulsed activation in PVA. Plots of the EDF vs the TDF calculated for different values of t_d and for a circular region corresponding to a circular subsection (R=2 μm) of the excitation area. The scale is enlarged to display probability values between 0 and 10%, corresponding to small intermolecular distances. (reprinted from Annibale *et al.* [40])

or more molecules fall in the same diffraction limited region is not anymore negligible. This condition permits also a quantitation as accurate as possible of the number of molecules present in the sample. The statistics of a typical single molecule experiment in-vitro allow to image up to one thousand isolated single molecules in the field of view. If the average *off*-time of the fluorophores exceeds the exposure time (e.g. 0.05 s), then regrouping the traces choosing a $t_d = 0.05$ s will obviously result in a significant overcounting, since multiple fluorescent bursts from the same molecule will be localized as independent fluorophores. However, understanding a-priori which should be the right t_d to regroup the fluorescent traces is not at all an obvious question, unless the sample is extremely diluted and molecules do not overlap spatially. In addition, both the fluorophore density and the activation rate will be relevant parameters to take into account.

To this goal we systematically compare the experimental outcomes of in-vitro measurements to simulated PALM experiments reproducing the fluorescent dynamics of mEos2 as understood from the single molecule fluorescent traces. More specifically, we compared the experimental data, in the form of counts vs t_d curves to the outcome of in-silico ensemble photoactivated localization microscopy simulating the stochastic *on*-*off* dynamics of individual mEos2 molecules based on the measured values extracted from the single molecule fluorescence traces in PAGE. The use of simulations provides information about how many molecules are counted multiple times or how many molecules are missed by regrouping together traces belonging to distinct molecules. We modeled the mEos2 fluorescent dynamics using the following parameters: the number of times that a molecule can switch back and forth between the *off* and *on* states and the distribution of the fluorescence *on*-times and *off*-times.

The number of molecules localized in an ensemble experiment in PAGE decays exponentially with t_d, and the CW *off*-times distribution is single exponential with a $\frac{1}{e}$ decay at approximately 0.1 s (one order of magnitude smaller than in PVA). Furthermore the intensity of the CW photoactivation determines a change in the average value of *on*-times (t_{on}), *off*-times (t_{off}) and number of blinks (n_{blinks}). Low values of the photoactivation (~ 10 mW/cm^2) determine longer *off*-times, shorter *on*-times and almost twice as much switching events than at high photoactivation values (~ 100 mW/cm^2), as displayed in figure 3.12. All faster dynamics is masked by the typical CCD exposure time of 0.05 s (yielding a frame rate slightly below 20 Hz in frame transfer mode). The observation that in PAGE the distribution of the *off*-times can be fit by a single exponential rather than the bi-exponential observed in PVA is an indication that the two timescales observed in PVA (namely the blinking and switching one, according to the model of Figure 3.2) are either overlapping in the new matrix, or the probability of one of the transitions has became exceedingly low.

We therefore opted for a four state (i.e. one dark state) scheme to model the dynamics of the fluorophores: inactive (green), active (red), dark and bleached (more on this point can be found in Appendix B). The inactive to active transition is assumed to be irreversible, whereas the active state can revert to a dark state and be recovered with a probability proportional to the intensity of the 405 nm irradiation. This reversible switching cycle between the bright and the dark state can occur until the molecule photobleaches, with a probability dependent on the amount of time it has been on. The four state model that we propose has the advantage of representing a first order variation with respect to the ideal photoactivatable probe envisioned in the original PALM concept [4], i.e. off-on-bleached, and, as we will demonstrate shortly, it fits well the data.

To simulate PALM experiments we used the following procedure [46]. First, N points representing the individual fluorescent proteins were randomly distributed in the field of view (35 x 35 μm^2). A discrete time dynamics of the emitting state of the fluorophores, while keeping their position fixed in order to reproduce the experiments in PAGE gel or fixed cells, is then started with all fluorophores in the inactive

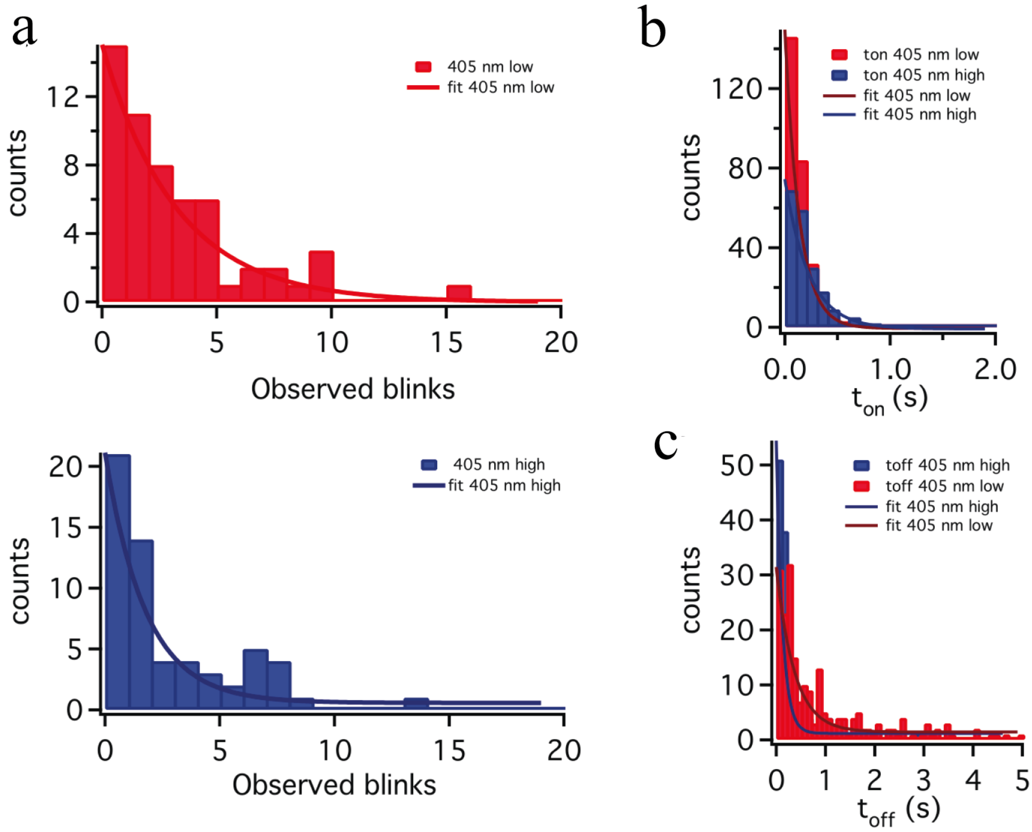

Figure 3.12: Photophysical parameters of mEos2 in PAGE. a) Histogram of the number of times a single mEos2 molecule undergoes photoblinking before definitive photobleaching. Experimental values and single exponential best fits are shown for two different conditions of activating power (low 405 nm laser CW power = 10 mW/cm^2 and high CW power = 100 mW/cm^2). 1/e decay values are $n_{blink-low}$ = 1.9 ± 0.2, $n_{blink-high}$ = 1.05± 0.11. Molecules are excited by a CW 561 nm diode laser in Total Internal Reflection. b) Histogram of the measured *off*-times $t_{off-low}$ = 0.45± 0.04 s, $t_{off-high}$ = 0.1± 0.01 s. c) Histogram of measured *on*-times t_{on-low} = 0.08 ± 0.005 s, $t_{on-high}$ = 0.16± 0.02 s (reprinted from Annibale *et al.* [46]).

state. At each time step, set to be equal to the acquisition integration time, each fluorophore could either remain in the *off*-state or change to the *on*-state in a stochastic way, such as to reproduce the activation probability arising from irradiation with 405 nm light of fixed intensity. Once activated, at each time step the fluorophores are then subjected to another stochastic process to determine whether to remain in the *on*-state or to switch either to a reversible *off*-state or to photobleach in a definitive way. In a similar manner, all fluorophores in the reversible *off*-state were tested at each time step whether to remain in this *off*-state or to turn back *on*. The simulation parameters for the discrete *on*/*off* dynamics were tuned such as to reproduce the following measured photophysical parameters: number of fluorophore activations per frame, *on*-times distribution, *off*-times distribution and distribution of number of blinks. An additive noise floor, due to false-positive localizations was also included, tailored on control experiments where the fluorophore was absent.

The on/off dynamics was then simulated for a fixed number of frames equal to the one used in the corresponding PALM experiment, and it was post-processed to reproduce the observations of a PALM experiment using the following constraints: (i) a finite resolution of ±1 pixel (e.g. 133 nm pixel size) around the fluorophore coordinates, such as that two simultaneous emitting fluorophores within this distance were detected as a single fluorophore, (ii) an allowed *off*-time (i.e. t_d) such that consecutive reactivations of the same fluorophore (or of a different fluorophore within the same pixel) within the allowed *off*-time were considered as a single detection instead of two consecutive ones (a multiple count for the same fluorophore or a missed count in the case of two colocalized molecules), (iii) a detection error obeying to a uniform distribution within ± 20 nm in x and y coordinates.

In principle, once the t_{on}, t_{off} and n_{blinks} have been determined from the single molecule fluorescent traces for a given photoactivation value, the only remaining parameter to insert in the simulation that models an experimental dataset is the number of molecules N. Figure 3.13 a, shows the counts curves for two experimental datasets, containing respectively ~ 1 and ~ 100 mEos2 molecules/μm^2 superposed to an array of simulated curves covering a range of densities going from a few to thousands of molecules/μm^2. The curves are displayed in a logarithmic scale in order to include the three orders of magnitude density range. We should note that at high densities (> 100 molecule/ μm^2) the simulated curves display a larger decay due to the increased grouping in time of fluorescent traces belonging to distinct molecules (missed counts). This effect becomes less severe by reducing the photoactivation power, as shown in the simulated curves of figure 3.13 b. Depending on the t_d value, the low and high density experimental points fall within a set of curves covering a simulated density from 0.7 to 1 molecules/μm^2 and from 70 to 100 molecules/μm^2 respectively, suggesting the need for the adjustments of the other simulation parameters to maximize the agreement between experiment and simulation.

We will now focus on a specific counts vs t_d curve. Figure 3.14 displays the experimental counts (markers) obtained on a sample of mEos2 molecules embedded in PAGE at a concentration of approximately ~ 2 μM. The simulated curve (line), where the number of molecules in the simulation is adjusted in order to maximize the agreement to the experimental points, yields a sample density of 135 molecules/μm^2. As anticipated, the simulated dataset provides an invaluable information about the overall number of molecules that, for a given t_d value, are either not counted since their traces are grouped together (missed counts) or are counted multiple times since they blink *off* for a time longer than t_d. The purple curve represents the behavior of the multiple counts (indicated as *double counts* in the figure legend) that modulate the decay of the counts at low t_d values. On the other hand, missed counts (green curve) increase steadily as a function of t_d, dominating above 1.5 s, where multiple counts are negligible. The exact number of molecules is recovered at a t_d value of 0.5 s, where missed counts

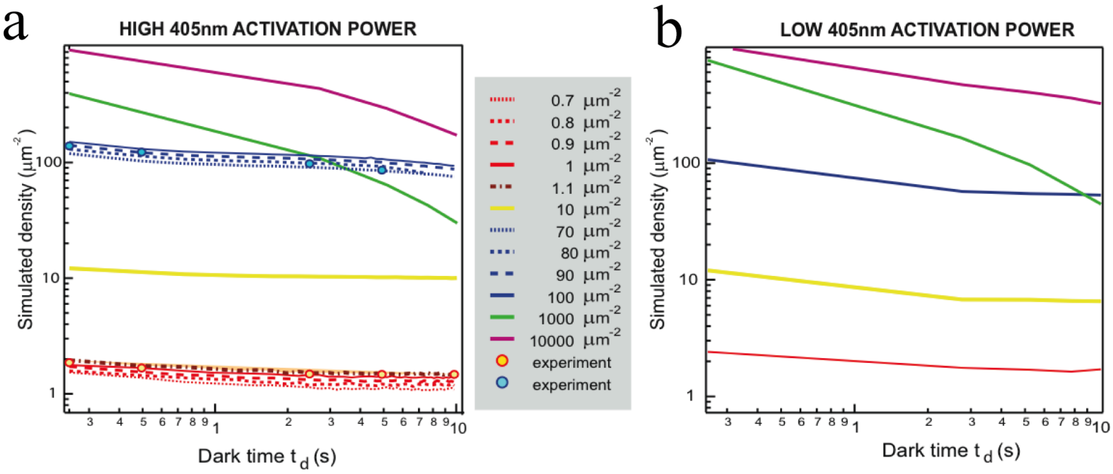

Figure 3.13: Simulated PALM localization density curves as a function of t_d (log-log). a) High 405 nm photoactivation light. The effect of blinking results in a twofold reduction of the measured density as t_d is increased ten times. At this density and high photoactivation rate the experiment falls in a regime dominated by missed counts. Superimposed to the simulated density curves are the experimental points corresponding to a high and low density mEos2 PAGE experimental datasets generated using a dilution ratio of 100 times. b) Same as in a) but for lower 405 nm photoactivation light. (reprinted from Annibale *et al.* [46])

and multiple counts compensate. This approach provides two key advantages: first, for a given sample density and photoactivation value, it is possible to analyze the data and obtain images corresponding either to an over-counting regime (yellow shading in figure) or an under-counting regime (blue shading in figure). Second, upon a good knowledge of the fluorophore photophysical behavior, it is possible to extract accurate concentration values, provided that most of the molecules have been activated.

It is clear that the principal requirement for this approach to work is that the fluorescent dynamics of the fluorophore (we have seen how for mEos2 it changes dramatically upon changing the immobilization matrix) is known beforehand and that it does not change from sample to sample. The method described well enough the experiments in PAGE, under controlled conditions. However, the distributions of *on*-times, *off*-times and number of switching cycles of a fluorescent protein within a fixed cell are not equally easy to determine, given the profound impact of the environment on the single molecule fluorescent dynamics. Figure 3.13 already showed that a ~ 30% discrepancy exists between the simulated curve and the experimental points, indicating that, aside from the density, the other photophysical parameters in the simulation need to be fine-adjusted to match the experimental dataset. To address this problem, we should therefore note that the experimental counts vs t_d curve already contains part of this photophysical information.

To clarify this point, let us now discuss, as anticipated in reference to figure 3.9, the connection existing between the $\frac{1}{e}$ decay constant of the curve and the *off*-times constant. In fact, the $\frac{1}{e}$ decay is exactly the *off*-times constant derived from the histograms, such as the one in figure 3.12 c. We define $c(t_d)$ as the number of molecules localized in the sample for a given t_d value.With the aid of figure 3.15 it is straightforward to observe that $c(t_d = 1) - c(t_d = 2) = A \cdot e^{-\frac{t_d=2}{t_{off}}}$, since the difference in counts corresponds exactly to the number of *off*-times equal to one CCD frame, i.e. the first bin of the

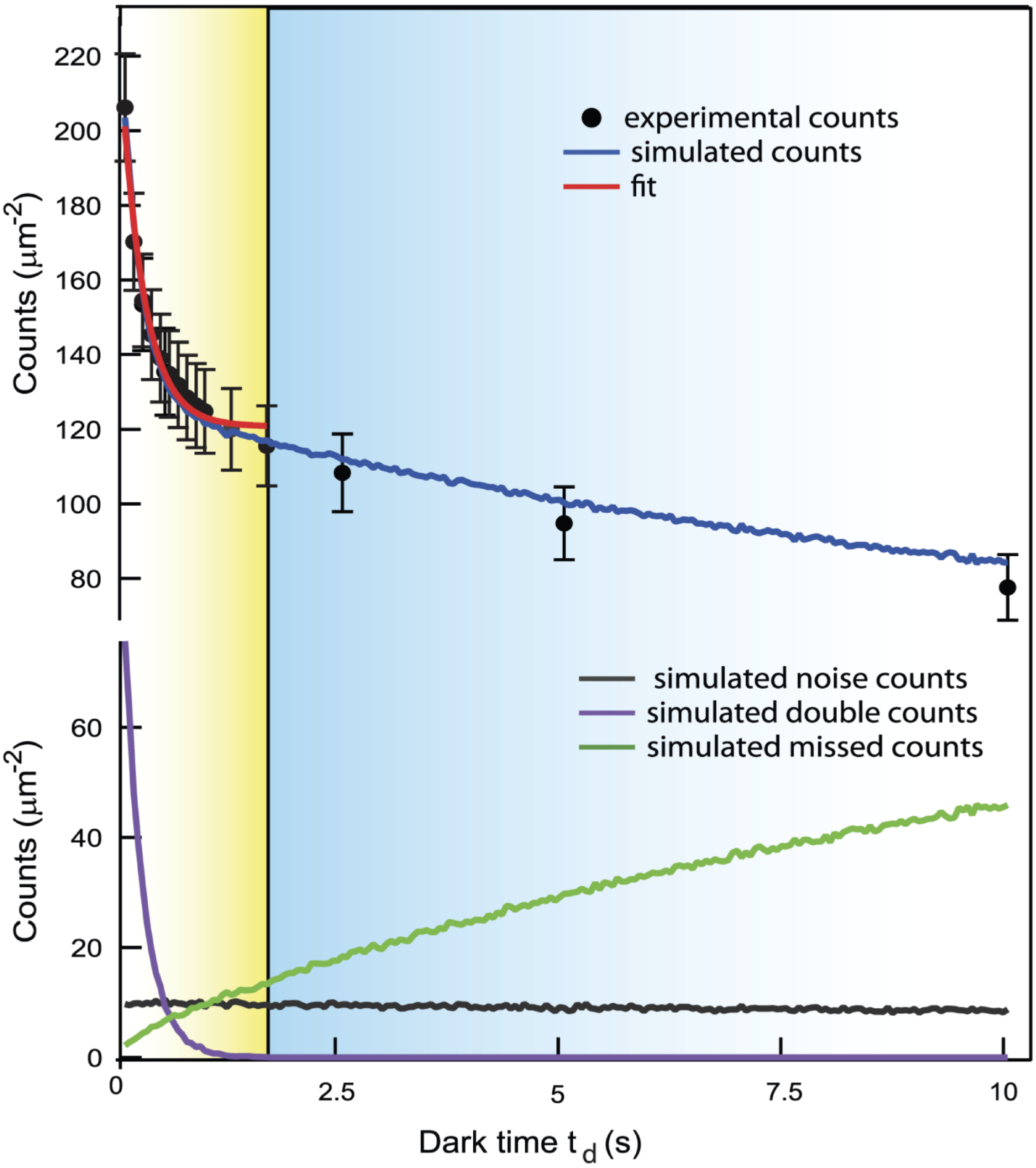

Figure 3.14: Experimental (markers) and simulated (blue line) total numbers of mEos2 molecules localized as a function of dark time t_d, where dark time t_d is time allowed for a molecule to go dark before being identified as a different molecule when fluorescence resumes. Simulated counts, out of total, ascribed respectively to missed counts (green), multiple counts (pink) and noise (gray). For all samples the duration of the acquisition is 20000 50 ms frames. The red curve shows best fit to data for dark time t_d values comprised between 0.05 s and 2 s. If no missed counts were to occur, the asymptote of the decaying curve of the observed counts would converge to the effective number of molecules present in the sample. Fitting to the equation 3.5 yields $t_{off} = 0.2 \pm 0.1$ s and $< n_{blinks} >= 0.7 \pm 0.1$ consistent with the values reported in figure 3.12. N from the fit yields $N = 121 \pm 6$ molecules$/\mu m^2$ whereas the total density of the simulated sample is 135 molecules$/\mu m^2$ including noise counts, giving a 10% agreement.

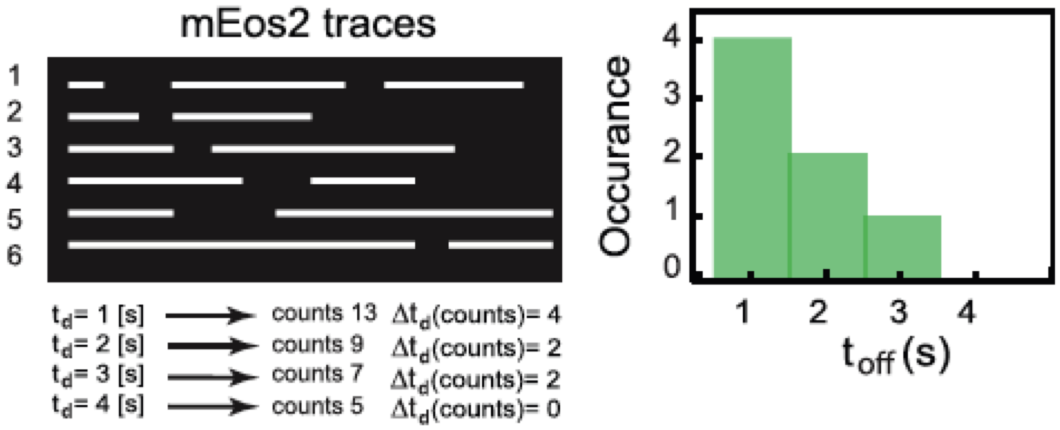

Figure 3.15: Single molecule kymographs of 6 blinking/reactivating molecules. The duration of the dark times spans from one to four units (0.05-0.15 s), resulting in the *off*-times histograms on the right hand side. If molecular localizations are performed considering a dark time t_d of 0.05 s, 0.1 s and 0.15 s, the resulting number of counts are 13, 9, and 7 respectively. The difference between these values corresponds to the values of the *off*-time histogram. (reprinted from Annibale *et al.* [46])

off-times histogram. Indicating with N the total number of molecules present in the sample then $c(t_d = n) - c(t_d = n+1) = A \cdot e^{-\frac{t_d=n+1}{t_{off}}}$, and in the ideal limit of $\Delta t_d \rightarrow 0$ then the expression can be integrated to yield:

$$c(t_d) = A \cdot t_{off} e^{-\frac{t_d}{t_{off}}} + B \cdot t_{off} \tag{3.3}$$

Using the boundary conditions $c(t_d = 1) = N + n_{blink} N$ (at low t_d the number of molecules is only due to over-counting) and $c(t_d = \infty) = N$) (true for a diluted sample where missed counts are absent, since no two molecules lie in the same position) we obtain

$$N \cdot (1 + n_{blinks}) = A \cdot t_{off} e^{\frac{-1}{t_{off}}} + N \tag{3.4}$$

finally obtaining

$$c(t_d) = N + N \cdot n_{blinks} \cdot e^{\frac{1-t_d}{t_{off}}} \tag{3.5}$$

This equation can be fit to the counts vs t_d curve in order to obtain both t_{off}, n_{blinks} and N. The fit to equation 3.5 is displayed as a red line in figure 3.14, obtaining a value for $N = 121 \pm 6$ molecules/μm^2, within a 10% agreement with the simulation value. It is important to notice that this equation can be fit to the curve as far as missed counts are negligible, the assumption that allowed us to set the boundary condition $c(t_d = \infty) = N$. A fit to the experimental data using this equation will therefore yield the total number of molecules N only if performed in a regime where missed counts are minimized. Since, for a given sample density and photoactivation value, the so-called overcounting regime is not known a-priori, this appears the only limitation of this approach.

This method of fitting the curve in the overcounting regime (small t_d values) provides a reliable estimation of the number of molecules as far the photoactivation rate is kept reasonably low when the sample is dense. Although the fitting equation does not explicitly take into account missed counts the method appears to work in samples as dense as 1000 molecules/μm^2, giving a result within at most 10% of the number of active molecules, as established by simulations. Figure 3.16 a-c, displays the simulated counts vs t_d curves for homogeneous samples generated with densities respectively of 10, 100 and 1000 molecules/μm^2 while keeping the photophysical parameters fixed. Fitting is performed using only the first five points of the curve, in order to avoid the missed counts region as much as possible. The number of molecules extracted from the fit is in excellent agreement with the simulated number of molecules up to 100 molecules/μm^2 declining to a 20% error only for a density of 1000 molecules/μm^2 or above. However, upon the reduction of the photoactivation power (and accordingly of the missed counts) the fit yields a value with the much smaller error of 5%, as reported in the summary table of figure 3.16.

In principle, it is also possible to take missed counts into consideration explicitly. The probability that two distinct molecules photoactivate in the same point within a temporal interval t_d under constant photoactivation power, is the one of a Poisson process and is given by $(1 - e^{-n \cdot t_d})$, where n is the temporal activation density (i.e. new molecules per frame in the diffraction limited spot). For t_d going to infinity the number of missed molecules should account for most of the molecules in the sample aside from the very first localizations occurred in each diffraction limited region. Hence it should be possible to extend equation 3.5 to take missed counts in considerations leading to:

$$c(t_d) = N + N \cdot n_{blinks} \cdot e^{\frac{1-t_d}{t_{off}}} - N' \cdot (1 - e^{-n \cdot (t_d - 1)}) + b \tag{3.6}$$

The last two terms appear to fit relatively well simulated missed counts data aside from an additive constant b, since at high density a certain number of concomitant activations occur, and missed counts can not be avoided even at $t_d = 1$ frame.

The validity of this method can be assessed upon performing the fit on in-vitro samples, prepared after having measured their exact concentration by absorbance spectroscopy. In figure 3.18 we plot N vs the concentration determined from absorbance data. We calculated the ratio (red markers) between the number of PALM counts at a fixed t_d (e.g. $t_d = 0.05$ s) and the number of molecules obtained using equation 3.5. From the obtained ratio it is obvious that our method prevents overcounting at all molecular densities.

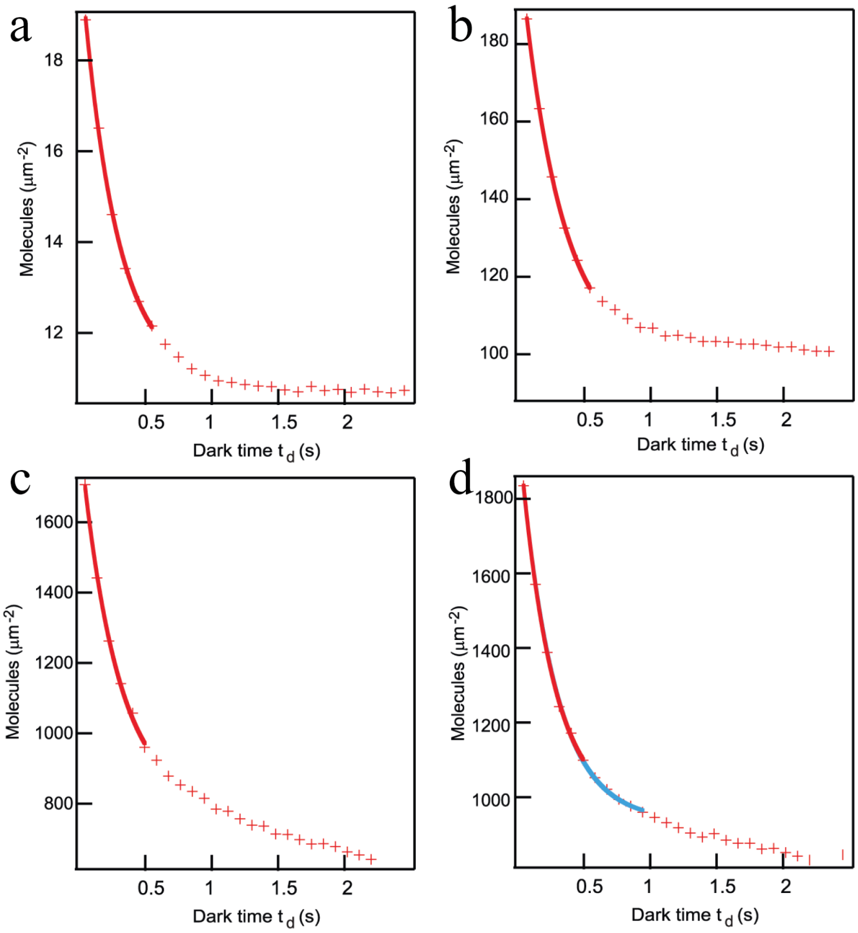

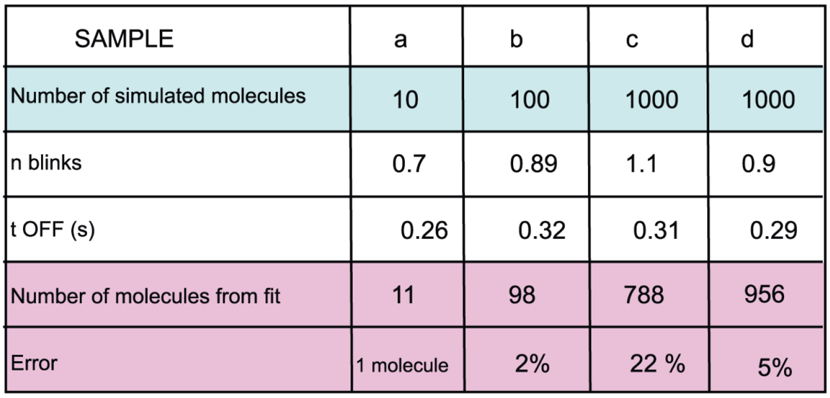

SAMPLE	a	b	c	d
Number of simulated molecules	10	100	1000	1000
n blinks	0.7	0.89	1.1	0.9
t OFF (s)	0.26	0.32	0.31	0.29
Number of molecules from fit	11	98	788	956
Error	1 molecule	2%	22 %	5%

Figure 3.16: Semi-empirical fit to simulated data. Simulated PALM experiments on in-silico samples generated at three different densities while keeping the photophysical parameters constant. a) 10, b) 100 and c) and d) 1000 molecules/μm^2. The simulated counts curves are fitted to equation 3.5 using only the first 5 points of the curve, up to a $t_d = 50 \cdot 10$ ms $= 0.5s$. (reprinted from Annibale *et al.* [46])

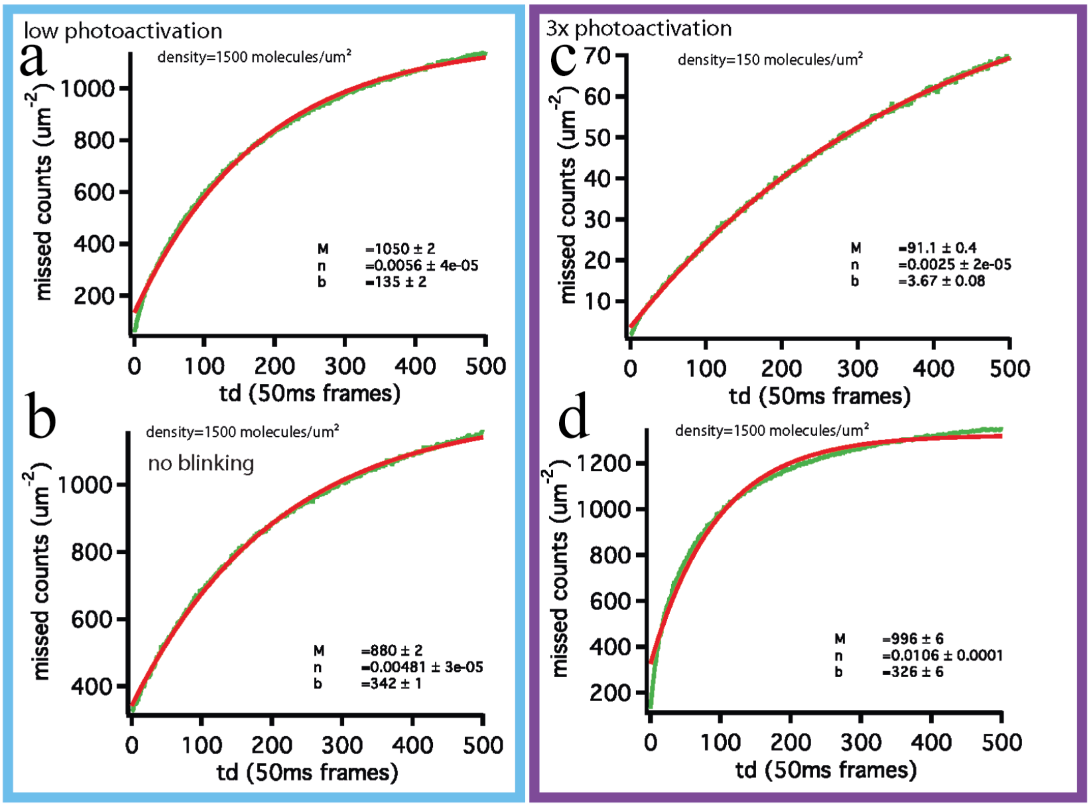

Figure 3.17: Fitting to simulated missed counts curves under different conditions. a) and c) 1500 molecules/μm^2, low photoactivation values. b) 150 molecules/μm^2, and d) 1500 molecules/μm^2, threefold higher photoactivation power. (reprinted from Annibale *et al.* [46])

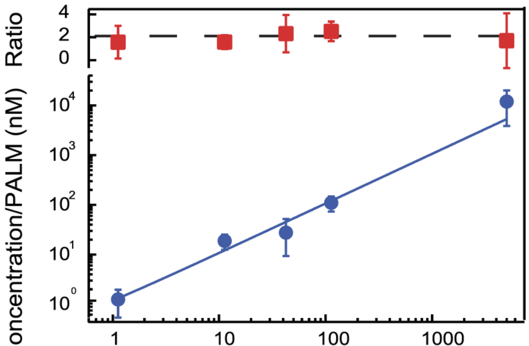

Figure 3.18: Calibration curve for the concentrations extracted by fitting eq. 3.5 to PALM data. Blue circles: reconstructed concentration from PALM experiments (0.06 molecules/μm^2/nM in TIRF) vs absorbance-derived concentration and best fit. Each point corresponds to the average of PALM experiments on three different samples. Red markers display the ratio between the concentration extracted directly from PALM at $t_d = 0.05$ s and the concentration obtained using our method. (reprinted from Annibale *et al.* [46])

3.3 Discussion

In conclusion, after an overview of the photochromic properties of photoactivatable fluorescent proteins, we report here a new and interesting finding regarding the single-molecule behavior of the mEos2 PA-FP. A significant fraction of mEos2 molecules can undergo multiple activations and deactivation cycles in the red photoconverted form, though not as efficiently as observed in reversible switching proteins such as Dronpa.

This is an important finding since any *counting* experiment using this protein should take into account the possibility of multiple counts of the same molecule. We have then systematically investigated the effect of molecular photoblinking and fluorescence dark times on a typical PALM experiment.

We propose a method to obtain a reliable estimation of the number of photoblinking molecules present in a sample by comparing simulations tailored on single molecule photophysics and in vitro experiments. We have identified a parameter, the dark time t_d, depending on which it is possible to move from an overcounting to an undercounting condition, outlining different regimes to conduct a PALM measurement. We have exploited the information present in the number of localizations at different dark times t_d to propose an equation (3.5) that fits the data allowing us to extract the average number of blinking fluorophores from the PALM measurement.

As we anticipated in the introduction, one of the main reasons to investigate in detail the quantitative capabilities of PALM is the possibility to obtain accurate information on the spatial arrangement of plasma membrane proteins. This will determine if this technique can be used to identify small aggregates or sub-diffraction limit heterogeneities that may provide further insight on the mechanism of signal transduction of membrane receptors such as GPCRs. The multiple counting of even a small number of molecules may clearly have an impact in the imaging of biological systems such as proteins expressed on the plasma membrane, where phenomena such as oligomerization and clustering can be properly identified only if the same molecule is not counted multiple times.

In the next chapter we will further explore the consequences of reversible switching of the red form of mEos2, in particular when they result in a few long *off*-times. We will specifically focus on the consequences of this behavior when imaging $\beta 2$, a prototypical GPCR, labeled with mEos2.

4 Identification of clustering artifacts in Photo Activated Localization Microscopy

4.1 Introduction

In the previous chapter we demonstrated that one of the most promising photoactivatable fluorescent proteins discovered so far, displays a non negligible degree of reversible photoswitching. We have analyzed in detail the consequences on the number of localized molecules in the sample and we have shown that, under the hypothesis of a four state model regulating the fluorescent dynamics of the red photoconverted form of mEos2, it is possible to calculate the average number of blinking molecules present in the sample. We will now address the issue of which t_d value should be chosen in order to obtain an image as accurate and revealing of the protein arrangement as possible. As anticipated in the introduction, for this purpose we chose as a model system the β2-Adrenergic Receptor, a prototypical member of the G protein coupled receptor family. The labeling of β2-AR with mEos2 (as well as with other photoactivatable fluorescent proteins) provided a functional chimaera, as discussed in more detail in Appendix C.

G protein-coupled receptors (GPCRs) are one of the most important membrane protein families. GPCRs act as the primary detectors of cell signals and are responsible for the majority of cellular responses to hormones and neurotransmitters, as well as sensory stimuli such as light, odor and taste senses. GPCRs are the targets of nearly half the drugs that are used for the healing of a wide range of human diseases, including psychiatric, neurodegenerative, and immune disorders, cardiovascular, gastrointestinal, renal, and pulmonary diseases, and finally cancer. Nearly 850 different human genes encode for GPCRs that are predicted to share a common molecular structure consisting of seven transmembrane helical domains connected by three intracellular and extracellular loops (see the review by Rosenbaum *et al.* and references therein [47]). Activation of the receptor through the binding of the specific agonist induces a functional interaction with its target, the heterotrimeric (α, β and γ subunits) Guanine nucleotide [1] binding protein (G protein).

The endogenous ligands for these receptors are very diverse, such as photons (for the rhodopsin receptor), cations (e.g. for the calcium sensing receptor), small organic compounds (e.g. for the adrenergic receptors), peptides. Activation of the receptor by an extracellular ligand induces a conformational change that is followed by G protein binding to the intracellular loops and C-terminus of the receptor, GTP substitution of GDP on the G_α subunit, dissociation of the G protein subunits (α and β-γ) from

---

[1] GTP is a purine nucleotide. GDP is the product of GTP dephosphorylation by GTPases, a class of cytosolic proteins.

the receptor and finally by their binding to their downstream effector proteins, such as enzymes, ion channels and kinases. A schematic depiction of this process, in the case of the β2-Adrenergic Receptor is displayed in figure 4.1. In this common way, many different cellular functions are controlled, such as neurotransmission, growth, movement and gene expression. Shortly after their response to agonists, GPCRs desensitize through phosphorylation carried out by G protein-receptor kinases (GRKs), aggregate on the cell surface and move from the plasma membrane into intracellular endosomes in processes known as sequestration (shorter timescales, reversible through recycling of the receptor) and downregulation (longer timescales, irreversible due to degradation of the receptor into lysosomes) [48] [49]. The phosphorylation facilitates β-arrestin binding and promotes receptor uncoupling from the G protein. Next, β-arrestin promotes receptor translocation to the endocytic machinery, typically involving clathrin [50], as in the case of β2-AR. The mechanism of agonist induced sequestration obviously requires a certain degree of lateral segregation of the receptors on the plasma membrane, as demonstrated by the punctuate distribution of labeled β2-AR observed either by confocal microscopy [50] or TIRF [51]. This is the first documented reason that can determine an heterogeneous arrangement of β2-AR throughout the cell membrane.

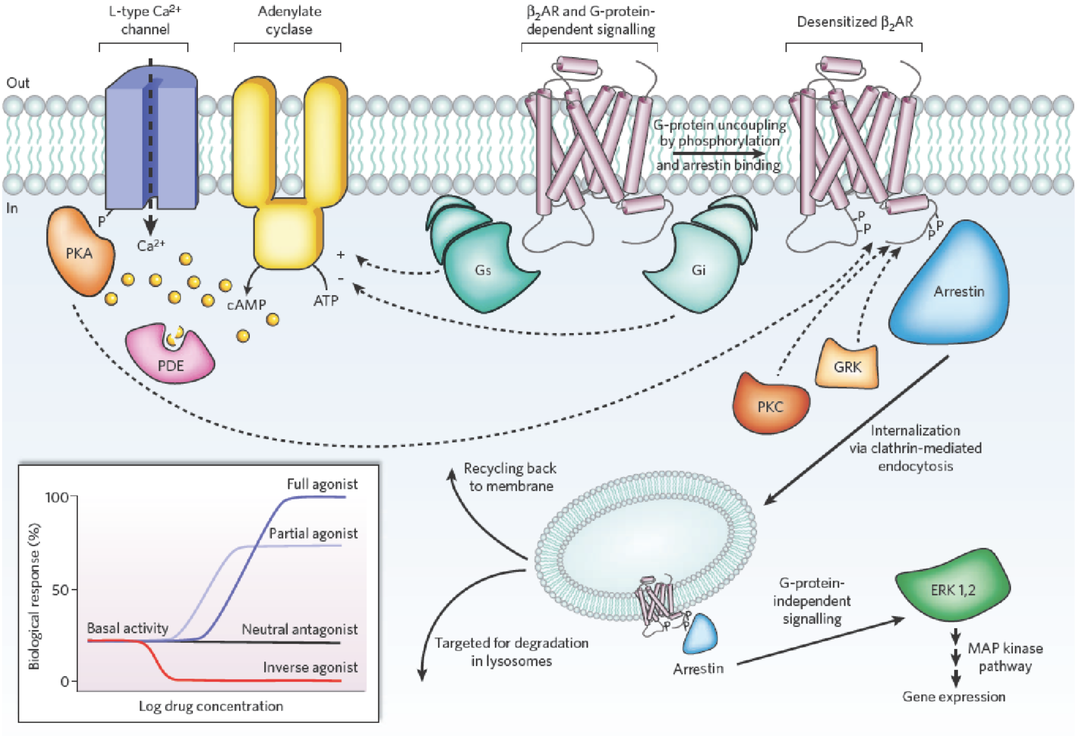

Figure 4.1: Schematics of activation of Adenylate Cyclase by β-Adrenergic Receptors. The Agonist (H)-bound β-adrenergic receptor, during its transient encounter with the G_s-Cyclase complex induces opening of the guanine nucleotide binding site. During this interval of time, GDP dissociates from the open site and is replaced by GTP; the agonist-bound receptor then dissociates from the GTP-loaded complex. The receptor-catalyzed nucleotide exchange results in the formation of an active, GTP-bound enzyme that produces cAMP. Arrestin is a signalling and regulatory protein that promotes the activation of extracellular signal-regulated kinases (ERK), prevents the activation of G proteins and promotes the internalization of the receptor through clathrin-coated pits. (Adapted from [47])

On the one hand, there are reports in favor of a largely monomeric basal GPCR population, freely diffusing on the plasma membrane, forming aggregates only transiently [52]. However, experimental data support the idea that the plasma membrane, far from being a neutral solvent in which proteins can diffuse, is a complex, regulated and highly dynamic structure compartmentalized in domains that favor interactions between specific proteins (see the review from J. A. Allen *et al.* and references therein [53]). As a matter of fact the hypothesis that these membrane receptors, as well as other membrane bound proteins, may be heterogeneously partitioned into signaling platforms, microdomains or lipid-rafts, has been highly debated and proposed as the way the cell maintains the correct fidelity and efficacy of the signal transduction (for a review the reader is referred to [54], [55]). Clustering of signaling molecules within particular cell membrane domains, such as lipid rafts, is a largely accepted concept, and many experimental data support the idea that GPCR signal transduction involves signaling microdomains [56] [57]. Although the role played by the the presence of plasma membrane nanoscale platforms, or *signalosomes*, in regulating GPCRs signaling is not yet fully understood, this would be the second major source of lateral heterogeneity for β2-AR or other GPCRs on the plasma membrane.

In summary, the arrangement of a prototypical GPCR such as β2 on the plasma membrane of a cell can fall in between two extreme cases: from a purely monomeric arrangement to the presence of aggregates, visible even by diffraction limited methods, that are required to sequester the receptor into the endocytic pathway. In between these two extremes, phenomena such as oligomerization [58] or the partitioning into signaling platforms may represent intermediate degrees of aggregation either in the basal state or in response to a stimulus.

We have anticipated that in diffraction limited imaging it is possible to observe the mechanism of agonist dependent sequestration, in particular in its later stages corresponding to the formation of endosomes in the cellular cytosol; unfortunately, direct inspection by conventional imaging is able to provide very little information about the existence of oligomers or signaling platforms for β2-AR and other GPCRs. Energy transfer techniques such as Förster Resonant Energy Transfer (FRET) can probe protein-protein interactions on lengthscales of a few nm, and they were used in order to study receptors oligomerization or the existence of signaling platforms [59]. However, no imaging technique was available until recently (scanning Near Field Optical microscopy (SNOM) [60] was used to observe the nanoscale arrangement of β2-Adrenergic Receptor on the surface of cardiomyocite-like cells reporting on the presence of nanoscale aggregates) to bridge the resolution gap between the nm lengthscale of FRET and the hundreds of nanometers offered by optical microscopy.

The limitation of diffraction limited imaging is well represented in figure 4.2, that displays the confocal image of a HeLa cell expressing β2-AR in basal conditions. Labeling is achieved using Tetra Methyl Rhodamine bound to a Snap-Tag fusion to the β2-AR. In figure 4.2 a, the large pixels size (650 nm) obscures any form of sub-diffraction limit heterogeneity. Given the relative thick z-section of the confocal image (~ 1 μm) it is likely that the few brighter pixels correspond to aggregates that reside within the cytoplasm of the cell, in the form of endosomes containing the labeled receptor. The increased pixel size (~ 50 nm) in the zoom of figure 4.2 b, fails to increase our understanding of the basal distribution of the receptor. In this scenario PALM represents a potentially powerful tool to obtain high resolution images and quantitatively unravel this heterogeneity. However, due to the considerations developed in the previous chapter, it is important to interpret the images in light of the properties of the fluorophore used.

Figure 4.3 a and b, display the TIRF and corresponding PALM (t_d = 10 s) images of an HeLa cell fixed after transiently expressing β2-mEos2. The TIRF image is obtained by summing up all the PALM single molecule frames. Both the TIRF and PALM images display a homogeneous distribution of the receptor, with a few bright puncta. The choice of rendering the image using a t_d = 10 s, the entire acquisition

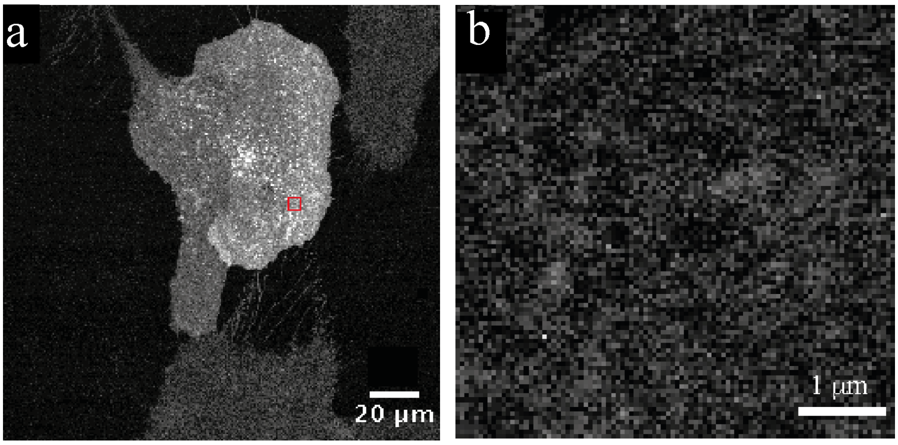

Figure 4.2: a) Confocal image of the plasma membrane of a pair of HeLa cell expressing the construct SNAP-β2, labeled using Tetra Methyl Rhodamine. At this zoom level the voxel size is 670 nm. b) confocal zoom showing the detail of the plasma membrane of the same cell. Voxel size is 52 nm, pixel dwell time is 25.4 μs, scale bar is 1 μm.

duration being 600 s, allows for at most 60 distinct molecules to be localized in the same diffraction limited spot.

Figure 4.3 c, displays the counts vs t_d curve, and the fit according to equation 3.5, presented in the previous chapter. The data reported confirms that in our experiments in fixed cells the counts vs t_d curve retains an exponential decay, validating that the distribution of *off*-times is also exponential, at least at the ensemble level. The measured t_{off} falls close to the upper limit of the range 0.13 s to 0.37 s observed in in-vitro samples and the average number of photo-blinks is only slightly underestimated with respect to what is reported in PAGE. The density value extracted from the fit, ~ 60 molecules/μm^2 is recovered at a t_d value of ~ 1 s. The choice of a t_d = 10 s therefore implies operating in the undercounting regime. The choice of a different t_d has a profound impact on the resulting image. This feature is prominently outlined by panels d-g, where up to t_d values of 5 s the image displays a non-negligible degree of clustering, that subsides only at a t_d of 10 s. Even the choice of t_d = 1 s, where missed counts balance multiple counts, does not rule out that a fraction of the molecules displays a switching behavior on longer timescales, resulting in apparent clusters and oligomers, such as those appearing in panels d-f.

If on the one hand the requirement for complete spatial randomness of the fluorophore could be used to determine the appropriate value of t_d in-vitro, on the other hand the distribution of the receptors in the cell is unknown *a-priori*. Figure 4.3 leaves therefore open the question about the effective arrangement of our blinking labels, and if the clusters observed at low t_d values are indeed there.

4.2 Analysis of clustering artifacts in Photo Activated Localization Microscopy

We introduce here a method to answer this question, and determine by direct inspection whether an observed cluster shall be ascribed or not to photoblinking of just one or a few fluorophores. We

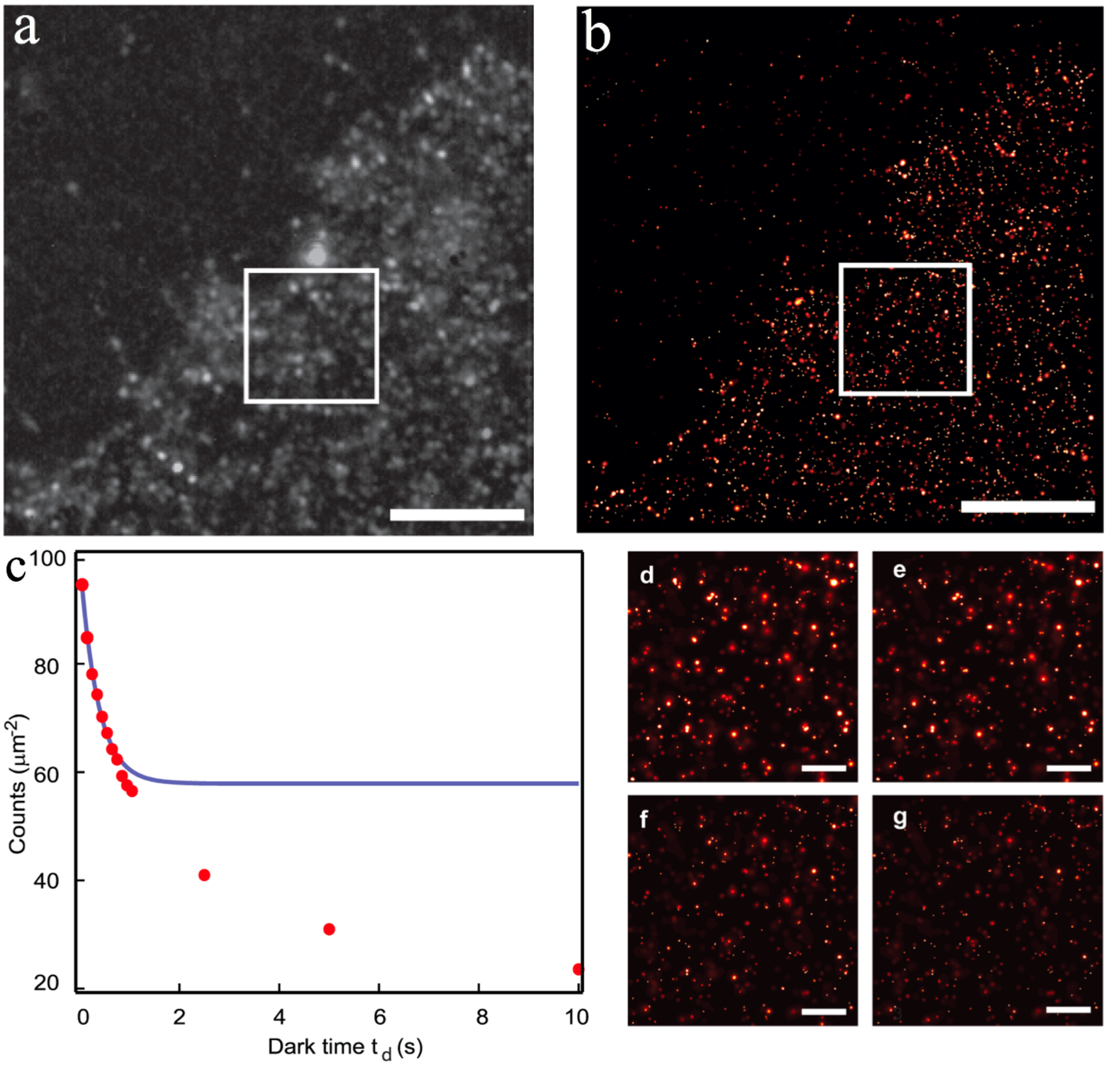

Figure 4.3: a) and b) TIRF-PALM image of a region of the cell expressing β2-mEos2 (t_d = 10 s, localization precision< 35 nm) c) Red Markers: number of localized molecules as a function of dark time t_d with density estimation in the cell. Blue line: fit using equation 3.5 limited to the overcounting regime yields an estimated density of approximately 60 molecules/μm^2, t_{off} = 0.36±0.05 s and n_{blink} = 0.63±0.07.d), e), f), and g) ROI from b) displaying isolated localized receptors by a gaussian function for four different dark time values d) t_d = 0.5 s e) t_d = 1 s f) t_d = 5 s and g) t_d = 10 s. Scale bar b) and c) 5 μm, d)-g) 1 μm. (reprinted from Annibale *et al.* [46])

compared a negative and a positive clustering control by using plasma membrane bound proteins labeled with mEos2 in order to show how photoblinking or reactivation induced artifacts may be erroneously interpreted as biological clusters. The PALM image of a fixed HeLa cell expressing as a negative clustering control the 15-aminoacids N-terminus of the protein Src (SrcN15) [61], showed that the localized single molecules form clusters over a lengthscale of a hundred nanometers (figure 4.4 a). Using a color code for the instant of localization of each molecule, as displayed in figure 4.4 b, it appears that most of the observed clusters are largely monochromatic, i.e. an indication of a suspicious concomitant spatial and temporal clustering that is confirmed by the clusters kymographs shown in figure 4.4 c. If we allow for longer molecular dark times t_d up to 10 s in regrouping the fluorescent traces, the artifact temporal clusters disappear (figure 4.4 d) yielding a pattern consistent with what is observed labeling SrcN15 with the photoconverting protein PSCFP2, as shown in figure 4.4 e.

As a positive control on physical clustering we imaged fixed cells expressing β2-AR a few minutes after stimulation with the agonist Isoproterenol. In these conditions β2-AR internalizes in endosomes forming on the cell membrane that are even visible in diffraction-limited TIRF images [51]. Figure 4.4 f, shows that in PALM we clearly detect endosomes as clusters even allowing for long fluorescence dark times (figure 4.4 g). In addition, the clusters kymographs in figure 4.4 h, clearly display that the temporal distribution of localizations of the molecules comprising clusters is homogeneous over the entire duration of data acquisition, consistent with the stochastic photoactivation mechanism at the base of PALM measurements.

Therefore, depending on the fluorophore used, scanning for temporal clusters is an effective strategy to identify photoblinking-induced artifacts in super-resolution images of small membrane proteins aggregates. It appears that allowing for longer single molecule fluorescence dark times in the data analysis allows to obtain images largely artifact free while retaining the essential information about physical clusters (figure 4.5), although more specific application-targeted methods to identify and remove temporal clustering can be envisioned, as we will discuss in the next two chapters.

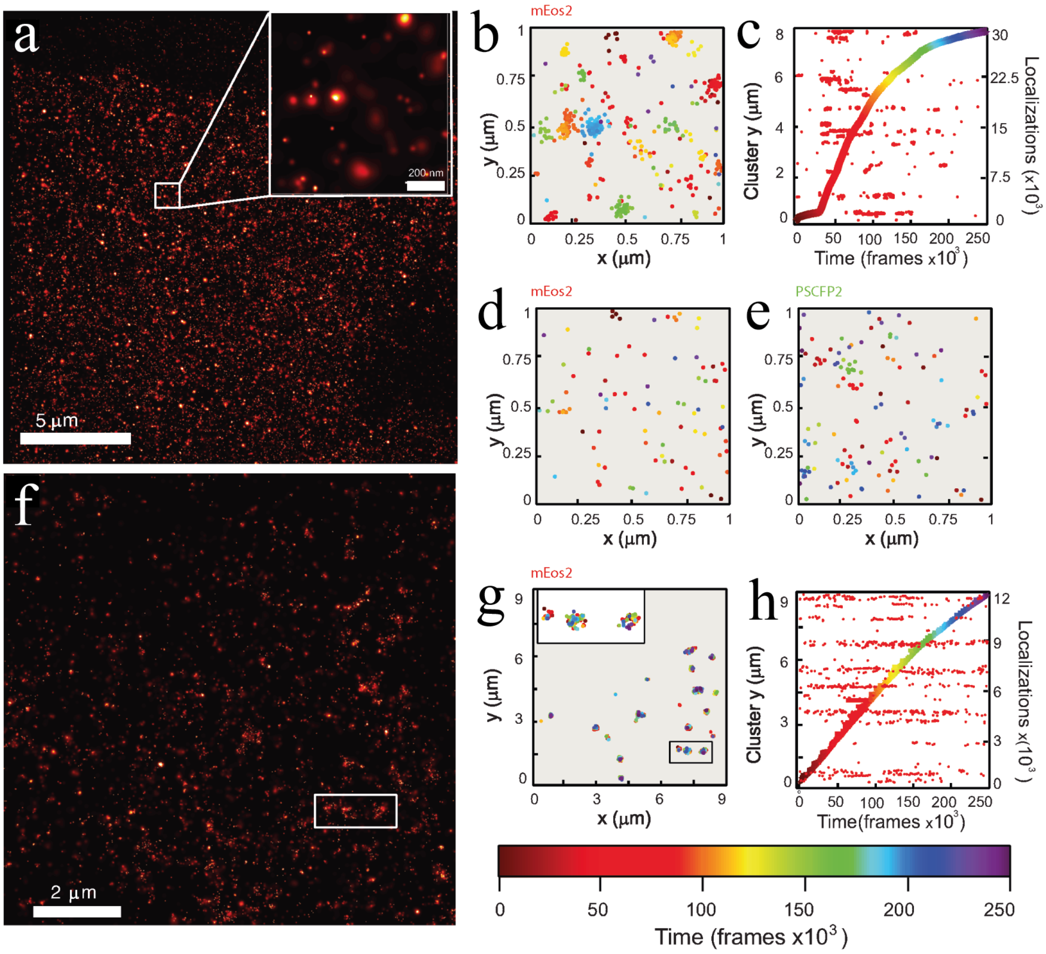

Figure 4.4: Protein clustering on plasma membrane a) TIRF-PALM image of a plasma membrane region of a fixed HeLa cell expressing SrcN15-mEos2 b) Map of the localized emission centers for each SrcN15-mEos2 molecule within the inset in a). The color scale identifies the temporal instant of molecular localization; dark time $t_d = 2$ s. c) Representative kymographs of those molecules shown in a) belonging to spatial clusters. Superimposed color coded curve shows localized molecules as a function of time d) Region shown in in b), for dark time $t_d = 20$ s. (e) Map of the localized emission centers for each SrcN15-PSCFP2 molecule; dark time $t_d = 2$ s. f) TIRF-PALM image of a fixed HeLa cell expressing β2-AR, labeled with mEos2, during endocytosis g) Map of the localized emission centers for each β2-mEos2 molecule; dark time $t_d = 20$ s. h) Representative kymographs of those molecules shown in f) belonging to spatial clusters. (reprinted from Annibale *et al.* [62])

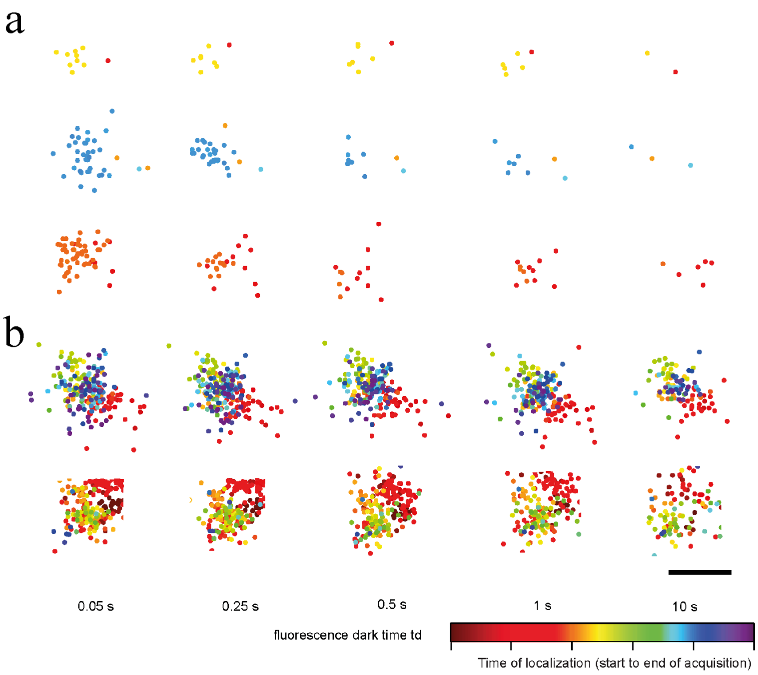

Figure 4.5: Snapshots of molecular clusters on the plasma membrane of fixed HeLa cells. Markers represent the fitted center of fluorescence of individual single molecules, and their color the instant of localization. a) Representative images of three artifact temporal clusters of SrcN15-mEos2 and their evolution for increasing values of the allowed fluorescence off-time t_d. b) Representative images of two physical β2-mEos2 clusters and their evolution upon an increase of the allowed fluorescence dark time t_d. A temporal artifact component (red sub-cluster) is also visible in the second physical cluster. The fitted location of the molecules changes slightly from one t_d value to another since the number of collected photons and their spatial distribution attributed to each localized molecules changes. Scale bar 100 nm. (reprinted from Annibale *et al.* [62])

4.3 Discussion

PALM provides a method to image plasma membrane protein arrangement below the diffraction limit. Compared to other imaging methods, it has the advantage to use genetically encoded labels, avoiding the requirement for secondary labels using antibodies that have been demonstrated to affect the lateral organization of plasma membrane proteins [63]. The use of one of the brightest probes available for PALM imaging, mEos2, allows high localization precision, but, as with most of the other photoactivatable fluorescent proteins, requires operating in a regime where photoblinking is not determining a systematic overcounting. We demonstrated a method to correctly interpret the images, taking into account photophysical artifacts (clusters due to longer than average *off*-times) that otherwise would compromise the understanding of the underlying biological process. The comparison of two opposite cases, monomeric distribution of a control chimaera and aggregates induced by long-time stimulation with an agonist molecule, that determines receptor segregation and sequestration, was used to validate this approach in the framework of GPCR imaging. In the next chapter we will discuss the use of PALM to probe the basal distribution of the β2-AR, moving from the HeLa cells, the standard cellular platform used throughout this chapter, to a more physiological host such as cardiomyocite-like cells H9C2.

5 The membrane distribution of β2-Adrenergic Receptor

5.1 Introduction

The cell membrane is a highly heterogeneous structure, and many years of research have addressed the reasons, functional role and implications of the observed micro and nano-scale heterogeneity. Depending on the function of each protein, the cell plasma membrane harbors large aggregates of thousands of molecules and a few micrometers in size, such as focal adhesion complexes, clusters of 50-100 nm in diameter such as clathrin coated pits that contain hundreds of sub-units and down to oligomeric complexes of a few nanometers in size and counting a handful of molecules. PALM has the potential to provide not only high resolution maps of densely labeled structures, but also to address semi-quantitatively interesting biological questions about sparser systems, such as those represented by the membrane proteins aggregates introduced in the previous chapter. Across this range of densities and sizes the description offered by PALM, i.e. a map of (x, y) coordinates corresponding to each localized protein, is a valuable tool to extract informations not only about the size and shape of these aggregates, but also about the number of their components.

In certain cases, diffraction limited imaging is already able to highlight some of these aggregates. Figure 5.1 a and b, display Total Internal Fluorescence Microscopy images of the cells expressing the SrcN15-mEos2 chimaera introduced in the previous chapter, in a), and of β2-mEos2 expressed in H9C2 cardiomyocyte-like cells, in b). The comparison between figure 5.1 a and b provides a clear example of protein-specific membrane heterogeneity, since the distribution of SrcN15-mEos2 is largely homogeneous as compared to the arrangement of the β2 receptor. Both images display a few bright puncta that probably correspond to vescicles belonging to the endocytic machinery of the cell. It should be highlighted that, even in TIRF, it is possible to identify spots arising from isolated single molecules. Endogenous expression levels of adrenergic receptors in H9C2 cells are the subject of a controversial literature [64], [65], [66], though most authors agree on a figure of approximately 10^5 β1 and β2 receptors per cell, yielding approximately 30 receptors/μm^2, with the stoichiometry in favor of β1. This is the main reason why the heterologous expression levels in the cells displayed and investigated in this study were kept relatively low, in order not to depart from these figures. Fluorescence from standards of known concentration was used in previous reports as a calibration tool for measuring the concentration of intracellular fluorescent species, under the assumption that fluorescence Quantum Yield and detection efficiencies are the same in vitro and within the cell [67], [68].

Comparison of the fluorescence measured on standard samples of purified protein (figure 5.2 a) to ensemble photobleaching curves of β2-mEos2 in HeLa cells (figure 5.2 c) allows for a tentative

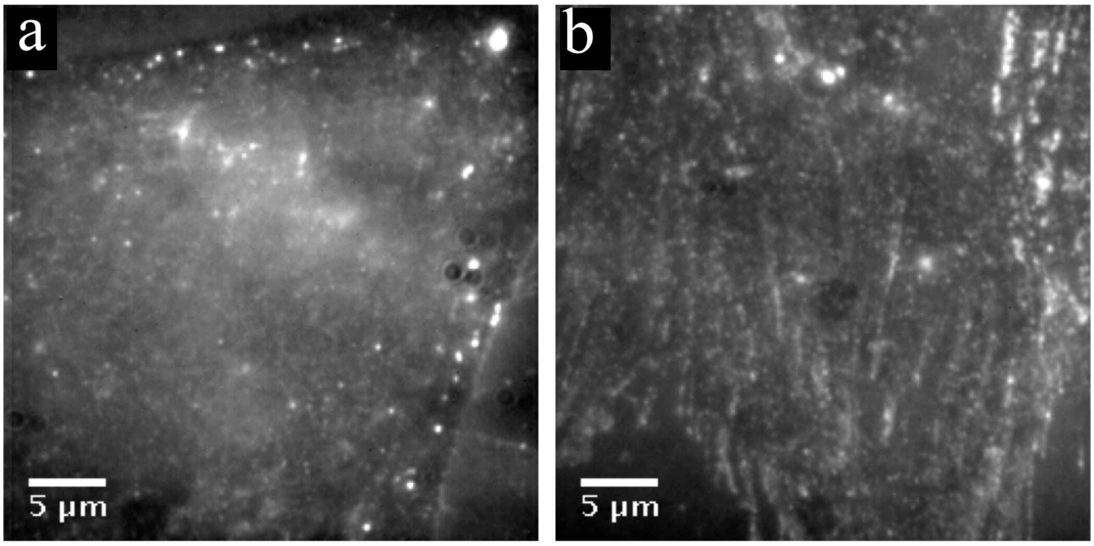

Figure 5.1: a) TIRF image of H9C2 cells expressing SrcN15-mEos2 and b) β2-mEos2 obtained by the superposition of ~ 50000 single molecule frames.

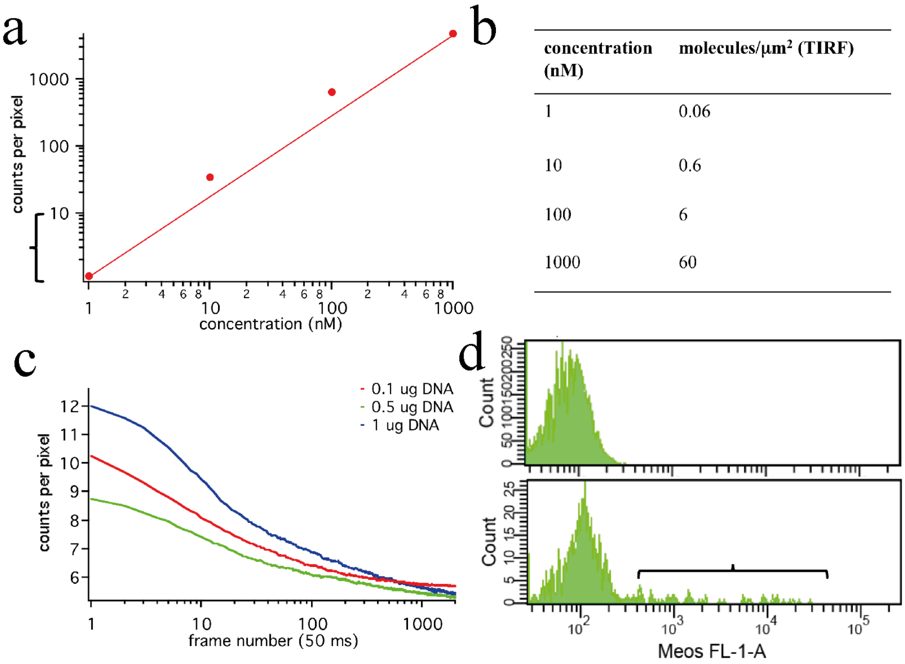

concentration (nM)	molecules/µm² (TIRF)
1	0.06
10	0.6
100	6
1000	60

Figure 5.2: Estimation of the transfection levels in H9C2 cells. a) Relationship between the measured counts/pixel and molar concentration of the fluorophore solution b) bleaching curve measured in TIRF of fluorescently labeled β2-AR expressed in HeLa cells (in counts/pixel). c) FACS measurement of the fluorescence level (a.u.) of a non transfected control (top) and of HeLa cells transfected with β2-mEos2 (bottom).

calibration of the measured fluorescence intensity and show how the expression level on the plasma membrane can be regulated down to a concentration of a few molecules $/\mu m^2$. The Fluorescence Activated Cell Sorting measurements of figure 5.2 d, display that the upper limit of the expression is approximately two orders of magnitude higher, reaching therefore up to ~100 molecules$/\mu m^2$. In this chapter we will therefore introduce the use of PALM to treat relatively sparse systems, with $10 < n < 100$ molecules $/\mu m^2$ using the (x, y) coordinates of each localized molecule.

Figure 5.3 compares the TIRF and PALM images of a region of the plasma membrane of an H9C2 cell expressing β2-mEos2, and focuses on a region where a prominent feature appears. The PALM image clearly shows the presence of molecular aggregates of ~ 100 nm in size. The use of PALM to semi-quantitatively probe the heterogeneous distribution of these receptors, as we will see in the following, allowed us to observe that the β2-AR is partially pre-associated in nanoscale-sized clusters in cardiomyocyte-like cells such as H9C2, but not in other cell lines, viz. HeLa and CHO (figures 5.10 and D.2 respectively).

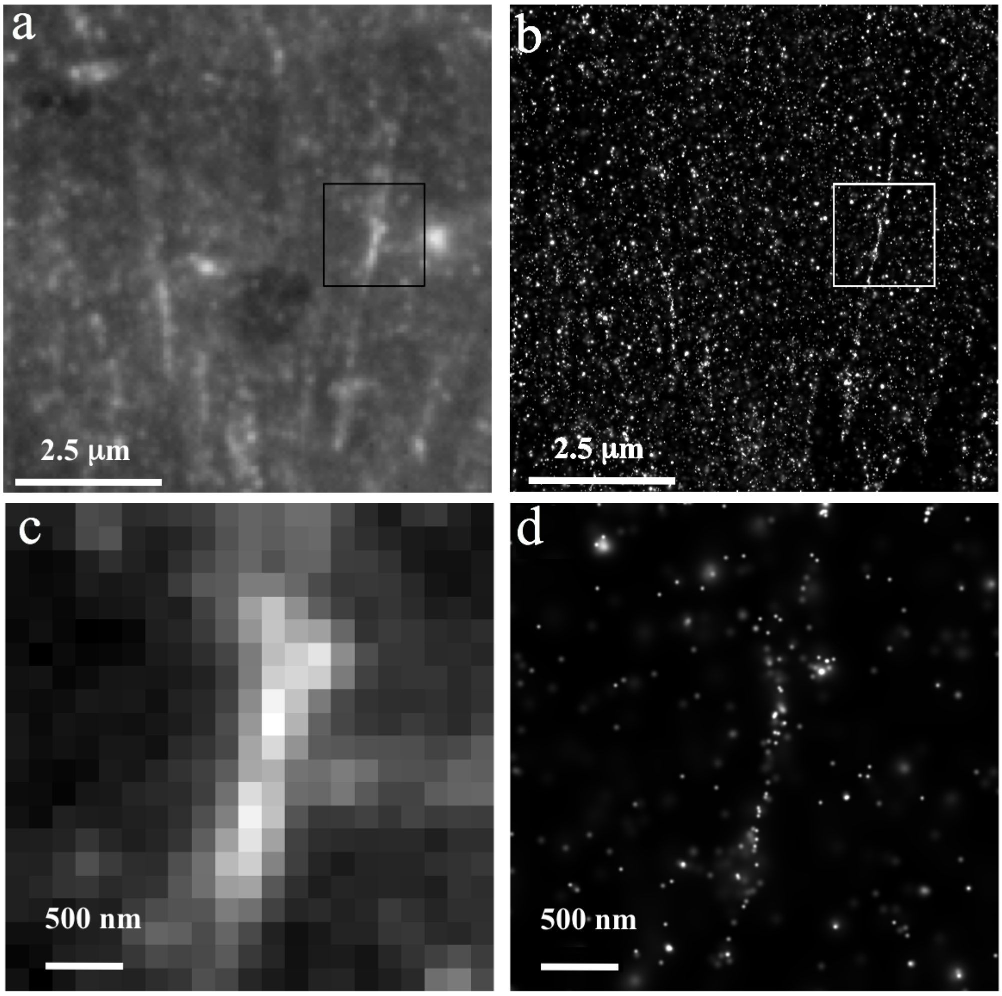

Figure 5.3: From TIRF to PALM of β2-mEos2 in H9C2 cells. a) TIRF image b) PALM image and zoom c) TIRF and d) PALM

As we anticipated in the previous chapter, one of the few attempts so far to elucidate the sub-diffraction limit arrangement of these receptors on the plasma membrane by optical nanoscopy methods, employed Scanning Near Field Optical Microscopy. Ianoul *et al.* [60] used immunostaining against endogenous receptors and the superior resolution offered by near-field detection of fluorescence to observe the arrangement of β2-AR in H9C2 cells into functional domains of an average 140 nm diameter, a cluster density of one/μm^2 and between 12 to 71 receptors per cluster. Given the endogenous expression levels indicated in the previous paragraph, according to this study most of the β2-AR molecules reside in clusters. We should notice that the use of immunostaining was demonstrated to determine a significant degree of clustering due to antibody cross-linking [63].

On the other hand numerous reports have emerged linking the nano and microscopic arrangement of adrenergic cell membrane receptors to the cytoskeletal structure. Among these proteins, the role of actin binding proteins such as NHERF-1 was highlighted, since it contains a PDZ-motif that can bind to the C-terminus of β2-AR, and was proposed as the possible link responsible for the aggregation in bundle-like structures of the receptor [69]. As an interesting and novel application of PALM microscopy, we will present in this chapter our results on the study of clustering of β2-AR, addressed by systematic comparison to a non-clustering peptide such as the SrcN15-mEos2 construct introduced in the previous chapter. Finally we will present our data on the effect of biochemical treatments in order to deplete the cell membrane of cholesterol and to disrupt the actin cytoskeleton. Our data appear to support the hypothesis of a cytoskeletal (actin) dependent arrangement of these important cell membrane receptors, at least in cardiomyocytes-like cells such as H9C2.

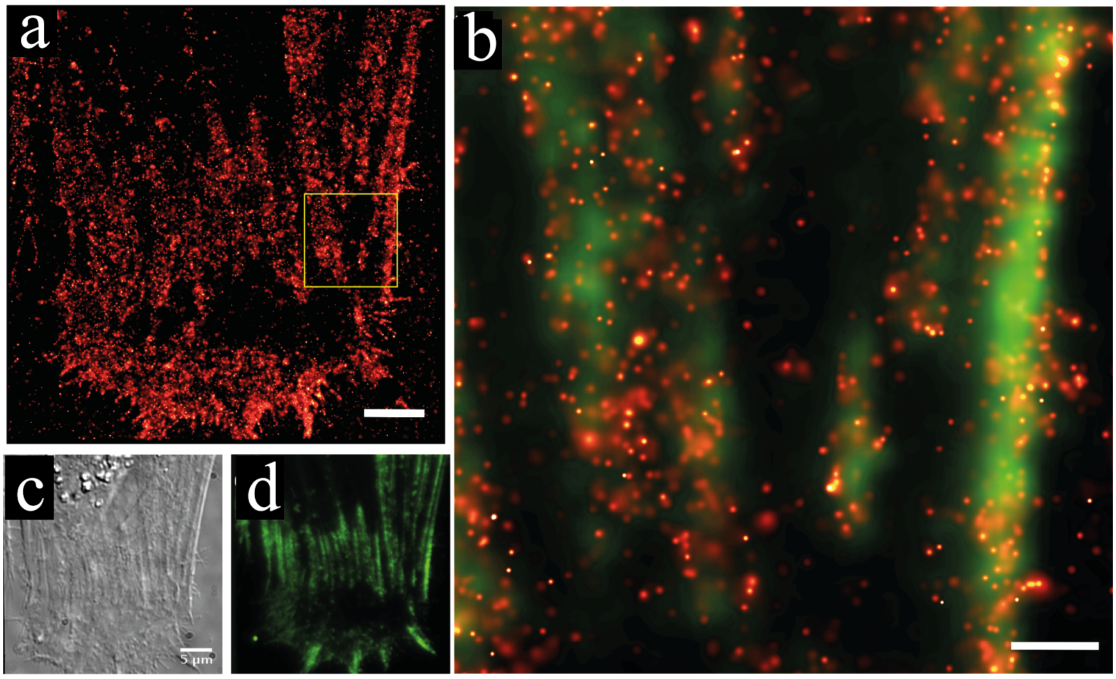

Figure 5.4: Colocalization of β2-AR and actin in an H9C2 cell. a) PALM image of β2-pamCherry1, scale bar 5 μm b) expanded inset showing co-localization of actin-EGFP and β2-pamCherry1 in correspondence to a few actin filaments near the edge of the cell; scale bar 1 μm c) DIC and d) Actin-EGFP fluorescence images of the same region displayed in a.

5.2 Treating membrane heterogeneities using the point pattern picture

Shortly after PALM development, in 2007 Hess and coworkers [9] used fPALM to observe the distribution of HA-Hemagglutinin-PAGFP on the plasma membrane of HAb2 live fibroblasts. The observation of sub-diffraction limit clusters and elongated aggregates across multiple lengthscales was complemented by the measurement of intermolecular distances histograms, based on the calculated centroids of each localized molecule. More specifically, the intermolecular distances histogram was observed in its evolution over time (i.e. distances between the i^{th} molecule at time t and the $1...N$ molecules at time t+τ) to extract the diffusive properties of the molecular species and, at fixed time intervals, to compute the Ripley's K function. Ripley's method, as discussed in more detail in the following section 5.2.2, is a popular spatial statistics approach originally developed in forestry studies, successfully applied in Electron Microscopy data [70], [71], and currently finding a growing application in super-resolution studies.

The initial work by Hess spearheaded a number of PALM studies relying on this latter approach, including the work from Greenfield *et al.* [12] who investigated the clustering of bacterial chemotaxis receptors and Lillemeier *et al.*, who in 2010 [72] studied the plasma membrane clustering of TCR and LAT receptors on immune system T cells. Greenfield *et al.* were the first to explicitly refer to the counting capability of PALM, and used it to formulate a biophysical model explaining the chemotaxis receptors arrangement within a single E. Coli bacterium. As we saw in the previous chapters, our group [40] investigated for the first time the issue of photo-blinking/molecular reactivations on super-resolution experiments and notably this concept was addressed again only in 2012 by Lippincott-Schwartz and co-workers and identified as a key limitation to a quantitative study of membrane heterogeneity, and instrumental in motivating their proposition of an ensemble method based on spatial correlation functions [73].

Using the spatial point pattern made of the localized centers of each fluorescent molecule puts a much larger emphasis on the precise quantification of the number of localized molecules. This approach represents one of the strenghts of PALM compared to other super-resolution methods and justifies the discussion carried on in the previous chapters about the investigation of photoblinking effects and their detection in order to obtain spatial point patterns as accurate as possible. In this context it should be clear the paramount importance of attributing in an unambiguous way each point to a molecule: the multiple localizations of a single blinking molecule will affect the interpretation of the spatial point pattern much more than in the probability distribution picture, where the net effect of multiple localizations of the same molecule (overcounting) will be a decrease of the average localization precision and a loss of resolution.

Our analysis of the membrane distribution of β2-AR in HeLa and H9C2 cell lines follows two parallel approaches: first, a density clustering method is used to indentify aggregates and the amount of molecules belonging to clusters. Second, the Ripley's method was used to detect departures from randomness across multiple lengthscales, and to quantitatively compare data-sets of similar density. The first approach considers part of a cluster only those molecules surrounded within a radius r by a local density that exceeds of m times the average density in the region of study. Multiple values for r and m were tested, and finally a combination (150 nm, 5 times) was chosen in order to reduce as much as possible the measured clustering in the negative controls. More details about the impact of changing one of these parameters, i.e. the radius r, will be provided in Appendix A. The estimation of clusters based on the local density has the advantage of providing an immediate quantification of the number of molecules part of a cluster, and on the size of the molecular clusters. On the other hand, Ripley's K function approach offers an appealing way to measure departures from a random distribution across multiple lengthscales.

In the next two sections we will provide further detail on each of the two methods.

5.2.1 The clustered fraction method

The approach used in this work to localize the fraction of clustered molecules relies on a unique density threshold m and a distance parameter r. A circle of radius r is drawn around each i^{th} molecule, and the local density estimated. If the number of molecules within $\pi \cdot r^2$ is at least m times larger than the average molecular density $\frac{N}{A}$ (where N and A are respectively the total number of molecules and the area of investigation), then the i^{th} molecule is attributed to a cluster. The pool of clustered molecules is then assigned a cluster index k using an iterative procedure. For each molecule in a cluster, informations such as the localization precision, the instant of localization, as well as, obviously, the (x, y) position, are stored. For each dataset the following informations are therefore readily available: total number of molecules residing in a cluster, number of clusters, number of composing molecules and size for each cluster. Figure 5.5 displays the clusters localized after the application of the algorithm in two cases: figure 5.5 a, displays the strong clustering of clathrin light chain labeled with pamCherry1 (this construct will be discussed in more detail in the chapter 6) in a HeLa cell. Figure 5.5 d, displays the β2-mEos2 clusters localized on the plasma membrane of an H9C2 cell. Histograms of the cluster diameter and of the number of molecules localized within each cluster for clathrin and β2-AR are displayed in figure 5.5 b, c, e and f, respectively. As was extensively discussed in the previous chapter, the density cluster analysis can be employed to a dataset only after that a certain t_d has been chosen. For the data analyzed in this chapter, in order to minimize the occurrence of artifacts in the cluster analysis, all datasets were analyzed in the undercounting regime, with a $t_d = 10$ s.

5.2.2 Ripley's K function analysis

Ripley's K function method allows to measure the departures of a measured spatial point pattern from a random distribution. Ripley's K function is calculated according to the formula (see [42] and references therein):

$$K(r) = \frac{A}{(N \cdot (N-1))} \cdot \sum_{i \neq j} w_{ij}^{-1} \cdot I(r_{ij}) \tag{5.1}$$

where $I(r_{ij}) = 1$ if molecule j is within the distance r from molecule i and 0 otherwise. w_{ij} are weights to take into account edge effects, and i and j span the entire number of molecules present in the sample. From the $K(r)$, that obviously grows as $\pi \cdot r^2$, it is possible to obtain a linearized version, called $L(r) - r$ function, given by:

$$L(r) - r = \sqrt{\frac{K(r)}{\pi}} - r \tag{5.2}$$

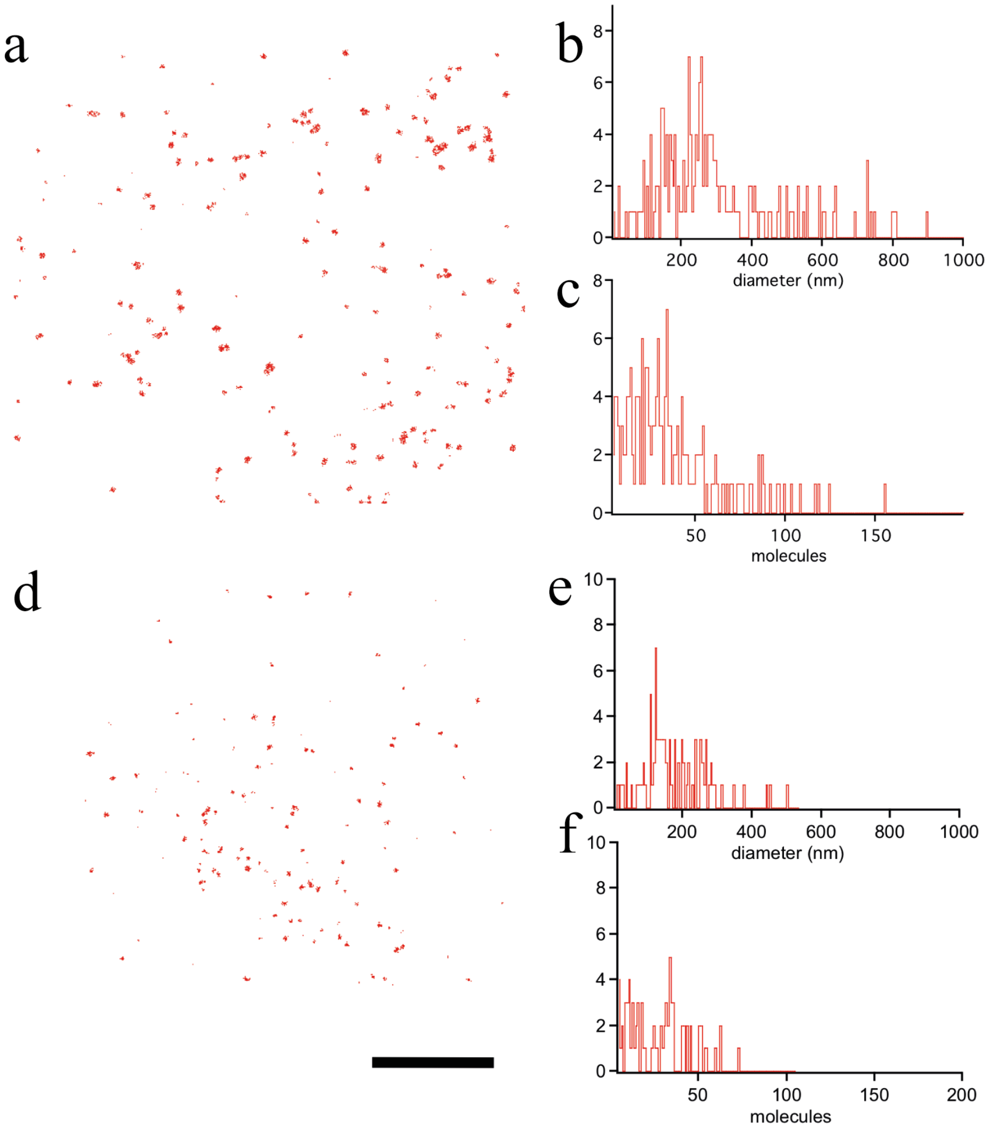

Figure 5.5: Clustering on the plasma membrane a) Clathrin light chain-pamCherry1 clusters identified on the plasma membrane of a HeLa cells using the density threshold $m = 5$ and a clustering radius $r = 150$ nm. b) Frequency histogram of the cluster diameters and c) of the number of molecules present in each cluster. d) Clusters of β2-mEos2 identified on the plasma membrane of H9C2 cells using the density threshold $m = 5$ and a clustering radius $r = 150$ nm. e) Frequency histogram of the cluster diameters and f) of the number of molecules present in each cluster. Scale bar is 5 μm.

employed in order to stabilize the sampling variance of the function over different r values. An application to a classical dataset (provided as a reference dataset in most of the spatial point pattern literature), the Redwood forest containing the locations of 62 conifers, is displayed in figure 5.6. $L(r)-r$ shows that the average size of trees clusters is approximately 3 m, and the average distance in between each cluster (including also isolated trees) is around 10 m. For a given number of points, confidence intervals for complete spatial randomness can be calculated by running multiple simulations of random patterns. For each lengthscale $\bar{r}$, it is possible to determine the confidence interval (e.g. 99%) by multiplying the standard deviation of the measured $L(\bar{r})-\bar{r}$ by 2.58. The $L(r)-r$ function can then be standardized by dividing it by the confidence interval.

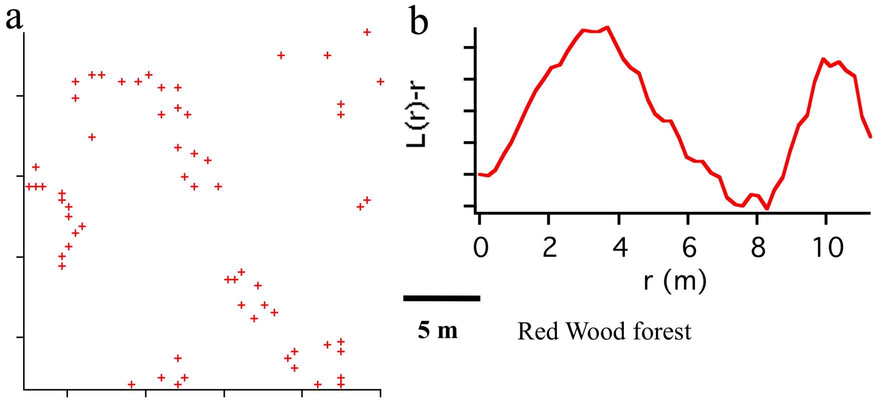

Figure 5.6: Ripley's analysis of redwood forest. a) Location of the conifers in a ~ $25\cdot25$ m^2 square region and b) $L(r)-r$ calculated for this dataset.

5.3 Measurement of the clustered fraction and $L(r)-r$ function of cell membrane receptors

Both the approaches discussed in the previous two sections can be applied to PALM data. Figure 5.7 displays an application of the protocol used to analyze the data in an HeLa cell expressing the negative control peptide SrcN15-mEos2. At $t_d = 1$ s the spatial point pattern displays a variety of aggregates that the color coding employed throughout the previous chapter denotes as temporal clusters, i.e. photoblinking artifacts. The Ripley's $L(r)-r$ function displays a marked peak at $r = 50$ nm, followed by a shoulder at $r = 130$ nm. These two values correspond to the dominating lengthscales of the observed aggregates, i.e. the cluster radius and the average inter-particle distance. The dashed line represents the 99% confidence envelope for $L(r)-r$ of a completely random pattern. The measured clustered fraction using the density threshold approach and a $r = 150$ nm, $m = 5$ combination yields a fraction of clustered molecules of 40%. Moving to $t_d = 10$ s most of the aggregation pattern has almost completely vanished and the clustered fraction drops to 3%, although the $L(r)-r$ still displays a peak above the spatial randomness envelope at $r = 50$ nm. This observation motivates the additional step taken in our data analysis method, namely the screening of each of the remaining clusters to determine whether they still display a significant degree of temporal correlation. This approach enables us to suppress the remaining contribution to $L(r)-r$ and to recover, as expected, complete spatial randomness.

A mixture of mEos2 and Dronpa molecules imaged in-vitro is used to illustrate the concept behind

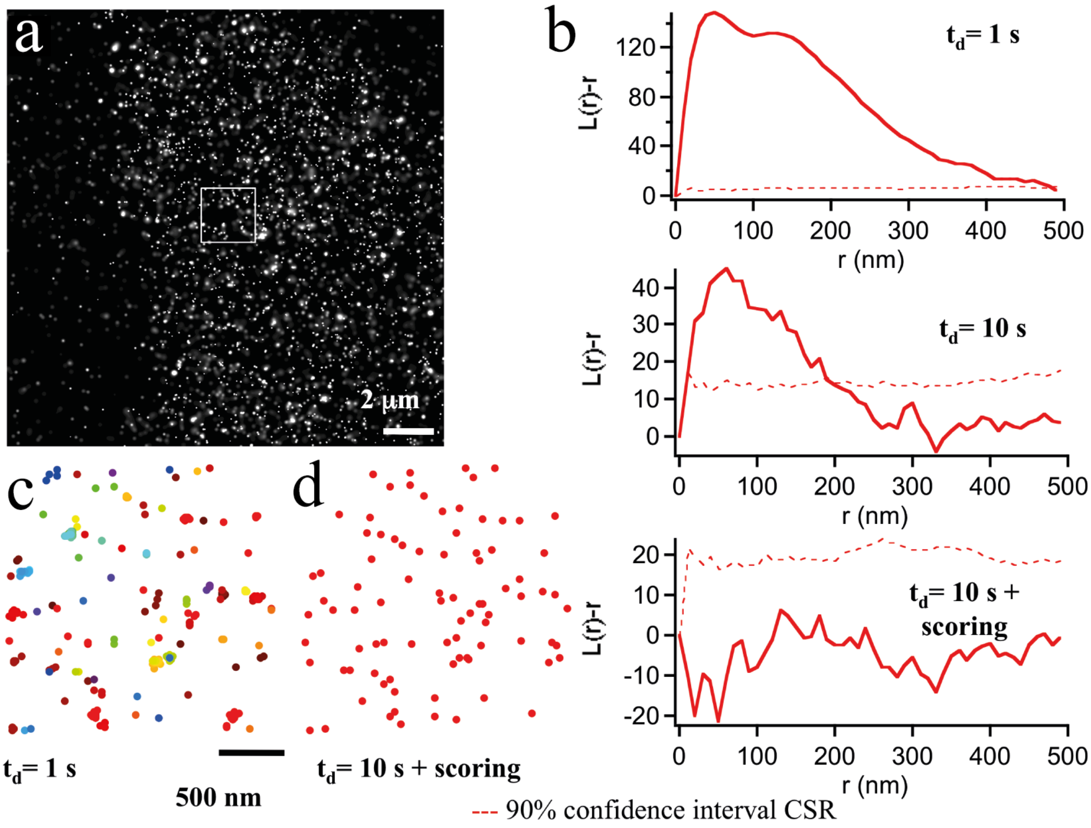

Figure 5.7: Spatial point pattern analysis of SrcN15-mEos2 on the plasma membrane of HeLa cells. a) PALM image. b) Markers representing of each localized fluorophore color coded according to the time of localization for $t_d = 1\text{s}$ and c) $t_d = 10\text{s}$. d) $L(r) - r$ functions for t_d values of 1 s, 10 s and 10 s with scoring. Dashed lines represent 99% confidence intervals calculated from 50 simulations of a random pattern.

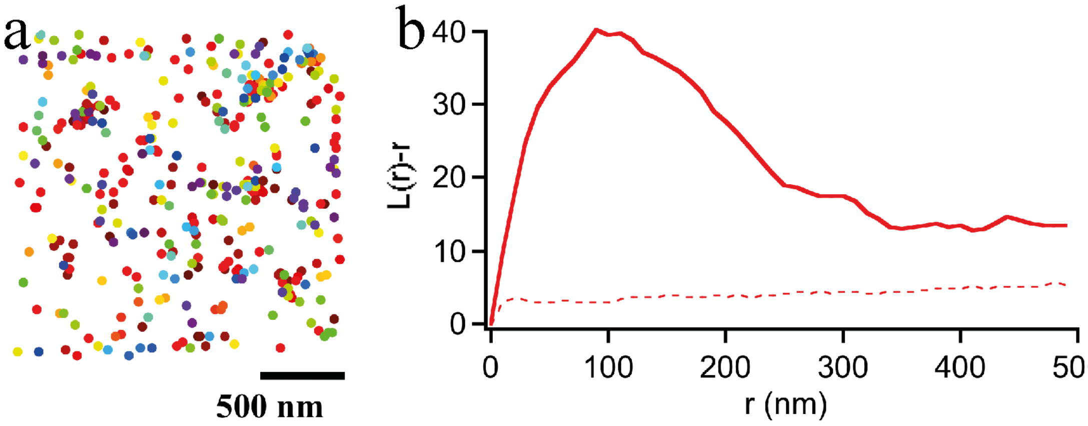

Figure 5.8: a) Point pattern of β2-mEos2 on the plasma membrane of an H9C2 cell for $t_d = 10$ s. Markers represent each localized fluorophore color coded according to the time of localization. b) Corresponding $L(r) - r$ function.

the definition of a score for the molecular clusters based on the degree of temporal proximity of the localization events. Figure 5.9 a, illustrates the spatial map arising from the PALM measurement of a nano Molar concentration mixture of mEos2 and Dronpa molecules in PAGE, analyzed at low t_d values. The observed aggregates are clearly due to blinking of individual molecules. Cluster kymographs for two arbitrarily selected aggregates are displayed in figure 5.9 b. The stochastic condition for photoactivation at the basis of PALM microscopy implies that in any given point the number of activated molecule per unit time obeys a Poisson's flow, and depends only on the local density (molecules/μm^2) and on the photoactivation rate (new molecules/s). This consideration is at the basis of the equation to treat missed counts proposed in chapter 3. Once a spatial cluster is identified by means of density thresholding, the known observables are the number of molecules within the cluster n_c, the time elapsed between the first and last localization τ_c and the total duration of the PALM acquisition T. Stochastic activation implies that the activation and localization of the molecules in the cluster should be homogeneously distributed through the entire duration of the acquisition T. The ratio between the number of localized molecules and the experiment duration determines the theoretical photoactivation rate r. The product $r \cdot \tau_c$ determines the average number of molecules m expected to be localized in this time interval. m is the average of a Poisson's distribution, that can be used to assess the probability p of detecting n_c molecules within the cluster. This probability is then used to score each cluster. Cumulative distribution functions (1-CDF) based on a Poisson distribution having as an average$m_{Eos} \sim 9$ and $m_{dronpa} \sim 23$ are displayed in figure 5.9 d. Clusters with a number of molecules n_c and a duration τ_c such that p is less that 0.01 are rejected as temporal artifacts and they are replaced by a localization event having a (x, y) position calculated based on the weighted mean (using the localization precision σ_i as a weight) of the position of all the n_c molecules and a localization precision given by their standard deviation.

It should be noted that scoring the clusters in the overcounting regime is also a viable strategy. In this case, applying the scoring algorithm to the datasets obtained with a $t_d = 1$ s yields a residual clustering fraction of only 2%. However, in the current chapter, we tailored our protocol to suppress clustering in the negative controls. To this goal, analyzing the data in the missed counts regime and then scoring the remaining clusters appears the most effective strategy. When this same approach is applied to a region

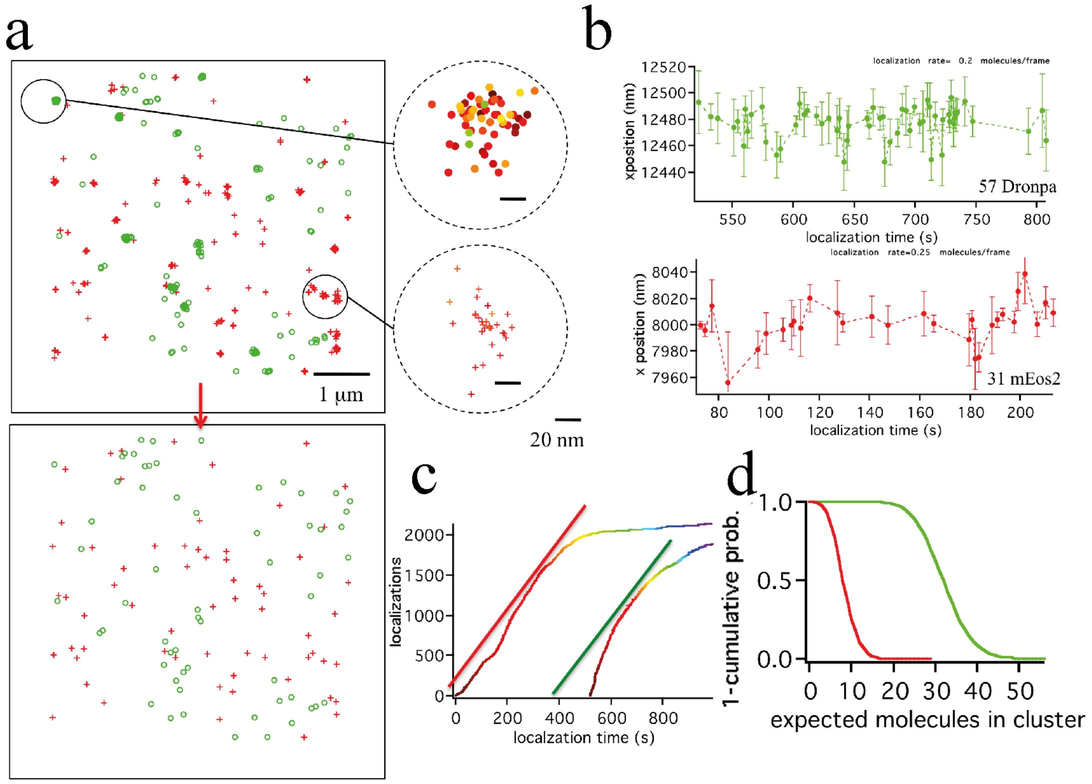

Figure 5.9: a) Map of the localized centers for mEos2 (red) and Dronpa (green) molecules activated in PAGE at low concentration. b) Two arbitrary clusters are selected and their kymographs displayed. c) The number of molecules activated in time for each species is displayed. Linear guide for the eye outlines the linear activation regime where the assumption of a Poisson flow for the arrival time of the localization events hold. d) Cumulative Distribution Functions for a Poisson Distribution calculated for the two clusters displayed in b. $m_{Eos} \sim 9$ and $m_{dronpa} \sim 23$.

of the plasma membrane of an H9C2 cell expressing β2-mEos2 receptor, figure 5.8 displays how a clustered pattern remains also in the missed counts regime, that the clusters are largely polychromatic and that the Ripley's $L(r) - r$ function signals a significant shift from randomness.

5.4 Cell-type specific and cytoskeletal dependence of β2-AR clusters in H9C2 cell line

Throughout our investigation of β2-AR clusters in H9C2 cells [74], the following approach was employed:

1. The distribution of the receptor was systematically compared to the one of a negative control, the SrcN15 peptide, both in HeLa cells and in H9C2 cells.
2. As we discussed in the previous section, datasets were analyzed in order to remove photoblinking induced artifacts and to extract meaningful information from the spatial point pattern representation of the arrangement of β2-AR on the surface of HeLa and H9C2 cell lines.
3. The signaling properties of β2-AR were exploited to modulate the degree of receptor heterogeneity, e.g. the clustering degree was increased by stimulating the receptor internalization.
4. Standard biochemical treatments such as the inhibition of the actin cytoskeleton polymerization or the removal of cholesterol were employed to investigate the effect on the β2-AR spatial maps and infer on the functional role of these clusters.

Overall more than 100 cells were imaged in PALM, and the resulting spatial point patterns were analyzed, extracting the fraction of clustered molecules and calculating the $L(r)-r$ function. A lengthscale $r = 150$ nm was employed to extract the clustered fraction (as reported in [74]). The use of another r value, e.g. $r = 50$ nm, would obviously yield a different clustered fraction, but appears to be qualitatively consistent in capturing the differences existing across multiple experimental subgroups. This issue is discussed in more detail in Appendix A.

The distribution of β2-AR in HeLa cells displays a degree of clustering comparable to the negative control, around 4%. The next obvious step, i.e. to measure the clustering fraction compared to a positive control, is achieved by stimulating receptor endocytosis, as we have extensively discussed in chapter 4. Figure 5.10 shows how the spatial heterogeneity of the arrangement of β2-mEos2 increases in a sample fixed after stimulation with the agonist Isoproterenol for ten minutes. Both the Gaussian probability map representation (figure 5.10 a, b, d, e) and the spatial point patterns (figure 5.10 c, f) clearly outline how the spatial arrangement of the receptor has changed, and that clusters are present in the stimulated cell. Figure 5.11 a, displays the clustered fraction measured for the negative control SrcN15 and β2-AR labeled with mEos2 in HeLa cells upon different treatments. The basal figure compares to the control, whereas upon stimulation with the agonist, the clustered fraction increases. This is confirmed by the direct inspection of figure 5.10 d, and is reinforced upon the use of the inhibitor of the clathrin dependent endocytosis Dynasore, as shown in figure 5.11 a. The large variability in the endocytosis data arises, in our opinion, due to the variability of the internalization process and the relatively low density of the forming endosomes on the plasma membrane (0.2-0.3/μm^2 as reported from TIRF measurements [51]). Incubation with Isoproterenol for shorter times, followed by instant fixation, did not determine any change in the measured level of clustering.

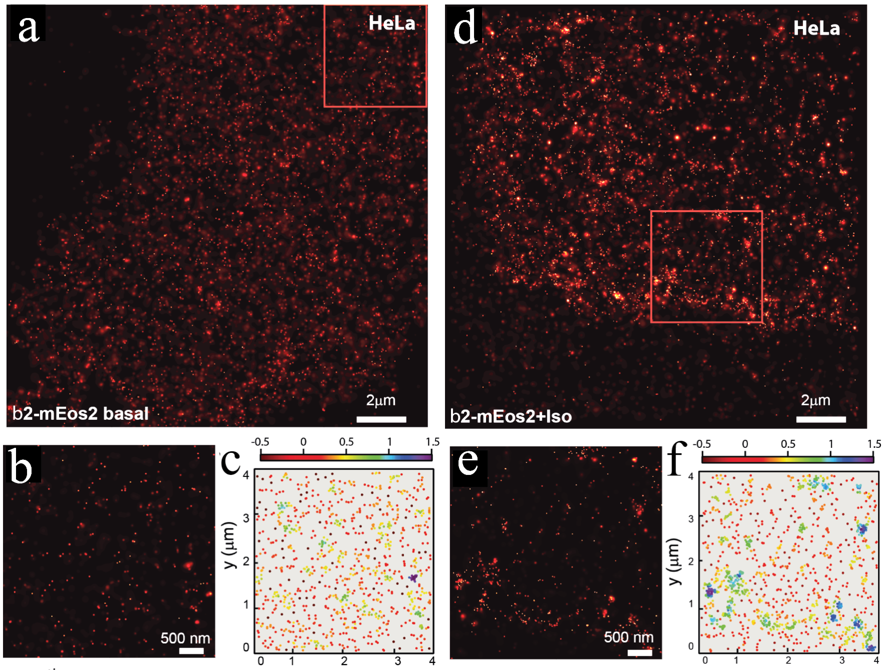

Figure 5.10: PALM images and cluster analysis of $\beta 2$-AR labeled with mEos2 ($\beta 2$-mEos2) on the plasma membrane of HeLa cells before and after agonist addition. a) PALM image in TIRF geometry of $\beta 2$-mEos2 in basal conditions on the plasma membrane of fixed HeLa cells. Images that are shown are representative of experiments that were repeated at least five times. b) Inset show magnified view. c) Schematic representation of the molecules distribution of the inset to visualize clusters (color coding represents clustering degree). d) PALM image in TIRF geometry of $\beta 2$-mEos2 on the plasma membrane of fixed HeLa cells after incubation with the agonist (Isoproterenol 10μM, 10 min) during endocytosis. Images that are shown are representative of experiments that were repeated at least five times. e) Inset show magnified view. f) Schematic representation of the molecules distribution of the inset to emphasize clusters. (Reprinted from Scarselli, Annibale and Radenovic [74])

When comparing datasets of similar density, the standardized Ripley's $L(r) - r$ function confirms the increased degree of clustering with respect to the control, and outlines very well the increased length-scale of the clustering with respect to the basal data, since the maximum of the function changes from a single peak at approximately ~ 100 nm in basal conditions up to a *plateau* ranging from 50 nm up to 200 nm or 300 nm when stimulated respectively with the agonist and with the agonist added to Dynasore.

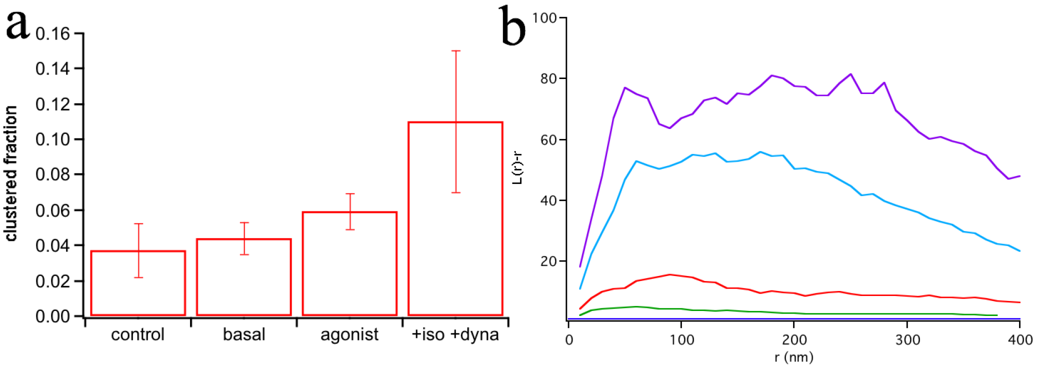

Figure 5.11: a) Histogram of the measured clustered fraction in HeLa under different stimulation conditions: SrcN15 as a control, β2-AR in basal conditions, β2-AR after stimulation with the agonist Isoproterenol 10 μM for 10 minutes, β2-AR after stimulation with Isoproterenol and incubation with Dynasore 80 μM. b) Ripley's $L(r) - r$ functions standardized to the 99% confidence interval. $L(r) - r$ functions, though standardized, were calculated on datasets of comparable densities. Legend: red-β2 basal, green-SrcN15, cyan- +Isoproterenol, purple- +Isoproterenol+Dynasore. (Adapted from Scarselli, Annibale and Radenovic [74])

The measurements performed on HeLa cells suggest the absence of any significant (aggregates larger than five molecules, according to our thresholds) basal clustering, in agreement with previous observations of other GPCRs based on single particle tracking [52]. Although we operated in the missed-counts regime and therefore all estimates on the number of localized molecules provide only a lower bound, the β2-AR surface density ranged from 10 to 160 molecules/μm^2, with an average of 59 /μm^2 and a median of 43 /μm^2. These values are in agreement with the literature values for endogenous receptor levels as well as with our initial estimation based on fluorescence measurements reported in figure 5.2.

As we have already shown in the previous section, the picture appears to change when moving from HeLa cells to the cardiomyocite-like H9C2 cells. Figure 5.12 a and d, compare the PALM image of the basal state of β2-AR and the image of the control SrcN15 in H9C2 cells. The basal state displays a detectable level of clustering when compared to the negative control. The average clustered fraction for H9C2 cells is 10%, comparing to approximately 3% of the control (figure 5.16).

The observation of basal clustering should compare to the Scanning Near Field Optical Microscopy measurement of Ianoul [60] et Vobornik [75], who observed a significant amount of basal clustering in H9C2 and HEK293 cell lines respectively, the clusters having an average diameter ~ 150 nm and a features density of approximately $1 - 1.4$ /μm^2. The data reported in figure 5.13 a and b, confirm that most of the cluster diameters fall in between 100 nm and 200 nm, whereas the average number of features /μm^2 is 0.2. Expression levels range from a few to 150 molecules /μm^2, with an average of 67 /μm^2 and a median of 47 /μm^2. As we discuss more thoroughly in Appendix A, in the basal state it was

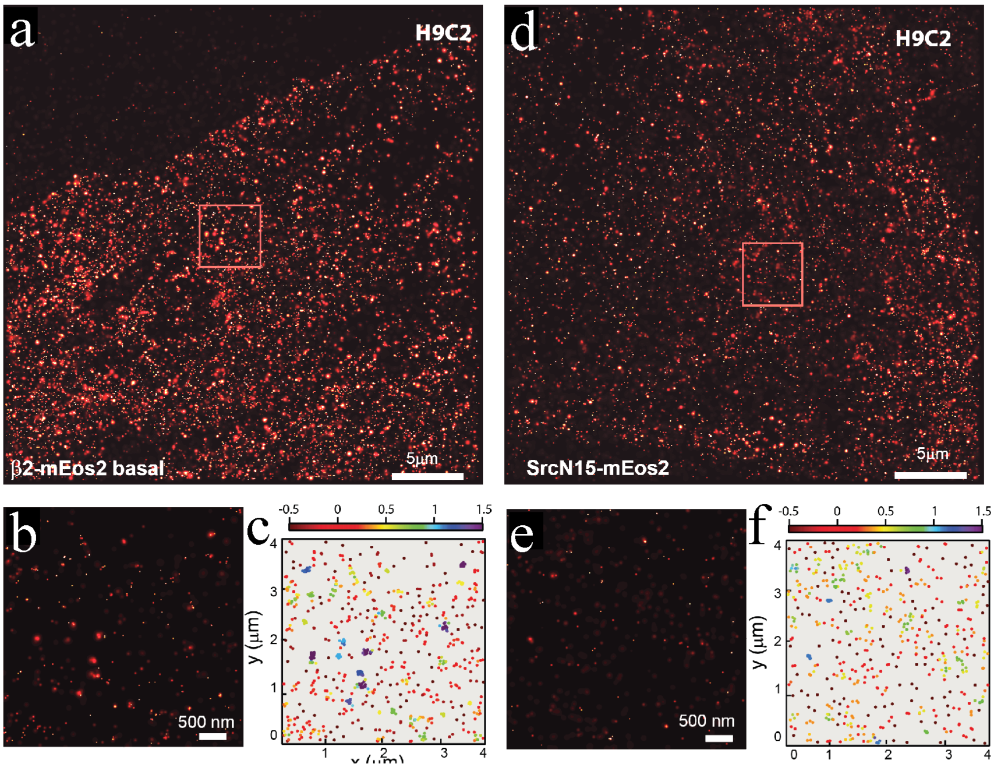

Figure 5.12: PALM images and cluster analysis of $\beta 2$-mEos2 on the plasma membrane of H9C2 cell line a) PALM image in TIRF geometry of $\beta 2$-mEos2 in basal conditions on the plasma membrane of fixed H9C2 cells. Images that are shown are representative of experiments that were repeated at least five times. b) Inset show magnified view. c) Schematic representation of the molecules distribution of the inset to visualize clusters (color coding represents clustering degree). d) PALM image in TIRF geometry of the non clustering peptide SrcN15-mEos2 on the plasma membrane of fixed H9C2 cells. Images that are shown are representative of experiments that were repeated at least five times. e) Inset show magnified view. f) Schematic representation of the molecules distribution of the inset to visualize clusters. (Reprinted from Scarselli, Annibale and Radenovic [74])

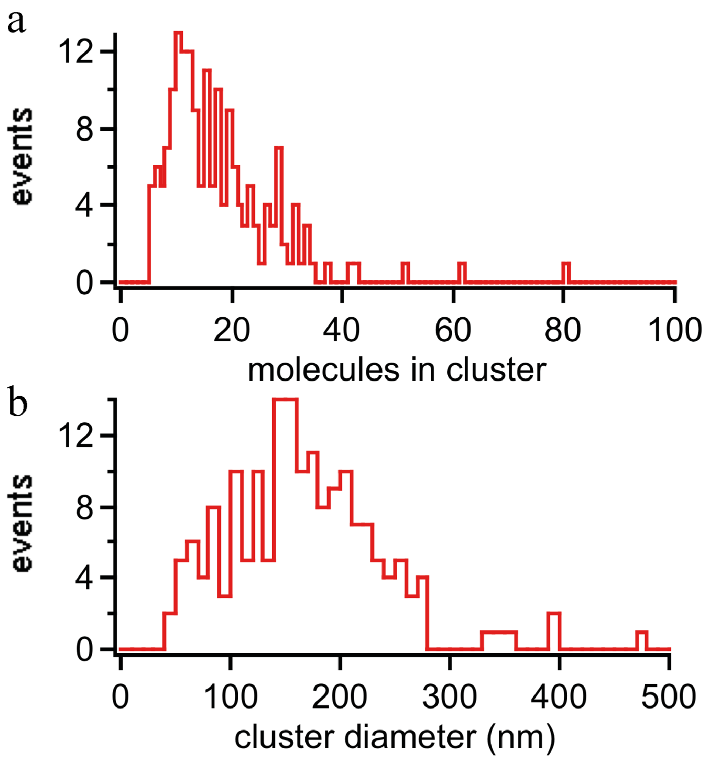

Figure 5.13: a) Histogram displaying the distribution of the number of molecules belonging to each clusters and b) of the cluster diameters. All data refer to measurements in H9C2 cells.

not possible to observe an increase of the clustered fraction upon the receptor density.

Figure 5.14 displays Ripley's $L(r) - r$ function from two data-sets of comparable densities, comparing β2-mEos2 to SrcN15-mEos2. Figure 5.14 confirms the finding from the clustered fraction approach and indicates an average clustering lengthscale slightly beyond 100 nm. Controls obtained expressing another receptor in H9C2 cells, such as the M3 muscarinic receptor, or β2-mEos2 in a third cell line, CHO, did not display any significant amount of clustering either, as displayed in figures D.1 and D.2.

In order to elucidate the mechanism governing the clustering of β2-ARs in H9C2, cells were incubated with an agonist for very short times (figure 5.16) and with an antagonist ICI118,551. It is significant to notice that when the agonist Isoproterenol was added 5 s before fixation, the clustered fraction was not significantly altered, and this was also the case with the antagonist.

Membrane altering agent such as Filipin (cholesterol sequestration) and Methyl-β-Cyclodextrin (MβCD) (cholesterol extraction) were used in order to investigate the possible dependence on cholesterol (and therefore the possible role of lipid rafts) of receptor clustering (see [76] and references therein). If MβCD rapidly extracts cholesterol from the plasma membrane and disrupts the lipid raft, Filipin binds and selectively sequesters cholesterol, only modifying raft properties. However, the use of MβCD, a stronger approach for cholesterol sequestration, causes more side effects due to its pleiotropic properties. For this reason, we decided to utilize both cholesterol-altering agents, Filipin with a preincubation of 30 min at the concentration of 12 μg/ml and MβCD with a preincubation of 30 min at the concentration of 5 mM. The acute addition of both treatments yielded similar results and did not change significantly the clustered fraction of β2-AR (-chol column in figure 5.16 a), indicating that receptor clustering does not seem to rely on lipid microdomains integrity.

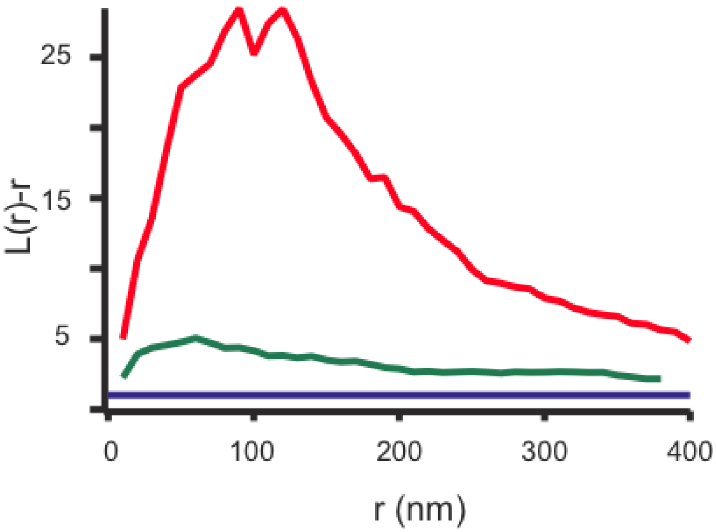

Figure 5.14: Comparison of Ripley's $L(r) - r$ function calculated for β2 in basal conditions (red) and for the negative clustering control SrcN15 (green). (Adapted from Scarselli, Annibale and Radenovic [74])

However a significant change in the clustered fraction is observed when cells were treated with Cytochalasin D, a chemical agent well known for altering the organization of the cytoskeleton [77] by inhibiting actin polimerization, as displayed in figure 5.15. Cytochalasin D treatment is known to determine morphological changes across a large number of cell types (such as cell arborization), the dissolution of stress fibers and the formation of actin *asters* throughout the cell body [78]. The functional role of the actin cytoskeleton in modulating GPCRs arrangement either directly or through intermediates has been discussed in detail in the past, and the specific effects of the disruption of the cytoskeleton on the arrangement [69] and diffusion coefficient of adrenergic receptors are well documented [79]. In the latter work H9C2 were treated with the actin-disrupting agent Latrunculin B and individual β2-ARs were tracked demonstrating a reduction of the confinement, i.e. proving the existence of some sort of a tethering mechanism to the actin cytoskeleton.

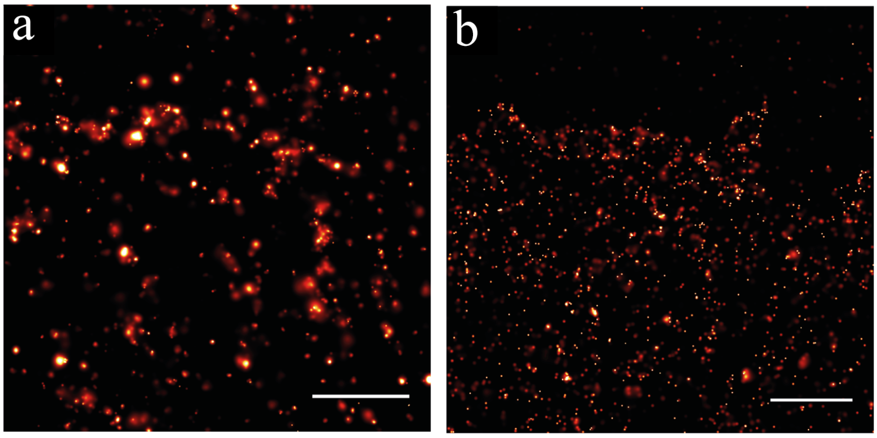

Figure 5.15: PALM images and cluster analysis of β2-mEos2 on the plasma membrane of H9C2 cells after cholesterol sequestration or actin microfilament disruption. a) PALM images in TIRF of β2-mEos2 on the plasma membrane of fixed H9C2 cells in basal condition and b), and after actin cytoskeleton disruption. Scale bars 1 μm. (Reprinted from Scarselli, Annibale and Radenovic [74])

The data reported in figure 5.16 a and b, based on the calculation of the clustered fraction and on $L(r) - r$ values respectively, suggest that the reduction of clusters due to the treatment with Cytochalasin D is statistically significant. Nevertheless it is not completely clear how the impact of a cytoskeletal reorganization can influence receptors arrangement on lenghtscales (i.e. 50-150 nm) such as the one investigated in our study. If it is true that Cytochalasin D was demonstrated to inhibit actin polymerization in-vitro, it was also shown that it acts in cells by determining a rearrangement of the actin filaments around focal points rather than completely de-polymerizing them. Furthermore, the role of intermediate proteins binding both to actin and to the receptors during actin rearrangement adds further complexity to this picture.

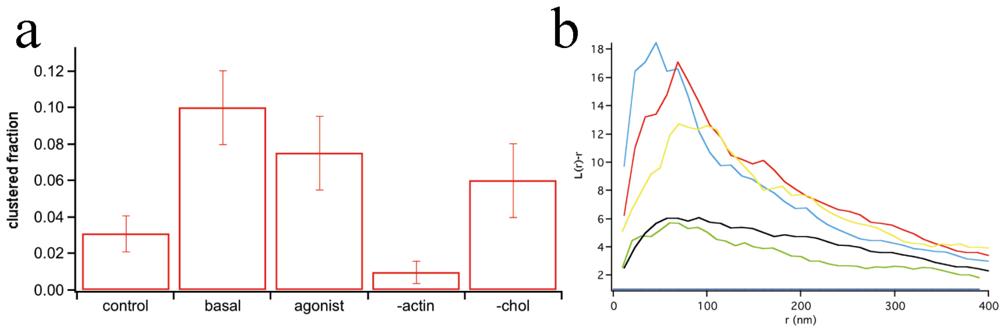

Figure 5.16: a) Histogram of the measured clustered fraction in H9C2 under different stimulation conditions: SrcN15 as a control, β2 in basal conditions, β2 after stimulation with the agonist Isoproterenol 10 μM for a few seconds, β2 after incubation with the actin polymerization inhibitor Cytochalasin D and β2 after incubation with either of the two cholesterol altering agents MβCD (5mM) or Filipin (12μg/mL). b) corresponding Ripley's $L(r) - r$ functions standardized to the 99% confidence interval. $L(r) - r$ functions were calculated on datasets of comparable density. Legend: red-β2 basal, green-SrcN15, cyan-Filipin, yellow-Mβ CD, black-CytochalasinD. (Adapted from Scarselli, Annibale and Radenovic [74])

A crucial experiment to determine whether the interaction with the actin cytoskeleton or the associated scaffolding proteins is the only reason for the observed clustering of β2-AR would be the observation of the receptor distribution on the plasma membrane alone. In this ideal case, the observed clustering, if any, could be only due to protein-protein or lipid-protein interactions. Many approaches were reported in order to obtain lipid bilayers incorporating, among the others, membrane receptors: either starting from purified cellular membranes, or using rip off methods from copper grids or sonication to separate membrane fragments from the bulk of the cell [80].

We followed the strategy pioneered by Perez *et al.* [81] in order to obtain planar supported membrane sheets. Supported membranes are obtained by direct detachment from the cell apical membranes using Poly-L-Lysine coated glass coverslips, after sandwiching osmotically swollen cells. The authors of the study demonstrated that this method allows the membrane to conserve its composition and maintain its fluidity by using α1b-AR in membrane sheets derived from HEK-293 cells.

PALM images of patches obtained from H9C2 cells expressing β2-mEos2, compared to the usual control peptide SrcN15, show (figure 5.17) that a residual clustering is still visible. The observed heterogeneity of the protein arrangement could be also attributed to a structural reason, such as the folding of the membrane on itself, as it is possible to observe at the edge of the patches. A reduction of the maximal

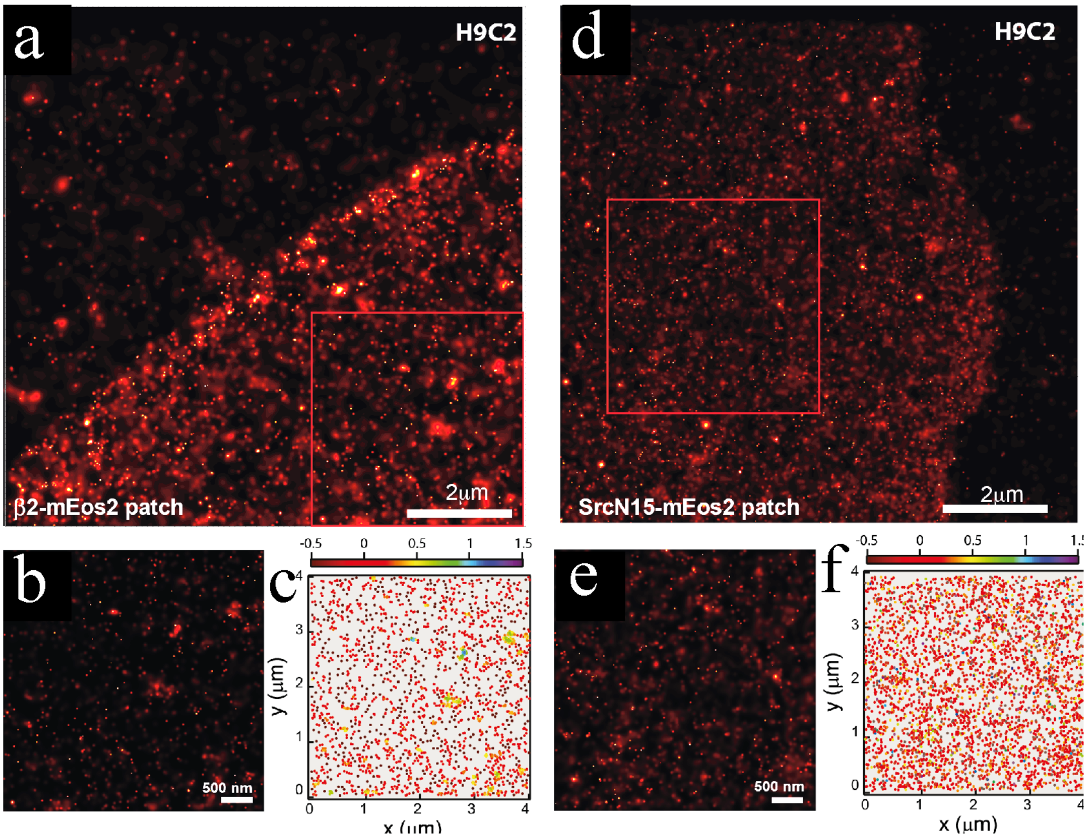

Figure 5.17: PALM images and cluster analysis of β2-mEos2 and of the non-clustering peptide SrcN15-mEos2 on supported cell-membrane sheets of H9C2 cells. a) PALM image in TIRF of β2-mEos2 in basal conditions on H9C2 membrane sheets obtained by transferring plasma membrane onto poly-L-lysine-coated coverslips and then fixing. Images that are shown are representative of experiments that were repeated at least three times. b) Inset shows magnified view. c) Schematic representation of the molecule distribution of the inset to visualize clusters (different colors represent clustering degree). d) PALM image in TIRF geometry of the non-clustering peptide SrcN15-mEos2 on H9C2 membrane sheets obtained using the same condition as in (a). e) Inset shows magnified view. f) Schematic representation of the molecule distribution in the inset to highlight clusters. (Reprinted from Scarselli, Annibale and Radenovic [74])

values of the $L(r) - r$ function was observed when comparing whole cells to patches. However further efforts will be required in order to single out the role of the actin cytoskeleton or a purely protein-protein interaction within the membrane as the main reason for the observed clustering: patches from cells transiently expressing actin-EGFP show, at least in our hands, that in most of the cases residuals of the actin cytoskeleton can be found, either as bundles or residual puncta, on the plasma membrane sheets.

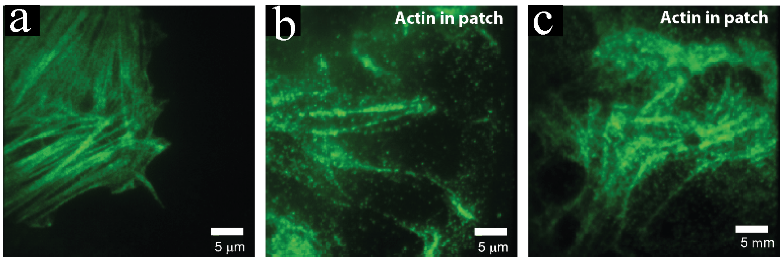

Figure 5.18: (a) H9C2 cells were transfected with GFP-actin, fixed and then imaged in TIRF geometry. (b,c) TIRF images of supported plasma membrane sheets on PLL coated coverslips indicate that actin microfilament are still present on the membrane patches, either as microfilaments or punctuate aggregates. (Reprinted from Scarselli, Annibale and Radenovic [74])

5.5 Discussion

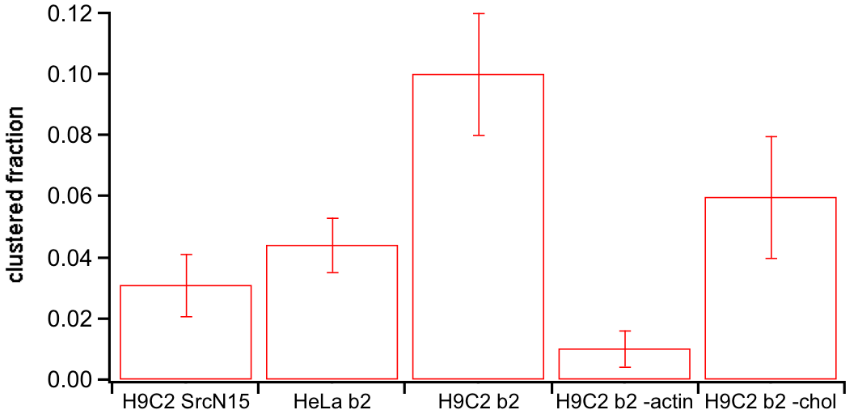

Figure 5.19: Comparison of the measured clustered fraction across different experimental subgroups. r = 150 nm and $m = 5$, t_d = 10 s + cluster scoring. (Adapted from Scarselli, Annibale and Radenovic [74])

In this chapter we discussed an original application of PALM to the study of the membrane arrangement of an important receptor, the β2-AR, a prototypical GPCR. The experimental approach is based on the collection of a spatial point pattern map, refined according to the considerations discussed in the previous chapters, in order to move as close as possible to the condition that each point corresponds unambiguously to a single receptor. This does not imply that all receptor molecules in the sample will be counted, given the presence of endogenous receptors and the fact that not all of the fluorophores are localized, as we will see in the next chapter. However, the approach that we have developed in this work guarantees that there will not be a gross overestimation of the number of labeled molecules nor the incorrect detection of cluster features that are simply due to multiple localizations of only one or a few molecules. Interestingly, the number of localizations measured was, on average, comparable to the reported levels of endogenous expression of this receptor.

We observed a qualitative heterogeneity in the arrangement of β2-AR on the plasma membrane of H9C2 cells, as compared to β2-AR expressed in HeLa cells and to the distribution of a negative control based on the polypeptide SrcN15 in both cell types. Using a straightforward approach based on the parallel application of a density threshold and of Ripley's method, the number of clustered molecules was calculated, measuring that approximately 10% of the β2-AR in H9C2 cells are part of clustered aggregates over length-scales between 50-200 nm. Figure 5.19 summarizes the main findings of the experiments discussed in this chapter indicating the presence of a significant difference in the clustering degree of β2-AR in H9C2 cells when compared to the control SrcN15 and to β2-AR clustering in HeLa. Standard biochemical treatments such as the extraction of cholesterol from the plasma membrane or the disruption of the actin cytoskeleton showed that, if the fraction of molecules part of clusters was not affected by the cholesterol treatment, it was by the actin network disruption operated by Cytochalasin D. The biophysical insight about the role of actin in modulating the heterogeneity of these cell membrane receptors in H9C2 cells was qualitatively confirmed by the study of supported membrane patches, although this approach can not rule out completely the role of actin due to the observed cytoskeletal residues on the membrane patches. Our observations fall in the framework of a sequence of reports [69], [79] linking the arrangement and diffusional properties of β2-AR to the actin cytoskeleton, either directly or through a set of intermediate proteins. The endogenous expression levels suggest that these receptors, if indeed connected to actin, decorate the cytoskeletal filaments piece-wise rather than continuously. Comparison of Ripley's $(L(r) - r)_{max}$ values to the clustered fraction, exploiting the observed variability in expression levels, seems to indicate that an increase of the β2-AR surface density in H9C2 cells results in larger clusters rather than in more clusters, as discussed in Appendix A.

PALM is able to image and quantitate the clusters, but we can only provide hypotheses regarding the mechanism driving the formation of these aggregates. PALM, by definition a static technique to be performed on fixed samples, did not allow to obtain any information about the dynamics of these aggregates, nor standard biochemical tests such as the cAMP stimulation after disruption of the actin network were able to detect any functional difference [74]. The role of actin polymerization in determining or stabilizing these aggregates suggests that further investigation on the role of cytoskeletal and related proteins should be performed. The relative low throughput of PALM measurements will first require to work at stable expression levels to reduce the observed variability and rule out that higher expression levels may induce mechanism such as density induced oligomerization or a saturation of the scaffolding proteins mediating the interaction with the cytoskeleton. Second, the static super-resolution picture offered by PALM should be complemented with dynamical information. Finally it will be important to observe at high resolution the relation between cytoskeletal proteins such as actin and the arrangement of the receptor. The next chapter will discuss our strategy in order to obtain accurate information from dual color PALM data.

6 Development of accurate dual-color PALM imaging

6.1 Introduction

This chapter elaborates on the main challenges faced when dealing with multi-color localization microscopy, on the strategy that we pursued to maximize the two-color measurement precision and on the rationale behind the choice and the use of a specific pair of photoactivatable fluorescent proteins.

One of the basic concepts in fluorescence microscopy is the use of photons from spectrally separated fluorophores to distinguish two different species, and it was successfully applied since decades in the cell biology field. The detection of the multiple wavelengths emitted can be performed either sequentially, using the same detector, or simultaneously, using two or more independent detectors (channels). The information obtained from the relative position or overlap of the fluorescent emission in the pixels of two or more detection channels can be used, for example, to draw conclusions about the relative affinity or interaction between two labeled species within a cell [82] [83]. Reference markers are typically used to align the two different images of the same scene, in a process that is well known as registration of the two images. The tolerances required by diffraction limited imaging are in the order of one Airy minimum (0.61λ), within the interval $\sim 250 - \sim 450$ nm in the visible range.

However, super-resolution microscopy, in particular the approach based on localization of single emitters, introduces four major challenges to this picture. First the pixel size of super-resolution images is below 10 nm [4] leading to a drastic decrease in the tolerance of the registration process. Second, the stochastic photoactivation and localization process implies that in most of the cases neighbouring fluorophores will be activated in widely separated instants of time, making control of mechanical drifts and the overall stability of the setup of paramount importance. Third, the photoactivation (switching) of the probes determines special constraints, adding to the requirement of spectral distinguishability, on the pairs of PhotoActivatable Fluorescent Proteins (PA-FPs) that can be used. Finally, the extended duration of these experiments challenges traditional methods of sample fixation to keep individual fluorophores immobilized at the nanoscale for the time required to build-up a PALM image.

The next section (section 6.2) will briefly review the multi-color super-resolution measurements reported thus far, with a focus on PALM-like experiments. The chapter will then elaborate on our strategy towards the maximization of the accuracy of dual-color experiments performed on a customized commercial fluorescence microscope setup. Section 6.3 is dedicated to discussing the performance of a revised fiducial-based registration protocol, and the following section 6.4 to the integration of the setup with an axial stabilization mechanism. A comparison of three pairs of photoactivatable fluorescent proteins is carried out in section 6.5, with a specific focus on the chosen pair of fluorophores, pamCherry1 and PSCFP2 (section 6.5.3). Ultimately, the application of the chosen pair using the optimized setup is presented in order to observe a pair of co-clustering membrane proteins.

6.2 Strategies in dual-color super-resolution microscopy

The first multi-color super-resolution imaging papers appeared in 2007, and were: Bates *et al.* dual-color STORM [84] investigation using the fluorescent label Cy2-Alexa647 and Cy3-Alexa-647; and Shroff *et al.* dual-color PALM paper [8], introducing the pairs of photoactivatable fluorescent proteins tdEos-Dronpa -PSCFP2. The former work observed the relationship between microtubules and clathrin coated pits, whereas the latter focused on proteins belonging to the adhesion complex machinery; in both cases a super-colocalization was not observed; in the case of the adhesion complex study, in fact, it was concluded that the two species do not interact since they do not display sub-diffraction limit colocalization. In neither of these papers the registration protocol used nor its accuracy were explicitly addressed. A 2008 paper [85] by the Zhuang group investigated the relationship between mitochondria and the microtubule network by means of dual-color STORM. In the same year the Jakobs group [86] proposed a group of new PA-FPs for use in dual-color studies, as well as an alternative approach to multicolor measurements based on the use of spectrally closely spaced probes to be assigned to a specific color based on the ratio of the photons detected for each emitter in each of the spectral channels.

This approach was further extended by Testa *et al.* in 2010 [87], to triple channel detection using Alexa dyes, whereas in the pure PALM field the sequential imaging approach based on the use of mEos2 and Dronpa was applied to the study of dendritic spines [88]. Approaches based on the use of new, red PA-FPs allowing for simultaneous imaging using PAGFP as a green partner, were reported in 2009 and 2010 by the Lippincott-Schwartz group [89], [90], in studies focusing on the assembly and clustering of plasma membrane proteins. The year 2010 was marked also by a key publication discussing the ultimate limits to registration and colocalization of spectrally separated emitters in CCD based measurements [91]. Active stabilization of the imaging optics allows for sub-nanometer registration accuracy, with the *caveat* that emitters need to fall within the same camera pixel for such a precision to hold. In 2011 another application of the mEos2-PSCFP2 pair [92], as well as two works using mEos2-Dronpa combination were published [93], [94]. A successful multi-color strategy was also demonstrated using dSTORM suitable dyes [95] or a combination of PALM/STORM approaches, as in the recent work by Hess and coworkers [96], leading to three color live cell super-resolution imaging. Since the original development of PALM/STORM in 2006, a large number of photoswitchable fluorescent proteins or labeling strategies with organic dyes are now available [97]. This work focuses only on the use of photoactivatable fluorescent proteins for two color super-resolution studies. The motivation for this approach is that it requires the minimum amount of staining and sample manipulation, aside from the DNA transfection, and therefore strategies to optimize its performance should be actively investigated. In addition, it should not be neglected that the *one label-one protein* condition offered by PALM is the prerequisite that will be able to ensure the most quantitative outcome among all the super-resolution methods.

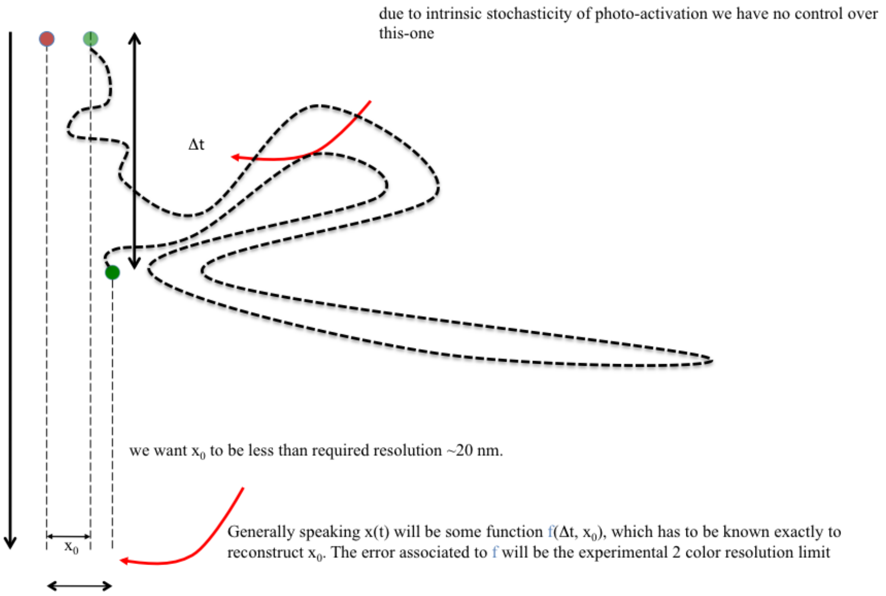

due to intrinsic stochasticity of photo-activation we have no control over this-one

we want x_0 to be less than required resolution ~20 nm.

Generally speaking x(t) will be some function f(Δt, x_0), which has to be known exactly to reconstruct x_0. The error associated to f will be the experimental 2 color resolution limit

Figure 6.1: Localization precision in dual-color PALM. The asynchronous nature of the colocalization of even neighboring fluorophores introduces an error in the determination of their relative distance that adds to the quadrature sum of their localization precisions. The final distance between the two fluorophores will be a function of their separation in time and space, and the error associated to this function will determine the ultimate localization precision.

6.3 Aligning the two-color imaging channels

Generally speaking, image registration is the process of aligning two or more images of the same scene. The first of the challenges of two-color super-resolution microscopy is to achieve routinely and reliably a good registration precision of the order of, or smaller than, the localization precision of the probes. The ultimate precision, below one nanometer, reported by Pertsinidis *et al.* [91] stands as a proof of principle of what can be achieved using a wide-field setup, but it clearly faces practical problems of applicability even to advanced microscopy users, let alone the average user of an imaging facility.

We therefore directed our efforts to establish a registration protocol that could be readily implemented after any PALM measurement in any commercial setup. We adapted and elaborated the concept, introduced by Churchman and Spudich in 2005, [98], based on the use of fluorescent fiducial markers to achieve registration of two images detected on the two halves of a CCD chip after separating the sample's fluorescence through a dichroic beamsplitter.

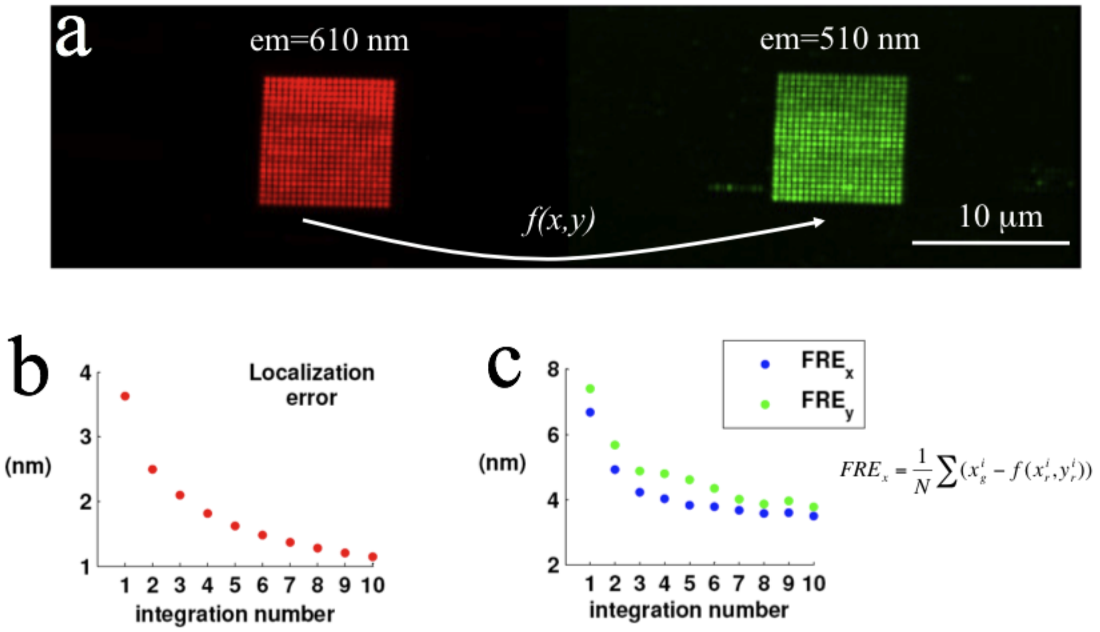

Figure 6.2: Registration protocol. a) Dual-color image of the grid obtained by integrating the images of a fiducial fluorescent bead scanned across a square matrix of approximately 10 μm side. b) Average localization precision of the individual fiducial nanoparticles as a function of the number of integrated frames (equivalent to multiples of the exposure time). c) Average Fiducial Registration Error following the Local Weighted Mean mapping of all the coordinates of the fiducial marker in the red channel and subtraction from the corresponding coordinates in the green. (graphics courtesy of Mattia Greco [99])

We used an $x-y-z$ sample piezo-stage (LPS Series, Mad City lab) to scan an isolated fluorescent bead in a grid, as displayed in figure 6.2, a. The fluorescent bead (Tetraspeck, Invitrogen) is a 100 nm diameter microsphere, stained with four different fluorescent dyes simultaneously: blue (365/430 nm), green (505/515 nm), orange (560/580 nm)and dark red (660/680 nm). It is excited simultaneously by both the 488 nm and a 561 nm lasers, and imaged on the EM-CCD camera with an integration time of 0.5 s. Each second the piezo moves the bead to the next position and another image is taken. The position of the peaks in each image and in each channel is localized based on a maximum likelihood Gaussian fitting [17]. Up to m user defined peaks per frame can be fit, for each of the N frames used to generate the complete grid. In each frame the peaks are identified based on their brightness. The pair of (x_i, y_i) coordinates from each fitted pair of corresponding peaks is then used to calculate the mapping function required for image registration.

The function used to map the localized red channel peaks onto the green channel is the local weighted mean algorithm introduced by Goshtasby [100] in 1988, and first applied by Churchman *et al.* [98] in the framework of single molecule experiments. The algorithm relies on the use of control points evenly spread throughout the field of view to locally evaluate polynomial functions to map each point of image 1 into the corresponding control point in image 2. Weights are introduced in order to decrease the influence of polynomials the further away from a given control point. The calculation of this mapping function, given the coordinates of a set of control points in the two imaging channels, is performed using the Matlab (The MathWorks) library *cp2tform*. The registration between the two channels of our acquisition is calculated off line, after that the actual super-resolution imaging sequence is performed and that the registration grid has been acquired. The accuracy of the registration process can be evaluated by calculating the mean residual offset, or Fiducial Registration Error (FRE), between the control points in one channel and their transformed counterparts. For the x direction, e.g. $FRE_x = \frac{1}{N}\sum_i^N x_g^i - f(x_r^i, y_r^i)$. It shall be noted that this indicator does not take into account the loss of registration precision occurring when the points to be mapped fall in between the control points. In addition, it is very important to consider that the registration process takes places at a given instant in time and at a given focal position, which does not necessarily match exactly those of the imaging, as will be discussed in more detail in the next section.

Nevertheless, the use of the Fiducial Registration Error is a practical benchmark, and we investigated its dependence upon the grid pitch and the localization precision of the control points. Where the grid pitch or the number of points did not appear to influence significantly the FRE, the localization of the fiducial markers clearly did. Figure 6.2, c shows how the FRE decay closely follows the localization precision, reaching a plateau below four nm when the localization precision falls below one nm. In addition, the smallest pixel size achievable in our setup, 80 nm with 100X magnification and 2X additional magnification after the tube lens, provided an improved FRE with respect to the data measured working with a 133 nm pixel size (60X Objective, 2X). The typical step size used to generate the grids for registering a PALM acquisition was 21 x 21 steps spaced by either 250 nm or 500 nm, hence covering 20 to 100 μm^2 . A detail showing the overlap of the centers of the localized beads in each channel is shown in figure 6.3 a. Our data illustrate that the two grids obtained plotting the coordinates of each fiducial marker displayed a constant offset and an additional linear component both in the x and y directions, (x offset vs x and y offset vs y). A crosstalk between the two axes is also present. Both the x and y offsets increase of about 50 nm every 5 μm, as illustrated in figure 6.3 b. In the experiment reported in figure 6.3 the offset between the two channels is below the image pixel size of 80 nm. This almost linear increase of the offset as a function of the (x,y) position in the field of view is consistent with previous reports describing a radial increase of the chromatic shift in moving away from the objective optical axis [101].

The origin of the offset between the two channels can be due to multiple factors. Besides chromatic shift, also the mechanical misalignment of the channels introduces one important source of error. The beam-splitting device (DV2) described in the experimental section allows to manually register the two channels within ±1 pixel accuracy. It is always possible that a sub-pixel offset or a slight angular tilt remain between the two images, and only a method based on the sub-diffraction limited localization

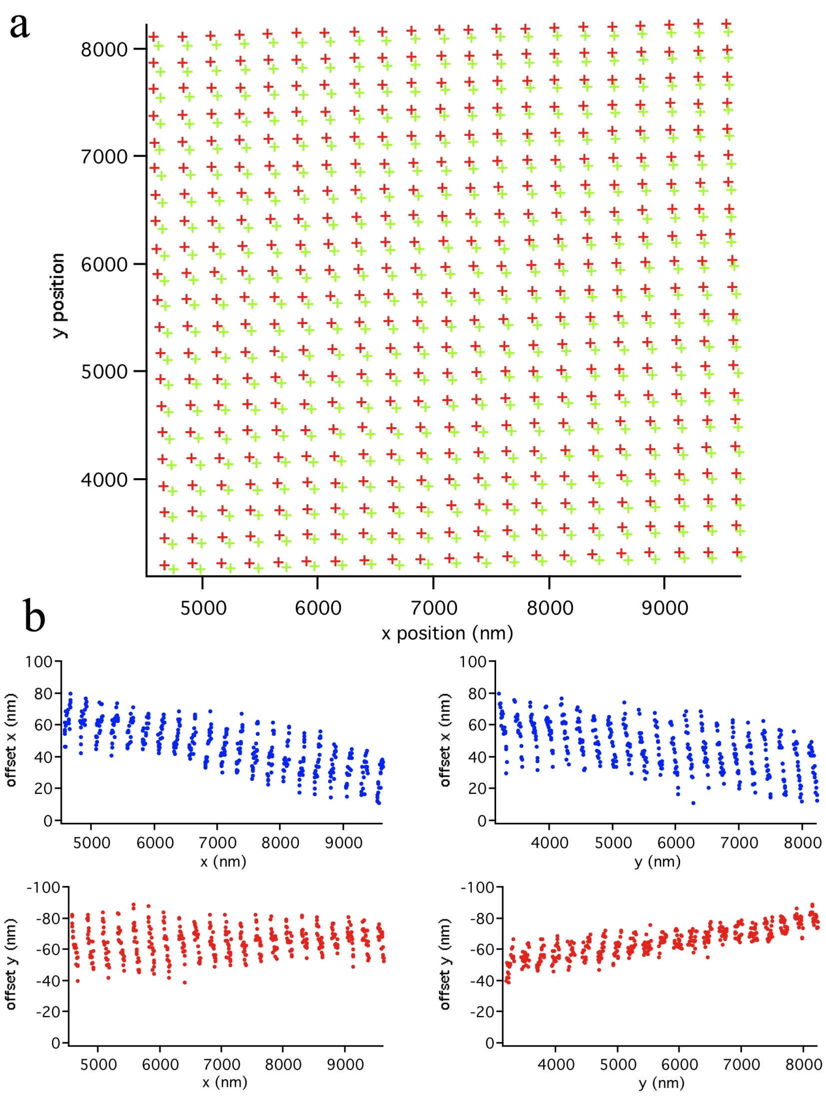

Figure 6.3: a) Overlap between the localized centers of the beads composing the grid in the two channels, prior to image registration. b) Relative chromatic offsets $x_r^i - x_g^i$ and $y_r^i - y_g^i$ in nm as a function of the position of the bead in the field of view.

of a set of control points allows to correct for these effects.

Figure 6.4 illustrates the effect of the registration on a typical dual-color PALM dataset. A supported membrane sheet from a cell expressing the fusion construct SrcN15-PSCFP2-mEos2 (a fusion of two fluorophores to the same membrane targeting sequence SrcN15, as we will see in more detail in section 6.5 and prepared as described in Appendix C) was generated by stripping the apical membrane of a HeLa cell with a Poly-L-Lysine (PLL) coated coverslip. The result is a patch seen as homogeneously labeled in both channels, displaying a few prominent features (such as the protruded front of the cell membrane or the aggregate indicated by the arrows) due to the process of non-uniform membrane detachment from the cell and adhesion on the coverslip. In addition, the choice of a dual-labeled construct guarantees that the exact same pattern, provided for the different localization precisions and photophysical properties of the two fluorophores, should be imaged.

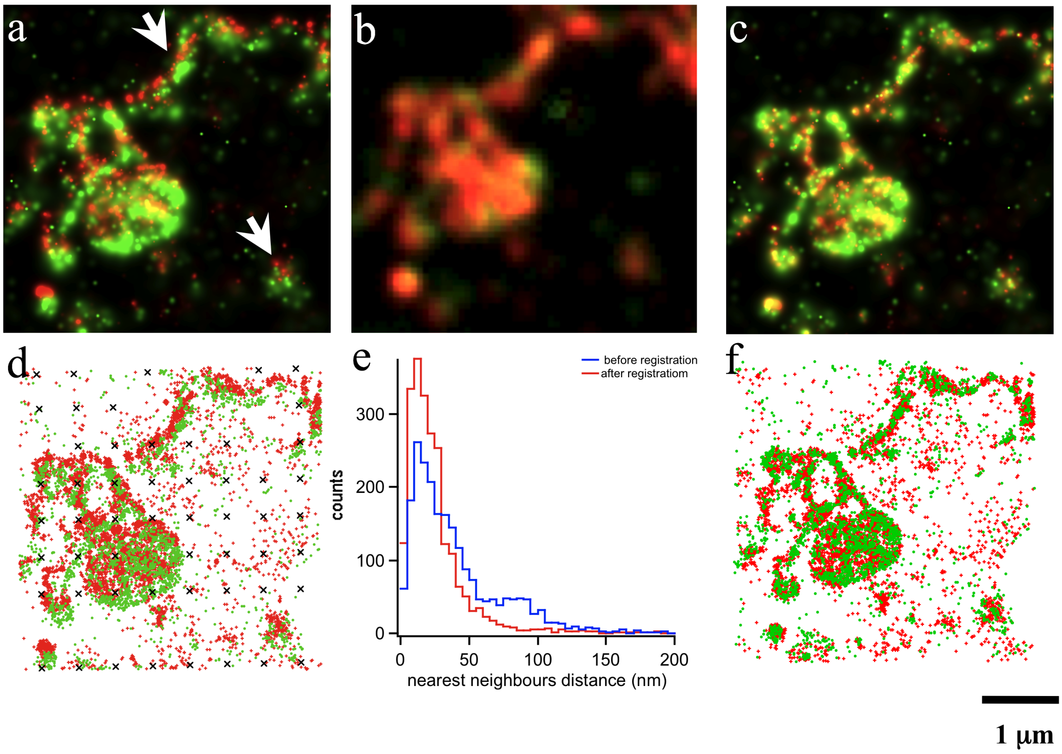

Figure 6.4: Overlap of the red and green PALM images of a membrane patch expressing the fusion construct SrcN15-PSCFP2-mEos2. Pixel size in the PALM image is 5 nm, for both channels, and the threshold on the localization precision of each fluorophore is 35 nm. a) PALM image prior to registration. b) Diffraction limited image prior to registration. c) PALM image after registration. d) Spatial point pattern map of the localized center of each fluorescent molecule corresponding to a, and overlap of localized centers of the fiducial markers used as the control points to determine the transformation function $f(x, y)$ (black crosses). e) Nearest neighbours distances before and after the registration. f) Spatial point pattern map of the localized center of each fluorescent molecule corresponding to c.

Figure 6.4 a, represents the direct overlay of the PALM images (and the corresponding point patterns of the localized fluorescence centers) prior to any registration algorithm. A slight shift between the red and green patterns is visible, mostly along the y axis. Figure 6.4 b, displays the same image than in a, but observed in a diffraction limited mode. When limited by diffraction, the effect of the small offset between the two channels is hardly noticeable. Panel d shows the point pattern corresponding to a. The points of the grid are spaced 500 nm, whereas the minimum radius of influence of the local weighted mean algorithm is as large as 2 μm. As a result the grid pitch allows a significant overlap of the radii of influence and guarantees that all the region within the grid is covered by the mapping function. The qualitative increase of the amount of yellow pixels in Figure 6.4 c, illustrates how after registration the degree of colocalization of the two labels improves significantly. Furthermore, the nearest neighbors distribution before and after the registration, displayed in figure 6.4 e, displays a marked increase in the number of events below 50 nm, after registration.

6.4 nm-range stabilization of the imaging plane

As mentioned in the previous section, the channel registration holds at one point in time. Throughout the relatively long PALM acquisition two occurrences may happen that would deteriorate the registration precision. First, a variation of the axial position of the sample. Second a mechanical displacement of the imaging optics of one channel with respect to the other one. It was demonstrated [102] that, in the presence of molecular dipoles that are not free to rotate, axial offsets can result into observed lateral offsets. This phenomenon can result in up to 2.8 nm lateral offset for 10 nm axial displacement. To counter this problem an axial stabilization system was put in place. The axial stabilized system is based on a feedback system using the total internal reflection of a near-infrared laser line, a concept originally proposed by Pertsinidis *et al.* [91]. As shown in the schematics of figure 6.5 a, the laser line from a 785 nm pigtailed diode is collimated and refocused on the back focal plane of the high N.A. objective used for imaging, achieving the condition for total internal reflection. The reflected laser line is then steered on a quadrant photo diode where the reflected spot moves along one direction proportionally to the separation between the objective lens and the coverslip. The difference signal from the two halves of the photodiode is then supplied to the NI USB 6229 acquisition card, and provides the input for the software PID feedback, driving the nano-positioning stage z-axis. The voltage value from the photodiode can be calibrated prior to any measurement by performing a z-ladder scan with the nano-positioning stage. Once a $\frac{nm}{V}$ conversion value is obtained it is used throughout the entire acquisition. As shown in figure 6.5 b, the sensitivity of this setup allows not only to avoid defocus and macroscopic blurring of the Point Spread Function of individual emitters, but also to maintain the axial position of the sample stable within 5 nm for extended periods of time (as shown in figure 6.5 c).

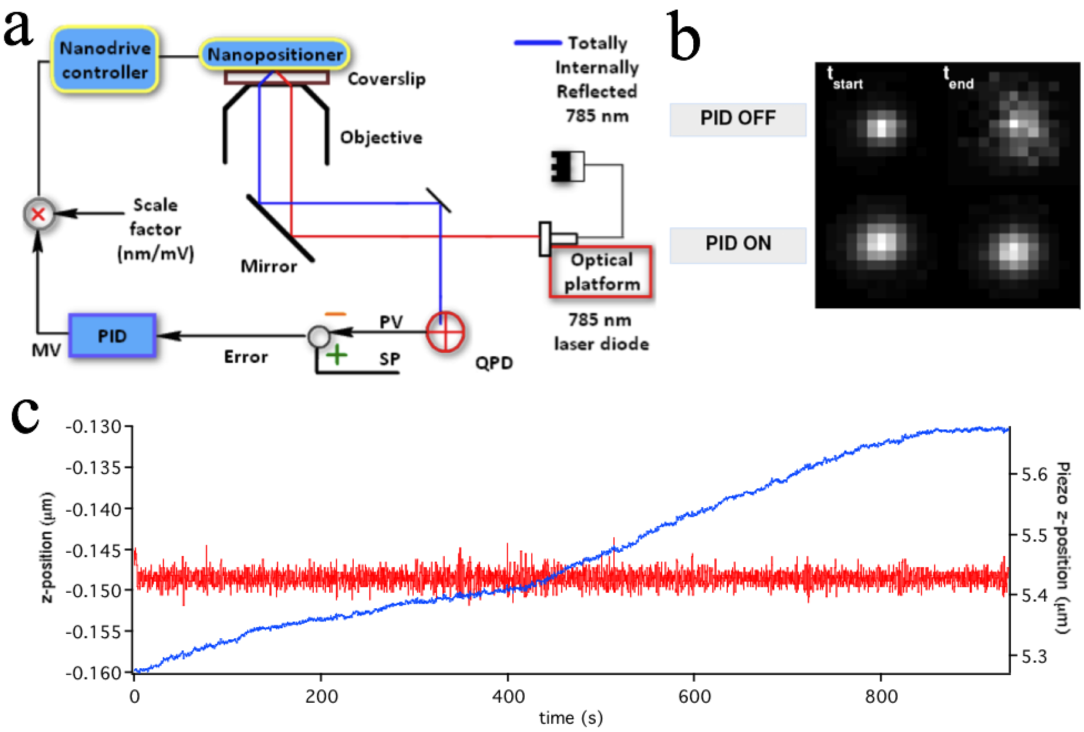

Figure 6.5: Registration protocol. a) Schematics of the optical setup obtained to achieve axial stabilization. A near-infrared laser line from a pigtailed diode (Thorlabs, Newton, New Jersey) is collimated and focused off-axis in the back-focal plane of the high NA TIRF objective used for imaging. The totally internally reflected laser-line (blue) is then steered on a quadrant photodiode QP50-6SD2 (Pacific Silicon, West Lake Village, California) (graphics courtesy of Mattia Greco). b) The net output of this setup is to maintain the relative distance between the objective and the sample fixed (i.e. the focal position), avoiding blurring of the PSF over time. c) A trace measured from the QPD over time, showing the feed-back signal (in red) and the z-displacement of the nano-positioning stage to counter the axial offset. The system is stable over extended periods of time within 5 nm peak-to-peak.

6.4.1 Experimental determination of the registration accuracy

By measuring a time-lapse movie of the position of a bright fluorescent bead in both imaging channels we can estimate the stability of the registration accuracy of the system over time. The spontaneous lateral $x-y$ drift allows the bead to explore an extended area of the field of view, in between the registration points, as displayed in figure 6.6, a. The fluorescent bead is localized to better than 2 nm (Figure 6.6 b) in both imaging channels, and its position in the red channel before and after the application of the mapping function is displayed. After mapping, the resulting offset falls in the nm range, as displayed in the scatter plot of figure 6.6, c. Notably, the points scatter beyond the expected error given by the combination of the localization precisions and the FRE, putting the effective registration precision of the setup to just above 10 nm. We will consider this figure as the empirical registration accuracy of our setup.

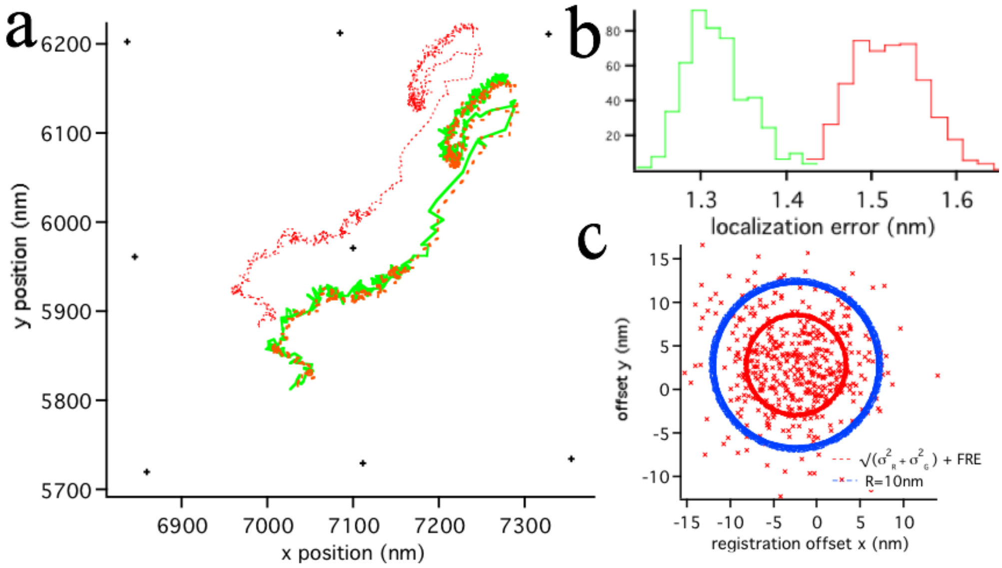

Figure 6.6: a) $x-y$ Trajectory of a 100 nm diameter fluorescent bead immobilized on the coverslip and imaged during a time lapse movie. The $x-y$ displacement is due to the sample drift. z position is stabilized by the axial feedback mechanism. Green trace is made of the measured position of the bead as seen in the green imaging channel. Red trace corresponds to the red imaging channel. The orange dashed trace is obtained after application of the registration function to the red points. Black crosses represent the positions of the fiducial markers. b) Histograms of the localization precision after Gaussian fitting of the bead (weighted least squares). $\langle\sigma_r\rangle \sim 1.5$ nm and $\langle\sigma_g\rangle \sim 1.3$ nm. c) Scatter plot of the residual x and y offset $x_g - x_r^t$ and $y_g - y_g^t$. The blue circle has a radius of 10 nm, the red circle has a radius given by $\sqrt{\sigma_r^2 + \sigma_g^2 + FRE^2}$.

The reason why the offset between the position of the bead in the two channels does not fall below the expected $\sqrt{\sigma_r^2 + \sigma_g^2 + FRE^2}$ is quite complex to address. We will limit our discussion to the fact that the relative drift in between the imaging channels may play a role by increasing the residual offset. Figure 6.7 displays the $x-y$ drift of a fiducial marker in an actual dual-color measurement: the fiducial drift follows a slightly different path when measured in each channel, and the relative drift, that should be constant, fluctuates approximately 10 nm (lower inset in figure 6.7). This relative drift can be corrected using the fiducial trajectories in the two channels when processing the dataset. However, as far as the average localization precision of the photoactivatable fluorescent proteins used in PALM is larger than 10 nm, the correction of such a residual offset appears incremental.

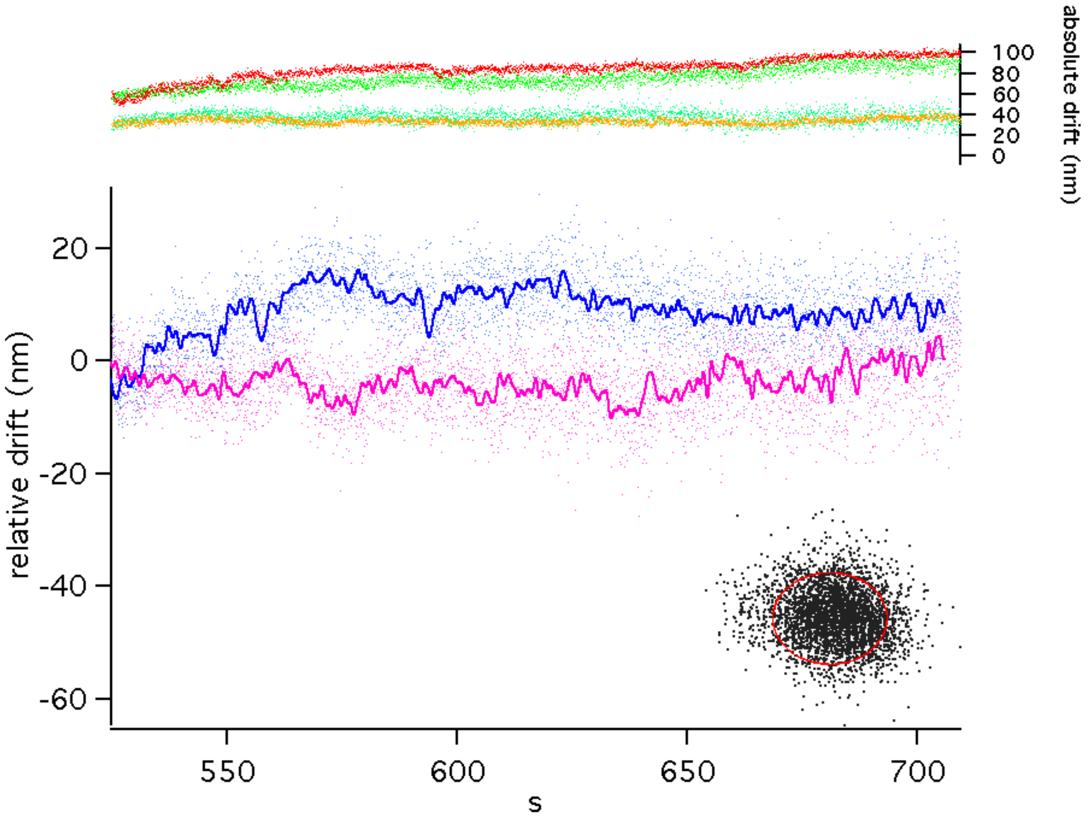

Figure 6.7: Measurement of the lateral drift. Upper graph: absolute drift, in the red and green channel, of one fiducial nanoparticle in a mEos2-PSCFP2 sample. Bottom graph: relative drift in the x and y directions. Lower inset: scatter plot of the residual offset between the green and red channel after approximately 520 s from the beginning of the acquisition till the end. The red circle has a radius of 10 nm.

Taking into account the above considerations, figure 6.8 summarizes the steps of the registration protocol that we recommend to be taken prior to dual-color acquisition. First the sample is brought into focus and the feedback is activated. Second fiducials are localized and PALM imaging is performed. Fiducial drift is tracked. Once all fluorophores in both channels have been activated and bleached, one of the fiducials is scanned through the field of view of the sample to generate a registration grid, maintaining the feedback active. Finally the combined information from the fiducial drift and the registration is used to correct the $x-y$ coordinates of all the localizations in both channels.

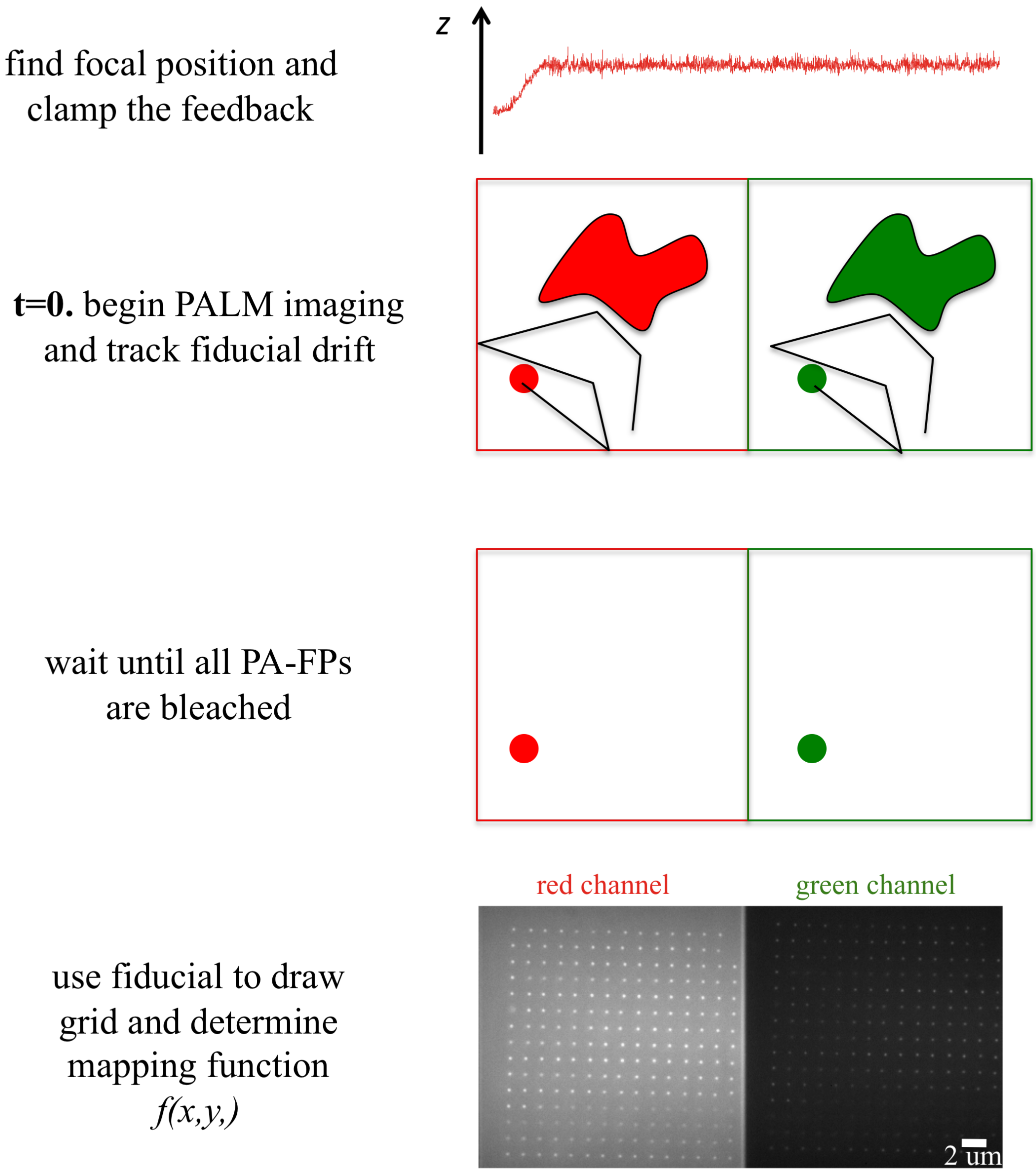

find focal position and
clamp the feedback

t=0. begin PALM imaging
and track fiducial drift

wait until all PA-FPs
are bleached

use fiducial to draw
grid and determine
mapping function
f(x,y,)

POST PROCESSING
correct position of each molecule with respect to t=0 using drift
information and apply *f(x,y)* to register red onto green channel

Figure 6.8: Schematic of the protocol employed in a dual-color imaging experiment

6.5 Choosing the fluorophore pair for dual-color PALM

A large number of possible fluorescent probe pairs were reported to date as candidates to perform dual-color super-resolution microscopy experiments. We deemed of interest to compare the performance of three pairs of PA-FPs. We investigated the pairs mEos2-Dronpa, mEos2-PSCFP2 and PSCFP2-pamCherry1. The first two were originally discussed by Shroff *et al.* [8], whereas the third one is an analogue of the pamCherry1-PAGFP pair proposed by Lippincott-Schwartz and co-workers, by replacement of PAGFP with PSCFP2. Although PAGFP is the archetype of photoactivatable probes, it has a relatively poor contrast ratio of ~ 100 as compared to ~ 1000 of psCFP [103].

We tested the performance of each pair by the use of a chimeric fusion constructs; surprisingly, no publications to date have reported on a similar approach. Engineering fusion pairs in principle provides two advantages: the exact same pattern is observed in each channel and the stoichiometry of the complex is fixed, allowing quantitative insight on the relative photoconversion and localization efficiency of the members of each pair. Purification of the constructs (as described in appendix C) allows to perform both ensemble absorbance measurements as well as single molecule colocalization experiments, the latter providing also a prompt test of the registration accuracy of the setup. Although single molecule asynchronous colocalization experiments are beyond the scope of PALM microscopy, they can nevertheless be exploited towards a quantitative measurement of the number of labeled proteins present in a sample, an appealing development of PALM based imaging.

Table 6.1 summarizes the experiments that were performed for each fusion construct. Purified fluorophores were used in absorbance experiments in cuvette using a spectrophotometer (Cary50, Varian) or immobilized in a PolyAcrylamide Matrix (15% Acrylamide concentration, 1:18 crosslinker ratio) sandwiched between two clean glass coverslips. Experiment in cells were performed by fusing the double fluorophore chimaeras to the membrane shuttling sequence SrcN15, that we already encountered multiple times in the previous sections of this work. In most cases we investigated plasma membrane patches, obtained according to the protocol discussed in chapter 5 in order to minimize background autofluorescence.

Fluorophore	PolyAcrylamide Gel	Plasma Membrane	Solution
Dronpa-mEos2	x		x
PSCFP2-mEos2	x	x	x
PSCFP2-pamCherry	x	x	x

Table 6.1: Test of three PALM PA-FPs fusion constructs in multiple environments

Dual-color PALM imaging can be performed either serially or in parallel. If the emission spectra of the *off*-state and *on*-state of each fluorophore do not overlap each other, then a parallel (or simultaneous) approach can be used. This is the reported case of pamCherry1-PAGFP and, partially, of pamCherry1-PSCFP2. On the other hand, if any of the spectra overlap (as is the case of Eos-like fluorophores, since their green fluorescence in the *off*-state overlaps with the *on*-state of all green fluorescent proteins), a serial (or sequential) approach must be used. Figure 6.9 graphically summarizes the concepts behind each mode of operation.

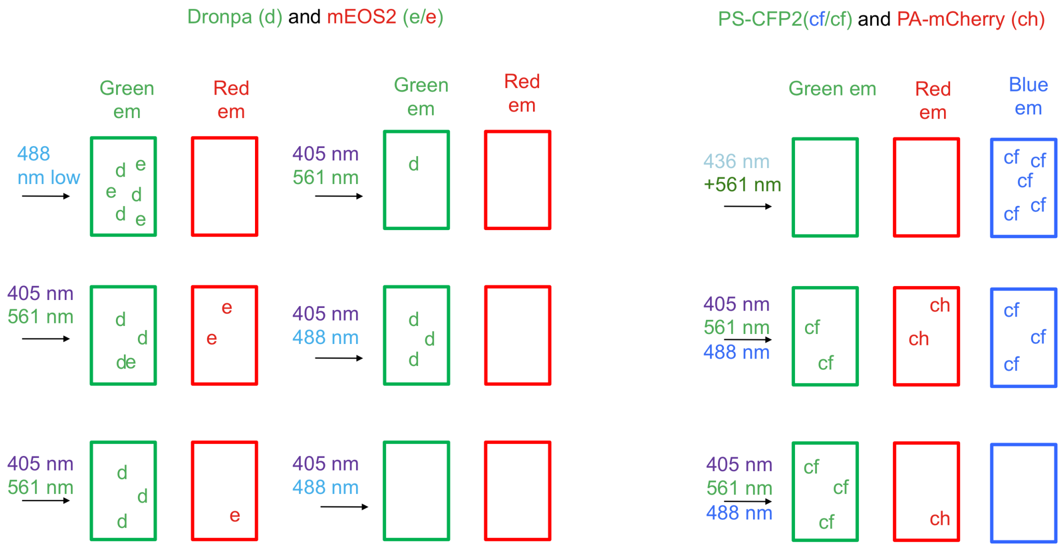

Figure 6.9: Schematic of sequential (left) and simultaneous (right) modes of operation in dual-color PALM imaging.

6.5.1 mEos2-Dronpa

The first pair of photoactivatable fluorescent proteins proposed for dual-color experiments was tdEos-Dronpa [8]. This combination is in principle suitable for a sequential dual-color imaging scheme, since the nominal reversible photoswitching ability of Dronpa allows to turn all of the fluorophore *off* and then to sparsely re-activate it again once the photoconversion of mEos2 is completed. Throughout our experiments we have encountered two significant issues limiting this approach. From the studies of absorbance in solution of the two individual fluorophores we observed that: first, the photoconversion of mEos2 in our hands was never complete, and second that the reversible activation of Dronpa in multiple cycles is limited, *de facto*, to a few switching cycles due to significant photobleaching. The evolution of the absorption spectrum of mEos2 at pH 8.5, upon 405 nm irradiation with a Xenon arc lamp (Lambda LS Xenon Arc Lamp System, Sutter Instrument) is displayed in figure 6.10. A careful inspection of the spectrum of figure 6.10 tells us that the the photoconversion follows a first order kinetics until saturation occurs, leaving a residual absorbance at 495 nm, with a green to red concentration ratio of 1.4 indicative of a ~ 60% photoconversion efficiency. Irradiation beyond this point results in a shift of the 510 nm isosbestic point, and an increase of the 270 nm band, hinting at a degradation of the chromophore. It is not obvious how to obtain a full photoconversion without degrading the fluorophore. This is not a new observation for the family of green to red photoconvertible fluorescent proteins pioneered by Kaede [104] and Eos [37], where remaining traces of the green form after extensive irradiation with 405 nm light were visible both in the absorption spectra and in the Western Blots.

This observation is relevant in the framework of dual-color PALM imaging, since any partial photoconversion of the Eos species stands in the way of an accurate and quantitative dual-color approach, requiring a precautionary bleaching step before the acquisition in the red channel in order to suppress any non-photoconverted molecules.

As far as Dronpa is concerned, neither the duration of the mEos2 acquisition phase (during which time it would be photoswitched to the *on*-state), nor the bleaching step (that would switch it to the *off*-state before commencing a sparse photoactivation cycle) should matter as far as a complete reversibility of the fluorophore holds. Multiple reports (e.g. [105]), however, as well as our experience, indicated that Dronpa loses a significant fraction of its fluorescence at each cycle. In addition, photodamage due to prolonged irradiation with 405 nm light is an additional source of concern. Although these considerations do not rule out the possibility of using Dronpa for the staining of dense structures, e.g. focal adhesions, they make it less promising for labeling sparser samples characterized by small aggregates, such as the membrane protein signaling aggregates that were one of the main subjects of this investigation. Figure 6.11 b, displays a bleaching curve for Dronpa under the prolonged irradiation of the typical 405 nm photoactivation power ($< 1\frac{W}{cm^2}$) required for mEos2 photoconversion. After 15 minutes, a relatively short time for PALM standards, the number of Dronpa molecules has decreased to $\frac{1}{e}$ of the original value. Figure 6.11 a shows a scatter plot of the number b^2 of background photons/pixel vs the total number N of signal photons/pixel overlaid to the contour plot showing localization precision isolines calculated according to $\sigma = \frac{s_a^2}{N}\cdot\left(\frac{16}{9}+\frac{8\pi s_a^2 b^2}{Na^2}\right)$. Dronpa molecules imaged in PAGE, despite the absence of autofluorescence background, display a relatively poor localization precision, most of the molecules localized with a σ between 20 and 30 nm consistent with the measured 28 nm of previous reports [8]. The poor localization precision adds to the bleaching problem, making it hard to localize all the fluorophores in the green channel.

After scoring for temporal clusters, the analysis at the single molecule level of the fusion construct (figure 6.12) displays that almost twice as many mEos2 molecules are typically localized than Dronpa molecules (in the case presented in figure 6.12, 129 mEos2 as compared to 76 Dronpa). Nearest neighbors distances allow to identify only 10 events corresponding to Dronpa to mEos2 euclidean distances below 200 nm, that at this dilution (the average intermolecular distance in a random sample of corresponding density is above 1 μm) can be identified as colocalization events. Therefore only 10 out of 76 events, i.e. around 13% of the minority species, appear to be co-localizations, indicating that

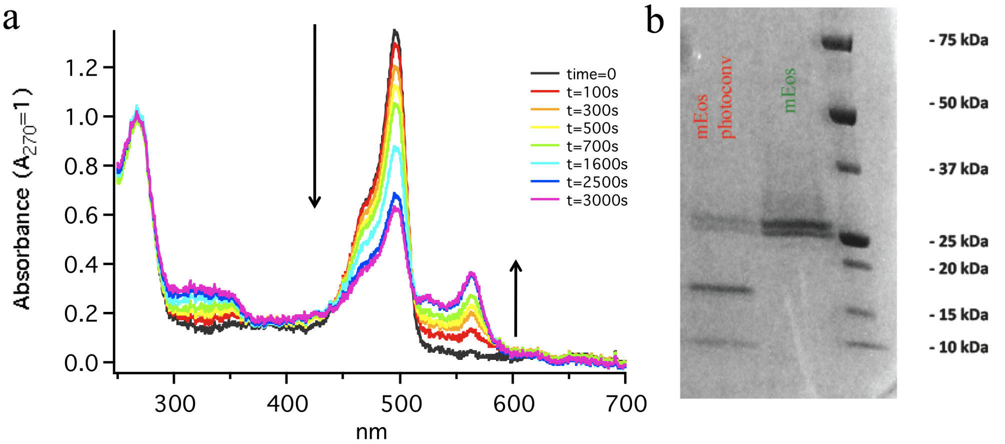

Figure 6.10: a) Evolution of the absorption spectrum of mEos2 upon 405 nm irradiation, at pH 7.9. It is important to notice that the photoconversion of the red form reaches a saturation before that the green form (488nm band) has completely disappeared. The ratio between the concentration of the green species and the red one at saturation is approximately 1.8. b) mEos2 bands before and after photoconversion (1h) in a Blue Coomassie 4-15% gradient denaturing gel.

a large fraction of each of the two fluorophores were not localized at all.

Experiments in cells, though following simultaneous transfection of two independent constructs (e.g. β2-mEos2 and G_s-Dronpa) yielded even less favourable results, with localization ratios of 15:1 in favour of mEos2. An immediate alternative is the PSCFP2-mEos2 pair, where instead of relying on the reversible photoswitching of the green protein of the pair, the much lower photoconversion efficiency of PSCFP2 can be exploited in order to achieve sequential imaging.

6.5.2 PSCFP2-mEos2

Among the PA-FPs developed thus far, PS-CFP2 [106] is probably one of the least characterized. Cyan to green photoconversion has the advantage of making this protein visible in the non-photoconverted state. However the same wavelength that excites (and bleaches) the non-photoconverted state also triggers photoconversion. We fused the genes of PSCFP2 and mEos2 one after the other, as detailed in Appendix C.

Figure 6.13 a, displays the time evolution of the fluorescence measured from PSCFP2 and mEos2 when imaged in TIRF on the plasma membrane of HeLa cells, subjected to the same amount of photoactivation light. Comparing the activation kinetics we see that by the time the red fluorescence from mEos2(R) has saturated, only 25% of the maximal PSCFP2 population has been photoconverted. It shall be noted that in this graph there is no information about the stoichiometry yet, and the curves are normalized to the maximal fluorescence observed for each species. Nevertheless this observation confirms that this combination can be used, to a certain extent, in a sequential dual-color approach; the only requirement is to perform a bleaching step to suppress the 25% activated PSCFP2 and the fraction of non-photoconverted mEos2 (as we saw in the previous section) before doing PALM in the green channel. PSCFP2(G) has an extinction coefficient similar to mEos2(G) (83%), but a much lower Q.Y. ~ 0.2, i.e. almost one quarter of mEos2(G). Therefore as a single molecule emitter it is outperformed by

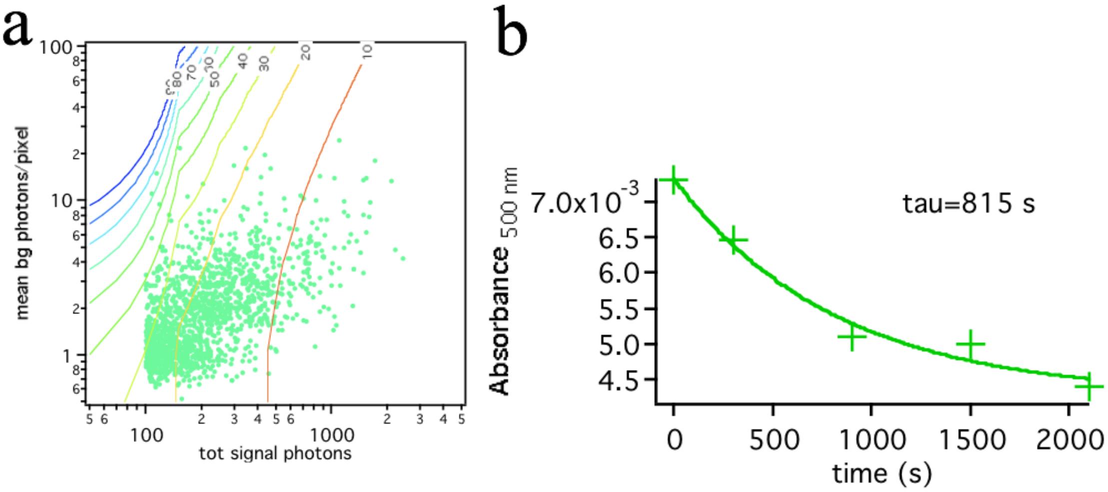

Figure 6.11: a) Contour plot of the localization precision of Dronpa in Poly Acrylamide immobilizing gel, displayed in a scatter plot showing total background photons/pixel vs total signal photons collected from the molecule. b) Bleaching of the fluorophore as a function of the irradiation with 405 nm laser light at typical irradiation powers used in PALM experiments.

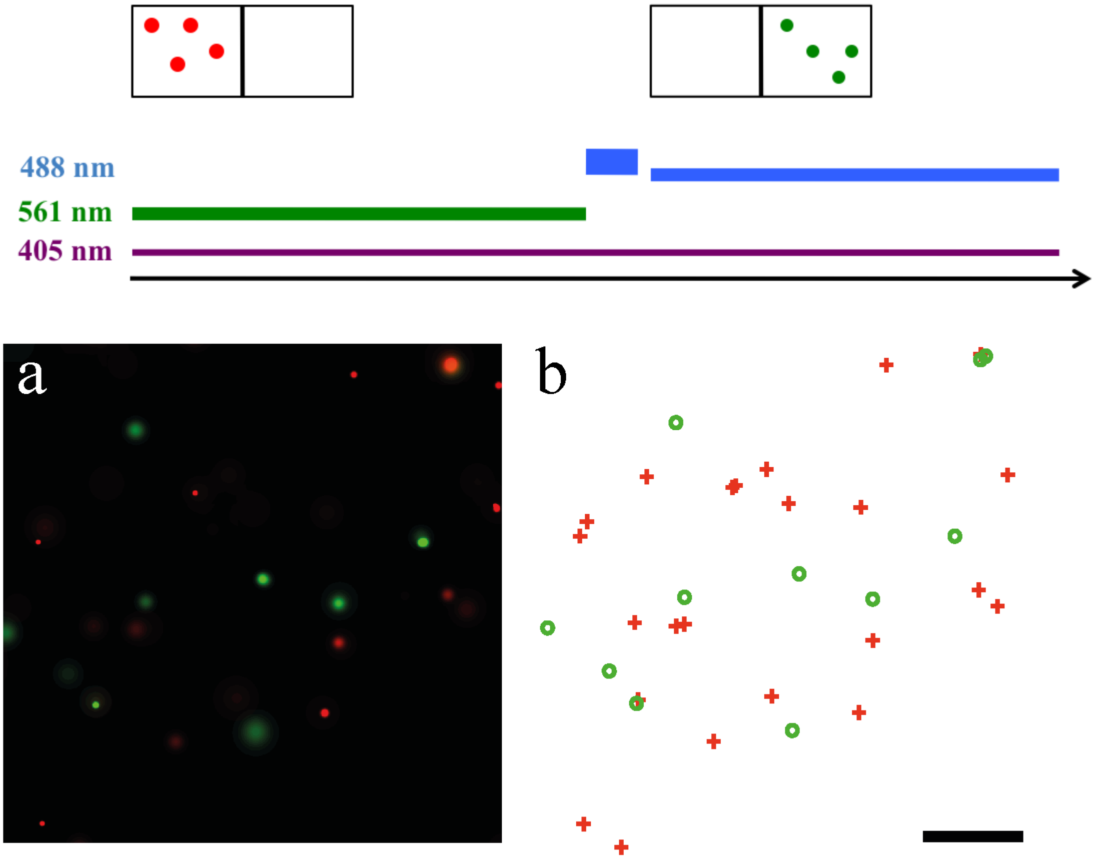

Figure 6.12: TOP: Cartoon showing the acquisition sequence for the mEos2-Dronpa pair. mEos2 molecules are activated and localized first, supplying both 405 nm and 561 nm laser lines. A bleaching step is then performed using the 488 nm laser, to remove the inactivated mEos2 molecules and switch-*off* Dronpa molecules. Imaging of Dronpa is then performed using moderate levels of 488 nm irradiation. BOTTOM: PALM image and corresponding map of the centers of the localized molecules image of the mEos2-Dronpa fusion construct in PAGE. Red crosses represent the localized positions of mEos2 molecules, whereas the green circles of Dronpa molecules.

mEos2.

However, in single molecule experiments performed using a high dilution of the fused construct in PAGE such as the one reported in figure 6.13 b, the amount of localized PSCFP2s molecules is greater than the number mEos2 molecules. We ascribe this observation to the saturation behaviour of mEos2 before full photoconversion occurs. Interestingly, the situation reverses for experiments performed at higher densities (Figure 6.13 c). When the acquisition time moves above a value in the order of tens of minutes, much less PSCFP2 molecules are localized than mEos2. Photobleaching of PSCFP2(C) is probably the main reason.

Steady state absorbance (Figure 6.14 a) of the purified fusion construct reveals that the efficiency in the formation of the chromophore is in favor of PSCFP2, with a 1:0.7 ratio to mEos2. Upon saturation of the activated form of mEos2, only a fraction of PSCFP2 has been photoconverted. After bleaching of the residual green fluorophores, photoactivation of PSCFP2 can be carried out until the number of localized single molecules saturates, as shown in figure Figure 6.14 b.

PALM experiments in vitro showed a negligible colocalization fraction, therefore confirming the observation arising from absorbance measurements that only a fraction of both species undergoes photoactivation and localization. Although this pair presents interesting perspectives, since the inactive forms of both proteins are fluorescent and can be exploited for other techniques prior to photoconversion, the imbalance in the photoactivation ratios reflected by the poor colocalization performance, prompted the search for a third pair. Since the photophysics of mEos2 proves a limiting factor towards a truly parallel acquisition, the next pair will use a new red photoactivatable fluorescent protein.

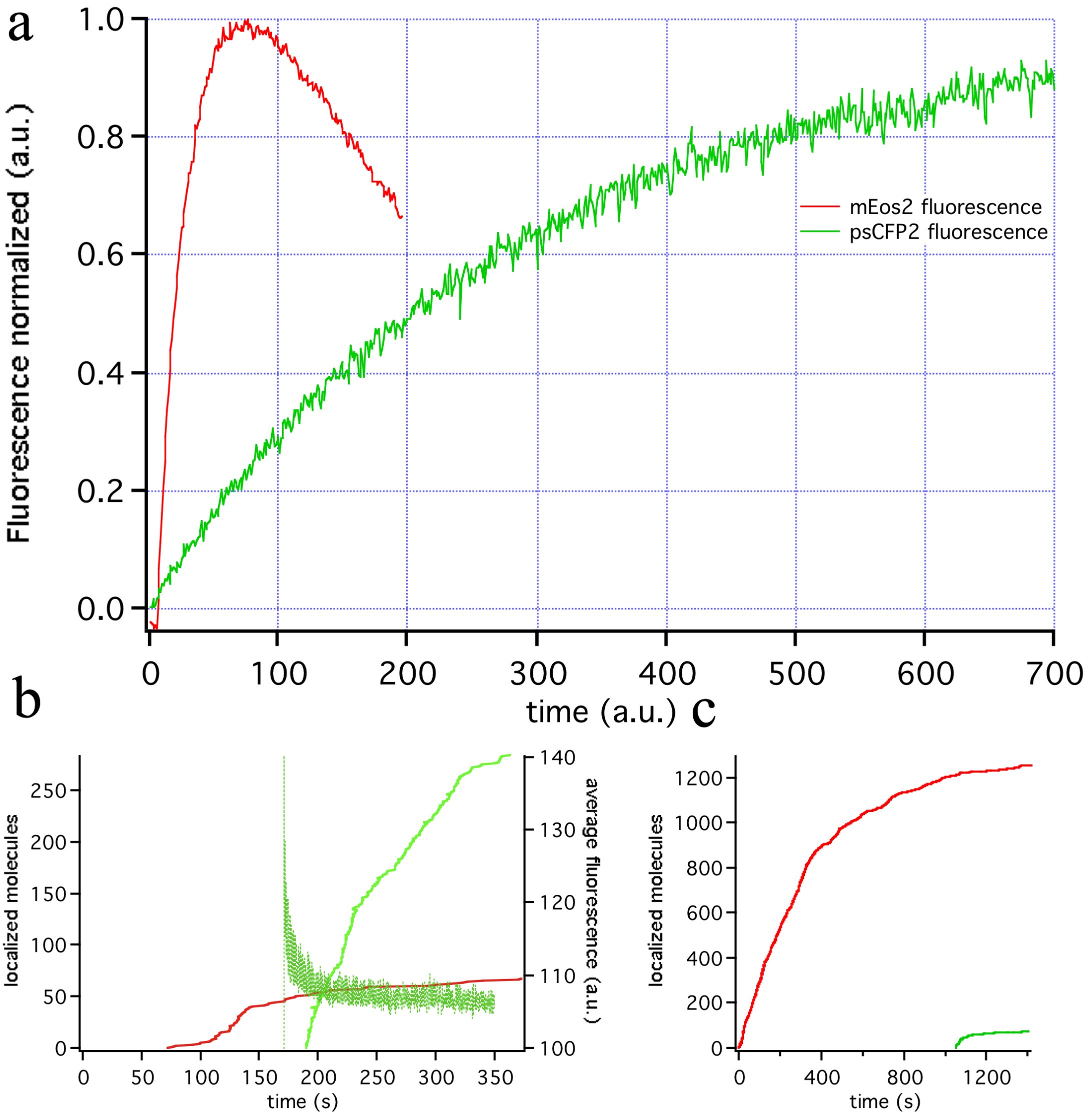

Figure 6.13: a)Evolution of the fluorescence signal of mEos2(R) and PSCFP2(G) imaged in TIRF under the same amount of photoactivation light (each curve was acquired on an independent sample). b) Number of mEos2 and PSCFP2 molecules localized in a Poly Acrylamide matrix upon 405 nm CW activation. After approximately 1000 frames the number of newly activated mEos2 declines, and at frame ~ 1700 a bleaching step is performed, as can be osberved by the exponential decay of the average fluorescence in the green channel. At frame 1900 the activation of PSCFP2 is commenced until saturation occurs, leading to a localization of approximately a fivefold amount of PSCFP2 as compared to mEos2. c) A prolonged exposure to 405 nm light to activate all of the mEos2 molecules results in the observation that the ratio of localized mEos2 to PSCFP2 reverses with respect to the previous example.

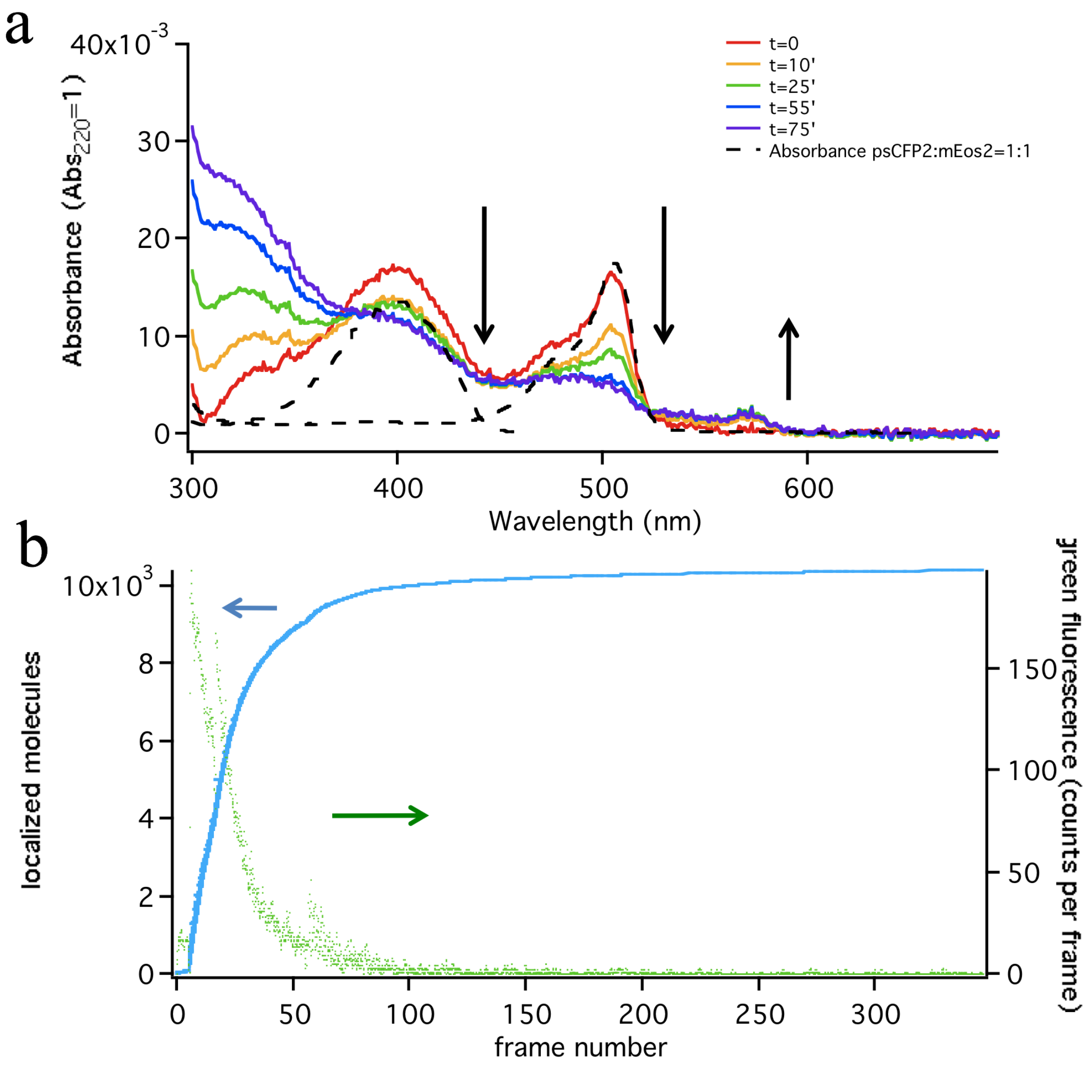

Figure 6.14: a) Absorption spectrum of PSCFP2-mEos2 fusion (after detrending to remove an exponential background). The evolution of the absorption spectrum is displayed in a color code up to 75 minutes of 405 nm irradiation, when no further increase of the absorbance of the mEos2(R) form is observed. The dashed line represents the theoretical PSCFP2-mEos2 spectrum (prior to photoconversion) at the expected 1:1 stoichiometry, normalized in order to match the peak mEos2(G) absorbance. An excess (1.3x) of PSCFP2 is observed. b) Photoactivation of PSCFP2 molecules after bleaching of the residual fluorescence in the green channel.

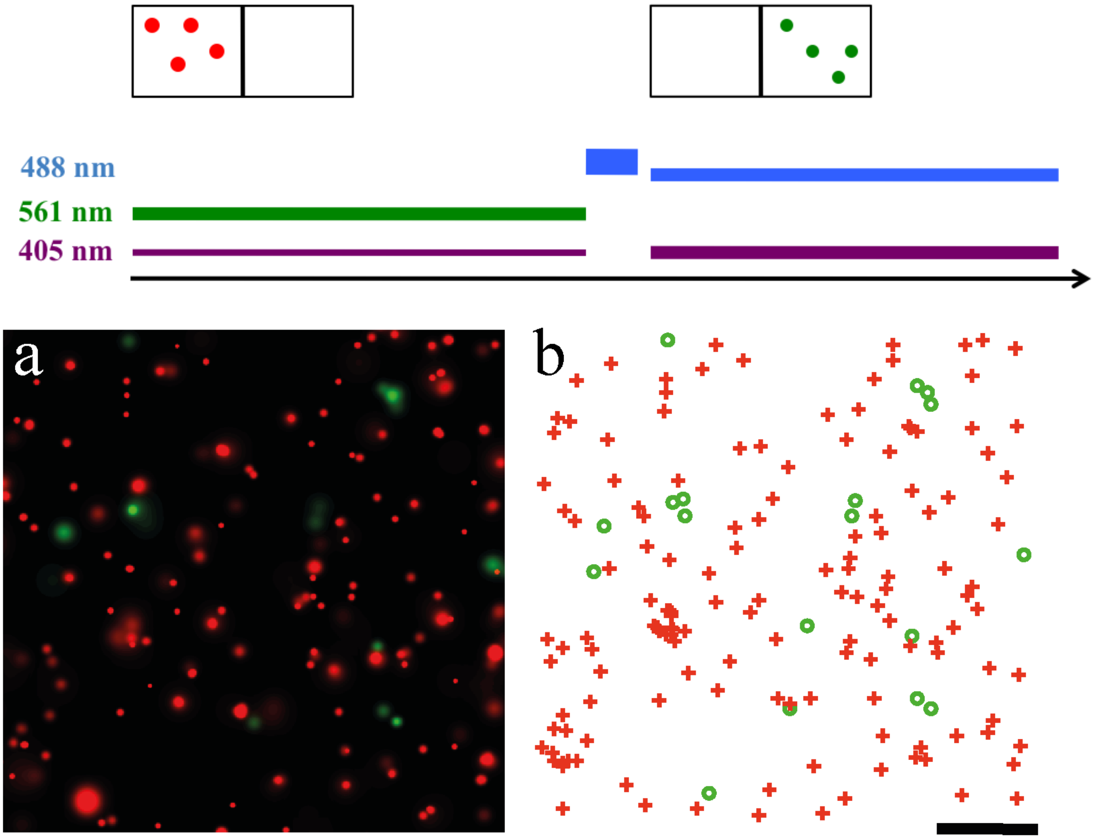

Figure 6.15: TOP: Cartoon showing the acquisition sequence for the mEos2-PSCFP2 pair. mEos2 molecules are activated and localized first, supplying both low level 405 nm and 561 nm laser lines. A bleaching step is then performed using the 488 nm laser, to remove the inactivated mEos2 molecules and the minority of PSCFP2 molecules activated. Imaging of PSCFP2 is then performed using moderate levels of 488 nm excitation and high levels of 405 nm activation power. BOTTOM: PALM image and corresponding centers of the localized molecules image of mEos2-PSCFP2 fusion construct in Poly Acrylamide Gel.

6.5.3 PSCFP2-pamCherry1

We investigated pamCherry1 as a possible replacement for mEos2 as a red partner in dual-color PALM measurements. pamCherry1 [89], developed by Lippincott-Schwartz and coworkers, is a photoactivatable fluorescent protein undergoing irreversible transition from a non emissive state to a red form upon the usual 405 nm irradiation. The obvious advantage of a non emissive *off*-state (as opposed to the green fluorescence of the mEos2 *off*-state) is that there will be no overlap at any time between the inactive form of pamCherry1, and the active form of PSCFP2. Investigation of the fusion construct in solution showed that, under the assumption of an initial 1:1 stoichiometry, the photoconversion efficiency of the two species is quite different. Approximately 58% of the pamCherry1 molecules photoconverts effectively, whereas PSCFP2 stops at 28%. These values can be readily extracted from the graph displayed in figure 6.16 by taking into account that:

$$\begin{aligned}
\frac{dB}{dt} &= -k_A \cdot C \\
\frac{dD}{dt} &= -k_C \cdot D \\
\epsilon_A \cdot A(t) + \epsilon_C \cdot C(t) &= Abs_{405}(t) \\
A(0) &= C(0) \\
A(0) &= \frac{Abs_{405}(0)}{\epsilon_A + \epsilon_C} \\
Abs_{405}(t) &= Abs_{405}(0) \cdot \left(\frac{\epsilon_A}{\epsilon_A + \epsilon_C} \cdot e^{-k_A \cdot t} + \frac{\epsilon_C}{\epsilon_A + \epsilon_C} \cdot e^{-k_C \cdot t}\right)
\end{aligned}$$

In addition, the photoactivation rate of pamCherry1 and PSCFP2 are markedly different. This results again in a semi-sequential mode of operation. Consistently with what we observed from absorbance measurements, during single molecule experiments in PAGE more pamCherry1 molecules are localized than PSCFP2 (4:1 ratio), though the localization precision of the two fluorophores is similar (figure 6.17 c).

In the single molecule colocalization experiments reported in figure 6.17 a, the colocalization ratio is around 15%, consistent with the $0.58 \cdot 0.28$ product expected from the photoconversion efficiencies measured by absorbance in solution. It should be also noted that pamCherry1 photoconversion is elicited also by 488 nm light. Therefore, the excitation wavelength for PSCFP2 should be brought on in steps, allowing for a sparse photoactivation of the pamCherry1 molecules.

The experiments performed in PAGE allow for a full control of the sample dilution. It is then possible to operate in a condition far from the super-resolution regime, e.g. where ~ one molecule per μm^2 is present, and therefore all pairs of fluorophores of different color falling within a distance of 200 nm one from the other can be considered with high likelihood as belonging to the same pair. As discussed in the introduction section, the distance between these two pairs may deviate from the root of the squared localization errors $\sqrt{\sigma_R^2 + \sigma_G^2}$ for multiple reasons, prominently the drift of the setup between the instants of localization of two adjacent molecules. We shall remember that this type of experiment is a form of asynchronous colocalization, since the time interval between the localization of two members of a heterodimer is stochastic.

Figure 6.17 d, displays the distance between the molecules part of a pair as a function of the temporal separation of their localization instant. Two populations are visible, one around 200 nm separation, the

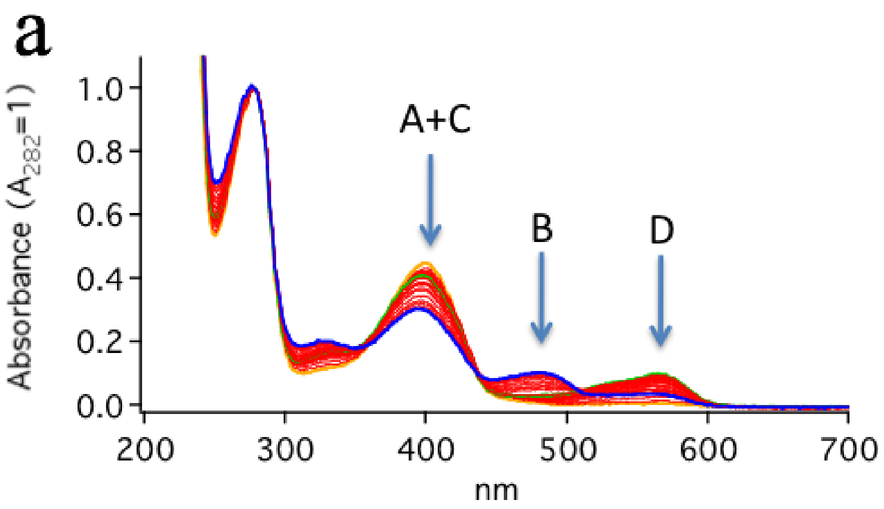

A=psCFP2 cyan [M/l], ε_a=43000 [$M^{-1}cm^{-1}$]
B=psCFP2 green, ε_b=47000 [$M^{-1}cm^{-1}$]
C=pamCherry1 dark, ε_c=6500 [$M^{-1}cm^{-1}$]
D=pamCherry1 red, ε_d=18000 [$M^{-1}cm^{-1}$]

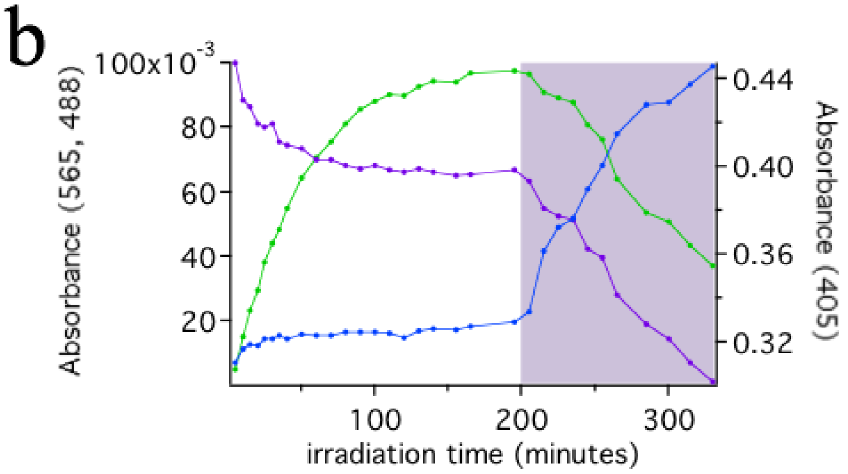

$A(0) = 1.6\ \mu M$
$D(\infty) = 930\ nM\ \eta_{pc} = 58\%$
$B(\infty) = 447\ nM\ \eta_{pc} = 28\%$

Figure 6.16: a) Ensemble spectroscopic characterization of PSCFP2-pamCherry fusion protein. Evolution of the absorption spectrum upon 405 nm laser light irradiation. Extinction coefficients for each species are quoted, and allow to reconstruct the final concentration of activated species. b) Evolution of the Absorbance in solution for the three main absorbance peaks upon 405 nm irradiation: 405 nm (purple), 488 nm (cyan), 565 nm (green). Shaded region corresponds to an increase of the 405 nm power.

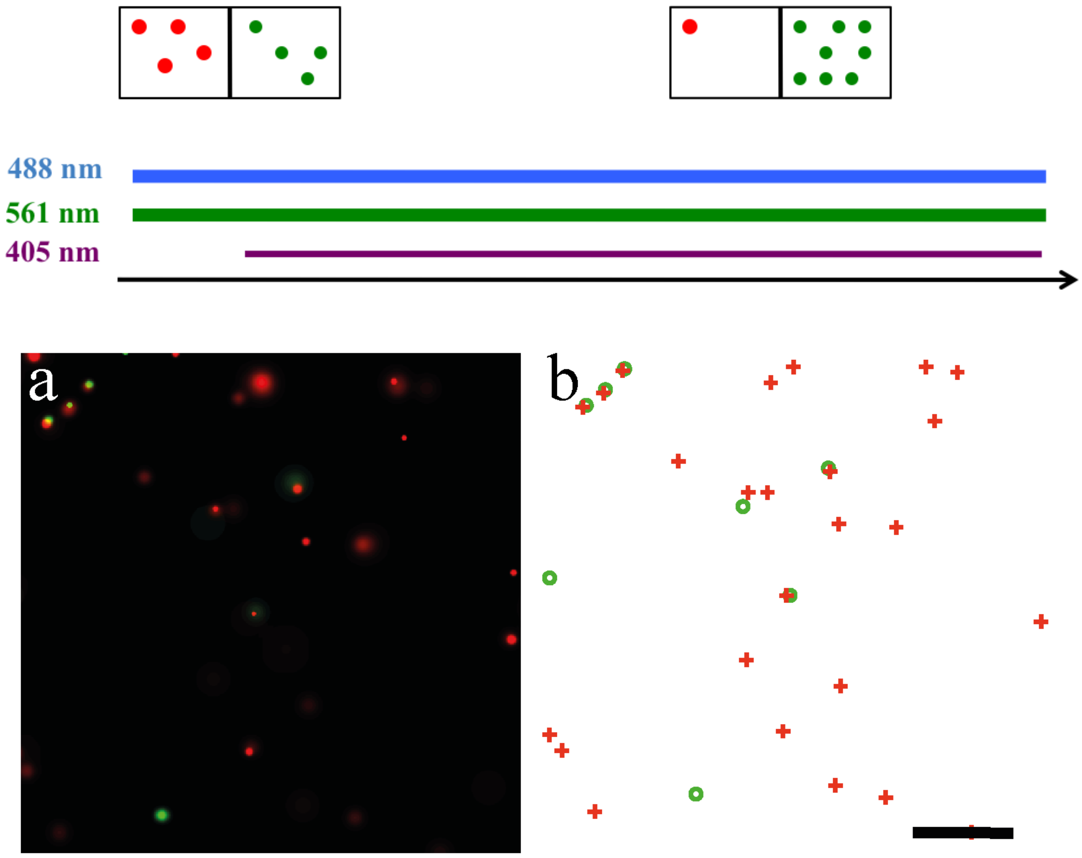

Figure 6.17: TOP: Cartoon showing the acquisition sequence for the pamCherry1-PSCFP2 pair. pamCherry1 molecules are activated and localized simultaneously with PSCFP2 molecules supplying both low level 405 nm activation and 488 nm and 561 nm excitation lines. Low level 488 nm irradiation is already sufficient to activate pamCherry1 molecules. The higher photoactivation threshold for PSCFP2 will determine a semi-sequential mode of acquisition. BOTTOM: Single molecule characterization of the PSCFP2-pamCherry1 fusion construct. PALM image of a dilution of PSCFP2-pamCherry1 molecules in a Poly Acrylamide matrix and corresponding map of the centers of emission of each localized fluorophore.

other one where the particles are separated below 50 nm. We attribute the population with the larger deviation to molecules suffering a residual diffusion within the pores of the PolyAcrylamide gel. On the other hand, the group of molecules localizing within 50 nm provides us with two important informations: first there is no significant drift of the colocalization as a function of time, indicating that the overall stabilization of the setup is effective. Second, the fact that the colocalization distances fall below 50 nm indicates that the setup is operating close to its *registration* limit. If we consider an average localization precision for both PSCFP2 and pamCherry1 of 25 nm, then the term $\sqrt{\sigma_R^2+\sigma_G^2+\sigma_{registration}^2}$ yields approximately 35 nm, in good agreement with our experimental points.

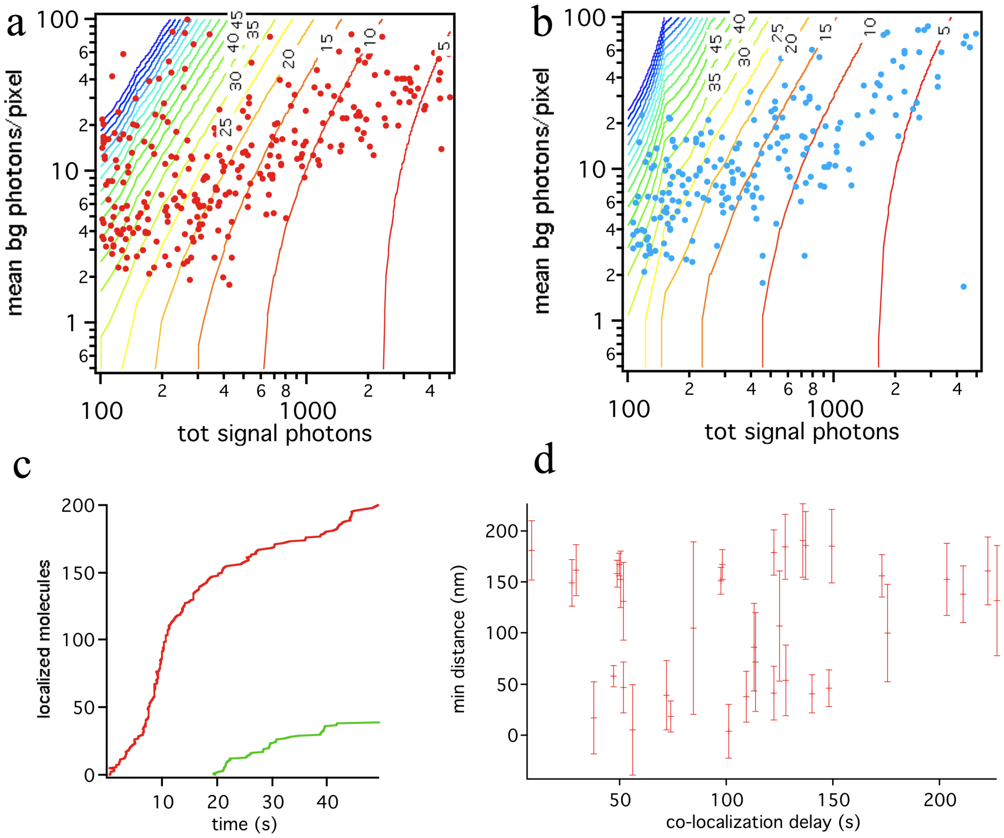

Figure 6.18: Contour plot of the localization precision of a) pamCherry1 and b) PSCFP2 showing total background photons/pixel vs total signal photons collected from each molecule. c) Number of molecules localized in each channel as a function of time (s). d) Intermolecular distance between co-localized molecules as a function of the temporal delay between localizations.

In conclusion, the combined use of absorbance spectroscopy and single molecule experiments on fusion constructs of pairs of photoactivatable fluorescent proteins, has enabled us to obtain information about the photoconversion efficiencies of each of the probes and therefore about their performance in dual-color PALM experiments. As we have seen in sections 6.5.1 and 6.5.2, when using a sequential pair of fluorophores that has an original defined stoichiometry, (e.g. 1:1 in the fusion constructs), the actual number of fluorophores to localize, and therefore the duration of the experiment, will determine the final stoichiometry. This is illustrated in figure 6.19, where we can observe that the combined effect of photobleaching and photoactivation of PSCFP2 while imaging mEos2 will determine the size of the remaining pool of inactivated PSCFP2 molecules.

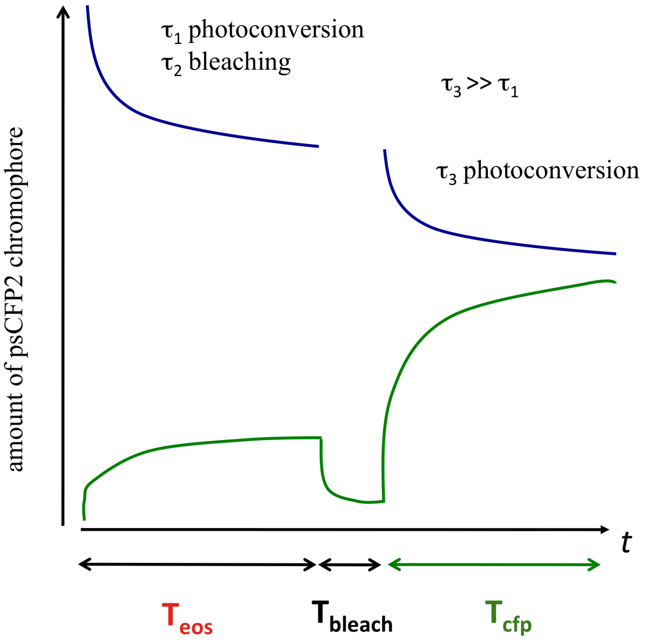

Figure 6.19: Evolution of the number of PSCFP2 fluorophores in a sequential dual-color experiment. The amount of PSCFP2 in the non-photoconcerted form (blue) decays during the mEos2 photoactivation and localization step due to both photoconversion and bleaching. A bleaching step is required to remove the pool of activated PSCFP2 molecules before beginning the photoactivation and localization step in the green channel.

The results of the photoconversion efficiencies and of the colocalization efficiencies can be found in table 6.2. In the light of these measurements we propose PSCFP2-pamCherry1 as the pair of choice towards dual-color imaging in PALM. .

fused fluorophore pair	long wavelength fluorophore (R) η	short wavelength fluorophore (G) η	colocalization fraction[1] (% of minority specie)
Dronpa-mEos2	53%	n.d.	13% [2]
PSCFP2-mEos2	53%	23% [3]	0 [4]
PSCFP2-pamCherry1	28%	58%	15%

Table 6.2: Photoconversion efficiencies for the three pairs of PA-FP investigated so far.

---

[1] defined as the number of fluorophore pairs falling within a 200 nm radius in a diluted sample

[2] this value depends on the number of mEos2 molecules to localize

[3] after bleaching step

[4] this value depends on the number of mEos2 molecules to localize

6.6 Dual-color imaging using PSCFP2-pamCherry1

In the previous chapters the use of the signaling response of a prototypical GPCR, in particular the internalization mechanism, as a tool to modulate the level and lengthscale of its aggregation on the plasma membrane was discussed. The obvious extension to dual-color imaging of this concept, and of the considerations that were developed regarding the correct identification of clusters, can be developed by imaging one of the partners of the receptor during the internalization process.

The obvious partner to use in this analysis is one of the proteins responsible for the formation of the endocytic vesicles, and our choice fell on clathrin. The use of clathrin as a dual-color partner in PALM experiments was first reported [89] in fusion to PAGFP for colocalization experiments with transferrin receptor (TfR is needed for the import of iron into the cell and is regulated in response to intracellular iron concentration: it imports iron by internalizing the transferrin-iron complex); Jones *et al.* [107] fused clathrin light chain to mEos2, and observed it in STORM mode together with TfR. Clathrin (see [108] and references therein) is the main protein of the coat surrounding the plasma membrane vesicles responsible for mediating the sorting and intracellular transport of membrane bound proteins. Clathrin was baptized after the chemical compound clathrate, given the basket-like appearance of the latter. As a matter of fact each clathrin has a triskelion (three legged) shape, each leg composed of a heavy polypeptide chain (chc) and one light chain (clc). Each leg has an L shape, the shorter segment forming the distal end of the leg, the longer segment fusing with the other two heavy chains at 120^o angle in a vertex. In the presence of membrane bound adaptor proteins the triskelia self-assemble in a basket-like structure, forming an hexagon mesh that surrounds and guides the membrane vesicle budding. Clathrin coated vesicles represent the main pathway for receptor mediated endocytosis, (for a recent review on the subject, see [109]), mainly upon stimulation regulated by an external agonist.

Signaling receptors such as GPCRs are one important cargo of clathrin coated vesicles, and they tend to internalize rapidly after stimulation and interaction with the adaptor proteins arrestins. Although PALM can provide only a fixed-time snapshot of the internalization process, i.e. a static information of a very dynamic process, a non-negligible degree of colocalization between receptor aggregates and clathrin should be observed in cells fixed after stimulation with an agonist. The internalization process is normally very rapid, and the residence time [51] of membrane clathrin-receptor complexes for GPCR is demonstrated to be typically in the range of 30 s-40 s; this value can increase up to above 70 s only in the presence of interactions with the actin cytoskeleton mediated by proteins possessing a PDZ motif. As we have seen the $\beta2$ receptor is one of the GPCRs possessing such PDZ-binding domains, and its permanence in membrane clathrin coated pits is therefore expected to be longer than average.

As we have extensively discussed in the previous chapters, identification of clusters should carefully take into account the potential presence of blinking-induced artifacts. We therefore treated the dual color images reported in this section selecting clusters based on a density threshold and then scoring them according to the protocol illustrated in figure 5.9, chapter 5. $\beta2$ receptors were labeled with PSCFP2, whereas clathrin light chain fused to pamCherry1 was used (kind gift of Mr. M. Davidson). For each species, after the clustering threshold, the information about two subgroups of molecules is available: on the one hand those molecules that are part of clusters, and on the other hand all the molecules (including the centers of mass of temporal clusters) that compose the so called monomer fraction. The first group can either be displayed alone to provide a selective image of only the physical clusters present in the sample, a strategy already employed by Jones *et al.* [107] or merged with the monomer fraction in order to obtain an artifact free PALM image.

Compared to ensemble statistical methods to identify clustering parameters devoid of blinking effects

[73] this strategy has the obvious advantage of providing an actual image, reconstructed without those clusters arising exclusively as photophysical artifacts. Figure 6.20 illustrates this concept, showing respectively the TIRF image of a HeLa cell expressing β2-adrenoreceptors and clathrin, the original PALM picture, the PALM picture corresponding to the clustering fraction and finally the recombined monomer and clustered fraction to provide an artifact free image.

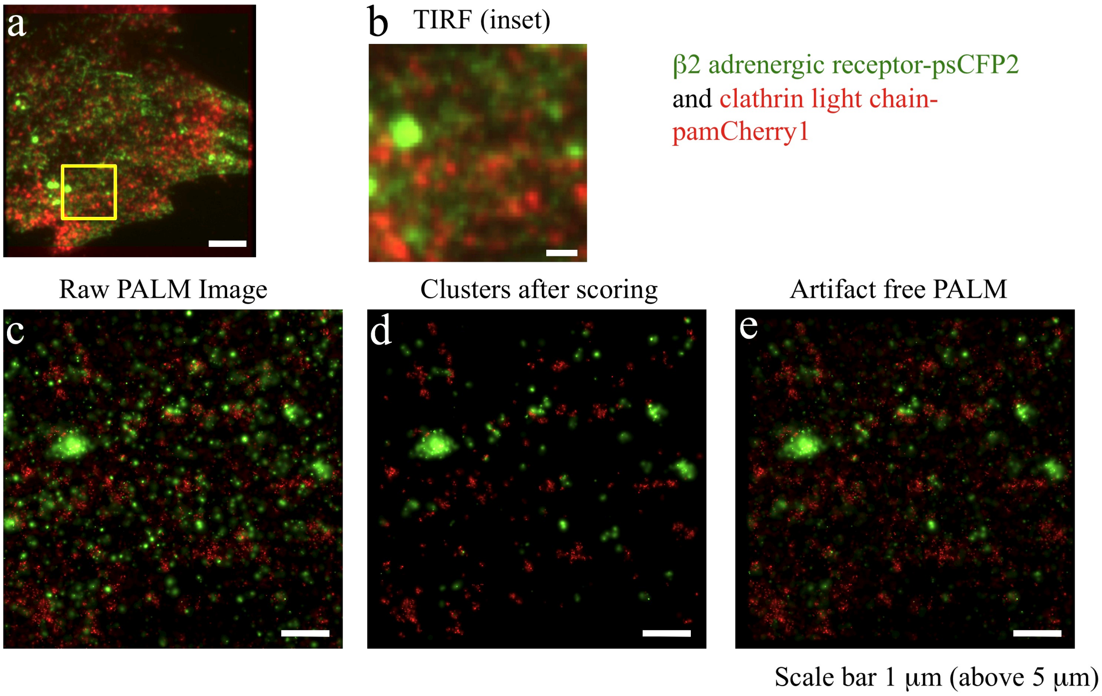

Figure 6.20: Dual-color artifact free imaging of a pair of membrane proteins. a) TIRF image of an HeLa cell expressing β2-PSCFP2 and CLC-Cherry (after an intense photoactivation pulse). b) Inset showing a relatively featureless surface aside from a large vescicle containing β2-PSCFP2 molecules. c) Raw PALM image showing a texture of small clusters, in particular green β2-PSCFP2 clusters. d) PALM image after suppression of the so-called temporal clusters. e) Artifact free PALM image obtained recombining the artifact-free PALM image with the monomeric fraction localized in the experiment.

Figure 6.21 a, displays an artifact free PALM image of the membrane of a HeLa cell expressing the two constructs β2-PSCFP2 and clc-pamCherry1 in basal conditions. Panel b shows the corresponding map of the localized fluorophores in both channels. Two clusters are arbitrarily selected and markers representing the molecules were color coded according to the instant of temporal localization: the molecules in each cluster obey the condition of temporal non correlation, and are therefore confirmed to be true molecular clusters. The insets, from one to three, outline colocalization events between the receptor and the clathrin clusters. Aside from this few colocalizations, most of the β2-AR clusters do not seem to be associated to clathrin pits, in agreement with the observation that constitutive endocytosis can be clathrin independent [110].

Figure 6.22 displays the dual-color TIRF and PALM images of a region of the plasma membrane of a HeLa cell after stimulation with the agonist isoproterenol. Panel a displays a DIC image together with the overlay of the region imaged in PALM. Small puncta corresponding to the clathrin coated

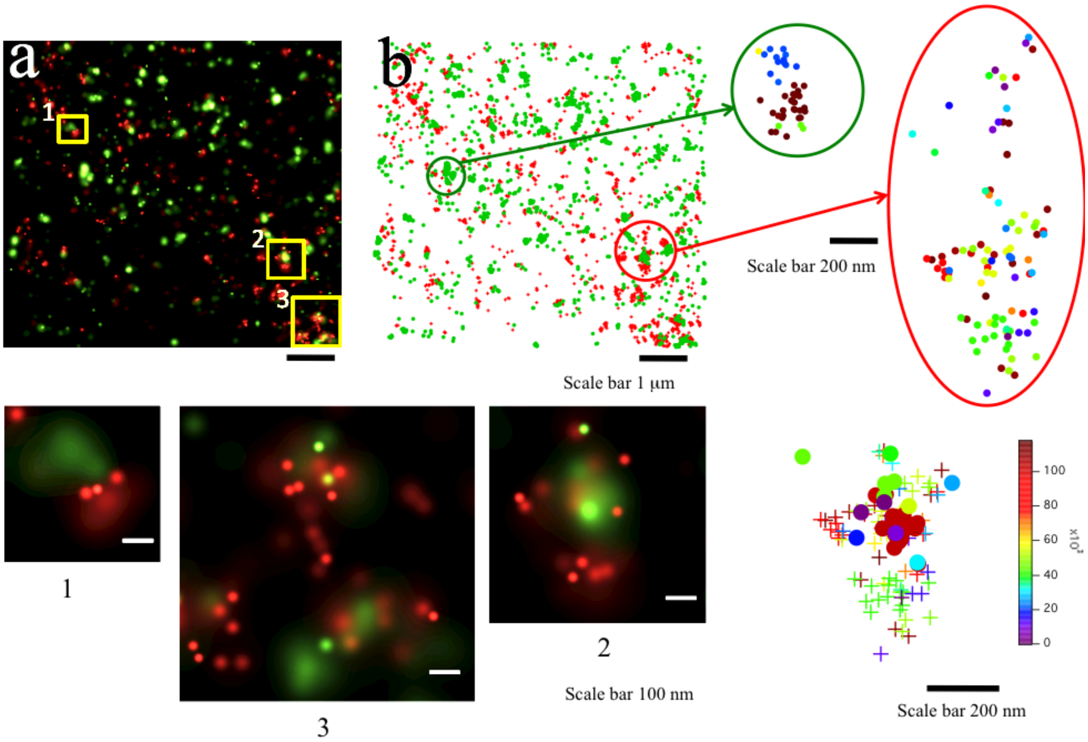

Figure 6.21: a)PALM image of the β2-AR undergoing constitutive intrnalization through clathrin. Both clathrin and β2-AR clusters are visible, and in a number of instances (e.g. insets 1, 2 and 3) they do overlap. b) Map of the centers of emission for each localized fluorophore. Color coding reflects the moment of localization of each molecule.

vesicles are visible already at this resolution level. Panels b and c display respectively the red and green TIRF images of the region within the square in a, and panel c displays the overlay of the two channel TIRF images. A large amount of aggregates in both imaging channel is visible, with some evident colocalization events. Panel d displays the corresponding dual-color raw PALM image. A much clearer picture emerges from the PALM image displaying only the clustered fraction and the corresponding map of the localized fluorescence centers (panels e and f). More than ten clathrin coated vesicles are detectable, and approximately five of them are clearly associated to $\beta 2$ clusters. An inset showing one of these colocalization events is displayed in panels g (TIRF) and h (PALM). The fact that half of the clathrin coated pits are associated to receptor clusters, a result in agreement with the observation from Puntanveedu *et al.* [51] that GPCR internalization occurs preferentially through a subset of clathrin coated vesicles.

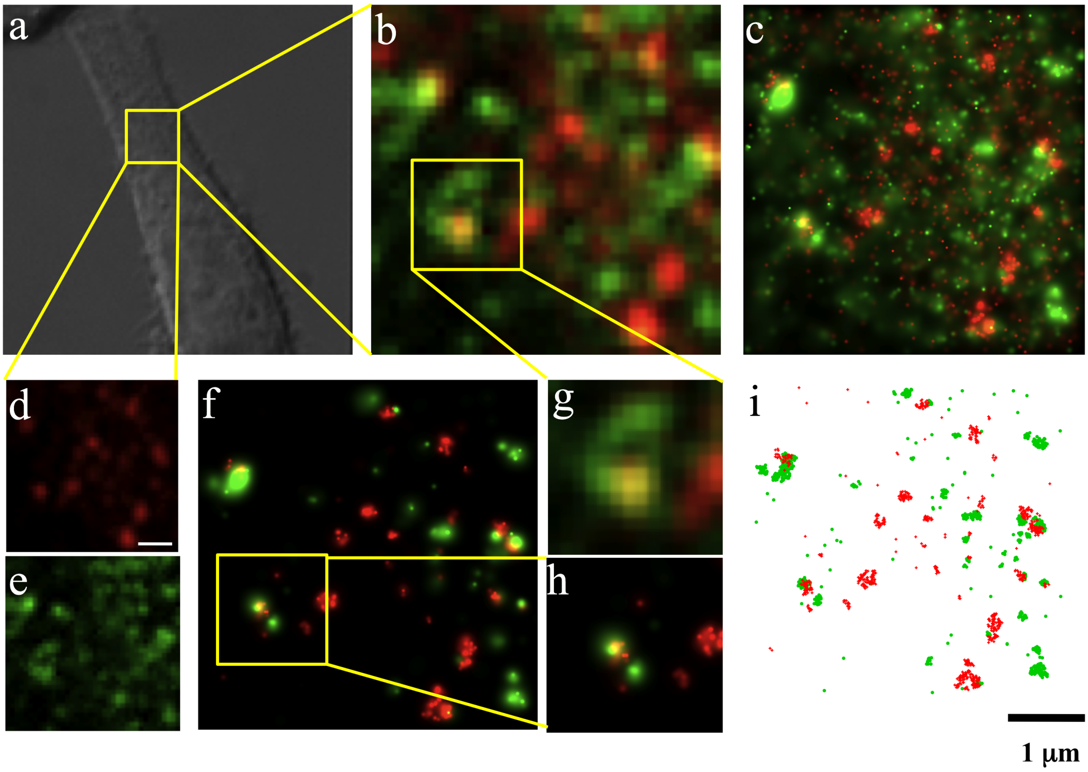

Figure 6.22: a) DIC image of HeLa cell and overlay of red channel PALM image showing clathrin coated pits on the plasma membrane. b) and c) TIRF green and red channels of the selected region in a. d) dual-color TIRF image of the region selected in a. e) raw dual-color PALM image of the region corresponding to d). f) Dual-color PALM image of the clustered fraction only g) localized map of the position of each fluorophore in both channel corresponding to f). h) and i) show a detail of a colocalization event between a clathrin coated pit and a $\beta 2$-AR cluster in TIRF and PALM (clustered fraction) respectively.

6.6.1 Protein fixation

One important point that was not discussed up to now is the assumption that the cell under observation can be frozen in a definite configuration by means of chemical fixation. The most commonly used fixatives in cell biology are aldehydes, most notably paraformaldehyde and gluteraldehyde. Paraformaldehyde, the polymer solid state form of formaldehyde (CH_2O, a gas, IUPAC name methanal), is exploited as a chemical fixative given its ability of binding amino groups, abundant in proteins, connecting them through what is known as a cross-linking methylene bridge. The other powerful fixative, introduced to satisfy the needs of electron microscopy towards the preservation of ultra-structures in biological specimens (cells or tissues) is gluteraldehyde (IUPAC Pentane-1,5-dial). Gluteraldehyde also possesses aldehyde groups on both ends ($COH-(CH_2)_3-COH$), that can bind amino groups. Free aldehyde groups need to be blocked, to avoid unwanted reactions (e.g. with antibodies during immuno-staining) and the formation of a fluorescence byproducts through a reaction involving Schiff bases [111]. This unwanted fluorescence can be quenched (i.e. the fluorescence amount decreased) by repeated washes with amino acids rich in nitric groups (e.g. lysine), the protein Bovine Serum Albumin or the compound Sodium Borohyrate (IUPAC Sodium tetrahydridoborate).

Typically, the slower acting paraformaldehyde is complemented by the addition of gluteraldehyde, to speed up the reaction and achieve a better fixation, in particular of membrane proteins. It has been demonstrated that unless gluteraldehyde is used, a significant fraction of both membrane anchored or transmembrane proteins tend to remain mobile [63]. An even more relevant question to PALM is how rapidly the fixation takes place, and how much time elapses before the majority of the molecules reduce significantly or halt their (membrane) diffusion. The answer to this question is crucial to establishing to what degree PALM can be used to observe transient highly dynamic interaction phenomena, upon observation of a frozen snapshot.

We addressed this question by means of single particle tracking, a growing field based on the localization in space of individual single particles (typically fluorescent molecules) at different instants of time to reconstruct a discrete trajectory. PALM, in one of its variant, namely sptPALM [112], is advantageous towards this goal since it allows to generate multiple sequential subsets of molecules by photoactivation, allowing on one hand to perform tracking in condition of sufficient dilution in order to be able to univocally identify individual traces, and on the other one to collect enough statistics from an individual cell. The tracks can then be used to investigate the diffusional properties of a molecular species, or to probe the heterogeneity of the local environment.

We performed tracking using the ImageJ plugin developed by the Mosaic Group (ETH Zurich, Switzerland) [113], obtaining for each sample a set of single molecule traces. Individual traces were analyzed using the method proposed by Schutz and Schmidt [114]. This approach allows to extract the average mean square displacement from a group of trajectories, fitting the cumulative probability distribution function of the square displacements. $P(r^2,t) = 1 - e^{-\frac{r^2}{r_0^2}}$ for pure single molecule diffusion, but the distribution can be easily extended to a two component diffusion (e.g. mobile and immobile fraction, fast and slow) to properly take into account the presence of multiple species. In this case $P(r^2,\alpha,t) = 1 - (\alpha e^{-\frac{r^2}{r_1^2}} + (1-\alpha)\cdot e^{-\frac{r^2}{r_2^2}})$. We performed PALM measurements on living cells, dividing our acquisition into three subgroups; one containing all frames prior to fixation ($t = 0$), the second containing the frames collected between $t = 0$ s and $t = 60$ s, and the third one with the frames collected between $t = 60$ s and $t = 120$ s. We extracted the parameter α, corresponding to the mobile fraction from fitting the two component function.

Figure 6.23 displays the mobile fraction at different lag times, for the three sub-sets of our dataset. The mobile component α prior to fixation and calculated from the fit amounts to 75% of the total traces, decreasing to 45% after an average of 30 s, indicating that only 40% of the mobile molecules was immobilized after 15 s incubation with the fixative mix. Considering that, given the typical diffusion coefficient of a transmembrane protein is in the range of $0.1 \frac{\mu m^2}{s}$ and the MSD scales as $< r^2 >= 4 \cdot D \cdot t$ we obtain a $< r^2 >$ in the range of 6 μm^2. After an average of 90 s, and a mean square displacement of 18 μm^2, 33% of the originally mobile molecules are still diffusing. A transient cluster, such as the clathrin coated vesicle at the plasma membrane, or a small receptor aggregate resulting from the temporary response to a stimulus, would be clearly blurred out or dissolved before complete fixation has occurred.

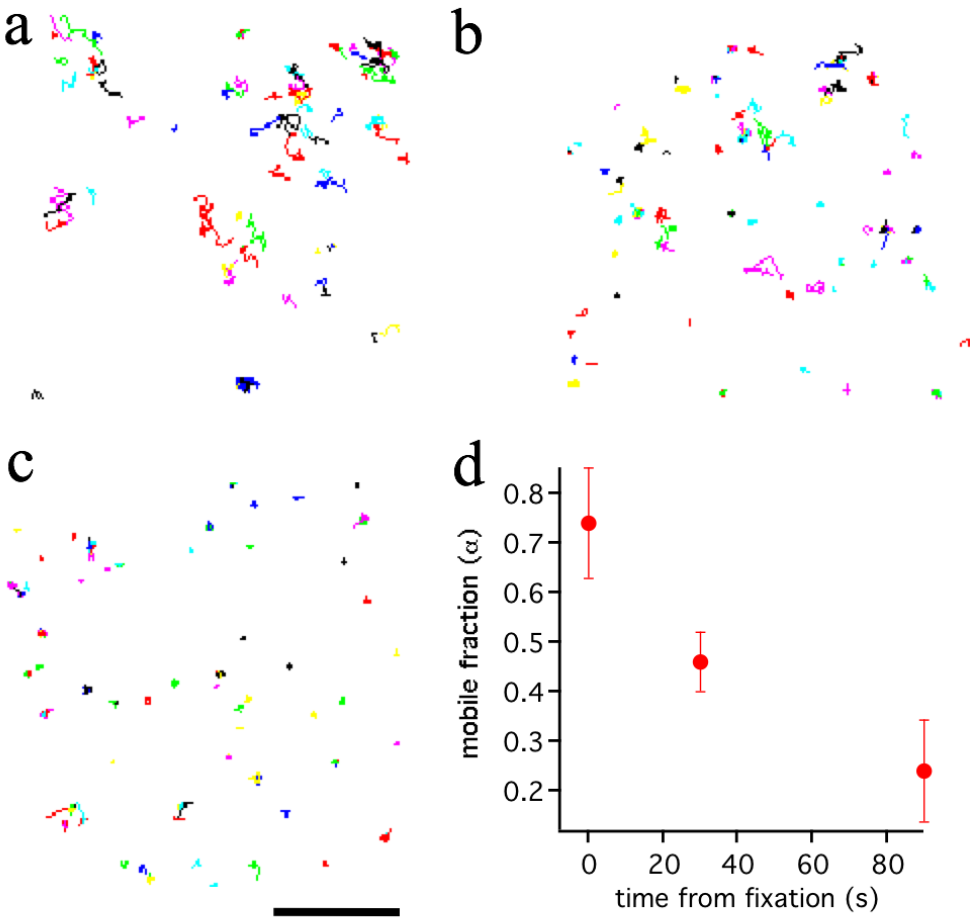

Figure 6.23: a) β2-mEos2 traces before fixation on the plasma membrane of a HeLa cell. b) After an average of 30 s after fxation. c) After an average of 90 s after fixation. Scale bar 5 μm. d) Evolution of the mobile fraction of β2-ARs on the plasma membrane of a HeLa cell α as a function of the time from fixation.

6.7 Discussion

In this perspective chapter we investigated some of the key technical steps and associated challenges encountered in multicolor super-resolution localization microscopy. We proposed an active stabilization mechanism based on a totally internally reflected laser line to compensate the effect of axial drift, enhance long term stability (< 5 nm) and to take full advantage of the registration accuracy of the setup. We identified the limit to the registration accuracy of our stabilized widefield setup over time, finding an effective registration precision systematically > 10 nm.

We reviewed in the introduction of this chapter that multiple strategies now exist towards multicolor super-resolution microscopy besides PALM, and they do not necessarily rely on the use of photoactivatable fluorescent proteins. However, PALM still stands its ground as far as it requires a minimally invasive sample preparation and guarantees that each protein of interest is targeted by only one genetic label. Therefore the quest for more efficient fluorescent proteins pairs for dual-color photoactivated localization microscopy remains an important research objective, and in this chapter we tried to address it by investigating the performance three pairs of photoactivatable fluorescent proteins.

We reviewed the original dual-color PALM pair Dronpa-mEos2, the more recent mEos2-PSCFP2 and finally we settled on the pair pamCherry1-PSCFP2, reporting an application that developes the path outlined in chapter 4 about the clustering of the β2-AR during clathrin dependend endocytosis, keeping an eye on the rejection of those clusters that clearly arise due to photophysics. We concluded this chapter with the observation that the requirements for long term stability do not apply only to the setup, but also to the sample itself. We investigated the diffusional properties of the β2-AR after fixation, observing that the immobilization of membrane bound proteins is a surprisingly slow process.

The conclusion that can be drawn from these experiments highlight the significant challenges that PALM and similar techniques face in relation to dual-color imaging if they want to stand up to the definition of super-resolution methods also in multicolor mode. The origin of certain limitations, such as the registration precision larger than 10 nm, is not obvious. Registration accuracies below 1 nm were demonstrated only in particular conditions, in vitro and over limited field of views (one pixel) [91]. The use of fusion constructs to identify the best candidate among the possible combination of PAFPs is also an approach that yielded interesting information about the final stoichiometries that can be achieved with these constructs. The couple pamCherry1-PSCFP2 is the only pair that does not require sequential imaging, maximizing the speed and at the same time increasing the quantitative outcome of the molecular counting process. The combination of a > 10 nm registration precision, ~ 20 nm localization precision and $\sim 60\%$ photoconversion efficiency in the best case effectively rules out the use of PALM to probe heteroligomerization processes quantitatively. However, co-clustering of larger and denser structures is a promising avenue. Co-clustering of β2-AR and clathrin is a promising control, but further studies should certainly address the relation between this receptor and the actin cytoskeleton in H9C2 cells, to answer some of the questions raised in chapter 5.

7 Conclusions and Perspectives

7.1 Conclusions

The first part of this thesis describes the construction of a PALM setup, and chapters 1 and 2 provide an introduction to the method in the framework of single molecule spectroscopy. The rest of the thesis addresses a number of issues motivated by a key question: to what extent is it possible to count proteins using PALM?

The first problem that we tried to solve is the one left open in the original publication by Betzig *et al.*: how to determine if two neighbouring molecular peaks, separated in time, should be localized independently or together? The authors foresaw a possible solution in the development of more photostable and controllable probes, while adopting a purely empirical standard based on allowing for a short dark time to regroup fluorescent traces.

To address this problem we explored the connection existing between single molecule fluorescence dynamics and PALM. We elucidated this connection by moving away from the super-resolution regime (many molecules in a small region of space) to an isolated single molecule regime (just one molecule). We studied in detail the single molecule fluorescent behavior of mEos2, the brightest, and most recent photoactivatable fluorescent protein available when this research began. Chapter 3 highlights that the behavior of mEos2 obeys to a quite general mechanism of reversible switching, shared with many other fluorescent proteins, making therefore the choice of mEos2 not only conventient, but also representative.

In the ideal case of an *off* to *on* to *bleach* behavior, any PALM measurement would intrinsically be also an accurate counting experiment. However, given the properties of individual probes, we saw that this is not the case, and the resulting number will depend on a combination of parameters including the average number of switching cycles that a molecule can do, the average duration of its *off*-times, the molecular density of the sample and the rate of photoactivation. We observed that the number of counted molecules decays exponentially as a function of how much time it is allowed for a molecule to go dark without bleaching, the parameter t_d used throughout this thesis. Changes on this parameter in the data analysis determine a shift from a multiple counting to a missed counts regime, and the resulting appearence of the PALM image. We demonstrated that, by studying the counts vs t_d curve of a given experiment, it is possible to calculate the average of the number of blinking molecules photoactivated and localized in the field of view.

However, this strategy, extensively discussed in chapter 3, leaves an important question unanswered: how to be sure of the proper identification of oligomers and clusters in the presence of a blinking probe? An oligomer (or cluster) is defined as such only if the number of its components can be properly identified, that is, counted. Clearly, ensemble averaging methods, even including those recently published [73], do not help in addressing this problem, since the repeated blinking of even just one molecule, e.g. 10 times, will result in an observed cluster, and therefore a structure with a biological significance.

For this reason we introduced the idea of looking at the temporal correlation of the localization events presented in chapter 4. To validate this approach in a relevant biological context we exploited the properties of β2-AR, a member of the very well studied family of GPCRs. The long time response to agonist stimulation was exploited to generate clustering on the plasma membrane, that was then compared to a negative control, i.e. a molecule distributed as a monomer. From these experiments we gained a significant insight into the potential of this technique to explore aggregation into clusters of 10-100 molecules and in a density regime of 10-200 molecules $/\mu m^2$. Although PALM was originally conceived to investigate densely labeled sub-diffraction limited structures, in our opinion such a low density regime is also one of the most promising applications of this method.

The study of the temporal correlation of individual clusters of labeled membrane proteins can be further used to generate spatial point patterns containing the coordinates of each localized molecule and devoid of any photophysical artifact. We applied this approach in chapter 5 to study the interesting problem of the basal distribution of β2-AR comparing two important cell lines. The systematic comparison to a negative control was instrumental to identify clustered aggregates in H9C2 cells as compared to HeLa. These clusters, containing on average 15-20 molecules and having a diameter comprised between 50 and 200 nm appeared to be disrupted by the inhibition of the polymerization of the actin cytoskeleton. This is one of the first quantitative applications of an optical super-resolution method to a member of the important GPCRs family.

The immediate next step, namely the high resolution co-localization of two or more species raises a few interesting issues that chapter 6 tries to address. What is the effective registration accuracy that can be achieved using a wide field optical setup, using commercial components and under normal operating conditions? The observation that the registration accuracy is inferiorly bound to 10-15 nm, paired to the fact that the typical localization precision falls in the ~ 20 nm range, suggests that PALM may ultimately bridge only a portion of the gap between diffraction limited optical microscopy and the FRET methods that probe molecular interactions. In the process of improving the overall stability of our setup, we came across an effective and practical approach to axially stabilize the microscope. Using a totally internally reflected near infrared laser line we were able to actuate a feedback mechanism keeping the objective to sample distance stable within 5 nm for up to one hour or more. We finally proposed the two proteins PSCFP2 and pamCherry1 as an effective dual color PALM pair. As a logic extension of the experiments discussed in chapter 4, we presented an application to the case of the β2-AR and its partner clathrin during agonist stimulated endocytosis, observing partial colocalization between the two.

The possibility of using PALM to study molecular interactions by bridging the resolution gap between the molecular level and the diffraction limit was one of the motivations of this thesis work. However, such a promising application represents the ultimate test of many underlying assumptions: the univocal identification of each protein, the activation and localization of the majority of the fluorescent labels as well as an outstanding long term mechanical stability and registration and finally the possibility to freeze the biological system in a given configuration. In the course of this thesis work we have therefore addressed, to a different degree of detail, most of these assumptions, exploring the limits of the technique and the accuracy that we could achieve with our setup.

7.2 Future directions

Following our conclusions, we would like to briefly discuss what could be the future directions of PALM, and how some of the issues addressed in this thesis could be further investigated by complementary techniques.

Accurate counting would clearly benefit from a full control over the fluorophore photophysics. The determination of temporal thresholds to separate distinct blinking molecules is complicated by the exponential distribution of the number of reactivations of the fluorophore, *off*-times and survival time in the active state before photobleaching. Other methods that could determine in a controllable way the permanent destruction of the fluorophore after a brief and intense emission should be considered. A possible direction was hinted by the 2-photon thermal bleaching experiments of Chirico *et al.* [115], demonstrating that the *on*-state lifetime of thermally bleached fluorophores has a Gaussian distribution, rather than the exponential distribution determined by photobleaching. The problem would be solved in the case that new, brighter and photostable fluorescent proteins became available. The recent development by Brakemann *et al.* [116] of a reversibly photoswitchable fluorescent protein where activation and deactivation are decoupled and respond to two different optical wavelengths is a promising step in this direction.

The problem of quantifying the number of fluorophores present in the sample is probably one of the most interesting applications of PALM. In this thesis we have developed a method to quantify the number of blinking molecules in an ensemble PALM experiment. An important next step beyond the in-vitro controls that are reported in chapter 3 would be the use of biological systems displaying a fixed stoichiometry. For example, to remain in the field of signaling molecules, $GABA_A$ receptors spontaneously aggregate in heteropentameric structures [117], that could be successfully employed both as a clustering and as a stoichiometry control, either in single or in dual color measurements.

One disadvantage of the one-by-one counting of PALM is clearly the need to deplete the entire pool of PA-FPs, since, depending on the density of the sample, this may be a lengthy process, competing with background localizations and requiring an immobile sample. Furthermore, the question about the effective fraction of properly folded or photoconverted fluorescent proteins requires further investigation. To this purpose, an interesting development would be to combine PALM with methods able to provide an independent quantification of the number of fluorophores in the sample. This could be achieved by exploiting photoactivatable fluorescent proteins that are bright also in the inactive form, such as mEos2 or PSCFP2, to cite two examples addressed in this thesis. The *off*-state of the fluorophore could be used to perform concentration estimations based on fluctuations methods such as Raster Image Correlation Spectroscopy [118] and Number and Brightness Analysis [119].

These methods provide reliable information both on the diffusional properties as well as the degree of aggregation of proteins in a living cell by using spatial and temporal fluctuations measured in a laser scanning microscope. A correlative approach based on the study of the dynamics of a sample, followed by fixation and PALM imaging could be a promising way to complement the super-resolution information.

The static picture of cell membrane receptor aggregation presented in chapters 4 and 5 would be beneficially complemented by such dynamical information. Furthermore, the connection between β2-AR and the cytoskeleton in H9C2 cells could be further addressed by the use of additional treatments to influence the cytoskeleton, such as depolimerization by Latrunculin B or the inhibition of motor proteins. Future experiments should make use of stable cell lines, to reduce the observed variability in expression levels and dual color imaging should be systematically employed in studying the relation between the actin cytoskeleton and GPCRs.

Appendix

A Choice of clustering parameters

The choice of $r = 150$ nm and $m = 5$ times, used throughout chapter 5, is clearly not the only possible, and a different choice of the parameters, such as a smaller radius $r = 50$ nm, will yield different values for the clustered fraction. This is illustrated in figure A.1, that displays side by side the clustered fraction values calculated using the two parameters.

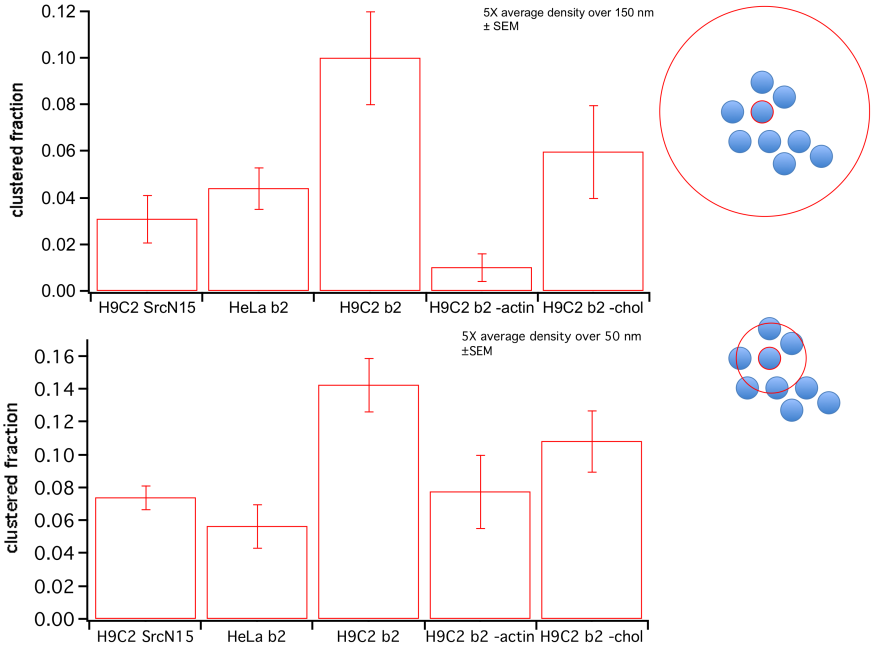

Figure A.1: Comparison of the measured clustered fraction across different experimental subgroups. Top: $r = 150$ nm and $m = 5$, bottom: $r = 50$ nm and $m = 5$.

The statistical significance of basal β2-AR clustering in H9C2 appears to be confirmed with respect to controls and to the samples treated with Cytochalasin D. However the absolute values of the clustered fraction appear to increase when a shorter radius r is employed.

Figure A.2 a and d, display the spatial point patterns of two H9C2 cells expressing at comparable levels

β2-mEos2 and SrcN15-mEos2 respectively. The pattern of clustered points obtained after thresholding with $r = 50$ nm or $r = 150$ nm is displayed in figure A.2 b, c, e and f. Choosing a combination $r = 150$ nm and $m = 5$ times appears much more selective than the choice of $r = 50$ nm. The use of a lower r value biases the analysis in favor of relatively small and compact clusters rather than spatially more extended but sparser aggregates. If the aggregation of the receptors is guided by an underlying pattern, e.g. clusters decorate the portion of the actin cytoskeleton closer to the plasma membrane through a tethering provided by some intermediate proteins, then a local thickening of this pattern may determine the observation of larger aggregates. Thinning of this pattern, as could be induced by the application of Cytochalasin D, may on the other hand result in a more homogeneous distribution of the cluster features in a background of monomers, making the detection of the clusters harder when operating with a larger clustering radius r.

Figure A.2: a) Spatial point pattern of β2-mEos2 measured in an H9C2 cell b) spatial point pattern after clustering threshold using $r = 50$ nm and $m = 5$ times and c) after the application of $r = 150$ nm and $m = 5$ times. d) Spatial point pattern of SrcN15-mEos2 measured in an H9C2 cell e) spatial point pattern after clustering threshold using $r = 50$ nm and $m = 5$ times and f) after the application of $r = 150$ nm and $m = 5$ times.

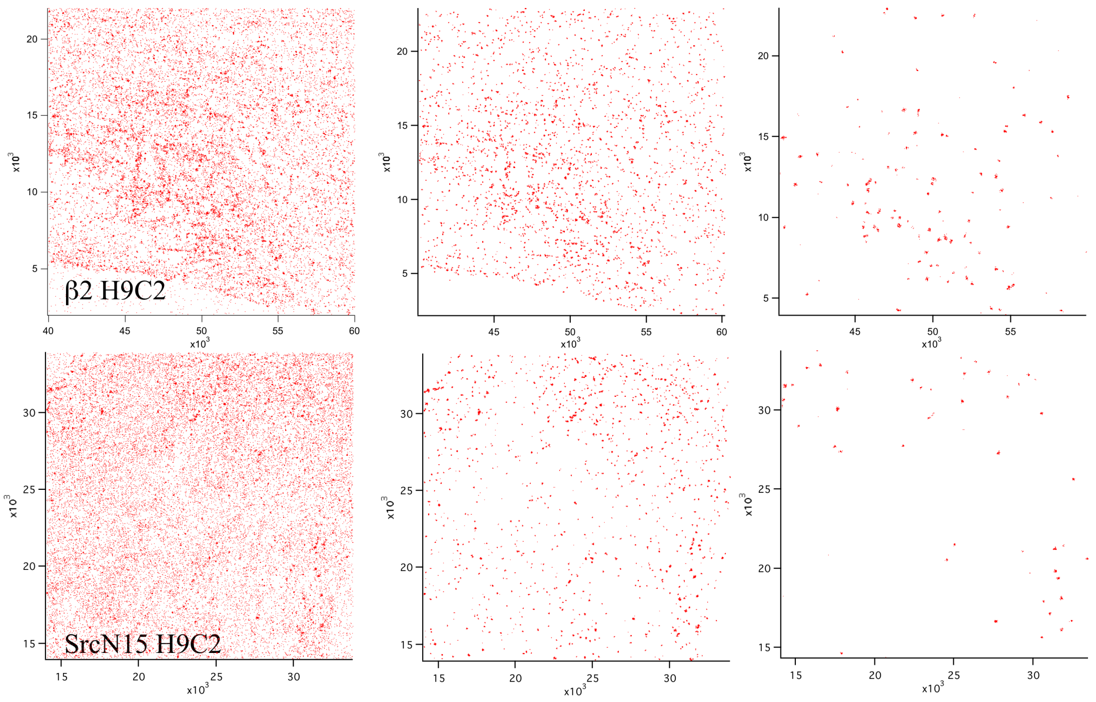

t_d=10 s + density threshold 5x over 50 nm

t_d=10 s + density threshold 5x over 150 nm

An intuitive interpretation of how the measured clustered fraction may depend upon the underlying pattern is provided in figure A.3, where two simulated clustered maps containing the same number of clustered molecules are compared. The clustering is generated according to a Poisson model, where a certain number of seeds (*parent* molecules) give rise to *offspring* molecules with a spatially Gaussian distribution around the parent and with a number of *offsprings* that is Poisson distributed. Both the standard deviation of the Gaussian distribution and the mean of the Poisson distribution are provided as parameters. Figure A.3 a displays the effect of seeding the parents molecule along a spiral pattern, each parent yielding an average of 7 *offsprings* scattered with a standard deviation of 50 nm. Clustering (r = 150 nm m = 5 times) is detected only in the inner rings of the spiral, and as the radius of the spiral increase, and hence the linear distance between the seeds, the measured clustered fraction falls off. When the *parent* molecules are randomly seeded, as shown in figure A.3 b, (though keeping the overall sample density and fraction of molecules belonging to clusters the same as in the spiral case) the clustering threshold algorithm does not detect any clusters.

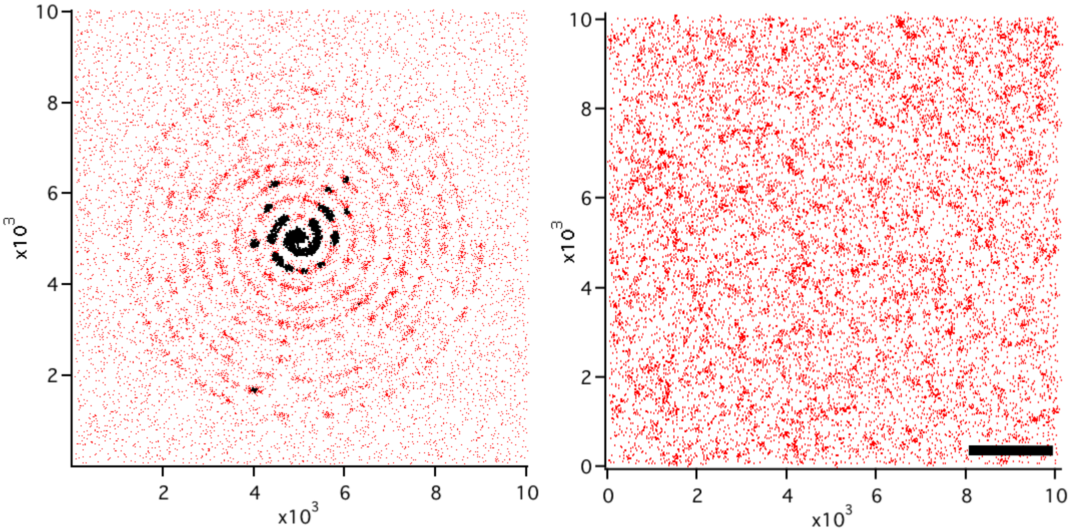

Figure A.3: Simulated spatial point patterns displaying clustering. A fraction of the total number of molecules is arranged in clusters around *parent* molecules. Each cluster has an number of molecules Poisson distributed with an average $m_c = 7 + 1$. a) *Parent* molecules are arranged in a spiral. Overall sample density is 170 $/\mu m^2$. A fraction f = 10% of the total molecules belongs to clusters. b) *Parent* molecules are randomly arranged in the sample. Molecules localized as part of a cluster r = 150 nm and m = 5 times) are highlighted in black. Scale bar is 2 μm.

As a matter of fact we may consider two basic models guiding the formation of a clustered pattern. We call these models the *growing nucleation centers* model and the *growing clusters model*. Both models generate Poissonian clusters around a certain number of *parent* molecules, but differ in the way an increase in the clustering (or in the density) is achieved: in the first case (used in figure A.3), the average number of molecules per cluster is fixed, and an increase either in the overall density or in the clustered fraction is achieved by an increase in the number of nucleation centers. In the second case, the number of nucleation centers is fixed, and any increase in density or in clustered fraction arises due to an increase in clusters size. It is possible to focus on the data measured from β2-AR in H9C2 in basal condition, and exploit the observed variability in the measured clustered fraction values to determine which of the two models appears to explain better the experimental data. The latter question can be answered observing the $(L(r) - r)_{max}$ values plotted against the experimental clustered fraction. The superposed dotted line represents the expected dependence upon a growing nucleations model and the dashed line upon a growing clusters model. The data points corresponding to the β2 H9C2 display a qualitatively better agreement to a growing cluster model, suggesting that increases in the surface density of β2 receptors on H9C2 cells result in larger aggregates rather than a larger number of

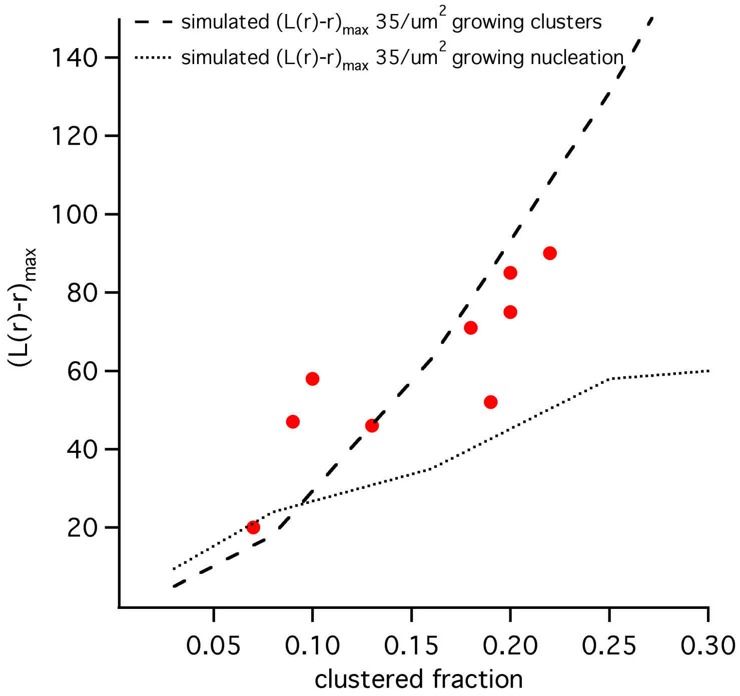

Figure A.4: $(L(r) - r)_{max}$ vs experimental clustered fraction for $\beta 2$ basal. Dotted line represents the expected dependence upon a growing nucleations model ($n_{off} = 7$) and the dashed line upon a growing clusters model ($n_{clusters} = 35$) for a constant surface density of $35/\mu m^2$.

clustering sites.

The plot in figure A.5 a, displays the clustered fraction data ($r = 50$ nm, $m = 5$) against the measured density for our key datasets, viz. $\beta 2$ in HeLa in basal conditions, $\beta 2$ in H9C2 in basal conditions, SrcN15 in H9C2, $\beta 2$ in H9C2 after treatment with Cytochalasin D and with MβCD.

Using the average clustered fraction measured for the $\beta 2$ in H9C2 in basal conditions (i.e. ~ 15%, ~ 0.2 cluster features/μm^2) we can simulate clustered datasets where the density increases but the fraction of clustered molecules remains constant, according to each of the two models proposed. The red dashed line represents the clustered fraction measured in a simulated sample generated according to the growing clusters model. The measured values are approximately flat throughout the entire density range. Although qualitative, the comparison to simulated datasets seems to confirm that the decrease of the measured clustered fraction of $\beta 2$ after Cytochalasin D treatment depends on an effective reduction of the clustered molecule in the sample.

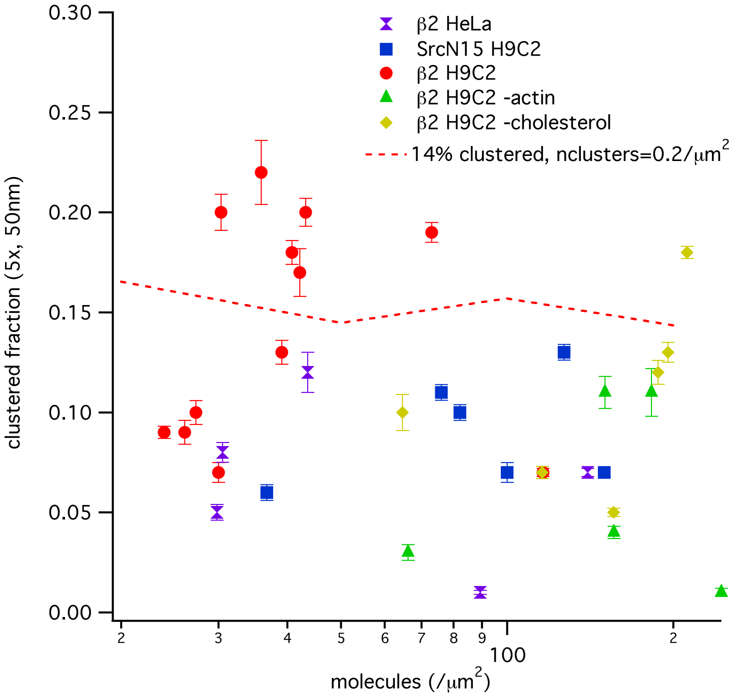

Figure A.5: Measured clustered fraction for $\beta2$ basal, SrcN15, $\beta2$ -actinand $\beta2$ -cholesterol in H9C2 cells plotted vs sample density. The dashed red line represents the measured clustered fraction in simulated datasets of increasing density having a clustered fraction of 14% and a constant number of cluster nucleation sites = 20 in a region of 100 μm^2.

B Photophysical model for mEos2

In this appendix we discuss in more detail the reason for choosing a four state model (i.e. one dark state) with respect to a more complex photophysical model. The observed bi-exponential distribution of the *off*-times in PVA may legitimately induce to ask why a reversible photoswitching molecule with two dark states was not modeled, as graphically shown in figure B.1. We assume that both dark states are recovered by 405 nm irradiation with different probabilities and therefore leading to two sizably different *off*-times.

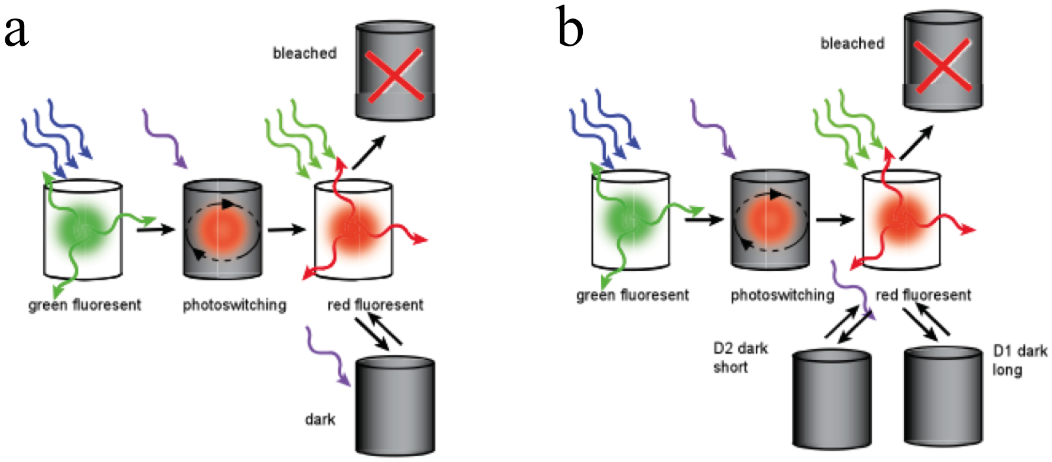

Figure B.1: Graphical comparison between a one and a two dark states models.

Our single exponential fitting method takes into account the reactivations resulting from only one of these states, the one displaying the faster of the two dynamics (shorter *off*-times). In the current form we will not consider the slower one. Figure B.2 a, displays the counts vs t_d curve (introduced in figure 3.14 a) for a very diluted mEos2 sample in PAGE (1nM). This condition rules out the presence of a significant fraction, if any, of missed counts. Counts vs t_d behavior is observed up to $t_d = 500$ s, and results in a single exponential decay. For the considerations developed in reference to figure 3.15 this observation confirms a single exponential distribution of the *off*-times, and therefore hints at the prevailing presence of a single dark state in the fluorescent dynamics of mEos2. We simulated the dynamics of a fluorophore with two dark states, characterized by two different recovery probabilities by 405 nm illumination. For low values of photoactivation light the most efficient state dominates the dynamics, whereas the impact of the second dark state becomes measurable only at high photoactivation values. Figure B.2 b, displays the experimentally measured *off*-time histogram compared to the histograms calculated from the simulations of both a one dark state model, as the one used in our work, and a model with an additional dark state (for both a low and a high photoactivation value). The experimental points are in good agreement with either a one dark state model or a low photoactivation two dark states model.

We have shown that in a typical PALM experiment, characterized by high molecular densities, it is necessary to work with photoactivation values as low as possible to avoid multiple simultaneous activations in the same diffraction limited spot, determining an excess of missed counts. Figure B.2 c, displays the comparison between the simulated counts vs t_d curves of a two dark states model and the four state model expected for the same (low) photoactivation value. The resulting curves display that the choice of the model is not dramatically influencing the shape of the curves, and that using a small t_d to treat the data will not make any difference. The amount of re-activations events due to the slower dynamics can be estimated in this case from the cumulative probability extracted from the *off*-times histogram. Figure B.2 d, displays how, assuming a two dark states model would result only in approximately 10% of the events displaying *off*-times longer than 2 s, the cut-off value observed in the one dark state simulation.

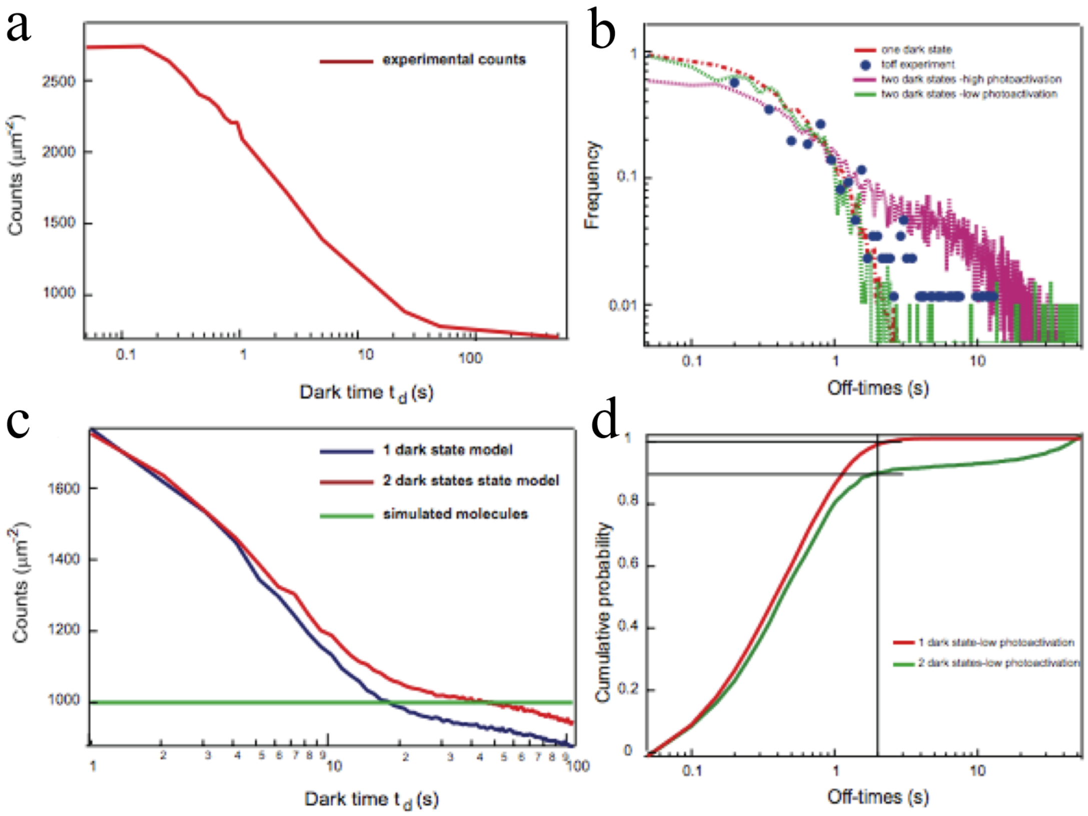

Figure B.2: Comparison between one and a two dark states models. a) Counts vs t_d curve for a diluted mEos2 in PAGE sample (1 nM) displaying a single exponential decay. b) Markers: experimental *off*-times measured from single molecule traces of mEos2 in PAGE. Red dashed curve: simulated *off*-times for a one dark state model. Purple dotted curve: simulated *off*-times for a two dark states model at high photoactivation values. Green dotted curve: simulated curve for a two dark states model at low photoactivation values. c) Simulated counts vs t_d curve and for a one dark state model (blue curve) compared to a two dark states model (red curve). d) Simulated cumulative *off*-time probability respectively for one (red) and two (green) dark states model. (reprinted from Annibale *et al.* [46])

C Materials and Methods

C.1 Molecular Biology

The mEos2 gene cloned into the plasmid pRSETA was purchased from AddGene (Addgene plasmid 20341, original material provided by Loren Looger HHMI).

The small peptide SrcN15 represents the N-terminal 15 amino acids of the protein Src, it is myristoylated, and was demonstrated to be associated to the non-raft domains of the plasma membrane [61]. The two DNA constructs *SrcN15-mEos2* and *SrcN15-PSCFP2* were synthesized and cloned in the mammalian expression vector pJ603 by the DNA 2.0 company (94025 CA, USA). The company claims that the pJexpress mammalian vectors show equivalent levels of protein expression as pCDNA3.1 when using the same insert. When, we compared the same construct present in the two different vectors, pJ603 and pCDNA3.1, the expression level was similar. All the clones coming from the DNA 2.0 were re-sequenced. For β2-AR chimaera we fused at the C-terminus the two different fluorophores tdEos and mEos2 (β2-tdEos and β2-mEos2).

For *β2-tdEos*, β2 sequence was amplified with PCR using the primers GATGAATTCCTTGGTACCACCATG (sense) and GGCGCGGCCGCTTCAGCAGTGAG-TCATT (antisense) in order to obtain the EcorI and NotI restrictions sites, and the deletion of the Stop codon. Then, the amplified β2 construct was inserted in the plasmid for mammalian expression pcDNA3-tdEos (from MoBiTec, 37083 Goettingen, Germany). For *β2-mEos2*, mEos2 substitutes tdEos in the β2-tdEos DNA construct. The mEos2 gene was amplified with PCR using the primers GTCGCGCTCGAGATGAGTGCGATTAAGCCA (sense) and CGTCGCGGGCCCTTATCGTCTGGCATTGTC (antisense) in order to create the XhoI and ApaI restrictions sites. We decided to use mEos2 fused to β2 because it is a monomer.

For the constructs *β2-PSCFP2* and *M3-PSCFP2*, we ordered the fluorophore PSCFP2 from the company Evrogen as pPS-CFP2-N (117997, Moscow, Russia) for mammalian expression. We subcloned the M3 construct at the N-terminus of PSCFP2 amplifying by PCR the M3 sequence with the primers CTTAAGCTTGGTACCACCATGTAC (sense) and CGCGGGCCCCCAAGGCCTGCTCGGG (antisense) in order to create the Ecor I and Apa I restriction sites. A similar approach was done to subclone β2 sequence in pPSCFP2-N, where the primers CTTAAGCTTGGTACCACCATGTAC (sense) and CGCGGGCCCCCAGCAGTGAGTCATT (antisense) were utilized.

The construct *Clathrin-EGFP* (light chain) was kindly given by Prof. Aurelien Roux (University of Geneva, Switzerland). *mGFP-actin* was purchased from AddGene (Addgene plasmid 21948).

Clathrin-pamCherry1 was a kind gift of Mr. Michael W. Davidson (National High Magnetic Field Laboratory, Florida State University, USA). The pamCherry1 construct was a kind gift of Prof. Jennifer Lippincott-Schwartz (NIH, Bethesda, USA). *β2-pamCherry1* was generated by replacing mEos2 in the β2-mEos2 construct by pamCherry1 using the XhoI and ApaI restriction sites. The primers ATCCGCGAACTCGAGATGGTCAGCAAGGGCGAG (sense) and AGGTCCGAGGGCCCCTTACTTGTACAGCTCGTC (antisense) were used to generate a XhoI and ApaI sites in the pamCherry1 insert by PCR.

Dronpa was purchased in the MN1 plasmid from MBL Amalgaam. The plasmid was opened using the restriction sites HindIII and NotI. β2 was extracted from the pcDNA3.1 purchased from cDNA (Missouri ST cDNA Resource Center) using the restriction sites HindIII and XbaI. The β2 sequence was amplified by PCR using the primers (antisense) to obtain a NotI site and remove the stop codon. *β2-Dronpa* was generated by inserting the PCR product in the pDG-MN1 plasmid containing Dronpa.

The *mEos2-Dronpa* construct was generated in the mammalian expression vector pJ603 from the company DNA 2.0 (Menlo Park, USA). It was subcloned in the pRSETA bacterial expression vector for protein expression in BL21(DE3) pLysS competent cells using a NotI and ApaI restriction sites. mEos2 and Dronpa were separated by a four alanines linker.

The construct coding for *S15-PSCFP2-mEos2* was purchased from DNA 2.0. S15 encodes the first 15 amino acid sequence of the protein Src, and is used as a plasma membrane targeting sequence of the construct. The amino acid sequence is: MGSSKSKPKDPSQRR AAAAVVEF, the latter 8 amino acids being used as a spacer sequence before the PSCFP2. PSCFP2 is followed by the amino acid linker sequence: AAAAVVEF. It is significant to note that after 61 aminoacids from the beginning of its sequence, mEos2 cleaves upon photoconversion. The sequence was subcloned in the pRSET1 plasmid upon removal of SRCN15 to enhance bacterial expression using the primers AAGGATCGATGGGGATCCATGGTGATGAGCAAGGGCGCCGAGCTG (sense) and GGCGGCGGTCACGAACTCGAGGTAGATCATGTGATCGCGCTT (antisense) allowing for restriction using XhoI and NcoI.

The *S15-psCFP2-pamCherry1* sequence is spaced respectively by four and three alanines. The sequence was expressed in the mammalian pJ603 and subcloned in the bacterial expression vector pRSETA using the restriction sites NotI and ApaI.

C.2 Functional assay

The functionality of the constructs, in particular of β2-mEos2, was demonstrated using a functional cAMP test. HeLa cells were electroporated with the specific DNA construct (β2, β2-mEos2 or β2-PSCFP2) for transient expression and were plated into 96-well plates at a density of 3 or 4 x 10^5 cells/well. On the day of the experiment (1 day after transfection), cells were preincubated in DMEM containing 4-(2-hydroxyethyl)-1-piperazineethanesulfonic acid (HEPES) 20 mM (pH 7.4) and albumin 0.1% at 37^oC for 30 min in the presence of rolipram 10 μM, the phosphodiesterase inhibitor, in order to allow cAMP accumulation. Then, in the same buffer, the agonist Isoproterenol was added at different concentrations for an additional 20 min. Receptor-mediated increases in intracellular cAMP were measured via the enzyme immunoassay method according to the manufacturer's protocol of the Amersham cAMP enzyme-immunoassay system (cAMP; Biotrak; GE Healthcare, Little Chalfont, UK). After cell lysis for 15 min at room temperature with the lysis solution, the supernatant from each sample was added to the specific 96-well plate from Amersham coated with donkey anti-rabbit immunoglobulin G. Then, to measure the level of cAMP for each well, the samples were incubated in a sequence for 1 hour with the rabbit anti-cAMP antibody, the cAMP horseradish peroxidase, and, at the end, the enzyme substrate 3,3, 5,5-tetramethylbenzidine. The assay is based on competition between unlabeled cAMP and a fixed quantity of peroxidase-labeled cAMP. A blue color develops at the end and the optical density (OD) can be read with the spectrophotometer plate-reader at 630 nm. As an alternative, it is also recommended to stop the reaction with sulfuric acid 1 M and then read at 450 nm. To convert the change in OD at 450 nm into the amount of cAMP produced in the sample (fmol/well), a proper calibration curve done with the cAMP standards (12.5-3200 fmol/well) was obtained.

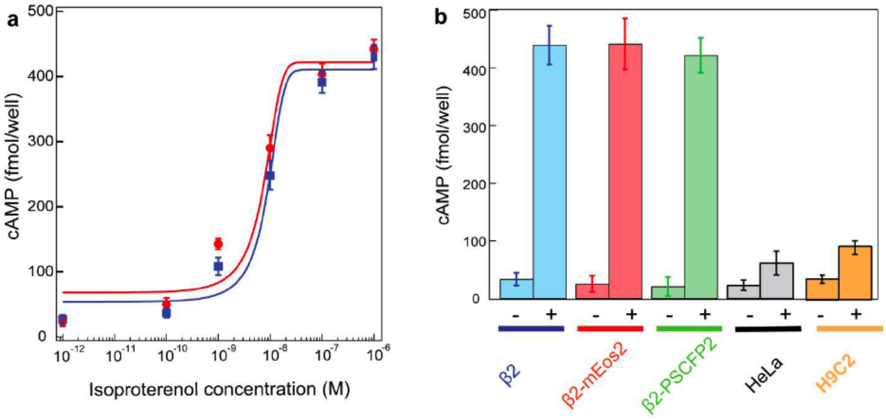

Figure C.1: Functional characterization and cell expression of the constructs β2-mEos2. a) Concentration-response curve in the cAMP accumulation assay in HeLa cells of β2-mEos2 (red) compared withβ2 WT (blue). The EC50 resulted 6.6±1.7 nM and 8.8±1.3 nM respectively. These data are representative of three different experiments. b) Maximum response in the cAMP accumulation assay in HeLa cells of β2-mEos2, β2-PSCFP2 and not transfected cells. (- basal state, + Isoprotenerol 10 μM). HeLa and H9C2 cells induce a limited amount of cAMP in the presence of Isoproterenol due to the endogenous β2 receptors. (Reprinted from Scarselli, Annibale and Radenovic [74])

C.3 Cell culture

HeLa cells were purchased by ATCC company (LGC Standards, 67123 Molsheim Cedex, France) and were grown in DMEM (without phenol red) supplemented with 10% fetal bovine serum, 100 mg/ml streptomycin, and 100 units/ml penicillin at 37 ^oC with 5% CO2. H9C2 cell line derived from embryonic rat heart were ordered by ATCC and were grown in DMEM supplemented with 10% fetal bovine serum, 100 mg/ml streptomycin, and 100 units/ml penicillin at 37 ^oC with 5% CO2. Both cell lines were transfected using the NeonTM Transfection System (Invitrogen) following the manufacturer's instructions. The electroporation was performed for a 6 well dish (500000-1000000 cells/well) using 0.5-2 μg of DNA for each sample following the manufacturer's parameters. For HeLa, the parameters for electroporation were 1005 V, 2 Pulses with a width of 35 ms. For H9C2 the parameters used were 1650 V, 3 Pulses with a width of 10 ms. The cells after electroporation were seeded directly onto the coverslips. Experiments were performed 24h after transfection. CHO (DHFR deficient) cells were kindly provided by Dr. Jumhua Qiao (EPFL) and were grown in DMEM/F12 1:1 (without phenol red) supplemented with 10% fetal bovine serum, 100 mg/ml streptomycin, 100 units/ml penicillin and HT supplements at 37 ^oC with 5% CO2. coverslips. For CHO the parameters used for electroporation were 1650 V, 3 Pulses with a width of 10ms. For cholesterol sequestration, we utilized Filipin with a preincubation of 30 min at the concentration of 12 μg/ml while for cholesterol removal we used MβCD preincubating for 30 min at the concentration of 5mM. For the internalization of β2-mEos2 in HeLa, cells were incubated at 37 ^oC in regular medium at different times with Isoproterenol 10μM (10 min was used as a reference time for internalization). The inhibitor of the clathrin-dependent endocytosis Dynasore, at the concentration of 80μM, was preincubated for 30 min at 37 ^oC before internalization. For receptor activation, the incubation was only a few seconds (5 s was used as a reference time for receptor activation). For the colocalization experiment with clathrin, the construct Clathrin-EGFP (light chain) was kindly given by Prof. Aurelien Roux (University of Geneva, Switzerland). mGFP-actin was purchased from AddGene (Addgene plasmid 21948). After the experiment, samples were fixed using standard procedures (see sample fixation). Then, to assess the role of actin cytoskeleton, we treated cells with the actin polymerization inhibitor Cytochalasin D 2μM, preincubating cells for 30 min. Isoproterenol hydrochloride, ICI 118551 hydrochloride, Filipin, Cytochalasin D, MβCD and Dynasore hydrate were purchased from Sigma-Aldrich. Following the protocol of Perez et al. [81], cells in a 6-well plate the day after transfection were washed 3 times with PBS and then covered with deionized water (pH 6-7) for 2 min to induce osmotic swelling. In the next step, a poly-L-lysine (0.1 %) coated coverslip was put on top of the cells for one minute and then removed allowing the transfer of the membrane patches on the glass coverslip. After rinsing the coverslip for 3 times with PBS, the membrane sheets were fixed according to the protocol.

C.4 Sample fixation

On the day of the experiment, the cells were incubated for 1 hour in DMEM with no serum in order to purge them. Then, after extensive washing with PBS, cells were fixed by incubating with 4% paraformaldehyde and 0.2% glutaraldehyde at 37 ^oC for 30-60 min in PHEM (60 mM PIPES, 25 mM HEPES, 10 mM ethylene glycol tetraacetic acid, and 2 mM MgCl2, pH 6.9) and washed 5x with PHEM. The presence of glutaraldehyde was necessary to reduce molecule mobility as reported by Tanaka *et al.* [63]. The glass coverslips (25.4 mm diameter, no. 1.5 thickness) were cleaned overnight in a solution obtained by mixing 125 ml of water with 25 ml of ammonium hydroxide (or Sulfuric Acid, in order to obtain Piranha Solution) and 25 ml of hydrogen peroxide 30%. A further step based on repeated rinsing with MilliQ water, immersion in spectroscopic grade methanol, nitrogen blowing, and a passage under the flame was performed.

C.5 Protein purification and in-vitro sample preparation

All pRSETA plasmids were transformed into the Bacterial strain BL21(DE3) pLysS (Stratagene, La Jolla, CA, USA). Cultures were grown overnight in Medium containing 100mg/mL ampicillin and 25mg/mL chloramphenicol to a 0.4-0.5 optical density and then induced with 1mM IPTG at 37 ^oC for 5 hours. The cells were harvested from a 500 ml culture by centrifugation and resuspended in 8 ml of lysis buffer (500 mM NaCl, 50 mM NaH2PO4, pH 8). Then, 8 mg of lysozyme was added and the reaction was incubated 30 minutes on ice. The solution was sonicated on ice 5 times with a sonicator equipped with a microtip using six 10 s bursts at high intensity with a 10 s cooling period between each burst. The lysate was centrifuged at 3000 x g for 15 min. to pellet cellular debris. The supernatant was transferred to a fresh tube and added to an equilibrated Invitrogen Ni-NTA purification Column. Binding was allowed for 1 hour with gentle agitation to keep the resin suspended in the lysate solution. The resin was allowed to settle by centrifugation (800 x g) and the supernatant was carefully aspirated. The column was washed with 8 ml of Native Wash Buffer with imidazole at low concentration (500 mM NaCl, 50 mM NaH2PO4, pH 8 and 20 mM imidazole). This last step was repeated three more times. The column was clamped in a vertical position and the cap was removed from the lower end in order to elute the protein with 12 ml native elution buffer (500 mM NaCl, 50 mM NaH2PO4, pH 8 and 250 mM imidazole). After purification, the proteins were dialyzed in Slide-A-Lyzer cassettes with 10000 MWCO (Pierce Chemical Company, Rockford, IL) using PBS and then concentrated.

For Polyvinyl Alchool (PVA) immobilization the purified protein solution was diluted in an aqueous solution of Polyvinyl Alchool (PVA) 1% (Mowiol 4-98 Sigma Aldrich), filtered through a 0.2 μm filter. PVA is obtained by hydrolysis of polyvinyl acetate and it is a water-soluble polymer. It can be used to immobilize proteins, as it has excellent film forming and adhesive properties. It is nontoxic, and has a high oxygen barrier property, thus it protects the protein from oxidative reactions. The PVA solution containing the fluorescent proteins was spin-coated on a glass cover-slip at 3000 RPM for 30 s.

For PolyAcrylamide Gel (PAGE) immobilization, single molecule fluorescent proteins samples were obtained by mixing the aqueous solution containing the proteins to Acrylamide and crosslinking solution and vortexing. PAGE was obtained by diluting in water a stock solution 30% Acrylamide (Sigma) with 1.6% Methylenebisacrylamide (Sigma) to a final Acrylamide concentration of 15%. Polymerization was obtained, after a few cycles of degassing in an essiccator and nitrogen flow, by adding Ammonium Persulfate Solution and TEMED and mixing. 20 μL of the polymerizing solution were immediately sandwiched between two 25.4 mm no. 1.5 clean circular glass coverslips. Fluorescence imaging was performed after 1h, and within at most a few hours, at room temperature.

C.6 Spectra

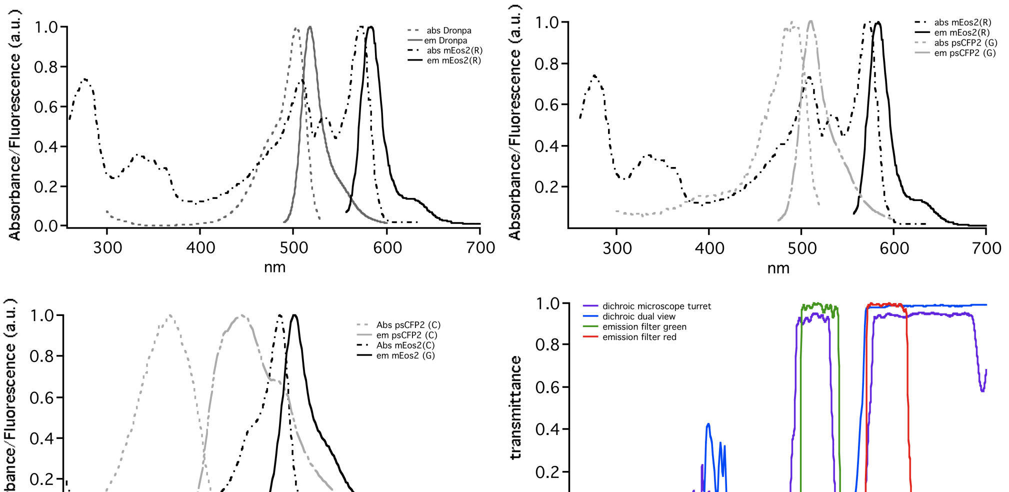

Figure C.2: Spectral signatures of the pairs of Photo-Activatable fluorescent proteins discussed in this chapter, as well as a combination of the optical filters used in the emission path. a) mEos2 and Dronpa. b) PSCFP2 and mEos2. c) and mEos2 prior to photoconversion. d) Set of dichroic mirrors and emission filters used in the dual color setup

D β2-AR in CHO cells and M3 muscarinic receptor in HeLa and H9C2 cell lines.

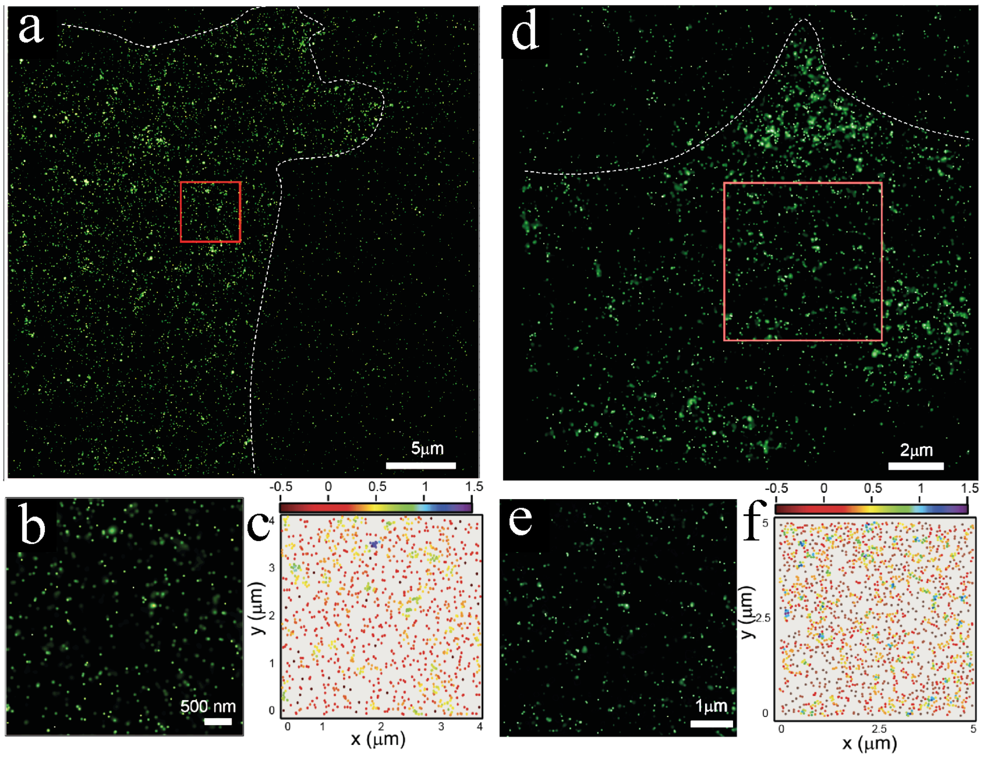

Figure D.1: a) PALM image of the M3 muscarinic receptor labeled with PSCFP2 (M3-PSCFP2) on the plasma membrane of fixed HeLa cells. b) Inset show magnified view. c) molecules distribution of the inset to visualize clusters (color coding represents clustering degree). d) M3-PSCFP2 on the plasma membrane of a fixed H9C2 cell. e) magnified view f) as c. (Reprinted from Scarselli, Annibale and Radenovic [74])

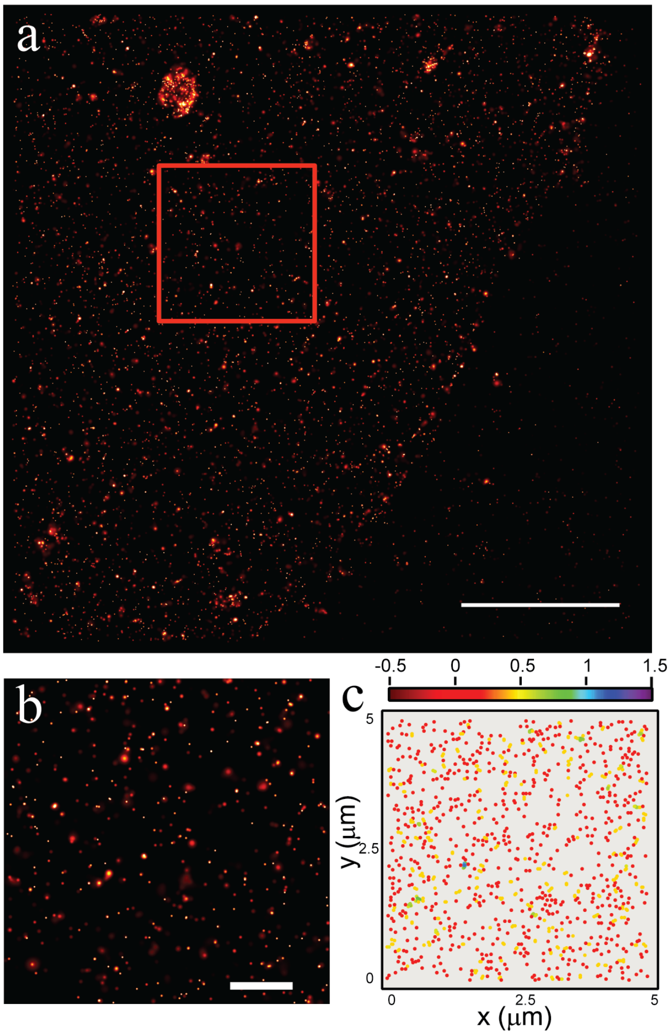

Figure D.2: a) PALM image of the $\beta 2$-mEos2 on the plasma membrane of fixed CHO cells. Scale bar 5 μm. b) Inset show magnified view. Scale bar 1 μm. c) Molecules distribution of the inset to visualize clusters (color coding represents clustering degree).

Abbreviations

A/D Analog to Digital

α1b-AR α1-Adrenergic Receptor

AOTF Acousto Optic Tunable Filter

β2-AR β2-Adrenergic Receptor

BFP Back Focal Plane

cAMP Cyclic Adenosine Mono Phosphate

COS cell monkey kidney tissue cells

CHO Chinese Hamster Ovary cells

CSR Complete Spatial Randomness

DMEM Dulbecco's Modified Eagle Medium

E-Coli Escherichia Coli

EGFP Enhanced Green Fluorescent Protein

EM-CCD Electron Multiplication Charge Coupled Device

FACS Fluorescence Activated Cell Sorting

fPALM Fluorescence PhotoActivation Localization Microscopy

FRE Fiducial Registration Error

FRET Förster Resonance Energy Transfer

FT Frame Transfer

GFP Green fluorescent protein

GPCR G protein-Coupled Receptor

H9C2 cardyomiocyte-like cells

HEK Human Embryonic Kidney 293 cells

HeLa cervical cancer cells

MβCD Methyl-β-Cyclo Dextrin

NA Numerical Aperture

NHERF Sodium Hydrogen Exchange Regulation Factor

PAGE PolyAcrylamide Gel

PAGFP Photo Activatable GFP

PALM Photo Activated Localization Microscopy

PBS Phosphate Buffered Saline

PDZ factor post synaptic density protein, Drosophila disc large tumor suppressor, and Zonula occludens-1 protein factor

PHEM Pipes Hepes EGTA MgCl2

PID Proportional Integral Derivative controller

PVA Poly Vinyl Alchool

QPD Quadrant Photo Diode

QY Quantum Yield

ROI Region of Interest

STORM STochastic Optical Reconstruction Microscopy

STED Stimulated Emission Depletion

$\sigma_{(xy)}$ localization precision

SNOM Scanning Near Field Optical Microscopy

SNR Signal to Noise Ratio

SrcN15 15 first aminoacids of the protein Src

θ_c TIRF critical angle

t_d maximum time interval between two consecutive reactivations of the same molecule

TEMED Tetramethylethylendiamin

TIRF Total Internal Reflection Fluorescence

TTL Transistor Transistor Logic

wtGFP wild type Green Fluorescent Protein

UV Ultra Violet

Bibliography

[1] P. Annibale, M. Scarselli, A. Kodiyan, and A. Radenovic, “Photoactivatable fluorescent protein meos2 displays repeated photoactivation after a long-lived dark state in the red photoconverted form,” *The Journal of Physical Chemistry Letters*, vol. 1, no. 9, pp. 1506–1510, 2010.

[2] E. Betzig, “Proposed method for molecular optical imaging,” *Opt. Lett.*, vol. 20, pp. 237–239, Feb 1995.

[3] A. M. van Oijen, J. Köhler, J. Schmidt, M. Müller, and G. J. Brakenhoff, “Far-field fluorescence microscopy beyond the diffraction limit,” *J. Opt. Soc. Am. A*, vol. 16, pp. 909–915, Apr 1999.

[4] X. Qu, D. Wu, L. Mets, and N. F. Scherer, “Nanometer-localized multiple single-molecule fluorescence microscopy,” *Proceedings of the National Academy of Sciences of the United States of America*, vol. 101, no. 31, pp. 11298–11303, 2004.

[5] E. Betzig, G. H. Patterson, R. Sougrat, O. W. Lindwasser, S. Olenych, J. S. Bonifacino, M. W. Davidson, J. Lippincott-Schwartz, and H. F. Hess, “Imaging Intracellular Fluorescent Proteins at Nanometer Resolution,” *Science*, vol. 313, no. 5793, pp. 1642–1645, 2006.

[6] S. T. Hess, T. P. Girirajan, and M. D. Mason, “Ultra-High Resolution Imaging by Fluorescence Photoactivation Localization Microscopy,” *Biophysical Journal*, vol. 91, no. 11, pp. 4258 – 4272, 2006.

[7] M. J. Rust, M. Bates, and X. Zhuang, “Sub-diffraction-limit imaging by stochastic optical reconstruction microscopy (STORM),” *Nature Methods*, vol. 3, no. 10, pp. 793–796, 2006.

[8] S. W. Hell and J. Wichmann, “Breaking the diffraction resolution limit by stimulated emission: stimulated-emission-depletion fluorescence microscopy,” *Opt. Lett.*, vol. 19, pp. 780–782, Jun 1994.

[9] H. Shroff, C. G. Galbraith, J. A. Galbraith, H. White, J. Gillette, S. Olenych, M. W. Davidson, and E. Betzig, “Dual-color superresolution imaging of genetically expressed probes within individual adhesion complexes,” *Proceedings of the National Academy of Sciences*, vol. 104, no. 51, pp. 20308–20313, 2007.

[10] S. T. Hess, T. J. Gould, M. V. Gudheti, S. A. Maas, K. D. Mills, and J. Zimmerberg, “Dynamic clustered distribution of hemagglutinin resolved at 40 nm in living cell membranes discriminates between raft theories,” *Proceedings of the National Academy of Sciences*, vol. 104, no. 44, pp. 17370–17375, 2007.

[11] H. Shroff, C. G. Galbraith, J. A. Galbraith, and E. Betzig, “Live-cell photoactivated localization microscopy of nanoscale adhesion dynamics,” *Nature Methods*, vol. 5, no. 5, pp. 417–423, 2008.

[12] G. Shtengel, J. A. Galbraith, C. G. Galbraith, J. Lippincott-Schwartz, J. M. Gillette, S. Manley, R. Sougrat, C. M. Waterman, P. Kanchanawong, M. W. Davidson, R. D. Fetter, and H. F. Hess, “Interferometric fluorescent super-resolution microscopy resolves 3D cellular ultrastructure,” *Proceedings of the National Academy of Sciences*, vol. 106, no. 9, pp. 3125–3130, 2009.

[13] D. Greenfield, A. L. McEvoy, H. Shroff, G. E. Crooks, N. S. Wingreen, E. Betzig, and J. Liphardt, “Self-organization of the <italic>escherichia coli</italic> chemotaxis network imaged with super-resolution light microscopy,” *PLoS Biol*, vol. 7, p. e1000137, 06 2009.

[14] W. E. Moerner and M. Orrit, “Illuminating Single Molecules in Condensed Matter,” *Science*, vol. 283, no. 5408, pp. 1670–1676, 1999.

[15] M. Chalfie, Y. Tu, G. Euskirchen, W. Ward, and D. Prasher, “Green fluorescent protein as a marker for gene expression,” *Science*, vol. 263, no. 5148, pp. 802–805, 1994.

[16] W. E. Moerner and D. P. Fromm, “Methods of single-molecule fluorescence spectroscopy and microscopy,” *Review of Scientific Instruments*, vol. 74, no. 8, pp. 3597–3619, 2003.

[17] R. E. Thompson, D. R. Larson, and W. W. Webb, “Precise nanometer localization analysis for individual fluorescent probes,” *Biophysical Journal*, vol. 82, no. 5, pp. 2775 – 2783, 2002.

[18] K. I. Mortensen, L. S. Churchman, J. A. Spudich, and H. Flyvbjerg, “Optimized localization analysis for single-molecule tracking and super-resolution microscopy,” *Nature Methods*, vol. 7, no. 5, pp. 377–381, 2010.

[19] H. Shroff, H. White, and E. Betzig, *Photoactivated Localization Microscopy (PALM) of Adhesion Complexes.* John Wiley and Sons, Inc., 2001.

[20] C. K. Carniglia, L. Mandel, and K. H. Drexhage, “Absorption and emission of evanescent photons,” *J. Opt. Soc. Am.*, vol. 62, pp. 479–486, Apr 1972.

[21] D. Axelrod, T. P. Burghardt, and N. L. Thompson, “Total internal reflection fluorescence,” *Annual Review of Biophysics and Bioengineering*, vol. 13, no. 1, pp. 247–268, 1984.

[22] W. Denk, J. Strickler, and W. Webb, “Two-photon laser scanning fluorescence microscopy,” *Science*, vol. 248, no. 4951, pp. 73–76, 1990.

[23] J. Huisken, J. Swoger, F. Del Bene, J. Wittbrodt, and E. H. K. Stelzer, “Optical sectioning deep inside live embryos by selective plane illumination microscopy,” *Science*, vol. 305, no. 5686, pp. 1007–1009, 2004.

[24] F. C. Zanacchi, Z. Lavagnino, M. P. Donnorso, A. Del Bue, L. Furia, M. Faretta, and A. Diaspro, “Live-cell 3D super-resolution imaging in thick biological samples,” *Nature Methods*, vol. 8, no. 12, pp. 1047–1049, 2011.

[25] D. Axelrod, “Total Internal Reflection Fluorescence Microscopy in Cell Biology,” *Traffic*, vol. 2, no. 11, pp. 764–774, 2001.

[26] A. L. Stout and D. Axelrod, “Evanescent field excitation of fluorescence by epi-illumination microscopy,” *Appl. Opt.*, vol. 28, pp. 5237–5242, Dec 1989.

[27] K. Hassler, M. Leutenegger, P. Rigler, R. Rao, R. Rigler, M. Gösch, and T. Lasser, “Total internal reflection fluorescence correlation spectroscopy (TIR-FCS) with low background and high count-rate per molecule,” *Opt. Express*, vol. 13, pp. 7415–7423, Sep 2005.

[28] J. Janesick, *Photon Transfer: Dn [Lambda].* Press Monographs, SPIE, 2007.

[29] J. R. Unruh and E. Gratton, "Analysis of molecular concentration and brightness from fluorescence fluctuation data with an electron multiplied CCD camera," *Biophysical Journal*, vol. 95, no. 11, pp. 5385 – 5398, 2008.

[30] R. E. Dickson, A. B. Cubitt, R. Y. Tsien, and W. E. Moerner, "On/off blinking and switching behaviour of single molecules of green fluorescent protein," *Nature*, vol. 388, no. 6640, pp. 355–358, 1997.

[31] M. Chattoraj, B. A. King, G. U. Bublitz, and S. G. Boxer, "Ultra-fast excited state dynamics in green fluorescent protein: multiple states and proton transfer," *Proceedings of the National Academy of Sciences*, vol. 93, no. 16, pp. 8362–8367, 1996.

[32] G. H. Patterson and J. Lippincott-Schwartz, "A photoactivatable GFP for selective photolabeling of proteins and cells," *Science*, vol. 297, no. 5588, pp. 1873–1877, 2002.

[33] R. Ando, H. Mizuno, and A. Miyawaki, "Regulated fast nucleocytoplasmic shuttling observed by reversible protein highlighting," *Science*, vol. 306, no. 5700, pp. 1370–1373, 2004.

[34] S. Habuchi, R. Ando, P. Dedecker, W. Verheijen, H. Mizuno, A. Miyawaki, and J. Hofkens, "Reversible single-molecule photoswitching in the GFP-like fluorescent protein dronpa," *Proceedings of the National Academy of Sciences of the United States of America*, vol. 102, no. 27, pp. 9511–9516, 2005.

[35] M. Andresen, M. C. Wahl, A. C. Stiel, F. Gruetter, L. V. Schaefer, S. Trowitzsch, G. Weber, C. Eggeling, H. Grubmueller, S. W. Hell, and S. Jakobs, "Structure and mechanism of the reversible photoswitch of a fluorescent protein," *Proceedings of the National Academy of Sciences of the United States of America*, vol. 102, no. 37, pp. 13070–13074, 2005.

[36] R. Bizzarri, M. Serresi, F. Cardarelli, S. Abbruzzetti, B. Campanini, C. Viappiani, and F. Beltram, "Single amino acid replacement makes aequorea victoria fluorescent proteins reversibly photoswitchable," *Journal of the American Chemical Society*, vol. 132, no. 1, pp. 85–95, 2010. PMID: 19958004.

[37] R. Ando, H. Hama, M. Yamamoto-Hino, H. Mizuno, and A. Miyawaki, "An optical marker based on the UV-induced green-to-red photoconversion of a fluorescent protein," *Proceedings of the National Academy of Sciences*, vol. 99, no. 20, pp. 12651–12656, 2002.

[38] J. Wiedenmann, S. Ivanchenko, F. Oswald, F. Schmitt, C. Roecker, A. Salih, K.-D. Spindler, and G. U. Nienhaus, "EosFP, a fluorescent marker protein with UV-inducible green-to-red fluorescence conversion," *Proceedings of the National Academy of Sciences of the United States of America*, vol. 101, no. 45, pp. 15905–15910, 2004.

[39] D. M. Chudakov, M. V. Matz, S. Lukyanov, and K. A. Lukyanov, "Fluorescent proteins and their applications in imaging living cells and tissues," *Physiological Reviews*, vol. 90, no. 3, pp. 1103–1163, 2010.

[40] S. A. McKinney, C. S. Murphy, K. L. Hazelwood, M. W. Davidson, and L. L. Looger, "A bright and photostable photoconvertible fluorescent protein," *Nature Methods*, vol. 6, no. 2, pp. 131–133, 2009.

[41] H. Chang, M. Zhang, W. Ji, J. Chen, Y. Zhang, B. Liu, J. Lu, J. Zhang, P. Xu, and T. Xu, "A unique series of reversibly switchable fluorescent proteins with beneficial properties for various applications," *Proceedings of the National Academy of Sciences*, 2012.

[42] P. J. Diggle, *Statistical Analysis of Spatial Point Patterns.* Arnold, London, 2003.

[43] J. M. Chambers, W. S. Cleveland, B. Kleiner, and P. A. Tukey, *Graphical Methods for Data Analysis*. Wadworth and Brooks, 1983.

[44] A. Chrambach and D. Rodbard, "Polyacrylamide gel electrophoresis," *Science*, vol. 172, no. 3982, pp. 440–451, 1971.

[45] R. M. Dickson, D. J. Norris, Y.-L. Tzeng, and W. E. Moerner, "Three-dimensional imaging of single molecules solvated in pores of poly(acrylamide) gels," *Science*, vol. 274, no. 5289, pp. 966–968, 1996.

[46] P. Annibale, S. Vanni, M. Scarselli, U. Rothlisberger, and A. Radenovic, "Quantitative photo activated localization microscopy: Unraveling the effects of photoblinking," *PLoS ONE*, vol. 6, p. e22678, 07 2011.

[47] D. M. Rosenbaum, S. G. F. Rasmussen, and B. Kobilka, "The structure and function of G-protein-coupled receptors," *Nature*, vol. 459, no. 7254, pp. 356–363, 2009.

[48] P. Tsao, T. Cao, and M. von Zastrow, "Role of endocytosis in mediating downregulation of G-protein-coupled receptors," *Trends in Pharmacological Sciences*, vol. 22, no. 2, pp. 91 – 96, 2001.

[49] M. von Zastrow and B. K. Kobilka, "Ligand-regulated internalization and recycling of human $\beta 2$-adrenergic receptors between the plasma membrane and endosomes containing transferrin receptors.," *Journal of Biological Chemistry*, vol. 267, no. 5, pp. 3530–3538, 1992.

[50] O. B. Goodman, J. G. Krupnick, F. Santini, V. V. Gurevich, R. B. Penn, A. W. Gagnon, J. H. Keen, and J. L. Benovic, "β-arrestin acts as a clathrin adaptor in endocytosis of the $\beta 2$-adrenergic receptor," *Nature*, vol. 383, no. 7254, pp. 447–450, 1996.

[51] M. A. Puthenveedu and M. von Zastrow, "Cargo regulates clathrin-coated pit dynamics," *Cell*, vol. 127, no. 1, pp. 113 – 124, 2006.

[52] J. A. Hern, A. H. Baig, G. I. Mashanov, B. Birdsall, J. E. T. Corrie, S. Lazareno, J. E. Molloy, and N. J. M. Birdsall, "Formation and dissociation of M1 muscarinic receptor dimers seen by total internal reflection fluorescence imaging of single molecules," *Proceedings of the National Academy of Sciences*, vol. 107, no. 6, pp. 2693–2698, 2010.

[53] J. A. Allen, R. A. Halverson-Tamboli, and M. M. Rasenick, "Lipid raft microdomains and neurotransmitter signalling," *Nature Reviews Neuroscience*, vol. 8, no. 2, pp. 128–140, 2007.

[54] W. M. Oldham and H. E. Hamm, "Heterotrimeric G protein activation by G protein-coupled receptors," *Nature Reviews Molecular and Cell Biology*, vol. 9, no. 1, pp. 60–71, 2008.

[55] G. Benga and R. P. Holmes, "Interactions between components in biological membranes and their implications for membrane function," *Progress in Biophysics and Molecular Biology*, vol. 43, no. 3, pp. 195 – 257, 1984.

[56] S. M. Pontier, Y. Percherancier, S. Galandrin, A. Breit, C. Gales, and M. Bouvier, "Cholesterol-dependent separation of the $\beta 2$-adrenergic receptor from its partners determines signaling efficacy," *Journal of Biological Chemistry*, vol. 283, no. 36, pp. 24659–24672, 2008.

[57] P. A. Insel, B. P. Head, R. S. Ostrom, H. H. Patel, J. S. Swaney, C.-M. Tang, and D. M. Roth, "Caveolae and lipid rafts: G protein-coupled receptor signaling microdomains in cardiac myocytes," *Annals of the New York Academy of Sciences*, vol. 1047, no. 1, pp. 166–172, 2005.

[58] R. Maggio, F. Novi, M. Scarselli, and G. U. Corsini, "The impact of G-protein-coupled receptor hetero-oligomerization on function and pharmacology," *FEBS Journal*, vol. 272, no. 12, pp. 2939–2946, 2005.

[59] M. Bouvier, “Oligomerization of g-protein-coupled transmembrane receptors,” *Nature Reviews Neuroscience*, vol. 2, pp. 274–282, 2001.

[60] A. Ianoul, D. D. Grant, Y. Rouleau, M. Bani-Yaghoub, L. J. Johnston, and J. P. Pezacki, “Imaging nanometer domains of β-adrenergic receptor complexes on the surface of cardiac myocytes,” *Nature Chemical Biology*, vol. 1, no. 4, pp. 196–202, 2005.

[61] G. R. Chichili and W. Rodgers, “Clustering of membrane raft proteins by the actin cytoskeleton,” *Journal of Biological Chemistry*, vol. 282, no. 50, pp. 36682–36691, 2007.

[62] P. Annibale, S. Vanni, M. Scarselli, U. Roetlisberger, and A. Radenovic, “Identification of clustering artifacts in photo activated localization microscopy,” *Nature Methods*, vol. 8, pp. 527–528, 2011.

[63] K. A. K. Tanaka, K. G. N. Suzuki, Y. M. Shirai, S. T. Shibutani, M. S. H. Miyahara, H. Tsuboi, M. Yahara, A. Yoshimura, S. Mayor, T. K. Fujiwara, and A. Kusumi, “Membrane molecules mobile even after chemical fixation,” *Nature Methods*, vol. 7, no. 11, pp. 865–866, 2010.

[64] I. L. Buxton and L. L. Brunton, “Direct analysis of β-adrenergic receptor subtypes on intact adult ventricular myocytes of the rat.,” *Circulation Research*, vol. 56, no. 1, pp. 126–32, 1985.

[65] S. R. Post, R. Hilal-Dandan, K. Urasawa, L. L. Brunton, and P. A. Insel, “Quantification of signalling components and amplification in the β-adrenergic-receptor-adenylate cyclase pathway in isolated adult rat ventricular myocytes.,” *Biochem. J.*, vol. 311, no. 1, pp. 75–0, 1995.

[66] O. Hegener, L. Prenner, F. Runkel, S. L. Baader, J. Kappler, and H. Hoeberlein, “Dynamics of β2-adrenergic receptor-ligand complexes on living cells,” *Biochemistry*, vol. 43, no. 20, pp. 6190–6199, 2004. PMID: 15147203.

[67] J.-Q. Wu and T. D. Pollard, “Counting cytokinesis proteins globally and locally in fission yeast,” *Science*, vol. 310, no. 5746, pp. 310–314, 2005.

[68] K. Hirschberg, R. D. Phair, and J. Lippincgtt-Schwartz, “Kinetic analysis of intracellular trafficking in single living cells with vesicular stomatitis virus protein G-green fluorescent protein hybrids,” in *Applications of Chimeric Genes and Hybrid Proteins - Part B: Cell Biology and Physiology* (S. D. E. Jeremy Thorner and J. N. Abelson, eds.), vol. 327 of *Methods in Enzymology*, pp. 69 – 89, Academic Press, 2000.

[69] D. Wheeler, W. B. Sneddon, B. Wang, P. A. Friedman, and G. Romero, “NHERF-1 and the cytoskeleton regulate the traffic and membrane dynamics of G protein-coupled receptors,” *Journal of Biological Chemistry*, vol. 282, no. 34, pp. 25076–25087, 2007.

[70] I. A. Prior, C. Muncke, R. G. Parton, and J. F. Hancock, “Direct visualization of ras proteins in spatially distinct cell surface microdomains,” *J. Cell Biol.*, vol. 160, no. 2, pp. 165–170, 2003.

[71] J. Zhang, K. Leiderman, J. R. Pfeiffer, B. S. Wilson, J. M. Oliver, and S. L. Steinberg, “Characterizing the topography of membrane receptors and signaling molecules from spatial patterns obtained using nanometer-scale electron-dense probes and electron microscopy,” *Micron*, vol. 37, no. 1, pp. 14 – 34, 2006.

[72] B. F. Lillemeier, M. A. Mortelmaier, M. B. Forstner, J. B. Huppa, J. T. Groves, and M. M. Davis, “Tcr and lat are expressed on separate protein islands on t cell membranes and concatenate during activation,” *Nature Immunology*, vol. 11, no. 1, pp. 90–96, 2010.

[73] P. Sengupta, T. Jovanovic Talisman, D. Skoko, M. Renz, S. Veatch, and J. Lippincott-Schwartz, “Probing protein heterogeneity in the plasma membrane using PALM and pair correlation analysis,” *Nature Methods*, vol. 8, no. 11, pp. 969–975, 2011.

[74] M. Scarselli, P. Annibale, and A. Radenovic, “Cell type specific β2-adrenergic receptor clusters identified using photoactivated localization microscopy are not lipid raft related, but depend on actin cytoskeleton integrity,” *Journal of Biological Chemistry*, vol. 287, no. 20, pp. 16768–16780, 2012.

[75] D. Vobornik, Y. Rouleau, J. Haley, M. Bani-Yaghoub, R. Taylor, L. J. Johnston, and J. P. Pezacki, “Nanoscale organization of β2-adrenergic receptor-venus fusion protein domains on the surface of mammalian cells,” *Biochemical and Biophysical Research Communications*, vol. 382, no. 1, pp. 85 – 90, 2009.

[76] Y. D. Paila and A. Chattopadhyay, “Membrane cholesterol in the function and organization of G-protein coupled receptors,” *Subcellular Biochemistry*, vol. 51, no. 1, pp. 439–466, 2010.

[77] M. Schliwa, “Action of cytochalasin D on cytoskeletal networks.,” *The Journal of Cell Biology*, vol. 92, no. 1, pp. 79–91, 1982.

[78] A. Verkhovsky, T. Svitkina, and G. Borisy, “Polarity sorting of actin filaments in cytochalasin-treated fibroblasts,” *Journal of Cell Science*, vol. 110, no. 15, pp. 1693–1704, 1997.

[79] C. D. Valentine and P. M. Haggie, “Confinement of β1- and β2-adrenergic receptors in the plasma membrane of cardiomyocyte-like H9c2 cells is mediated by selective interactions with PDZ domain and A-kinase anchoring proteins but not caveolae,” *Molecular Biology of the Cell*, vol. 22, no. 16, pp. 2970–2982, 2011.

[80] V. Fruah, A. P. Ijzerman, and G. Siegal, “How to catch a membrane protein in action: A review of functional membrane protein immobilization strategies and their applications,” *Chemical Reviews*, vol. 111, no. 2, pp. 640–656, 2011.

[81] J.-B. Perez, K. L. Martinez, J.-M. Segura, and H. Vogel, “Supported cell-membrane sheets for functional fluorescence imaging of membrane proteins,” *Advanced Functional Materials*, vol. 16, no. 2, pp. 306–312, 2006.

[82] E. Manders, J. Stap, G. Brakenhoff, R. van Driel, and J. Aten, “Dynamics of three-dimensional replication patterns during the s-phase, analysed by double labelling of DNA and confocal microscopy,” *Journal of Cell Science*, vol. 103, no. 3, pp. 857–862, 1992.

[83] E. M. M. Manders, F. J. Verbeek, and J. A. Aten, “Measurement of co-localization of objects in dual-colour confocal images,” *Journal of Microscopy*, vol. 169, no. 3, pp. 375–382, 1993.

[84] M. Bates, B. Huang, G. T. Dempsey, and X. Zhuang, “Multicolor super-resolution imaging with photo-switchable fluorescent probes,” *Science*, vol. 317, no. 5845, pp. 1749–1753, 2007.

[85] B. Huang, S. A. Jones, B. Brandenburg, and X. Zhuang, “Whole-cell 3D STORM reveals interactions between cellular structures with nanometer-scale resolution,” *Nature Methods*, vol. 5, no. 12, pp. 1047–1052, 2009.

[86] M. Andresen, A. C. Stiel, J. Foelling, D. Wenzel, A. Schoenle, A. Egner, C. Eggeling, S. W. Hell, and S. Jakobs, “Photoswitchable fluorescent proteins enable monochromatic multilabel imaging and dual color fluorescence nanoscopy,” *Nature Biotechnology*, vol. 26, no. 9, pp. 1035–1040, 2008.

[87] I. Testa, C. A. Wurm, R. Medda, E. Rothermel, C. von Middendorf, J. Foelling, S. Jakobs, A. Schoenle, S. W. Hell, and C. Eggeling, “Multicolor fluorescence nanoscopy in fixed and living cells by exciting conventional fluorophores with a single wavelength,” *Biophysical Journal*, vol. 99, no. 8, pp. 2686 – 2694, 2010.

[88] N. A. Frost, H. Shroff, H. Kong, E. Betzig, and T. A. Blanpied, “Single-molecule discrimination of discrete perisynaptic and distributed sites of actin filament assembly within dendritic spines,” *Neuron*, vol. 67, no. 1, pp. 86 – 99, 2010.

[89] F. V. Subach, G. H. Patterson, S. Manley, J. M. Gillette, J. Lippincott-Schwartz, and V. V. Verkhusha, “Photoactivatable mcherry for high-resolution two-color fluorescence microscopy,” *Nature Methods*, vol. 6, no. 2, pp. 153–159, 2009.

[90] F. V. Subach, G. H. Patterson, M. Renz, J. Lippincott-Schwartz, and V. V. Verkhusha, “Bright monomeric photoactivatable red fluorescent protein for two-color super-resolution sptPALM of live cells,” *Journal of the American Chemical Society*, vol. 132, no. 18, pp. 6481–6491, 2010.

[91] A. Pertsinidis, Y. Zhang, and S. Chu, “Subnanometre single-molecule localization, registration and distance measurements,” *Nature*, vol. 466, no. 6306, pp. 647–651, 2010.

[92] J. Yao, R. D. Fetter, P. Hu, E. Betzig, and R. Tjian, “Subnuclear segregation of genes and core promoter factors in myogenesis,” *Genes and Development*, vol. 25, no. 6, pp. 569–580, 2011.

[93] C.-J. Hsu and T. Baumgart, “Spatial association of signaling proteins and F-actin effects on cluster assembly analyzed via photoactivation localization microscopy in T cells,” *PLoS ONE*, vol. 6, p. e23586, 08 2011.

[94] M. Lehmann, S. Rocha, B. Mangeat, F. Blanchet, H. Uji-i, J. Hofkens, and V. Piguet, “Quantitative multicolor super-resolution microscopy reveals tetherin hiv-1 interaction,” *PLoS Pathog*, vol. 7, p. e1002456, 12 2011.

[95] D. Baddeley, D. Crossman, S. Rossberger, J. E. Cheyne, J. M. Montgomery, I. D. Jayasinghe, C. Cremer, M. B. Cannell, and C. Soeller, “4D super-resolution microscopy with conventional fluorophores and single wavelength excitation in optically thick cells and tissues,” *PLoS ONE*, vol. 6, p. e20645, 05 2011.

[96] S. Wilmes, M. Staufenbiel, D. Lisse, C. P. Richter, O. Beutel, K. B. Busch, S. T. Hess, and J. Piehler, “Triple-color super-resolution imaging of live cells: Resolving submicroscopic receptor organization in the plasma membrane,” *Angewandte Chemie International Edition*, vol. 51, no. 20, pp. 4868–4871, 2012.

[97] G. Patterson, M. Davidson, S. Manley, and J. Lippincott-Schwartz, “Superresolution imaging using single-molecule localization,” *Annual Review of Physical Chemistry*, vol. 61, no. 1, pp. 345–367, 2010.

[98] L. S. Churchman, Z. Okten, R. S. Rock, J. F. Dawson, and J. A. Spudich, “Single molecule high-resolution colocalization of Cy3 and Cy5 attached to macromolecules measures intramolecular distances through time,” *Proceedings of the National Academy of Sciences of the United States of America*, vol. 102, no. 5, pp. 1419–1423, 2005.

[99] M. Greco, “An experimental protocol for the alignment of the imaging channels and the long-term axial stability of an optical system for superresolution dual-color PALM microscopy,” diploma thesis, Politecnico di Torino, December 2011.

[100] A. Goshtasby, “Image registration by local approximation methods,” *Image and Vision Computing*, vol. 6, no. 4, pp. 255 – 261, 1988.

[101] M. Kozubek and P. Matula, “An efficient algorithm for measurement and correction of chromatic aberrations in fluorescence microscopy,” *Journal of Microscopy*, vol. 200, no. 3, pp. 206–217, 2000.

[102] J. Engelhardt, J. Keller, P. Hoyer, M. Reuss, T. Staudt, and S. W. Hell, “Molecular orientation affects localization accuracy in superresolution far-field fluorescence microscopy,” *Nano Letters*, vol. 11, no. 1, pp. 209–213, 2011.

[103] D. M. Chudakov, V. V. Verkusha, D. B. Staroverov, E. A. Souslova, S. Lukyanov, and K. A. Lukyanov, “Photoswitchable cyan fluorescent protein for protein tracking,” *Nature Biotechnology*, vol. 22, no. 11, pp. 1435–1439, 2004.

[104] R. Ando, H. Hama, M. Yamamoto-Hino, H. Mizuno, and A. Miyawaki, “An optical marker based on the uv-induced green-to-red photoconversion of a fluorescent protein,” *Proceedings of the National Academy of Sciences*, vol. 99, no. 20, pp. 12651–12656, 2002.

[105] E. H. Rego, L. Shao, J. J. Macklin, L. Winoto, G. A. Johansson, N. Kamps-Hughes, M. W. Davidson, and M. G. L. Gustafsson, “Nonlinear structured-illumination microscopy with a photoswitchable protein reveals cellular structures at 50-nm resolution,” *Proceedings of the National Academy of Sciences*, vol. 109, no. 3, pp. E135–E143, 2012.

[106] D. M. Chudakov, S. Lukyanov, and K. A. Lukyanov, “Tracking intracellular protein movements using photoswitchable fluorescent proteins PS-CFP2 and Dendra2,” *Nature Protocols*, vol. 2, no. 18, pp. 2024–2032, 2007.

[107] S. Jones, S. H. Shim, J. He, and X. Zhuang, “Fast, three-dimensional super-resolution imaging of live cells,” *Nature Methods*, vol. 8, no. 6, pp. 499–505, 2011.

[108] F. M. Brodsky, C.-Y. Chen, C. Knuehl, M. C. Towler, and D. E. Wakeham, “Biological basket weaving: Formation and function of clathrin-coated vesicles,” *Annual Review of Cell and Developmental Biology*, vol. 17, no. 1, pp. 517–568, 2001.

[109] A. Marchese, M. M. Paing, B. R. Temple, and J. Trejo, “G protein-coupled receptor sorting to endosomes and lysosomes,” *Annual Review of Pharmacology and Toxicology*, vol. 48, no. 1, pp. 601–629, 2008.

[110] M. Scarselli and J. G. Donaldson, “Constitutive internalization of G protein-coupled receptors and G proteins via clathrin-independent endocytosis,” *Journal of Biological Chemistry*, vol. 284, no. 6, pp. 3577–3585, 2009.

[111] J. S. Collins and T. H. Goldsmith, “Spectral properties of fluorescence induced by glutaraldehyde fixation.,” *Journal of Histochemistry and Cytochemistry*, vol. 29, no. 3, pp. 411–4, 1981.

[112] S. Manley, J. M. Gillette, G. H. Patterson, H. Shroff, H. F. Hess, E. Betzig, and J. Lippincott-Schwartz, “High-density mapping of single-molecule trajectories with photoactivated localization microscopy,” *Nature Methods*, vol. 5, no. 2, pp. 155–157, 2008.

[113] I. Sbalzarini and P. Koumoutsakos, “Feature point tracking and trajectory analysis for video imaging in cell biology,” *Journal of Structural Biology*, vol. 151, no. 2, pp. 182 – 195, 2005.

[114] G. Schütz, H. Schindler, and T. Schmidt, “Single-molecule microscopy on model membranes reveals anomalous diffusion,” *Biophysical Journal*, vol. 73, no. 2, pp. 1073 – 1080, 1997.

[115] G. Chirico, F. Cannone, G. Baldini, and A. Diaspro, “Two-photon thermal bleaching of single fluorescent molecules,” *Biophysical Journal*, vol. 84, no. 1, pp. 588 – 598, 2003.

[116] T. Brakemann, A. C. Stiel, G. Weber, M. Andresen, I. Testa, T. Grotjohann, M. Leutenegger, U. Plessmann, H. Urlaub, C. Eggeling, M. C. Wahl, S. W. Hell, and S. Jakobs, “A reversibly photoswitchable GFP-like protein with fluorescence excitation decoupled from switching,” *Nature Biotechnology*, vol. 29, no. 10, pp. 942–947, 2011.

[117] R. W. Olsen and A. J. Tobin, “Molecular biology of GABAA receptors.,” *The FASEB Journal*, vol. 4, no. 5, pp. 1469–80, 1990.

[118] M. A. Digman, C. M. Brown, P. Sengupta, P. W. Wiseman, A. R. Horwitz, and E. Gratton, “Measuring fast dynamics in solutions and cells with a laser scanning microscope,” *Biophysical Journal*, vol. 89, no. 2, pp. 1317 – 1327, 2005.

[119] M. A. Digman, R. Dalal, A. F. Horwitz, and E. Gratton, “Mapping the number of molecules and brightness in the laser scanning microscope,” *Biophysical Journal*, vol. 94, no. 6, pp. 2320 – 2332, 2008.

Acknowledgements

I would first like to thank Prof. Aleksandra Radenovic, my PI, for having taken me in her yet-to-be lab, and having allowed me to work independently while maintaining her constant support for this project. I would also like to acknowledge the great energy she put in getting the lab started from scratch.

During the course of this project I benefited from a number of interactions, ranging from lab hospitality to insightful discussions, with many stimulating and supportive scientists. I would therefore like to thank Prof. Enrico Gratton for his hospitality in the LFD in Irvine. Ranieri Bizzarri from Scuola Normale in Pisa for sharing his expertise on fluorescent proteins. Prof. Luca Scorrano for generously hosting a physicist in their very biological mitochondrial group meetings in Geneva and for his constant interest in dual-color PALM imaging.

I would also like to thank Prof. Alberto Diaspro, Prof. Roberto Maggio and Prof. Aleksander Verkhovski, as well as Prof. Henrik Rønnow, for taking the time to read this thesis and being part of the jury.

Within EPFL I would like to thank Prof. Hilal Lashuel and Annalisa Ansaloni for advice and support regarding the purification and spectroscopic characterization of mEos2 and Prof. Ursula Roethlisberger and Stefano Vanni for their collaboration and support in the counting project. I should also thank Dr. Graham Knott for his help in preparing thin sections. Prof. Georg Fantner and Pascal Odermatt for developing the idea of AFM-PALM. Prof. Theo Lasser for insightful comments on TIRF design. Prof. László Forró and Dr. Sylvia Jeney for opening the doors of their lab prior to the beginning of my PhD. Prof. Aleksander Verkhovskhy for many insightful suggestions. I would also like to acknowledge the professional support from the staff of the BM mechanical workshop, electronics support from Ronald Gianotti and help from Vincent Berseth in giving to the LabView code an efficient shape.

A special thank you goes to Marco, for his close collaboration on a large part of this project, for his teachings in cell and molecular biology and for the many outstanding dinners at his and Ethel's place. I would then like to thank all my other colleagues and neigbours for creating a friendly working environment. Thanks to Jacopo, Alessandro, Floriano, Andreas, Camille, Serena, Simone, Lely, Lorenz, Metin, Fabrizia, Helen, Sudhir, Arun for keeping the environment friendly and cooperative. I would like to thank Mattia for his dedicated and supportive collaboration on the dual-color registration project.

I would like to use this page to thank also Prof. Fabio Biscarini and Dr. Eugenio Lunedei for their generous scientific guidance after my graduation in 2006 and to acknowledge the wise suggestion of Prof. Giacinto Scoles to pursue a PhD in biophysics, as well as to thank him for his understanding.

Without the loving and patient support of Valentina this work would not have been possible, and it is to her, as well as to my family, that I dedicate this thesis.

Paolo Annibale

p_annibale@yahoo.com
+41762700624
+393384824434

Professional experience

EPF Lausanne – **Scientific Assistant** *Laboratory of Nanoscale Biology* Realization of a Photo Activated Localization Microscopy setup to characterize the nanoscale spatial organization of plasma membrane receptors involved in cellular signaling. Supervision of two undergraduate students working on related projects *Principal Investigator: Aleksandra Radenovic*	Lausanne, Switzerland 10/2008-present
National Research Council of Italy – **Research Fellow** *Institute for the Studies of Nanostructured Materials (CNR-ISMN)* Investigation the local electrostatic potential in working organic ultra-thin film transistors using scanning probe methods *Principal Investigator: Fabio Biscarini*	Bologna, Italy 04/2007-04/2008
Paul Scherrer Institut – **Intern** *Swiss Light Source, Protein Crystallography Beamlines* Design of an automatic system to align protein crystals to the X-Ray beam using their ultraviolet fluorescence *Principal Investigator: Clemens Schulze-Briese*	Villigen, Switzerland 07/2005-09/2005
National Institute for Nuclear Physics – **Intern** *ALICE Time of Flight group* Design and test of an optical automatic system for the quality control of the detectors used in the Time of Flight detector of ALICE, one of the experiments of the Large Hadron Collider in Geneva *Principal Investigator: Maurizio Basile*	Bologna, Italy 06/2004-10/2004

Education

PhD Candidate, Faculty of Basic Sciences, EPF Lausanne *Thesis:* Investigating the impact of single molecule fluorescence dynamics on Photo Activated Localization Microscopy experiments *Advisor: Aleksandra Radenovic*		Lausanne, Switzerland 12/2008-present
Licenza del Collegio Superiore Alma Mater Studiorum *Competitive fellowship offering interdisciplinary course, granting exemption from tuition fees and covering boarding and living expenses. 30 top students enrolled to the University of Bologna are selected each year*		Bologna, Italy 12/2006
Masters Degree in Solid State Physics, University of Bologna *Thesis:* Scanning probe microscopy for the study of organic thin film transistors *Advisor: Fabio Biscarini*	**110/110 cum laude**	Bologna, Italy 10/2006
Bachelor Degree in Physics, University of Bologna *Thesis*: Ideation and test of an automatic quality control system for the Multigap Resistive Plate Chambers of the Time Of Flight of ALICE (A Large Ion Collider Experiment) *Advisor: Maurizio Basile*	**110/110 cum laude**	Bologna, Italy 10/2004
Maturità Classica Sperimentale Liceo Classico Gian Domenico Romagnosi	**100/100 cum laude**	Parma, Italy 07/2001

Publications

Journal Articles

1. M. Scarselli*, **P. Annibale*** and A. Radenovic, Cell-type-specific β2 adrenergic receptor clusters identified using photo-activated localization microscopy are not lipid raft related, but depend on actin cytoskeleton integrity, *Journal of Biological Chemistry*, 287, 16768-16780 (2012) (*equal contribution)
2. **P. Annibale**, S. Vanni, M. Scarselli, U. Rothlisberger and A. Radenovic, Identification of clustering artifacts in photoactivated localization microscopy, *Nature Methods*, 8, 527-528 (2011)
3. **P. Annibale**, S. Vanni, M. Scarselli, U. Rothlisberger and A. Radenovic, Quantitative PhotoActivated Localization Microscopy: unraveling the effects of photoblinking, *PLoS One* 6(7) (2011)
4. S. Husale, S. Sahoo, A. Radenovic, F. Traversi, **P. Annibale** and A. Kis, ssDNA Binding Reveals the Atomic Structure of Graphene, *Langmuir*, 26, 23, 18078-18082 (2010)
5. **P. Annibale**, M. Scarselli, A. Kodiyan, A. Radenovic, Photoactivatable Fluorescent Protein mEos2 Displays Repeated Photoactivation after a Long-Lived Dark State in the Red Photoconverted Form, *The Journal of Physical Chemistry Letters* 1 (9), 1506-1510 (2010)
6. P. Stoliar, E. Bystrenova, S. D. Quiroga, **P. Annibale**, M. Facchini, M. Spijkman, S. Setayesh, D. de Leeuw and F. Biscarini, DNA adsorption measured with ultra-thin film organic field effect transistors, *Biosensors and Bioelectronics*, 24, 2935–2938 (2009)
7. J. Preiner, N. S. Losilla, A. Ebner, **P. Annibale**, F. Biscarini, R. Garcia and P. Hinterdorfer, Imaging and Detection of Single Molecule Recognition Events on Organic Semiconductor Surfaces, *Nano Letters*, 9(2), 571–575 (2009)
8. **P. Annibale**, C. Albonetti, P. Stoliar, F. Biscarini, High resolution mapping of the electrostatic potential in organic thin film transistors by phase electrostratic force microscopy, *Journal of Physical Chemistry A*, 111, 12854-12858 (2007)
9. P. Stoliar, M. Massi, R. Krishnagar, **P. Annibale**, C. Albonetti, F. Biscarini, D. de Leeuw, Charge Injection across self assembled monolayers in organic field effect transistor: Odd-Even effects, *Journal of the American Chemical Society*, 129, 6477-6484 (2007)

Oral presentations

1. Towards dual color PALM imaging, *OWLS 2012*, Genoa July 4th-6th 2012
2. Investigating the impact of photo-blinking on Photo Activated Localization Microscopy experiments: an application to dual color imaging of cell membrane receptors, *Focus On Microscopy 2012*, Singapore April 1st-4th 2012
3. High resolution mapping of the electrostatic potential in organic thin film transistors by phase electrostratic force microscopy, *DPG Spring Meeting*, Berlin February 25th-29th 2008

Posters

1. Investigating the impact of photoblinking on Photo Activated Localization Microscopy experiments, *Biophysical Society Meeting*, San Diego, February 25th-February 29th 2012
2. Realization of a dual-color Photo Activated Localization Microscopy experimental setup for the direct visualization the G protein and G Protein Coupled Receptor partners on the cell plasma membrane, *Gordon Research Conference Single Molecules Approaches to Biology*, Lucca Italy June 27th -July 2nd 2010
3. Towards a quantitative definition of the charge distribution of T6 films by Phase electrostatic force microscopy, *Nanoitaly*, Miramare (TS) 22nd-24th May 2006

Honors and awards

Registration award, 6th LFD Workshop in Advanced Fluorescence Imaging and Dynamics, Irvine	2011
EPFL award for outstanding performance	2011
Fellowship from Collegio Superiore Università di Bologna covering tuition fees and living expenses	2001-2006

Languages

Italian: native; **English**: excellent; **French**: good;

Technical skills

Optical Fluorescence Microscopy, Confocal and Total Interna Reflection, Super Resolution Fluorescence Microscopy
Optical Trapping
Scanning Probe Microscopies (Atomic and Electrostatic Force Microscopy, Scanning Tunneling Microscopy)
Electrical measurements and characterization of organic electronic devices
Organic molecular thin film growth and characterization
High and Ultra High Vacuum technology, evaporation systems
Soft Lithography
Molecular and cell biology
Programming and data analysis: LabView, Matlab, IgorPro, CAD

Other experiences

Elected ***representative*** of PhD student in the Phyiscs Doctoral Program Commission, EPF Lausanne (2010-2012), Elected ***representative*** of students in the board of the Faculty of Science of the University of Bologna (2006), kitchen porter at ***Harrods Knightsbridge*** London (2000), winner of ***Italian Air Force*** competition for High Schools (2000), ***AFS international student exchange*** to ***Australia*** (1999-2000); Conservatory of Parma, ***Pianoforte*** (1996-2000); ***webmaster*** of High School Website (1998-2001); director of the ***school magazine*** (1995-1996); volounteer in a ***public library*** in Rome (1995-1996)

Interests

Hiking, science fiction, ancient history, model aircrafts, classical music